



Estimation of the amplitude of the Martian hum from Global circulation models and expected observation challenges

Yasuhiro Nishikawa

► To cite this version:

Yasuhiro Nishikawa. Estimation of the amplitude of the Martian hum from Global circulation models and expected observation challenges. Earth Sciences. Université Paris Cité, 2020. English. NNT : 2020UNIP7237 . tel-03510578

HAL Id: tel-03510578

<https://theses.hal.science/tel-03510578>

Submitted on 4 Jan 2022

HAL is a multi-disciplinary open access archive for the deposit and dissemination of scientific research documents, whether they are published or not. The documents may come from teaching and research institutions in France or abroad, or from public or private research centers.

L'archive ouverte pluridisciplinaire **HAL**, est destinée au dépôt et à la diffusion de documents scientifiques de niveau recherche, publiés ou non, émanant des établissements d'enseignement et de recherche français ou étrangers, des laboratoires publics ou privés.

Université de Paris

Ecole doctorale STEP'UP 560

Institut de physique du globe de Paris

**Estimation of the amplitude of the Martian hum
from Global circulation models and expected
observation challenges**

Par Yasuhiro NISHIKAWA

Thèse de doctorat de Sciences de la Terre et de l'Environnement

Dirigée par Philippe Lognonné

Présentée et soutenue publiquement le 15 Décembre 2020

Devant un jury composé de :

Mme Séverine ROSAT, Chargée de Recherche, CNRS, HDR, Rapportrice
(Institut de physique du globe de Strasbourg)
Mr Kiwamu NISHIDA, Professeur Associé, Rapporteur (Université de TOKYO, ERI)
Mr David MIMOUN, Professeur, Examineur (ISAE SUPAERO)
Mme Éléonore STUTZMANN, Physicienne, Examinatrice
(Institut de physique du globe de Paris)
Mme. Aymeric SPIGA, Maître de Conférence- HDR, Examineur
(Sorbonne Université, Laboratoire de Météorologie Dynamique)
Mr. Philippe Lognonné, Professeur, Directeur de thèse
(Institut de physique du globe de Paris)
Mr. Taichi KAWAMURA, Maître de conférence, co-encadrant invité
(Institut de physique du globe de Paris)



Except where otherwise noted, this work is licensed under
<https://creativecommons.org/licenses/by-nc-nd/3.0/fr/>

REMERCIEMENTS

First of all, I would like to thank my Ph.D. supervisor, Philippe Lognonné, who is the smartest person I know. He taught me not only scientific theories but also how to face science seriously. He has truly taught me a new world. He would answer my questions, but sometimes he would spend hours solving problems with me. That was an irreplaceable time for me. He always had positive words, encouraging me to do what little I could to help when I was nervous. I cannot thank him enough.

Secondly, I would like to thank my co-supervisor, Kei Kurita, who taught me what research and inspiration are. He introduced many precious people to me. He is precisely the origin of my research life. My sincere thanks must also go to Taichi Kawamura and his family, both in my public and private lives. I could not have done this thesis without their support.

The GCMs and Martian climate data were obtained from LMD team, Aymeric Spiga, François Forget, and Tanguy Bertrand. They always welcomed me when I go to their laboratory every time. My special thanks are due to Eléonore Stutzmann for valuable discussion. Her helpful comments improve my paper and this thesis both. This thesis owes much to the thoughtful and helpful discussion with my best friend Virgile. We were solving many equations until it got dark. My family and his family get along well too. I cannot thank them too much for their hospitality. I am indebted to ERI and JAXA people. Kiwamu Nishida and Naoki Kobayashi are great pioneers, Akito Araya provided knowledge of engineering seismology to me. My ERI colleagues took great care of me even after my leaving Japan. I wish to thank Severine Rosat for reading the entire thesis. Her accurate and quick advice improved this thesis. The two months of study at UC Berkeley, which Barbara Romanowicz recommended me to go, gave me a good idea for my thesis.

I gratefully acknowledge helpful discussions with InSight science team on several points in the thesis. Especially David Mimoun, Naomi Murdoch, and Raphael Garcia for helpful suggestions. I wish to express my gratitude to my colleagues at IPGP - Balthasar, Foivos, Mélanie, Clé-

ment, Baptiste, Alicia, Pierdavide, Agnès, Elvira, Lucile, and Claudine. They have supported me and had to put up with my stresses and bad French for the past four years of study. My sincere thanks also go to Ken-ichiro Gida and Hirobe, who are my classmates from Japan. They came to see me from 10,000km far from Paris. Their visit encouraged me greatly. The thesis writing was made possible largely through grants from Centre national d'Etudes spatiales (CNES), Japan student services organization (JASSO), IPGP contribution, and InSight contribution.

Finally, thank my family from the bottom of my heart. I sincerely appreciate my father and mother's devoted concern. My sister and brother came home to meet me. My late grandparents were happier than anyone else to hear about my entrance into the university. I can never thank them enough.

Osaka, le 14 décembre 2020.

Titre Estimation du hum martien à partir des modèles de circulation globales et du défis des observations attendues.

Résumé La structure interne de Mars est essentielle pour comprendre la formation et l'évolution des planètes tellurique, y compris la Terre. La plupart des informations sur l'intérieur de la Terre proviennent de la sismologie. Ainsi, l'exploration sismique de Mars devrait jouer un rôle tout aussi important dans les études de structure interne. Pour acquérir et analyser des données sismiques sur Mars, la réduction du bruit et la modélisation du signal sismique sont essentielles. Cette thèse comporte donc une première partie liée aux aspects expérimentaux de la sismologie martienne et les trois autres liées aux aspects de modélisation.

Tout d'abord, j'ai conçu, dans le cadre de l'effort japonais pour explorer Mars avec un futur lander martien, un pare-vent efficace pour la réduction du bruit du vent. Cela a été réalisé grâce à des tests en soufflerie et des simulations CFD (calcul en dynamique des fluides). Le design est nettement plus léger que le pare-vent d'InSight. Les tests en soufflerie dans un environnement similaire à Mars (basse pression et vitesse du vent élevé) ont particulièrement montré que le couple est plus critique que la force de portance pour la génération du bruit sismique. Le couple a en outre changé radicalement avec la forme du pare-vent. Nous avons conçu un pare-vent sans couple par CFD et démontrons une efficacité environ 8 fois meilleure qu'un simple pare-vent. Le pare-vent sans couple pourrait être proposé pour une future mission et optimise fortement l'allocation de masse par rapport à InSight.

Dans la section modélisation, je propose une estimation de l'amplitude des MBF (oscillations du bruit de fond sismique de Mars) excitées par les GCM (General Circular Models). La modélisation a été réalisée avec deux approches différentes. Le premier considère les forces de pression à la surface de Mars, tandis que le second considère mieux le couplage solide-atmosphère en tenant compte des ondes compressibles (ondes acoustiques) dans l'atmosphère. Les sismogrammes MBF résultants sont ensuite comparés au bruit propre de l'instrument InSight VBB. Les signaux sont estimés à environ $5 \times 10^{-11} m/s^2 / \sqrt{Hz}$, qui sont plus petits que le bruit instrumental et le bruit thermique du sismomètre. Les MBF peuvent ne pas être détectés à ce niveau sans stacking. La météorologie martienne est cependant dominée par le flux solaire et l'heure locale. Nous analysons donc la périodicité de la force d'excitation des MBF et concluons que les signaux des MBF pourraient être

détectés avec plusieurs mois de stacking en raison de sa périodicité. La sensibilité des MBF au manteau peu profond et moyen est également étudiée. Enfin, je calcule les nombres de Love de Mars pour étudier leur sensibilité au manteau inférieur et au noyau, car on ne s'attend pas à des détections d'oscillations libres sensibles à grande profondeur. Bien qu'elle ne soit pas encore utilisée pour Mars, cette partie a été utilisée pour les données lunaires et nous avons analysé l'impact du modèle de Burgers étendu sur les contraintes sur la température de l'intérieur profond lunaire avec une implication sur la sismicité du tremblement de lune profond.

Mots-clés Mars, atmosphère, modes propres, structure interne, nombres de Love, sismologie planétaire

Title Estimation of the amplitude of the Martian hum from Global circulation models and expected observation challenges.

Abstract Le résumé en anglais.

The internal structure of Mars is key for understanding the formation and evolution of terrestrial planets, including Earth. Most of the Earth's interior information comes from seismology. Thus, Mars seismic exploration is expected to play an equally important role in internal structure investigations. To acquire and analyze seismic data on Mars, noise reduction, and seismic signal modeling are critical. This Ph.D. has therefore a first part related to experimental aspects of Mars seismology and the three others related to modeling aspects.

First, I designed, in the frame of the Japan effort to explore Mars with a future Mars lander, an efficient wind shield for wind noise reduction. This was made through wind tunnel tests and CFD (computation fluid dynamics) simulations. The design is significantly lighter than the Wind Shield of InSight. Wind tunnel tests under a similar environment to Mars (low pressure and high wind speed) have especially shown that torque more critical than lift force for seismic noise generation. Torque also changed dramatically with the shape of wind shield. I designed a torque-less wind shield by CFD and demonstrated an efficiency of about 8 times better than a simple wind shield. The torque-less wind shield might be proposed for future missions and is strongly optimizing the mass allocation as compared to InSight.

In the modeling section, I provide the estimation of the amplitude of MBFs (Mars Background Free oscillations) as excited by GCMs (General Circular Models). The modeling has been made with two different approaches. The first one is considering pressure forces at the surface of Mars, while the second one is better considering the solid-atmosphere coupling by accounting for compressible waves (acoustic waves) in the atmosphere. The resulting MBF seismograms are then compared with the self-noise of the InSight VBB instrument. Signals are estimated to about $5 \times 10^{-11} m/s^2 / \sqrt{Hz}$, which are smaller than the seismometer instrumental noise and thermal noise. The MBFs might not be detected at this level without stacking. Martian weather is however dominated by solar flux and local time. I, therefore, analyze the periodicity of the excitation force of MBFs and conclude that the MBFs signals might be detected with several months of the stack due to its periodicity. The MBFs sensitivity to the shallow and middle mantle is finally studied.

Finally, I calculate the Love numbers of Mars to study their sensitivity to the lower mantle and core. Although not yet used for Mars, this part has been used for Moon data and I have analyzed the impact of the extended Burgers model on constraints on the Lunar deep interior temperature, with implication on the deep moonquake seismicity.

Keywords Mars, atmosphere, Normal mode, internal structure, Tidal deformation, Love number, Planetary seismology

TABLE DES MATIÈRES

TABLE DES MATIÈRES	10
LISTE DES FIGURES	12
LISTE DES TABLEAUX	22
1 INTRODUCTION	1
1.1 MARS INTERNAL STRUTCURE	1
1.2 SEISMIC OBSERVATION.	4
1.2.1 Normal mode observation.	5
1.2.2 Planetary background free oscillations.	8
1.3 MARTIAN ATMOSPHERE	13
1.3.1 Observation	14
1.3.2 Martian General Circular Models	15
1.3.3 Seismological point of view	19
1.4 TIDAL DEFORMATION	21
1.5 SCOPE OF THIS STUDY.	22
2 WIND SHIELD DEVELOPMENT FOR JAPANESE MISSION	25
2.1 INTRODUCTION	25
2.2 PAST STUDIES	27
2.3 WIND SHIELD DEVELOPMENT	28
2.3.1 Design principles	29
2.4 WIND TUNNEL TEST	29
2.5 NUMERICAL SIMULATIONS	30
2.5.1 Simulation conditions	33
2.5.2 Calculation methods of lift force and torque.	35
2.6 RESULTS	35
2.6.1 Wind tunnel test result	35
2.6.2 Numerical simulation	39
2.7 DISCUSSION	42
2.7.1 Stability of the wind shield	47
2.7.2 Tilt noise	47

2.8	CONCLUSION	51
3	NORMAL MODE PROPAGATION AND COUPLING WITH THE ATMOSPHERE AND GROUND.	53
3.1	NORMAL MODE WITH ATMOSPHERE	55
3.2	SIMPLIFIED NORMAL MODE COMPUTATION	58
3.2.1	Approximation of the excitation force terms	63
3.2.2	Moment tensor of the excitation.	66
3.3	SOLUTIONS FOR THE NORMAL MODES	69
3.3.1	Strain and Stress	69
3.3.2	Normal modes properties	69
4	MARS BACKGROUND FREE OSCILLATIONS	73
4.1	THE MARS GENERAL CIRCULATION MODEL	77
4.2	MARTIAN NORMAL MODES	80
4.2.1	The Martian Model	80
4.2.2	Normal Modes excitation	80
4.3	RESULTS AND DISCUSSION	84
4.3.1	Normal Modes Amplitude.	84
4.3.2	Normal Modes Detection and Seismometer Performances.	86
4.3.3	Internal model dependency.	88
4.3.4	Daily repetition of martian weather and spectral stacking method.	89
4.3.5	Estimation of the seismic magnitude of the MBF signal	90
4.4	CONCLUSION	93
5	LOVE NUMBERS AND DEEP INTERNAL STRUCTURE.	95
5.1	Q AND K2 OBSERVATION.	96
5.2	RHEOLOGY	99
5.2.1	On Theory	101
5.3	BENCH MARK TEST BY MOON.	102
5.3.1	Comparison with observation data.	103
5.4	IMPLICATION FOR INSIGHT	106
5.5	CONCLUSION	108
	CONCLUSION GÉNÉRALE	111
A	ANNEXES	115
A.1	CANONICAL BASIS AND GENERALIZED SPHERICAL HARMONICS	119
A.1.1	Spherical basis	120
A.1.2	Canonical basis	120
A.1.3	Passage from the spherical basis to canonical	120

A.1.4	generalized spherical harmonics	122
A.2	DATA INTERPOLATION.	123
A.2.1	Linear interpolation	123
A.2.2	Spline interpolation	124
BIBLIOGRAPHIE		187

LISTE DES FIGURES

1.1	Possible Mars internal models (<i>Smrekar et al.</i> , 2019). The models are estimated by geodetic observations, chemical experiments and chemical analysis of the SNC meteorites, for which a Martian origin is commonly accepted, since we have no seismic information about Mars.	2
1.2	Internal structure of terrestrial planets (https://solarsystem.nasa.gov). Some scientific measurements indicate that interior of these planets are different from each other. The differences likely come from their thermal evolutions and origins.	3
1.3	Possible density structure of Mars <i>Harder</i> (1998). Solid (0 %), dotted (14 %), and dashed (36.5 %), lines indicate sulphur content of the core. It is found that, the depth of the spinel to perovskite transformation is 1910 km, which corresponds to a radius of about 1500 km. Thus a perovskite layer exists in Mars if the core radius is small. This affects not only present internal structure but also mantle convection and evolution of Mars.	4

1.4	Seismic exploration techniques by travel-time analysis. (A) : Seismic waves propagate in every direction, one of them propagates directly toward an observing station, some of them propagate in layers. Wave reflections and refractions occur between layers discontinuities. In addition to the direct waves, some reflected and refracted waves also reach the observation station. By analyzing seismic waves that reach the station with different paths, we can investigate the seismic velocity structure of a planet. (B) : Surface wave propagates in a surface layer and reaches a observe station. Body waves (P-wave and S-wave) propagate in internal layers. Body waves reflect and refract in the layers. Wave velocities of these surface waves and body waves are different which provides us information on the stratification and their mechanical properties.	6
1.5	Spectrum of the Earth free oscillations. The frequency and amplitude of the modes are derived as a function of the Earth's internal structure and its size (<i>Park et al.</i> , 2005). . . .	7
1.6	Earth and Mars weather models. The weathers of the Earth and Mars are very different. On Earth, the weather depends on several parameters. These factors are mainly risen by water in liquid, gaseous, or ice forms. Water generates clouds, sea, and rivers which make atmospheric activities complex. On Mars, solar flux is the only major factor of weather. This makes Martian atmospheric activity far more simple compared to that of the Earth and generates daily cyclic atmospheric activities.	14
1.7	Typical scales of martian atmospheric simulations and meteorological models suitable for their analysis <i>Spiga and Lewis</i> (2010). MBFs are global seismic event which is excited by global atmospheric activities. Thus GCMs are suitable for the calculation of MBFs.	16
1.8	3D wind velocity field generated with GCMs. GCMs can simulate the whole 3D martian atmospheric activities. . . .	17

1.9	Spectrum of GCM pressure and observed pressure. The observational data were acquired by Mars Pathfinder (LS=170°). The GCM spectrum is computed for the same location as the observational data of Mars Pathfinder (LS = 0°). The results differ by an order of magnitude, implying that GCMs cannot fully explain the observed energy, which is likely due to inadequate modeling in GCMs of local-scale turbulences. Thus, MBFs calculated by using GCMs should be regarded as a lower limit of possible excitations.	20
1.10	Mechanism of two water tides of the ocean. The tidal force is summation of centrifugal force and gravitational force. The tide acts not only at the ocean but also Earth and Lunar solid body. The solid part deformation occurs from the surface to the core. In short, the tidal deformation includes whole internal structure of the sold body.	23
2.1	Forces related to wind shield design. The lift force reduces static frictional force. Large wind forces and small static frictional forces slide the wind shield. The torques strain the ground. Large strain generates ground tilt which is expected to be noise for seismic observation.	30
2.2	Planetary environment wind tunnel(JAXA/ISAS Sagamihara)	31
2.3	Geometry of the wind tunnel facility (left) top view above and (right) side view.The size of the table is 1-by-1.5m. A diameter of the wind tunnel is 2m. I measured weight of wind shield weight at red 3 points.	31
2.4	Semisphere wind shield (left) top view above and (right) side view. This stainless-steel wind shield is 40cm diameter and 16cm height. The windshield has an edge but the edge is thin enough that it does not interfere the test.	32
2.5	Truncated circular cone wind shield from (left) above and (right) side. This stainless-steel wind shield is 40cm diameter and 16cm height.	32
2.6	Simulation conditions. I put a wind shield of 40 <i>cm</i> in diameter and 16 <i>cm</i> in height. The wind flows into the box from one side and flow out to the other side.	35
2.7	Wind shield's torque and lift force calculation.	36

2.8	Wind tunnel results of the lift forces with error bars. The straight lines are calculated by the least square method. I found a proportional relationship between lift force and dynamic pressure.	38
2.9	Wind tunnel results of the torques with error bars. Using the least square method and I found a proportional relationship between torque force and dynamic pressure.	39
2.10	Semispherical and circular truncated cone wind shield's pressure distribution view from the top. The simulation is done under 20 m/s wind velocity and 0.1 atm which is close to the wind tunnel test's conditions.	40
2.11	Semispherical and circular truncated cone wind shield's pressure distribution view from the side. The simulation is done under 20 m/s wind velocity and 0.1 atm which is close to the wind tunnel test's conditions.	40
2.12	Designed wind shield's pressure distribution. The simulation is done under 20 m/s wind velocity and 0.1 atm which is close to the wind tunnel test's conditions.	41
2.13	Stream lines seen from the top. Red and blue color show positive and negative pressure respectibly. Torque direction is explained by the balance between the positive and negative pressure.	43
2.14	Stream lines seen from the side	44
2.15	Velocity vectors at just leeward from the shields (at the red line of Fig. 2.16). Arrows show wind vectors. We can see the Eddies have been developed at this area.	45
2.16	Streamwire velocity and turbulent and stream bending areas. The turbulence (green area) pulls the wind shields to upward. The bending wind (red area) generates torque to roll the windshield.	46
2.17	Martian wind data at Phoenix landing site. Location : E-125.7 N68.2, Sampling : 50 s, Local time : daytime of Mars, Average velocity : 5.1 m/s. The observation data has high amplitude in the range of around $10^{-3}Hz$	49

2.18	Expected noise and sensitivity of the seismometer. The sensitivity of the seismometer is a requirement of the InSight mission seismometer. The ground tilt would be a noise source if the expected noise rises the sensitivity. The average of the wind velocities is 5 m/s, 20 m/s, and 50 m/s at Phoenix landing site, windy site, and stormy site respectively. In windy and stormy conditions, only the designed shield is effective to protect the seismometer.	50
3.1	Variation of atmospheric scale height in a day. The red area is hot and blue is the opposite. Because of the big temperature variation, the scale height changes from 8 to 12 km thickness in a day. During day time, the atmosphere expands to 12 km height, during night time it is opposite, it shrinks to 8 km height. The scale height variation affects normal mode structure directly. The iso-sphere model cannot describe this lateral effect.	56
3.2	Kernel sensitivity of normal modes in the air. Blue one includes radiative boundary, viscosity and relaxation. Green one consider only for wave propagation and transmission. Solid lines and dot lines are real part and imaginary part respectably. In $n \geq 10$ order, the gaps between 2 normal modes are small under scale height.	58
3.3	Kernel sensitivity of normal modes in air. At the normal mode of angular order nine, the large gaps occur because of the resonance between the atmosphere and the solid part. The normal mode cannot describe this resonance, so the normal mode calculation only works for angular order 10. Below angular order 10, normal modes are hard to detect because of the low-frequency thermal noise.	59
3.4	Relative atmospheric energy of surface wave in the Mars atmosphere for Rayleigh surface waves. From left to right, the number of the angular order is 2,3,4 ... up to 39. The peak of the fraction is at angular order 9 (around 2.2 mHz). At the first peak, there is a strong resonance between atmosphere and solid part.	59

3.5	GCM wind velocity field. Horizontal winds (North-South and East-West winds) are much faster than vertical wind. Thus the main contribution of reynolds stress of excitation force (ρvv in eq 3.12 is composed by horizontal winds.	62
3.6	The derivative of elastic pressure in the air. The magnitude of the amplitudes are $\approx 10^{-7} Pa \cdot s^{-1}$. They are enough small compare to the derivative of static pressure.	63
3.7	Pressure fields at 4.5[m] height. The upper figure is atmospheric pressure field. The middle figure is time differentiated atmospheric pressure. The middle figure is height differentiated atmospheric pressure. Amplitude of the time differentiated pressure is $\approx 10^{-3} Pa \cdot s^{-1}$. This time differentiated pressure is significantly larger compare to the derivative of elastic pressures $\approx 10^{-7} Pa \cdot s^{-1}$	64
3.8	Air density, temperature and time differentiated air density at the surface. The air density varies about $10^{-3} kg m^{-3}$ between day time and night time. The amplitude of the time differentiated air density is about $10^{-7} kg m^{-3} s^{-1}$	65
4.1	Martian atmospheric pressure fluctuations as are simulated by the LMD GCM for the Mars meridian of longitude 0° . All pressure records have been demeaned and only the variation of pressure is shown. The vertical axis is latitude, the horizontal axis is local time hr The large pressure fluctuations occur at sunrise and sunset. The shape of the pressure fluctuations repeats very similarly day after day. This strong daily repetition is not common on Earth.	74
4.2	Martian atmospheric pressure fluctuation in the frequency band where normal modes concentrate. I applied a band-pass filter between 1.0 and 2.0 mHz to the raw pressure data (shown in Fig. 4.1). The daily repetition of Martian weather processes is clearly shown in the pattern. The band of the pattern 1.0 - 2.0 mHz corresponds to low degree (angular order 2-8) MBFs frequencies. The pressure fluctuations in the atmosphere excite daily coherent MBFs.	75

4.3	Martian atmospheric pressure fluctuation at frequency band where normal modes concentrate. I applied a band-pass filter between 2.0 and 3.0 mHz to the raw pressure data (shown in 4.1). Big pressure fluctuations at this band occur 2 times a day (at sunrise and sunset). The frequency band corresponds with middle degree (angular order 9-15) MBFs. Normal modes at this frequency are sensitive to upper mantle (see Fig. 4.5).	76
4.4	Pressure spectrum of GCMs' pressure and observed pressure. The observation data is measured by Mars Pathfinder (LS=170 degree). The spectrum of GCMs is computed at the same location as the observation data of Mars Pathfinder (LS=0 degree). GCMs lose some energy in this frequency period. But the MBFs calculations using GCMs are useful as lower limit estimations.	79
4.5	Vertical amplitude of spheroidal fundamental normal modes in the solid part of Mars. Low degree normal modes are low frequency. Large amplitude area concentrate the mode's energy and sensitivity. Low degree waves (angular order 2-9) have sensitivities at core and deep mantle. High degree waves (angular order 10-39) have sensitivities at middle and shallow part of mantle. Each mode has sensitivity at a different depth.	81
4.6	Pressure glut and reynolds stress of GCM. Variation of pressure amplitude of pressure glut is stronger than reynolds stress (in left figure). Pressure glut is stronger than reynolds stress at low frequency and it is reversed at high frequency. At the high frequency, main contribution of the pressure variation is eddies. The eddies generate reynolds stress by its wind variations. GCM loses energy of eddies at low frequency.	84
4.7	7 martian days MBF acceleration. The MBF is sum of angular order 2 to 39 fundamental normal modes. The amplitude is nanogals ($10^{-11}m/s^2$). The MBF continues for days since the normal modes are excited by continuous atmospheric activities. The first 3 sols data is meaningless results in a boundary condition of GCMs and stability of MBFs.	85

4.8	Acceleration power spectrum density of MBF. Each peak shows its normal mode. There is 38 peaks in this figure from angular order 2 to 39 respectably. The time step of GCM is 61.5s (=8.13 mHz). I cannot calculate MBFs above 39th angular order.	85
4.9	Power spectrum acceleration density of MBF and instrumental, environmental noise. Above 5 mHz (angular order 22), thermal noise is much larger than signals. Below 6.5 mHz (angular order 30), the MBF signal overcome both instrumental and thermal noise. The signal may be detected MBF by high gain mode SEIS seismometer during night time. The overcame signals have sensitivities at middle and shallow part of mantle.	88
4.10	Example of difference in MBF spectra from different Martian inner structure. I use two internal models of Mars. These two models have different mantle thicknesses. The position of peaks is different. The figure clearly shows different peak positions for different mars models. The difference in peak positions is about 0.1 mHz, which will be the frequency resolution required to discriminate between the 2 models.	89
4.11	Pressure correlations at normal mode band frequency. High correlations are in exactly day and semi-diurnal. One day high correlations are sunrise - sunrise and sunset - sunset correlation. Semi-diurnal correlations are sunrise - sunset and sunset - sunrise correlations (semi-diurnal thermal tide). The periodic excitation force generates high efficiency of stacking. This precise phenomenon occurs on Mars but not on Earth.	90
4.12	Pressure correlations at normal mode band. High correlations are exactly in a day and semi-diurnal period. One day high correlations are sunrise - sunrise and sunset - sunset correlation. Semi-diurnal correlations are sunrise - sunset and sunset - sunrise correlations (semi-diurnal thermal tide).	91
4.13	One week stacking effect. The daily stacking makes large and clear peaks. When MBFs are stacked more and more, the normal mode peaks become bigger and sharper.	91

4.14	Acceleration spectral density of MBF and free oscillations. The MBFs are excited by Martian atmosphere and others are theoretical spectra assuming seismic excitations of seismic events. The magnitudes of the events are M4.5, 5.0 and 5.5. MBFs is close to M5.0 oscillations. This result is consistent with estimations made with different approaches.	93
5.1	Deformation mechanism of planets and satellites. In case of perfect elastic body planet, its major axis points exactly toward the satellite. The direction of the major axis delays because of its friction. Torque resulting from the delay changes planet and satellite orbits and dissipates planetary energy. .	96
5.2	Principle of measurement. If the planet is perfect elastic body, deformation response occurs immediately and the bulge angle $\Delta\theta$ is 0. Actual value of the bulge angle is not 0. The bulge angle and deformation delay are generated by friction inside planet. In conversely, observation of the bulge angle enables me to estimate internal structure of the celestial body.	98
5.3	Basic stress models. Basically, materials can be divided into two groups according to the rheological reaction. The solid group is elastic and reversible deformation. The liquid group is plasticity and irreversible deformation. This stress is described by its rigidity and viscosity respectively. Viscoelastic materials are composed of these 2 types of rheology.	99
5.4	Viscoelastic models. These models are more complex than Maxwell model (simple viscoelastic model). More parameters and equations are required for these models than Maxwell model. These models, however, can calculate broadband phenomenon as like both tidal and seismic reaction of celestial body. Burgers is theoretical, Andrade is experimental model respectively.	101
5.5	Left figure shows shear modulus as a function of temperature and period. High temperature gives low shear modulus, but the differences are big at k_2 period. Right figure shows dissipation as a function of temperature and period. Low Q value (above of the figure) means more dissipative, the differences are big at tidal frequency of the Moon. . . .	103

5.6	Wave velocity in seismic frequency and tidal frequency. Wave velocity changes with frequencies. In the case shown in the figure, wave velocity at seismic frequency is 10 percentage faster than tidal frequency. The difference affects Love number calculations and estimations of internal structure.	104
5.7	Q calculation results at seismic frequency. Temperature and density profiles are input information. The profiles are estimated by observation and assumption of heat flux. Bottom left figure shows obtained wave velocity profile at seismic frequency. Wave velocity becomes slow when temperature becomes high. Bottom right is Q profile, the Q value is 100-150 at deep mantle.	105
5.8	Q calculation results at tidal frequency. Temperature and density profiles are same as the seismic frequency case. Bottom left figure shows obtained wave velocity profile at seismic frequency. Wave velocity becomes slow when temperature becomes high. Bottom right is Q profile, the Q value is less than 50 at deep mantle. The Q values are smaller than seismic frequency case.	106
5.9	Different results of Q value. Left and center figures are input temperature and seismic velocity (<i>Kawamura et al.</i> (2017)). Solid lines of right figure shows Q calculation results. Lines are input Q value to calculate net Q value. Calculation results of this model are $k_2 = 0.0257$ and $Q_{1mm} = 39.8$, $Q_{1cm} = 74.8$ ($k_2 = 0.02416 \pm 0.00022$ and $Q = 37.5 \pm 4$ <i>Williams et al.</i> (2014)). Grain size is important factor of Q value (eq (5.25)). .	107
5.10	Bench mark test of lunar k_2 and core status. Blue curve is k_2 and blue area is observed k_2 area. I fixed crust and mantle status (these status are determined by seismic observations). I changed thickness of outer core from 20 to 150 km to estimate the possible thickness. In this case, possible thickness of outer core is 50 to 130 km.	107

5.1	Sohl internal structure model and ± 100 km core lines. Seismic observations (MBFs observations) can estimate crust and shallow middle mantle structure, in other words, core and deep mantle structures are not observable in this case. 2 degree Love numbers (Tidal deformations) work as low degree normal mode. The Love numbers will provide information to distinguish between the 3 core sizes (sohl core, large core and small core) and fill-in the blank of internal structure estimation of seismic observations.	109
5.12	Simple sensitivity tests of InSight observation data. The tests provide a detection threshold of about 30 nanogal, likely about 100 times larger than the expected MBFs.	112
A.1	Spherical basis	119
A.2	Difference between the excitation calculated by Fortran and Matlab, sinusoidal excitation pressure and force. The magnitudes of the difference are 10^{-14} smaller than the signals.	124
A.3	Top 2 $p_k(t)$ s (excitations) are calculated by analytic and linear interpolation method (p_{k_linear} and p_{k_theory}). Bottom left figure is the $p_k(t)$ by linear interpolation (p_{k_linear}). Bottom right figure is the difference between p_{k_linear} and p_{k_theory} . This ratio of p_k signal and p_k difference is the error (precision) of our linear interpolation.	125
A.4	These lines are computation of 3 degree interpolation, analytic and linear interpolation results. Time step of cubic interpolation is 10[s], linear interpolation one is 61.5 s. The differences are error of interpolation method.	128
A.5	This figure shows spline interpolated p_k and its error. The error value is about 3%	128

Liste des tableaux

2.1	Calculation conditions	33
2.2	Semispherical shield's wind tunnel test results, average lift force and torque with errors.	37

2.3	Circular truncated cone shield's wind tunnel test results, average lift force and torque with errors.	37
2.4	Shape factors of the semispherical, circular truncated cone and designed shield and associated Torque coefficient	42
2.5	Ratio of noise free period with respect to the whole observation period. The ratio indicates the efficiency of the wind shields. The improvement introduced by the new design is particularly significant for higher-wind environments.	51
5.1	k2 numbers calculated by input models. Calculation results of 3 models. 1st model is Sohl model, 2nd model has same internal structure from surface to bottom of mantle, but the core is 100 km larger than Sohl model. 3rd one is similar with 2nd one, but the core is 100 km smaller than Sohl model.	108

INTRODUCTION

1

Mars is a neighborhood of ours. It is more than 60 million km distance but one of the closest friends from our home. It can be seen in the sky as a red bright star. Mars is one of the most familiar friends in the world. The planet has been handed down over many centuries. We have observed it for a long time by telescopes, orbits, landers, and vehicles. We know well the planetary surface by the observations, however, we know much less about its interior. This is one-sided knowledge, the interior of Mars is a clue of the history. Thus I started on the best way to get information on Martian deep structure.

1.1 MARS INTERNAL STRUCTURE

The internal structure of Mars provides an important piece of information on the origin and thermal evolution of Mars. Mars is one of the most observed celestial bodies. We launched many orbiters and sent landers and rovers which count up to more than 50 with those scheduled for launch in 2020 (e.g *Soffen and Snyder (1976); Malin et al. (1998); Smith et al. (1997); Crisp et al. (2003); McEwen et al. (2007); Hecht et al. (2009); Zeitlin et al. (2013)*). Most of the observations were either focused on the surface of Mars or were limited to the first 100 meters below the Martian surface, such as those by the radar onboard MarsExpress (*Jordan et al., 2009*). Our understandings of the internal structure are, therefore, limited due to the small number of observational pieces of evidence. We know the radius and the mass of the planet from telescopic observation of Martian natural satellites and remote sensing data (see *Smrekar et al. (2019)* for a review on the knowledge prior to InSight landing). We also have estimates of the moment of inertia and the k_2 Love number, which also constrain the internal structure of Mars, but the uncertainty is much

larger compared to the three previous parameters (Smrekar *et al.*, 2019). We also have some geochemical constraints from SNC meteorites, which are suspected to come from Mars (Dreibus and Wanke, 1985). These pieces of information were compiled to construct several models of internal structures of Mars. While, a variety of remote sensing and experimental information is useful to constrain the internal structure, lack of in-situ measurement related to the internal structure leaves large uncertainties on the model, especially in the deep region of the planet Fig. 1.1.

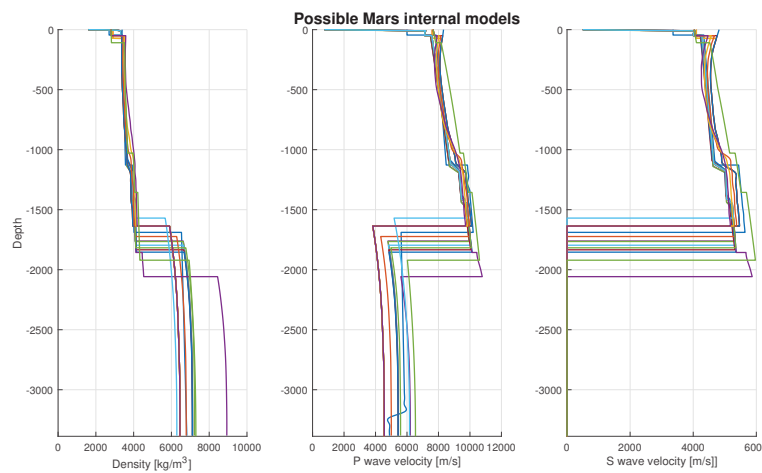


FIGURE 1.1 – Possible Mars internal models (Smrekar *et al.*, 2019). The models are estimated by geodetic observations, chemical experiments and chemical analysis of the SNC meteorites, for which a Martian origin is commonly accepted, since we have no seismic information about Mars.

The current internal structure is key information of rocky planet evolution. Gravitational, magnetic, or seismological measurements indicate that terrestrial bodies differentiate into layers with different characteristics such as core, mantle, and crust (Fig. 1.2). The planets are formed out of planetesimals. Potential energy from these planetesimals was converted to heat on the surface of the planets during accretion. The heat released by the planetesimal accretion was released to outer space and transported into planets by thermal convections and conductions. This heats the planets' interior and differentiates the terrestrial body resulting in a layered structure of core, mantle, crust, and atmosphere/hydrosphere. However, the details of the dif-

ferentiation scenario or the thermal evolution of Mars are largely unknown due to the lack of our knowledge of the internal structure. For example, the current uncertainty of the core radius is 1700 ± 300 km (Smrekar *et al.*, 2019). The uncertainty on the core radius makes it difficult to judge whether the perovskite transformation, which is likely to occur at 1900km depth, takes place in the mantle or not. As the transition has a strong effect on mantle convection and thermal evolution of Mars (Fig. 1.3), thermal evolution of Mars, including the formation of the Tharsis (where volcanic activities were active), are not constrained and multiple scenarios have been proposed.

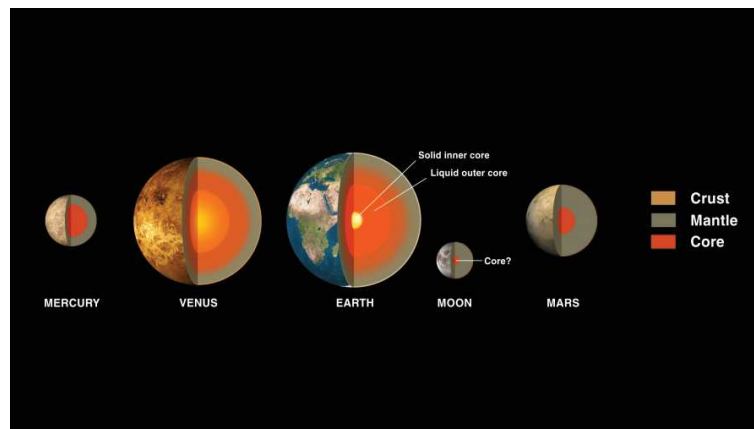


FIGURE 1.2 – *Internal structure of terrestrial planets* (<https://solarsystem.nasa.gov>). Some scientific measurements indicate that interior of these planets are different from each other. The differences likely come from their thermal evolutions and origins.

Now we have a chance to perform in-situ observations by InSight mission (Banerdt *et al.*, 2020). InSight (Interior exploration using Seismic Investigations, geodesy and heat transport) is a NASA Discovery Program mission which deployed in late 2018 a single geophysical lander on Mars to study its deep interior. Lander of the mission is a near-copy of the lander for a successful Phoenix mission. Main payloads are SEIS (Seismic Experiment for Interior Structure) (Lognonné *et al.*, 2019), RISE (Rotation and Interior Structure Experiment) (Folkner *et al.*, 2018) and HP3 (Heat Flow and Physical Properties Probe) (Spohn *et al.*, 2018). These geophysical observations will be the new source of information for us to improve the understanding of Ma-

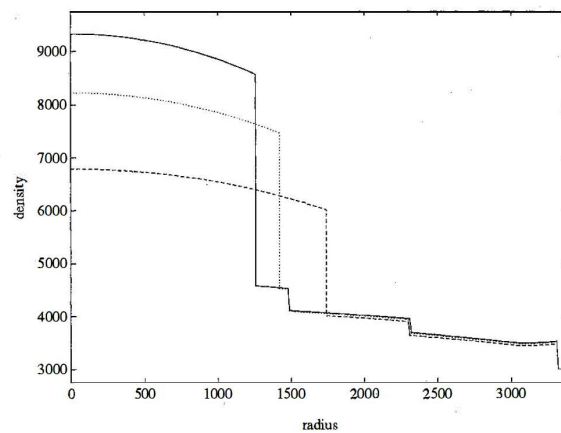


FIGURE 1.3 – Possible density structure of Mars Harder (1998). Solid (0 %), dotted (14 %), and dashed (36.5 %), lines indicate sulphur content of the core. It is found that, the depth of the spinel to perovskite transformation is 1910 km, which corresponds to a radius of about 1500 km. Thus a perovskite layer exists in Mars if the core radius is small. This affects not only present internal structure but also mantle convection and evolution of Mars.

rian internal structure and thermal evolution (Banfield *et al.* (2019); Panning and Kedar (2019)).

1.2 SEISMIC OBSERVATION.

Seismic observation is one of the most successful techniques to estimate the internal structures of planets and satellites. On the Earth, seismic observations successfully uncovered the internal structure from the surface to the center of the core. (e.g. Dziewonski and Anderson (1981)). There are many techniques for seismic observation. One of the major techniques is reflection and refraction analysis. When seismic waves propagate through the layered structure, the seismic waves are reflected and refracted at the boundaries (Fig. 1.4 (A)). These reflection, refraction, and direct waves are observed by seismometers. These different seismic phases propagate with different ray paths thus appear differently in the observed waveform. The time delays enable us to estimate the layered structure with both the recorded P and S waves (Fig. 1.4 (B)). The location of the seismic source is, however, required for these travel time analyses. For a simple model with a crust and a mantle, the determination of the 4 parameters

is requesting at least 3 stations. Seismic waves have different velocities because of the difference in characteristics of P and S waves. These wave velocities are different because of the difference in characteristics of seismic waves. Thus, travel-times of the waves make a difference as well. The differences in travel-time enable us to estimate the internal structure of the planet. A dense seismic network will moreover be required to probe the detailed internal structure of a satellite and/or planets. While such networks are well established on Earth, it would be challenging to have any dense seismic network on other celestial bodies. So far, this has been achieved only on the Moon (except on the Earth) with 4 stations networks, augmented by a gravimeter (*Kawamura et al. (2015)*). See *Lognonné and Johnson (2015)* for a review of Planetary seismology and of the results of the Apollo seismic network, as well as *Garcia et al. (2020)* for one of the most recent reviews on the achievement of Lunar seismology. All past attempts to deploy such a network on Mars, including with the InterMarsnet (*Lognonné et al. (1996)*), Netlander (*Lognonné et al. (2003)*) projects, failed for cost reasons. See *Lognonné (2005)* for a historical review of the different attempts.

1.2.1 Normal mode observation.

Normal mode is the specific vibration of an object. When an object is vibrating, the wave propagates in the body and reaches the object's free surface. Waves are reflected at the free surface, or for the surface boundary with the atmosphere are partially reflected, with small energy escaping the body (*Lognonné and Clévéde, 2002*). For specific frequencies, the reflected waves are building constructive interferences. The associated frequencies are called eigenfrequencies, while the shape of the wavefield in the body is the associated normal mode. Every object has a specific eigenfrequencies spectrum, which means an infinite set of frequencies depending only on the model. These eigenfrequencies are depending on the internal structure and the size of the body. The same can be said for planetary bodies such as the Earth, Mars, Sun, and Moon. Fig. 1.5 shows the vibration spectrum of the Earth. Each peak is associated with one normal mode of

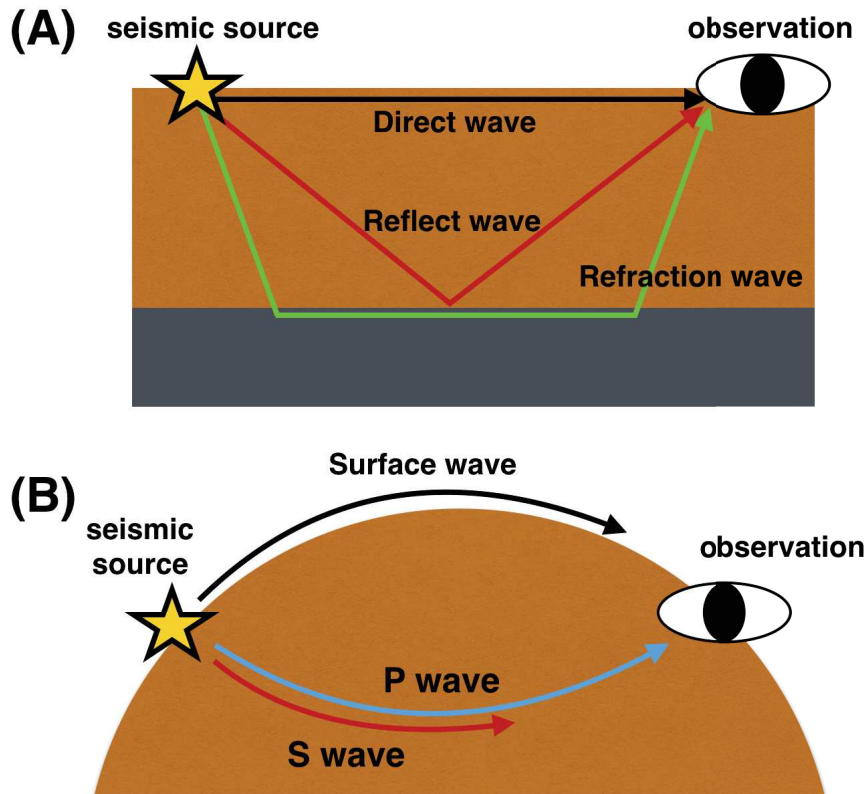


FIGURE 1.4 – Seismic exploration techniques by travel-time analysis. (A) : Seismic waves propagate in every direction, one of them propagates directly toward an observing station, some of them propagate in layers. Wave reflections and refractions occur between layers discontinuities. In addition to the direct waves, some reflected and refracted waves also reach the observation station. By analyzing seismic waves that reach the station with different paths, we can investigate the seismic velocity structure of a planet. (B) : Surface wave propagates in a surface layer and reaches a observe station. Body waves (P-wave and S-wave) propagate in internal layers. Body waves reflect and refract in the layers. Wave velocities of these surface waves and body waves are different which provides us information on the stratification and their mechanical properties.

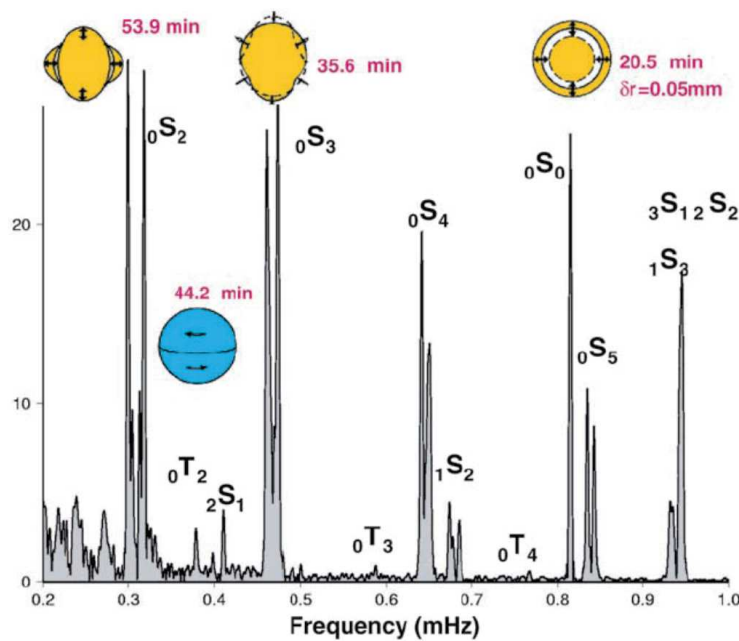


FIGURE 1.5 – Spectrum of the Earth free oscillations. The frequency and amplitude of the modes are derived as a function of the Earth's internal structure and its size (Park *et al.*, 2005).

the Earth, and these are called free oscillations.

The first search for Earth's free oscillations started by the late 1950s (Benioff *et al.*, 1959) and the detection of those oscillations was first made following the great Chilean earthquake of May 1960 (Benioff *et al.*, 1961). The further development of long-period seismometers and global networks then led to the accumulation of the observations at normal mode frequencies, which were then used for the inversion of structure models for the Earth interior, including the famous Preliminary Earth Reference Model PREM (Dziewonski and Anderson, 1981). Further inversions were then carried out with the splitting properties of the normal modes. Due to lateral variations and rotation, normal modes with identical frequencies for the spherical model, called multiplets, have indeed slightly different frequencies. The analysis of this splitting is providing models of the three-dimensional structure of the Earth. An extensive description of the observation and use of the normal modes in the determination of Earth interior structure can be found in Woodhouse and Deuss (2015); Laske and Widmer-Schmidrig (2015); Montagner (2015) and Romanowicz

and Mitchell (2015), while theoretical description can be found in Lognonné (1991); Dahlen and Tromp (1998) and Millot-Langet et al. (2002). In this study, I investigate normal mode observation, which is a one station observation method. It can therefore overcome such a problem and provide the best constraints on the deep inner structure of Mars with a single seismic station.

1.2.2 Planetary background free oscillations.

As the determination of the frequency of normal modes can be made with only one record of a large quake, the detection of normal modes has been therefore proposed as one of the overarching goals of a seismological mission to Mars, from the early times of space exploration (Kovach and Anderson, 1965; Bolt and Derr, 1969) to Viking (Okal and Anderson, 1978) and the more recent projects such as Mesur (Solomon et al., 1991), Intermarsnet (Lognonné et al., 1996), NetLander (Lognonné and Giardini, 2000). Detection techniques have been detailed in several papers (Lognonné and Mosser, 1993; Zharkov and Gudkova, 1997; Gudkova and Zharkov, 2004; Lognonné, 2005; Lognonné and Johnson, 2007, 2015). The detection of normal modes on Mars is one of the goals in the near-future seismic monitoring of InSight after its landing and deployment in 2019 and of the SEIS experiment (Lognonné et al., 2019).

Planetary free oscillations are an indeed powerful tool to investigate the internal structure of the planet, as illustrated by (Panning et al., 2017) with a synthetic structure inversion of the fundamental spheroidal normal modes. To perform seismic observations on Mars, several difficult problems shall be overcome.

One issue is related to Mars itself, which lacks plate tectonics and therefore will be devoid of the large magnitude quakes ($M > 7$) generally used on the Earth for the analysis of normal modes. All seismicity models of Mars (Phillips and Grimm, 1991; Golombek et al., 1992; Knapmeyer et al., 2006) suggests that the largest quake per year will be in the moment magnitude range of 5.2-6, e.g. $10^{17} - 10^{18}$ Nm – although larger but very rare quakes cannot be excluded more than 18 months of monitoring, SEIS has furthermore not detected any quake

large enough for exciting either surface waves or normal modes (Lognonné *et al.*, 2020; Giardini *et al.*, 2020).

The second difficulty is the expected seismic noise induced by the surface installation of InSight. Mars' surface is known to undergo large variations of temperature and wind. These generate long-period noise much larger than the one measured on the Earth seismic vaults, which are the typical location required for Earth normal modes observations. The InSight SEIS noise model, described in detail by Mimoun *et al.* (2017), suggests that for a long period, most of the SEIS processed data noise will be related to the thermal noise, which is expected to grow below 10 mHz as $f^{-2.5}$, with amplitude at 10 mHz in the range of $1 - 2.5 \times 10^{-9} \text{ m/s}^2/\text{Hz}^{1/2}$ depending on the local time. Observations show that this model provide, during the night time, correct amplitude (Lognonné *et al.*, 2020; Giardini *et al.*, 2020). I will therefore use it in this work for all future modeling. As shown by Lognonné (2005), seismic signals of normal modes exceed the noise level with seismic moment larger than amplitudes globally if a marsquake with moment larger than $2 \times 10^{17} \text{ Nm}$ occurs. Even if such a moment corresponds to the upper limit of the seismicity prediction per year, the Poisson statistic of such a rare event suggests that several years of operation will be requested to achieve significant occurrence probability. I, therefore, consider in this thesis the other, non-seismogenic, sources of normal mode excitation.

One of the possible sources of excitation is atmospheric phenomena (Spiga *et al.*, 2018). Mars is known to have a very active atmosphere, with weather processes generating high winds, dust devils, and storms (Read and Lewis, 2004; Spiga and Forget, 2009). Cloud tracking method shows that Martian wind speeds easily reach 80 m/s at altitudes above 30 km (Kaydash *et al.*, 2006), while the surface wind can be as high as 20 m/s according to measurements by the Viking landers (e.g. Murphy *et al.*, 1990a). Martian lander observations also show that the Martian atmosphere has a regular diurnal cycle of wind and pressure (Schofield *et al.*, 1997).

The non-acoustic pressure variations associated with the global weather, as well as the Reynold stress associated with the wind,

from the turbulent gusts in the Planetary Boundary Layer (PBL) to the high-altitude planetary-scale winds, are all acting as excitation forces for planetary free oscillations (*Kobayashi and Nishida, 1998a,b*), with theoretical details in *Tanimoto and Um (1999)*. Part of the excitation forces has frequencies in the bandwidth of the normal modes, corresponding to eigenfrequencies of Martian normal mode between 0.4 mHz and 20-30 mHz. These particular excitation forces can excite the corresponding normal modes efficiently, globally, and continuously. This continuous excitation force is therefore a possible source of Mars' background free oscillations (MBFs).

This idea for the observation of MBF was suggested shortly after the first observation of Earth's background free oscillations (EBFs) (*Suda et al., 1998*). Oceanic excitation was then first proposed by *Wataida and Masters (2001)*. Nevertheless, the first interpretations proposed that the entire excitation is produced by atmospheric turbulence in the Earth's PBL, which suggests that a simple scaling may exist between Earth and Mars (*Kobayashi and Nishida, 1998a,b*). The seasonal variations in the continuous excitation later observed by *Nishida et al. (2000)* also support an atmospheric origin, while *Tanimoto and Um (1999)* proposed a simplified theory. However, the most recent studies show that the major source of continuous excitation on Earth is over the oceans (*Tanimoto, 2005; Rhie and Romanowicz, 2004, 2006*) and that, in this process, infragravity waves over the continental shelves are much more efficient seismic sources (*Webb, 2007*) than atmospheric turbulence. However, excitation by atmospheric sources remains significantly below 5 mHz (*Nishida, 2013a*). Note that coupled modes exist between the atmosphere and the solid earth (*Lognonné et al., 1998a, 2016; Nishida et al., 2000*), as well as all planets with atmosphere, e.g. Venus and Mars (*Lognonné et al., 2005, 2016*) and that pressure sources at the bottom of the ocean (*Nishida, 2014*) cannot explain this larger excitation; instead, integrated atmospheric excitations at the base of Earth's atmosphere must be involved. Observed EBFs are on the order of 0.5 nanogal ($1 \text{ nano gal} = 10^{-11} \text{ ms}^{-2}$) (*Nishida, 2013b*) per individual mode. Stacking techniques can enhance the peak amplitude of normal modes to over-

come instrument- and station-induced noise, which allows the mode eigenfrequencies to be determined. These eigenfrequencies may then be used to invert the internal structure as was done for quakes, as illustrated by *Nishida et al.* (2009). The same phenomenon should occur on Mars, meaning that the observation of MBFs should allow us to determine the frequencies of fundamental spheroidal normal modes, which would constrain models for Mars's interior.

Kobayashi and Nishida (1998a) estimated the magnitude of MBFs by using a theoretical scaling based on the solar energy received by the planet (related to the planetary albedo and distance to the Sun) and on the thickness of the PBL. They assumed that turbulence in the PBL provides the main excitation force for MBFs, which led them to estimate a free oscillation amplitude of several nanogals, a value quite close to that of the Earth. *Tanimoto* (2001) estimated the relative modal amplitude between Earth and Mars by using several parameters for the atmosphere and terrestrial part. Estimates of the MBF amplitude are about 30-50 % of the EBFs. *Lognonné* (2005) and *Lognonné and Johnson* (2007) focused on very-long-period MBFs and, by using more realistic Martian-climate models and normal mode summations, produced MBF seismograms for periods ranging 300 to 400 s, which correspond to angular orders 12 to 15. This approach is based on the assumption that, for these very long periods and wavelengths, the major source of excitation is not Reynolds stresses or non-acoustic pressure related to the PBL, but the non-acoustic pressure related to global atmospheric circulation. They estimated the free oscillation amplitude to be several hundredths of nanogals, which corresponds to amplitudes typically ten times smaller than those of EBFs of the same angular order.

The generation of seismic waves by atmospheric activity is not only associated with non-acoustic pressure acting on the surface, but also with the acoustic waves generated in the atmosphere and converted into seismic waves at the surface. *Lognonné et al.* (1998a), *Watada and Kanamori* (2010), and *Lognonné et al.* (2016) simplified this concept by demonstrating that the overall excitation in the atmosphere may be estimated based on the normal modes of the coupled

solid-atmosphere system and on the atmospheric force volumetric density, which acts throughout the atmosphere and is subject to wind and non-acoustic pressure fluctuations. This approach requires integrating, over the full atmospheric seismogenic volume to calculate the excitation force of the atmosphere. As shown more precisely by *Lognonné et al.* (1994) the latter is associated with seismic forces related to non-acoustic pressure and nonlinear Reynolds stresses in the atmosphere and can be expressed as

$$\Pi_i^j = -p_{glut}\delta_i^j - \rho v_i v^j, \quad (1.1)$$

where p_{glut} non-acoustic pressure \mathbf{v} , is the atmospheric wind, ρ is atmospheric density, and δ_i^j is the Kronecker delta. p_{glut} is defined as $p_{glut} = p_{true} - p_{Hooke}$. p_{Hooke} is the pressure modeled by the Hooke pressure, which is expressed as $p_{Hooke} = -\kappa \nabla \cdot \mathbf{v}$, which involves the linear model used in linear acoustics or seismology. Therefore, following the proposition made by *Backus and Mulcahy* (1976a) for localized sources in Earth seismology and by *Goldreich and Keeley* (1977) for globally distributed sources in Solar seismology, I generalize here the concept of stress glut to the pressure induced by nonlinear Reynolds stresses that occur in the Martian PBL. This generalization considers that all true volumetric forces, apart from those generated by Hooke pressure, are source terms captured by the seismic moment of Eq.(1). Thus, I consider that the pressure glut and wind are respectively written as

$$p_{glut} = p_{glut,global} + p_{glut,PBL}, \mathbf{v} = \mathbf{v}_{global} + \mathbf{v}_{PBL}. \quad (1.2)$$

Practically speaking, the wind and pressure glut associated with the PBL turbulence will be at much higher frequencies and on a smaller scale than those associated with the global circulation, but both will contribute to the overall excitation processes through Eq.(1). Therefore, the two estimates seem to provide the two end members of the general case, with *Lognonné and Johnson* (2007) focusing on the global contribution of the excitation and *Kobayashi and Nishida* (1998a) focusing on the local effect from the PBL.

Major differences in PBL thickness exist between the Earth PBL, which ranges from 0.2 to 2 km, and the Martian PBL, which is much

thicker (about 5 to 6 km, typically) (*Petrosyan et al.*, 2011; *Spiga*, 2011). Because the speed of sound is less on Mars than on Earth (220 m/s compared with 340 m/s), the volumetric excitation is likely much more important on Mars than on Earth where, moreover, most of the energy of the atmospheric winds is transferred to oceanic waves, which then play a major role in the excitation of EBFs. In other words, the Earth view, where most EBF excitation may be modeled by invoking bottom-oceanic and near-surface forces, is not likely to be valid on Mars.

1.3 MARTIAN ATMOSPHERE

The characteristics of the martian atmosphere are far different from the Earth's one. The atmospheric status was observed by Viking (*Murphy et al.*, 1990b), Phoenix (*Taylor et al.*, 2008), Mars Pathfinder (*Schofield et al.*, 1997) and Mars Science Laboratory (*Gómez-Elvira et al.*, 2012). Mars has a thin atmosphere and its average pressure is about 600-1000 Pa, which is 1/100 times smaller than that of the Earth. The composition of the martian atmosphere is dominated by CO₂. Earth's atmosphere is mostly O₂ and N₂, with O₂ resulting from life and with only 400 ppm of CO₂, as most of the CO₂ is on Earth trapped in the crust and upper mantle. Another important difference is the very dry composition of the Martian atmosphere. The waterless environment generates weather conditions specific to Mars. When the sun rises, temperature increases and this acts as a trigger of weather phenomenon. Due to the waterless soil, the heat capacity of the ground is very low, clouds are very thin (almost nothing), and no sea (Fig. 1.6). In other words, a large thermal reservoir does not exist on Mars and the temperature is strongly solar flux dependent. Solar flux heats the ground and the ground transfers its heat to the air. The heat generates gas expansion and convections, which results in active atmospheric activity on Mars.

Given that the Martian weather is controlled mainly by solar flux, they show a periodic features day by day coherence with the variation of the solar flux, which is not the case on the Earth. The daily

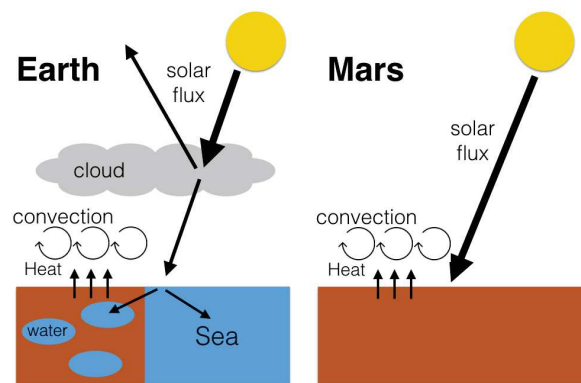


FIGURE 1.6 – *Earth and Mars weather models. The weathers of the Earth and Mars are very different. On Earth, the weather depends on several parameters. These factors are mainly risen by water in liquid, gaseous, or ice forms. Water generates clouds, sea, and rivers which make atmospheric activities complex. On Mars, solar flux is the only major factor of weather. This makes Martian atmospheric activity far more simple compared to that of the Earth and generates daily cyclic atmospheric activities.*

repetition of martian weather is very important for MBFs calculations (see chapter 4.3.4 for details).

1.3.1 Observation

Martian climate and weather were observed by meteorological sensors on the series of Martian landers. Viking Landers observed wind velocity, 2D wind direction, pressure, and temperature (Hess *et al.*, 1977). The sampling rate of Viking 1 is almost one hour and the data length is 200 sols (martian days). The sampling rate of Viking 2 is 1 sol and the length of the data is 1050 sols.

Mars Pathfinder recorded martian weather for 76 sols by MET (Meteorology Suite - Pressure and Temperature) system. The collected data include atmospheric pressure, temperature, and wind velocity (Schofield *et al.*, 1997).

Phoenix recorded martian weather for 152 sols. The MET (Meteorology Suite - Pressure and Temperature) measured atmospheric pressure, temperature, and wind velocity at 0.5 Hz (Taylor *et al.*, 2008).

Curiosity continues weather observation on Mars at least 5 minutes of data at 1Hz each hour, every sol for more than 2200 sols. The Rover Environmental Monitoring Station (REMS) sensors recording air and ground temperatures, pressure, relative humidity, wind velocity in the horizontal and vertical directions (*Gómez-Elvira et al., 2012*).

These observations are local observations at the landing sites. What is required for the evaluation of global MBF excitation is global 3D Martian atmospheric data. Such a big and high-resolution observation data doesn't exist. Thus, in this study, I use results from the meteorological simulation of the Martian atmosphere.

1.3.2 Martian General Circular Models

It is necessary to use a whole martian atmospheric model to calculate MBFs. The wind flow and pressure fluctuations are spreading from the ground surface to the top of the atmosphere. Naturally, it changes day by day and second by second. Only such a model can provide the time and 3D spatial resolution sufficient for the MBF computation, contrary to the existing observations which are only limited to a few points on the surface with very limited sampling. There are 3 types of Martian climate models, General Circular Model (GCM), Mesoscale Model and Large Eddy Simulation (LES). The major difference of the models is the spatial and temporal scales and resolutions (*Spiga and Lewis, 2010*).

To predict the atmospheric excitation force, I used Mars Global Climate Model (GCM) which is designed to simulate large-scale atmospheric dynamics over an entire planetary sphere (Fig. 1.8), provided by Laboratoire de Météorologie Dynamique (LMD). The characteristics of the model are described in *Forget et al. (1999)*. I use the latest and the most realistic, version of the model featuring interactive dust transport (*Madeleine et al., 2011*), radiatively active water ice clouds (*Navarro et al., 2014*), and a thermal plume model for the boundary layer (*Colaïtis et al., 2013*).

Computing normal mode excitation requires a GCM simulation

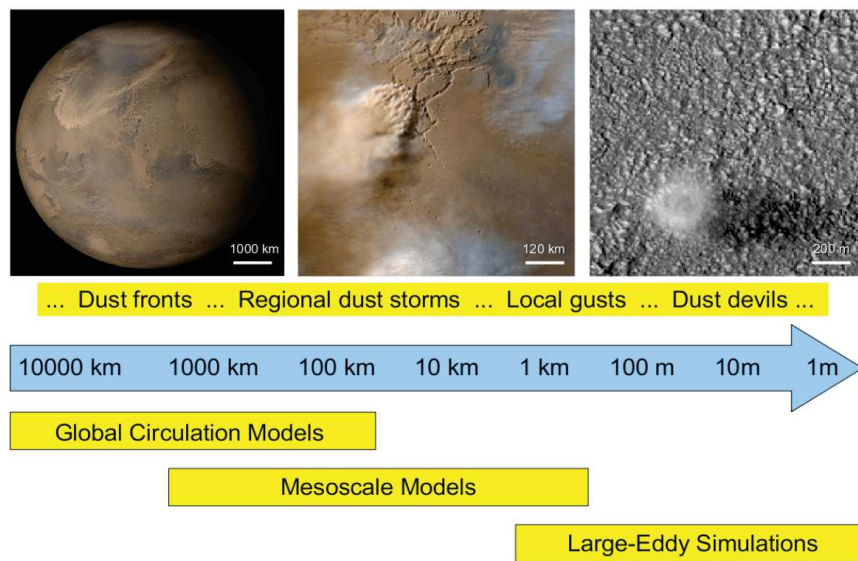


FIGURE 1.7 – Typical scales of martian atmospheric simulations and meteorological models suitable for their analysis Spiga and Lewis (2010). MBFs are global seismic event which is excited by global atmospheric activities. Thus GCMs are suitable for the calculation of MBFs.

that is able to characterize the temporal variation of pressure and winds of Mars at 0.01 Hz (period 100s) with a horizontal resolution suitable for normal modes (i.e., about 7 degree latitude and longitude for $l=50$, which corresponds to 100 sec normal modes on Mars). These requirements, dictated by seismic computations, are somewhat paradoxical from a meteorological point of view. A timescale of 100 s is associated with atmospheric circulations evolving over typical spatial scales of tens to hundreds of meters, which are challenging to resolve with GCMs, even with the best available supercomputing cluster. Most of the 100 s variability of the Martian atmosphere is instead captured through limited-area, turbulence-resolving modeling [large-eddy simulations; see, e.g., (Spiga and Lewis, 2010); see also Kenda *et al.* (2017); Murdoch *et al.* (2017) for a discussion of local seismic signature]. The remainder of this variability (i.e., the contribution that is not caused by microscale turbulence) is associated with mid-latitude baroclinic fronts and regional slope winds (which impact the global dynamics) and can be satisfactorily simulated through GCMs with a horizontal resolution of 1° . Conversely,

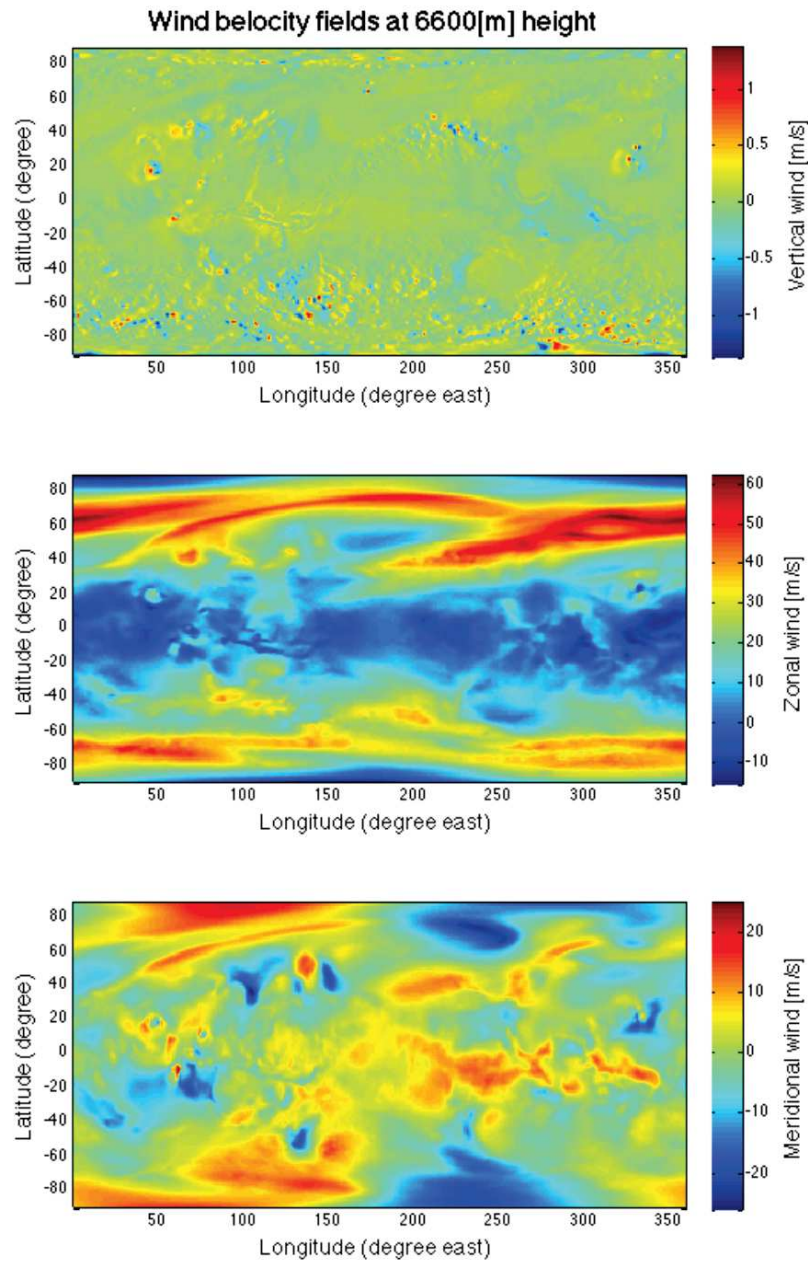


FIGURE 1.8 – *3D wind velocity field generated with GCMs. GCMs can simulate the whole 3D martian atmospheric activities.*

nearly three decades of Mars GCM studies have consistently demonstrated that the global dynamics (at spatial scales of about 10° latitude and longitude) are well simulated by using a typical time step of 925 s in the GCM.

I also use in this study Martian GCM simulations specifically tailored for the seismic computations. The LMD GCM simulations used a 60 s time step, 360 longitude grid points, and 180 latitude grid points, corresponding to a mesh spacing of $1^\circ \times 1^\circ$ and a horizontal resolution of 60 km [in a setting of GCM simulations described in *Pottier et al.* (2017)]. In the vertical direction, 25 levels are typically used with most of the levels located in the first 15 km to ensure a suitable resolution in the lower troposphere and the boundary layer. Above 10 km, the vertical resolution is about one scale height and the altitude of the top level is about 60 km, which corresponds to about 6 scale heights. This vertical grid thus offers both the refined near-surface resolution and accounts for the vast majority of the atmospheric mass, which allows us to deal with all possible seismic coupling in subsequent computations. It is important to note that turbulent motions developing at high frequency are not resolved by the GCM : the PBL mixing they cause is parameterized in the LMD GCM by dedicated schemes (*Colaïtis et al.*, 2013). The GCM results used to compute normal modes thus only feature atmospheric variability at scales ranging from regional to global, and frequencies typically of the order 10^{-3} Hz and lower. This is therefore modeling only the part of the excitation and must be considered as a lower estimation of the amplitude.

Typical GCM simulations of the Martian climate are needed so that the resulting analysis of normal modes applies to the conditions of the InSight mission. However, this does not require as many simulations as would be expected from equivalent terrestrial studies. Both the low thermal inertia of the Martian surface and the fast radiative timescale of the thin Martian atmosphere imply a very low Martian-climate inter-annual variability (except during the dust storm season, but InSight will land in 2018 at the end of this season) (*Read and Lewis*, 2004). Furthermore, given the key role played by the

atmospheric-dust loading in driving the Martian climate as well as the small inter-annual variability of this parameter in the first half of the Martian year (*Montabone et al.*, 2015) running one GCM simulation for the year in which the InSight mission occurs will provide sufficiently accurate predictions for all Martian years (outside the dust storm season). The dust scenario used thus corresponds to the Martian Year 27 which is a typical clear atmosphere scenario (dust visible opacity around 0.2) with no effects from a global dust storm. GCM simulations start at $L_s = 0^\circ$ (northern spring), which corresponds to the first months of the InSight mission on Mars, and are performed for 20 Martian sols with a fixed dust profile. Given that gravity waves are partly resolved in our $1^\circ \times 1^\circ$ GCM simulation, I do not use the subgrid-scale scheme to model the effect of those waves on the large-scale flow. The outputs of the model, which are used as inputs for the modeling of the seismic moment density as defined by relation Eq.(1), are surface pressure and temperature, as well as atmospheric density, temperature, and winds.

The observed atmospheric status differs from that predicted by the GCM, despite the location being the same. This is illustrated in Fig. 1.9 for the Pathfinder location. Parts of these discrepancies are related to both the pitot pressure (associated with the local wind) and to the local-scale eddies, which are not resolved by the GCM but are discussed above.

As I mentioned above, this is a challenging problem because our approach relies on GCMs. It is dependent on the environment in which the observation is made, the season, and other factors. Notably, at conditions where GCMs lose energy at Martian normal mode frequencies, large uncertainties would be expected (Fig. 1.9).

1.3.3 Seismological point of view

The daily repetition of the weather patterns is important for MBFs. This is mostly related to the larger contribution of the solar flux to the weather patterns which is a consequence of the lack of other major sources of atmospheric energy such as humidity and water in the terrestrial case. For Mars, solid tides are the only tidal effects and

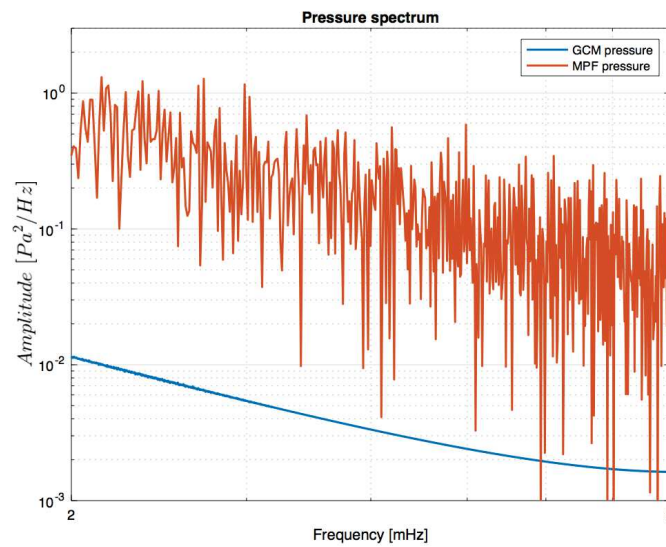


FIGURE 1.9 – Spectrum of GCM pressure and observed pressure. The observational data were acquired by Mars Pathfinder (LS=170 °). The GCM spectrum is computed for the same location as the observational data of Mars Pathfinder (LS = 0°). The results differ by an order of magnitude, implying that GCMs cannot fully explain the observed energy, which is likely due to inadequate modeling in GCMs of local-scale turbulences. Thus, MBFs calculated by using GCMs should be regarded as a lower limit of possible excitations.

generate sub-cm amplitude surface deformations for the Sun tide, and sub-mm for the Phobos tide. Although this appears first in the temperature variations, which can be represented fairly well by Fourier series (e.g. *Van Hoolst et al.*, 2003), this is also the case for the pressure field. The atmospheric activities on Mars are the excitation of MBFs. At the same time, it may be noise observations. If the intensity of atmospheric activity becomes strong, the signal of MBFs and noise of seismic observation become strong. A big signal is a favorable situation but big noise is not for seismic observations. I need to focus on both faces of the atmospheric activities. MBFs are excited by global atmospheric activities, but the noise of seismometers is generated by local ones. It is necessary to reduce the effects of local atmospheric activities for good observations. This explains why both InSight and future projects, like the MELOS mission, took care of windshield protections.

1.4 TIDAL DEFORMATION

On the Earth, the tidal force is mostly observed as variations of sea level in addition to the solid tide deforming the Earth. The tidal fluctuation is caused by the gravitational pull of the moon and Sun and centrifugal acceleration. Love numbers k, h, l are rigidity parameter of the planetary body to describe the tidal force (*Love*, 1908).

Surface waves or the Rayleigh associated with Normal modes will provide us information only on the Martian upper mantle. In order to know the whole martian internal structure, it is necessary to perform the additional investigation which enables us to probe deep internal structure the planet. Tidal deformations, which is one of the longest period seismic signals, might provide this information on the deep mantle and core. The combination of surface wave, MBFs, and tidal deformations methods might therefore enable us to know Mars internal structure from the surface to the core.

Tides generated by a body on a planet are related to the difference between the planet's inertial acceleration, which result from the gra-

vitational attraction of this body on the planet, and the gravitational attraction of the body on any point of the planet. (Fig. 1.10).

This is valid for the solid and fluid parts of the planet. The tidal force is acting regardless of the materials (liquid or solid). The displacement of the solid body's is smaller than that on the ocean. The difference in the displacement comes from the difference in the rigidity and this is defined as Love number h . By the method of A.E.H. Love (*Love, 1908*), the solid body's displacement is the product of Love number h and tidal displacement on the ocean. The Love number h of the Earth is about 0.6. Since Earth's tidal bulge is 0.5 m in a day, displacement of a solid body is $0.5 \times h = 0.3$ m in a day. The solid body's displacement of the Earth is observed.

The solid body bulge also happens on Mars. Spacecrafts in orbit around Mars are sensitive to the gravitational perturbation generated by Sun tide and therefore to the k_2 Love number. The k_2 potential Love number will be estimated from Doppler tracking of the Earth and the spacecraft. If I calculate the Love number of Mars, I can estimate its deep internal structure. SEIS is also expected to measure the gravimetric factor, associated with the tidal effects on the surface. In this thesis, I will show the method to estimate deep internal structure using the Love numbers by taking the data observed on the Moon as a benchmark test (section 5). The methodology I take for the Moon can be directly applied to Mars once we have appropriate and sufficient data. It is good preparation for the InSight mission and deep internal structure estimation of Mars that is compatible with both seismic and geodetic data.

1.5 SCOPE OF THIS STUDY.

The final goal of this study is to establish and test the methodology to estimate the mantle and core status of Mars with the global free oscillations of Mars and possibly with the estimation of the gravimetric factor. This Ph.D. thesis is however only one of the first steps of this long term project. I will discuss this with a detailed investigation of the seismic signal and the noise generated by the

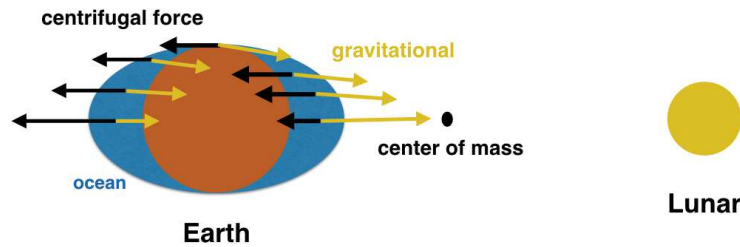


FIGURE 1.10 – Mechanism of two water tides of the ocean. The tidal force is summation of centrifugal force and gravitational force. The tide acts not only at the ocean but also Earth and Lunar solid body. The solid part deformation occurs from the surface to the core. In short, the tidal deformation includes whole internal structure of the solid body.

atmospheric activity of Mars. First, I discuss the atmospheric noise of Mars in Chapter 2. During the first year of this Ph.D., I finalized a study aiming to design for a Japanese project (MELOS), a low mass windshield. The SEIS windshield is indeed more than 10 kg and such a mass might not be available for future missions. The first chapter of this Ph.D. is presenting the results of this analysis. I designed the optimum shape for a windshield for a martian seismometer to evaluate the realistic noise level expected on Mars. Then, I evaluate the signal levels of Mars background free oscillation, which will be used to estimate the shallow and middle mantle status in Chapter 3, 4. I will also discuss its detectability through the noise level obtained previously. Finally, I study the possibility of probing the deep internal structure through geodetic observation, such as tidal and k_2 love numbers in Chapter 5. This will be a complement observation to the observation of the Mars background free oscillation and will be a way to explore, without quakes, explore full deep internal structure through the mantle to the core. I will conclude by discussing the pos-

sible achievements expected from the joint inversion of seismic and geodetic observation that will be made with the InSight mission.

WIND SHIELD DEVELOPMENT FOR JAPANESE MISSION

2

SOMMAIRE

2.1	INTRODUCTION	25
2.2	PAST STUDIES	27
2.3	WIND SHIELD DEVELOPMENT	28
2.3.1	Design principles	29
2.4	WIND TUNNEL TEST	29
2.5	NUMERICAL SIMULATIONS	30
2.5.1	Simulation conditions	33
2.5.2	Calculation methods of lift force and torque.	35
2.6	RESULTS	35
2.6.1	Wind tunnel test result	35
2.6.2	Numerical simulation	39
2.7	DISCUSSION	42
2.7.1	Stability of the wind shield	47
2.7.2	Tilt noise	47
2.8	CONCLUSION	51

2.1 INTRODUCTION

This section is published in *Nishikawa et al. (2014)* A.2.2. On Mars, there exist several difficult problems to overcome to perform quality seismic observations. They are mostly due to the severe environments of Mars; extreme temperature variation, high cosmic rays, ultraviolet irradiation, and strong surface wind. Almost all the problems have some remedies proposed, but no countermeasures have been taken for the effect of strong wind on the seismometer. Strong wind on Mars will generate significant seismic noise either by directly shaking the seismometer or by causing a ground tilt.

The seismometer on Viking Lander could not detect the mars-quake because of the surface wind. While some signals were detected by the seismometer, they were highly correlated with wind data obtained simultaneously. Thus, it was identified that the obtained signals were atmospheric noise generated by surface wind and since then, the surface wind was regarded as the main source of noise in seismic observation on Mars. Not only vibrations but also torque prevents the seismic observations. Large torque tilts the seismometer and the tilt angle makes critical noise especially for the broadband seismometer. I have mentioned before, martian atmospheric activities have energy at low frequency band and the activities have a daily cycle. In other words, the daily cycle of atmospheric activities can be an efficient seismic source and efficient seismic noise at the same time. Therefore we have to consider to reduce the effect of wind. The ground tilt is one of the seismic noise sources, it can be explained by torque acting on a wind shield. The torque brings about a difference in ground strain. Here I report optimized torque-less wind shield to protect a seismometer from the wind, the designing method, and evaluating method of the background noise level. I have conducted wind tunnel tests and numerical simulations with several types of designs and obtained an effective shape to minimize the torque by the wind. The designed torque-less wind shield has smaller ground tilt noise than typical shape wind shields by one order of magnitude. This will enable me to achieve more than 90% of the noise-free condition during a year even for the windiest condition on the martian surface.

2.2 PAST STUDIES

Viking seismometer could not detect marsquakes because of the location of the seismometer and martian strong winds. It was placed on top of the lander and the lander was shaken by winds. The seismometer had not worked so much as a seismometer but as a wind sensor (*Anderson and Miller, 1977; Lorenz, 2012*). The failure of Viking seismic observation should be an important lesson for us. I am facing an urgent need to protect a Martian seismometer from the wind. Even if we put the seismometer on the ground directly, the effects of winds are still existing. The best way to protect a seismometer from winds and temperatures is to locate the seismometer in a calm place like a seismic vault or to bury the seismometer. If possible, we would locate a seismometer in a seismic vault but it is technologically difficult. A more realistic suggestion will be to place the seismometer under a wind shield, as I will discuss here. Covering a seismometer with wind shield is a very simple and powerful way to protect the seismometer from winds. InSight mission also uses a wind shield to protect the seismometers. Wind shield over the seismometer would be indispensable to reduce the effect of wind if we install the sensor on the surface (*Lognonné et al., 1996*). In order to evaluate the effectiveness of wind shields, they performed 3 tests. They deployed a seismometer in a seismic vault, another outside the seismic vault on the ground surface, both utilizing a simplified prototype of a windshield. The third seismometer was deployed directly on the surface without a shield. They measured seismic noise in these 3 settings. Seismic noise under the shield was one digit smaller than that without the shield. The noise spectral amplitude on the vertical component reaches a level less than $2 \times 10^{-9} m/s^{-2} Hz^{-1/2}$, very close to the martian expected Low Noise Model (*Lognonné et al., 1996*). The windshield prevented the seismometer from shaking by the surface wind. They used only a simplified prototype of the wind shield and used stones to load in situ the basement of the windshield, which might not be possible for robotic installation. The induced effect depends on the shape of the wind shields. In particular, dynamic pres-

sure on the wind shield generates torque and the ground is pushed and inclined by the torque. This inclination potentially influences the observation results of marsquakes. I should optimize the size, shape, and weight of the wind shield to fit the seismometer and payload of the mission. This study focuses on the efficiency of the shape of a wind shield, thus I fixed the size and weight of the wind shields. I report wind forces acting on the wind shields by using wind tunnel tests and numerical fluid dynamics simulations (CFD simulations) under the specific condition which simulate observations on Mars (low atmospheric pressure and high wind speed). First, I conducted wind tunnel tests under atmospheric pressure relatively high compared to Martian pressure (0.2 atm) for two extreme cases in terms of the wind shields' shape. This was done to study the behaviors of the wind shields against winds and pressure variations. Then, I ran numerical simulations under the same condition as the wind tunnel tests using CFD to test the consistency between the numerical simulations and the experiments. Though CFD is a well-accepted method to simulate fluids' behaviors, this is usually used for higher pressure compared to our settings and I needed to verify its capability to simulate such low atmospheric pressure. Next, I used the CFD to simulate the low atmospheric pressure of Mars to search in the parameter space to design an efficient shape for the wind shield. Finally, I tested our designed the wind shield in a wind tunnel test to evaluate its efficiency, again in 0.2 atm condition. On the basis of the results, I present an effective shape for the wind shield of the seismometer.

2.3 WIND SHIELD DEVELOPMENT

To design the wind shield, I first performed wind tunnel tests with semi-spherical and circular truncated cone wind shields. Then I searched for optimized shape with numerical simulations. Finally, I verify my simulations with a wind tunnel test. In this study, I studied 3 types of shields; semispherical, circular truncated cone, and designed wind shield. All shields are 40cm in diameter, 16cm in height, and 1kg in weight.

2.3.1 Design principles

The design of the wind shield for the Martian seismometer has been carried out in the following steps. I fixed the size to meet the requirements for the MELOS mission; a circular truncated cone shape with 40 *cm* in diameter, 16 *cm* in height, and 1kg of weight (without seismometer. Note that this is about 10x lighter than the InSight/SEIS windshield.). The size is enough to contain a martian seismometer which is under development based on a high sensitivity borehole seismometer [one vertical axis seismometer 14 *cm* diameter and 12 *cm* height (*Araya et al.*, 2007)]. I assumed that the weight of the wind shield to be 1 kg so that the payload can be carried with a robotic arm for a Martian rover (*Trebi-Ollennu et al.*, 2005). I selected an effective design of the shield so as to minimize the noise induction from winds. Thus, I limit the number of wind tunnel tests to two end members and validate the numerical simulations with the results. Once the simulation is validated, I fill in the gap of the two end members to search for optimal wind shield design for realistic Martian environment.

I focused on the lift force and the torque which are generated by the wind. Large lift force and torque can slide the shield and strain the ground respectively which will be the main source of noise for seismometers (Fig. 2.1).

2.4 WIND TUNNEL TEST

I used a planetary environment wind tunnel facility at JAXA/ISAS in Sagamihara (Fig. 2.2). The wind tunnel generate high speed wind under various atmospheric pressure ; 10-30m/s , 0.1 - 1.0 atm (in case of Mars; 0 to 50 *m/s* , 0.005 to 0.01 *atm*). With the representative dimension of the wind shield of 40 *cm*, the corresponding Reynolds number is less than 4000. In the wind tunnel, I placed a wind shield on a table and measured the weight with a set of 3 loadcells (Fig. 2.3) and changed the atmospheric pressure from 0.1 to 0.3 *atm* and the wind velocities from 13 to 27 *m/s*. Note that this test does not

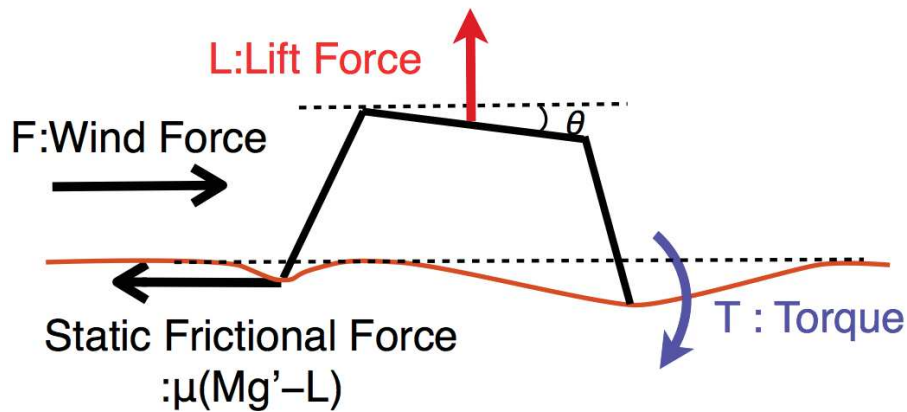


FIGURE 2.1 – Forces related to wind shield design. The lift force reduces static frictional force. Large wind forces and small static frictional forces slide the wind shield. The torques strain the ground. Large strain generates ground tilt which is expected to be noise for seismic observation.

represent the Martian condition. The wind tunnel I used was not capable of injecting winds in low atmospheric pressure. Thus the tests were run to understand the behavior of wind shields against winds and pressure variation, which will then be used to extrapolate the Martian condition through numerical simulations. Lift force is calculated from the difference between the shield's original weight and the sum of these loadcells. Torque calculated from the difference between front loadcells and a back loadcell (A negative torque value means to roll over to the upflow direction.).

I carried out a wind tunnel test to evaluate the performance of the wind shields. I focused on lift force and torque which are generated by the wind, because large lift force and torque can slide and roll over the wind shield. I measured the shield's weight at 3 points with 100-Hz sampling. I can calculate lift force and torque by the weight measurements. I used two typical types of shields, one is a semispherical shield (Fig. 2.4) and another is a circular truncated cone shield (Fig. 2.5).

2.5 NUMERICAL SIMULATIONS

To understand the behavior of winds and dynamic pressure on the wind shield under the condition I cannot realize with the wind

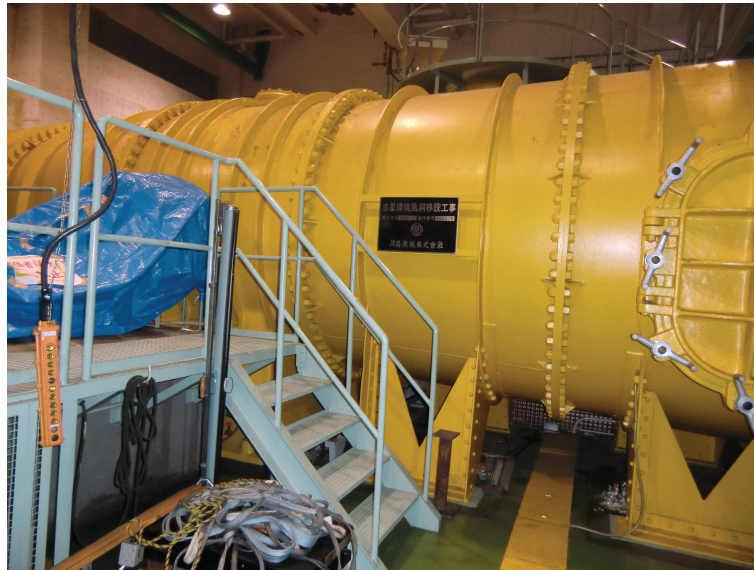


FIGURE 2.2 – *Planetary environment wind tunnel(JAXA/ISAS Sagamihara)*

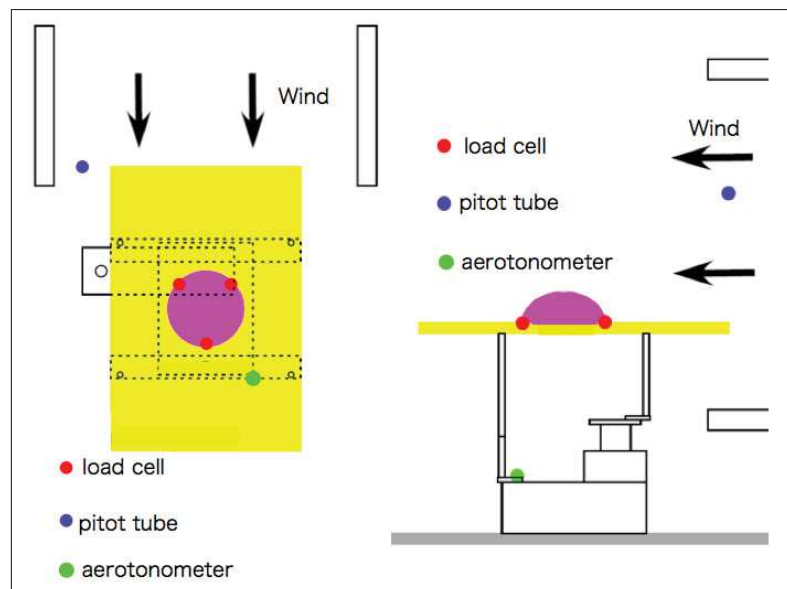


FIGURE 2.3 – *Geometry of the wind tunnel facility (left) top view above and (right) side view. The size of the table is 1-by-1.5m. A diameter of the wind tunnel is 2m. I measured weight of wind shield weight at red 3 points.*



FIGURE 2.4 – *Semisphere wind shield (left) top view above and (right) side view. This stainless-steel wind shield is 40cm diameter and 16cm height. The windshield has an edge but the edge is thin enough that it does not interfere the test.*



FIGURE 2.5 – *Truncated circular cone wind shield from (left) above and (right) side. This stainless-steel wind shield is 40cm diameter and 16cm height.*

tunnel, I performed numerical simulations. I solved the incompressible flow simulation with the finite volume method by using OpenFORM. OpenFOAM is a free , open source CFD(Computational Fluid Dynamics) software(www.openfoam.com/). I calculated the surface pressure of wind shields with various shapes of the wind shields as a function of wind speed. I evaluate the lift force acting on the wind shield through the numerical simulation.

2.5.1 Simulation conditions

In this study, I used SIMPLE (Semi-implicit Method for pressure-Linked Equation) algorithm to solve the Navier-Stokes equations (NS equations). The SIMPLE is a widely used numerical simulations to solve the NS equations. I solved NS equations under the following conditions.

Calculation conditions.	
Space discretization procedure	Finite volume method
grad(U)	Gauss linear
div(phi,U)	Gauss upwind
Compression	Incompressible flow
Viscosity	Viscosity fluid
Steadiness	Steady analysis
Turbulence model	$k - \epsilon$

TABLE 2.1 – *Calculation conditions*

I used a steady-state solver for incompressible, turbulent flow of non Newtonian fluids. Incompressible means that the density $\rho = \text{const}$. The NS equations for a single-phase flow with a constant density and viscosity are the following.

$$\nabla \cdot (\rho \vec{U}) = 0, \quad (2.1)$$

$$\frac{\partial \vec{U}}{\partial t} + \nabla \cdot (\vec{v} \vec{v}) - \nabla \cdot (\nu \nabla \vec{v}) = -\frac{1}{\rho} \nabla \mathbf{p} + \mathbf{g}, \quad (2.2)$$

where μ and $\nu = \mu / \rho$ are coefficient of viscosity and dynamic coefficient of viscosity.

I chose the standard $k - \epsilon$ turbulence model, which is one of the eddy viscosity models with 2 transport equations. k is turbu-

lence energy m^2/s^2 ; under assumption of incompressibility and the density(ρ) omitted from the equation. ϵ is turbulent energy dissipation rate m^2/s^3 ; conversion rate from fluid motion to heat of friction. The initial values for k and ϵ are set using an estimated fluctuating component of velocity U' and turbulent length scale, l . k and ϵ are defined with these parameters as follows :

$$k = \frac{1}{2} \overline{U' \cdot U'} \quad (2.3)$$

$$\epsilon = \frac{C_\mu^{0.75} k^{1.5}}{l} \quad (2.4)$$

where C_μ is a constant of the $k - \epsilon$ model equal to 0.09. For a Cartesian coordinate system (Versteeg and Malalasekera (2007)). k is given by :

$$k = \frac{1}{2} (U_x^2 + U_y^2 + U_z^2) \quad (2.5)$$

where U_x^2 , U_y^2 , U_z^2 are fluctuating components of velocity in the x, y and z directions respectively. I assumed the initial turbulence is non-isotropic and $U_x = 20\text{m/s}$, $U_y = U_z = 0$, which correspond to 5% of the lid velocity. l was set to 1.5m corresponding to the 20% of the box width. Finally, k and ϵ are given by :

$$U_x = \frac{5}{100} \times 20\text{ms}^{-1}, U_y = U_z = 0 \quad (2.6)$$

$$k = 5.0 \times 10^{-1} \text{m}^2 \text{s}^{-2} \quad (2.7)$$

$$\epsilon = \frac{1}{l} C_\mu^{0.75} k^{1.5} \sim 2.9 \times 10^{-1} \text{m}^2 \text{s}^{-3} \quad (2.8)$$

These expressions define the initial conditions for k and ϵ .

Fig. 2.6 depicts the simulation condition. The mesh is composed of 180,000 cells (4500(base) \times 40(vertical)). The air enters perpendicularly to the inlet at a velocity U . U changes between 10 and 30 m/s. The atmosphere pressure is p changes between 1.0×10^3 and 3.0×10^4 Pa.

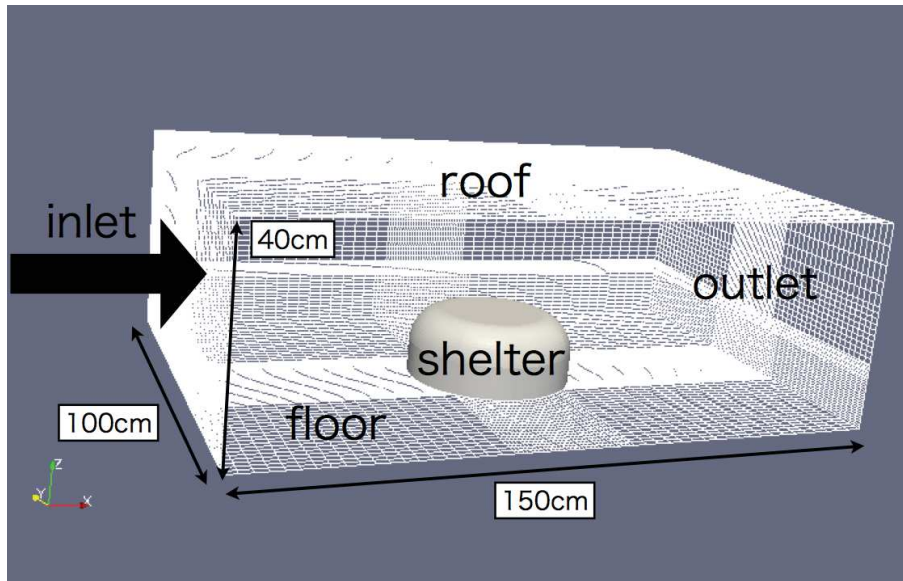


FIGURE 2.6 – Simulation conditions. I put a wind shield of 40 cm in diameter and 16 cm in height. The wind flows into the box from one side and flow out to the other side.

2.5.2 Calculation methods of lift force and torque.

I calculated distribution of the surface pressure on the wind shields with various wind velocity and atmospheric pressure. Lift force (L) is equal to the sum of p_z . Torque (T) is equal to the sum of the outer product of p and d

$$L = \int \vec{p}_z dS = \int \vec{p} \cdot \vec{e}_z dS \quad (2.9)$$

$$T = \int \vec{p} \times \vec{d} dS \quad (2.10)$$

where \vec{e}_z , \vec{p} and \vec{d} are unit vector parallel to the z axis for surface pressure vector on the shield and the position vector (Fig 2.7).

2.6 RESULTS

2.6.1 Wind tunnel test result

The results of wind tunnel test is summarized in tables 2.2 and 2.3. Errors (σ) are estimated by the standard deviation (root of variance) of results from different runs.

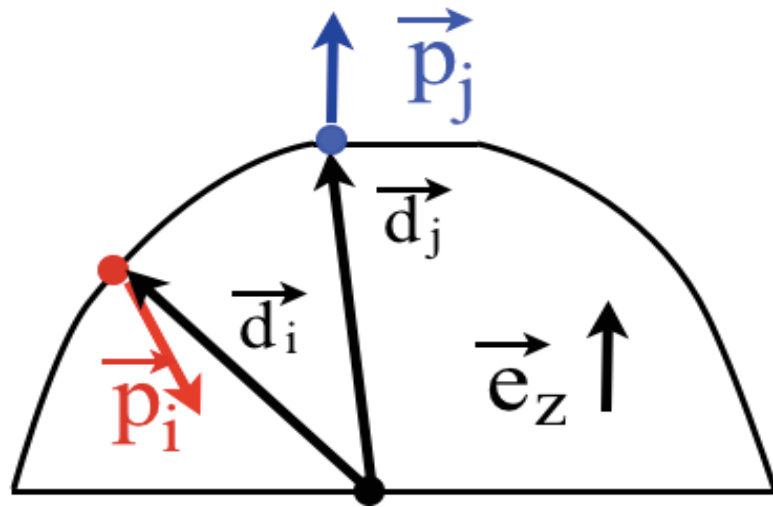


FIGURE 2.7 – Wind shield's torque and lift force calculation.

I assumed that the surface pressure of the shield is proportional to the dynamic pressure (P_D). The wind has total pressure (P_T). The total pressure is equal to the sum of the dynamic pressure and static pressure ($P_S : \text{const}$).

$$P_T = P_S + P_D = P_S + \frac{\rho}{2} \cdot U^2, \quad (2.11)$$

where ρ and U are density of the air and the wind velocity. It is assumed that the air is ideal gas and air density (ρ) will follow the equation of state for ideal gas.

$$pV = nRT, \quad (2.12)$$

$$p = \frac{n}{V}RT = \frac{\rho}{n}MRT, \quad (2.13)$$

where M is molecular weight . M is about 29 on the Earth, thus the air density is about

$$\rho = 1.2(\text{kg} \cdot \text{atm}^{-1} \cdot \text{m}^{-3}) \times p(\text{atm}) \quad (2.14)$$

By using these equations , I can calculate dynamic pressure as a function of atmospheric pressure and wind velocity.

Next, I calculated error value of the 10,000 observed data by using

standard deviation.

$$\sigma = \sqrt{\frac{\sum_{m=1}^{10000} (x_m - \bar{x})^2}{n}} \quad (2.15)$$

where x_m and \bar{x} are data value and mean value. As the wind velocity and atmospheric pressure increase, the lift force and absolute value of the rotational moment become larger.

Semispherical shield's wind tunnel test results.		
Test conditions pressure , wind velocity	Lift force N	Torque Nm
0.1atm,13m/s	0.38±0.15	-0.014±0.006
20m/s	0.93±0.34	-0.010±0.016
27m/s	1.82±0.18	-0.015±0.009
0.2atm,13m/s	0.65±0.12	-0.008±0.006
20m/s	1.74±0.31	-0.012±0.017
27m/s	3.60±0.18	-0.034±0.009
0.3atm,13m/s	0.90±0.20	-0.016±0.010
20m/s	2.81±0.21	-0.026±0.011

TABLE 2.2 – *Semispherical shield's wind tunnel test results, average lift force and torque with errors.*

Circular truncated cone shield's wind tunnel test results.		
Test conditions pressure , wind velocity	Lift force N	Torque Nm
0.1atm,13m/s	0.28±0.27	0.024±0.005
20m/s	0.77±0.23	0.052±0.009
27m/s	1.18±0.18	0.077±0.013
0.2atm,13m/s	0.42±0.31	0.033±0.005
20m/s	1.09±0.34	0.070±0.030
27m/s	2.47±0.17	0.140±0.020
0.3atm,13m/s	0.61±0.21	0.047±0.006
20m/s	1.72±0.20	0.102±0.013

TABLE 2.3 – *Circular truncated cone shield's wind tunnel test results, average lift force and torque with errors.*

I fitted observed lift force and torque by using the least square method (Fig 2.8 and 2.9). As the results of the fitting, I determined the relationship between lift force, torque, and atmospheric pressure wind velocity. Hereafter, I will refer to this coefficient as a shape factor S .

$$L(N) = S_L[m^2] \times \rho U^2 = S_L \times 1.2 \times pU^2, \quad (2.16)$$

$$T(Nm) = S_T[m^3] \times \rho U^2 = S_T \times 1.2 \times pU^2, \quad (2.17)$$

where the S_L and S_T parameters are defined as :

$$S_L[m^2] = \frac{SC_L}{2}, \quad (2.18)$$

$$S_T[m^3] = \frac{SDC_T}{2}, \quad (2.19)$$

S being the circular area of the shield, D its diameter and C_L and C_T the adimensional lift force and torque parameters.

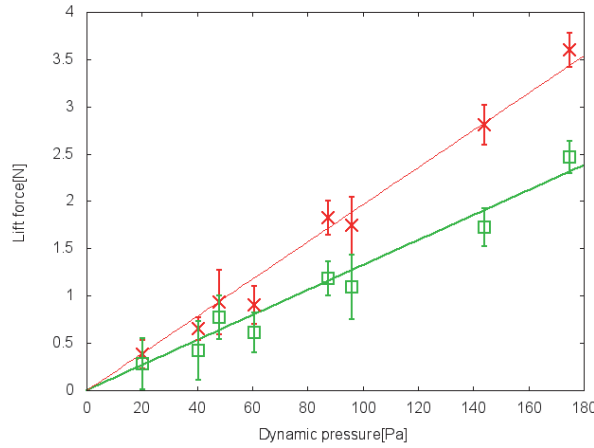


FIGURE 2.8 – Wind tunnel results of the lift forces with error bars. The straight lines are calculated by the least square method. I found a proportional relationship between lift force and dynamic pressure.

As the result of fitting, I obtained $S_L = 2.0 \times 10^{-2} m^2$ for the semisphere, $S_L = 1.3 \times 10^{-2} m^2$ for circular truncated cone, corresponding to dimensionless coefficients C_L of 0.32 and 0.21 respectively. $S_T = -2.0 \times 10^{-4} m^3$ for the semisphere, and $S_T = 8.1 \times 10^{-4} m^3$ for the circular truncated cone, corresponding to dimensionless coefficients of C_L of -0.008 and 0.0032. I can evaluate the performance of a wind shield by comparing these shape factors (S). Large S_L means that the shape has a large lift force (not good shape for lift force) and a large absolute value of S_T means that the shape has a large torque (not good shape for torque).

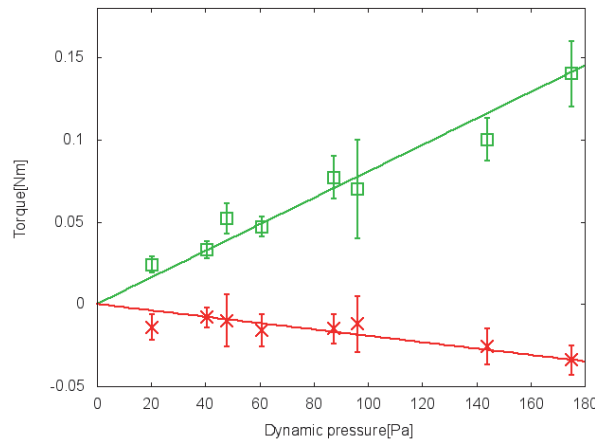


FIGURE 2.9 – Wind tunnel results of the torques with error bars. Using the least square method and I found a proportional relationship between torque force and dynamic pressure.

2.6.2 Numerical simulation

I focused on the shield's torque because even though Mars' surface wind is fast, lift forces are small enough judging from the wind tunnel test and numerical simulations. Fig. 2.10 and 2.11 are simulation results of shield's surface differential pressure. Shield's surface has a -30 to 20 Pa differential pressure. Negative pressure means that the shield is pulled by wind, and positive pressure means that the shield is pushed by the wind.

Simulated S_T of the semispherical shield is $-1.7 \times 10^{-4} m^3$ and simulated S_T of the circular truncated cone shield is $7.5 \times 10^{-4} m^3$. These numerically simulated factors are nearly equal to the observed shape factors $-2.0 \times 10^{-4} m^3$ and $8.1 \times 10^{-4} m^3$, respectably. Under the proportional condition between dynamic pressure and lift force and torque, these numerical simulation conditions are proved trustworthy.

To optimize the design of the wind shield, I focused on the torque direction of them to design an optimized wind shield. From the wind tunnel test and the numerical simulation, I found that the semispherical shield and the circular truncated cone have opposite torque direction. The semispherical shield roll over to the upstream direction while the circular truncated cone shield roll over to the

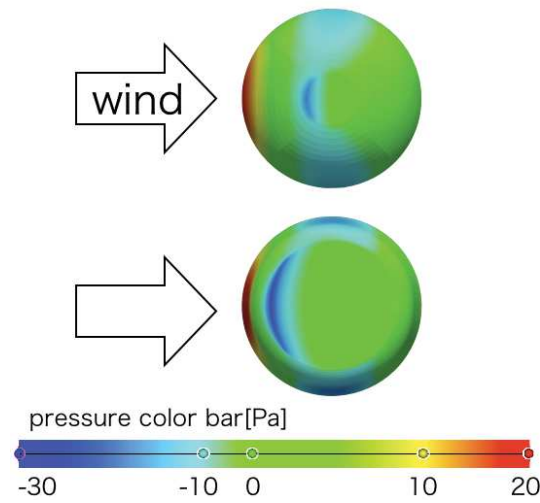


FIGURE 2.10 – *Semispherical and circular truncated cone wind shield's pressure distribution view from the top. The simulation is done under 20 m/s wind velocity and 0.1 atm which is close to the wind tunnel test's conditions.*

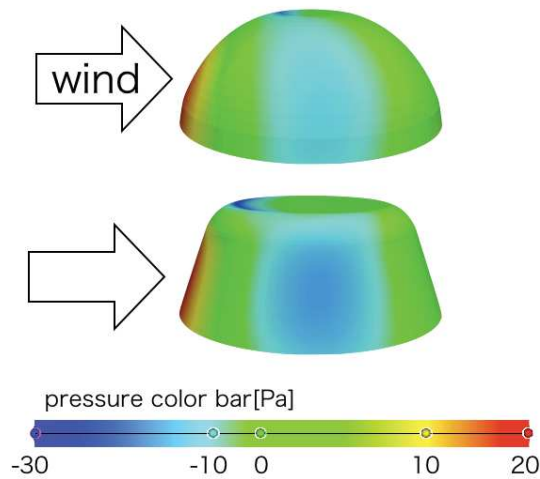


FIGURE 2.11 – *Semispherical and circular truncated cone wind shield's pressure distribution view from the side. The simulation is done under 20 m/s wind velocity and 0.1 atm which is close to the wind tunnel test's conditions.*

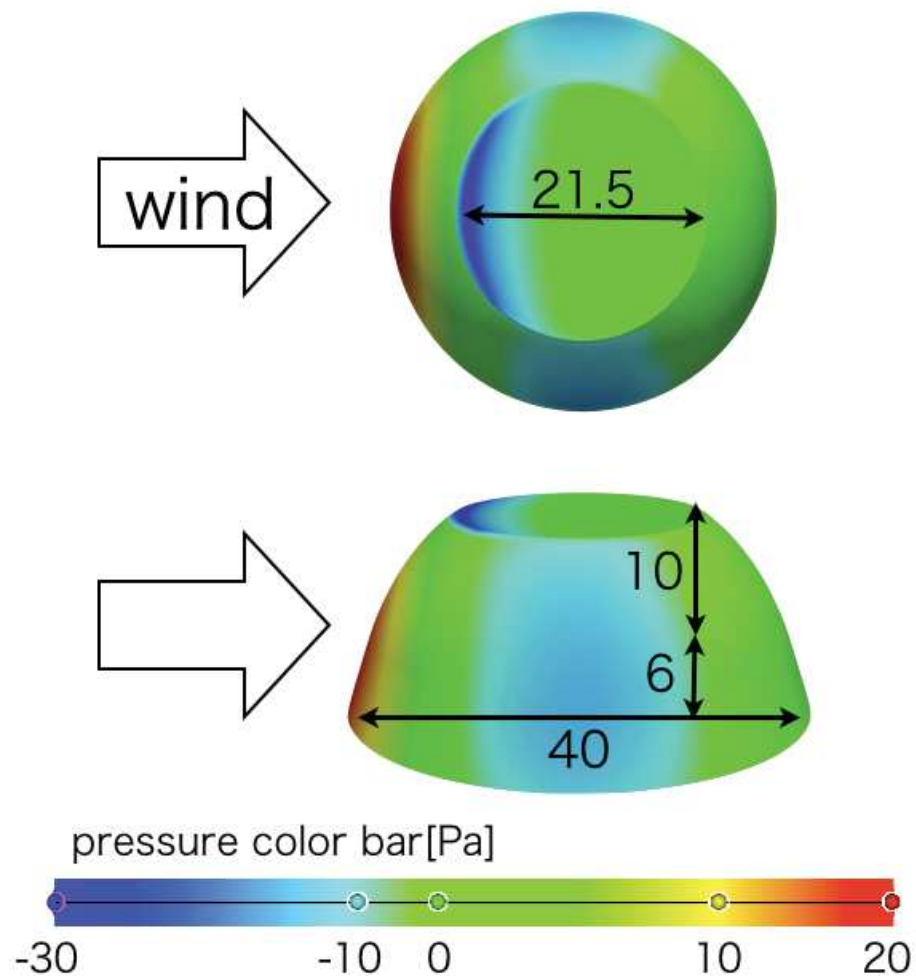


FIGURE 2.12 – *Designed wind shield's pressure distribution. The simulation is done under 20 m/s wind velocity and 0.1 atm which is close to the wind tunnel test's conditions.*

downstream direction. These results imply that the combination of the two will enable us to obtain a torque-less design for the wind shield. Thus, I combined them with various proportions. Finally, I designed a wind shield with almost 0 torque as shown in Fig. 2.12. S_T of this designed shield is $-2.5 \times 10^{-5} m^3$ (table 2.4). The bottom part of the wind shield up to 6cm height is made of the circular truncated cone and the upper part 6cm height to the top (16cm height) is made of the semisphere. Diameters of the bottom and top are 40cm and 21.5cm. According to the results of shape factor compiled by numerical simulation, the customized shape is more efficient compared to the semispherical shield and circular truncated cone shield by a factor of 8 and 30, respectively.

Shape	Condition	Shape factor(S_T)[m^3]	Torque coefficient(C_T)
Semisphere	Wind tunnel test	-2.0×10^{-4}	-0.008
	Numerical simulation	-1.7×10^{-4}	-0.0068
Circular truncated cone	Wind tunnel test	8.1×10^{-4}	0.0323
	Numerical simulation	7.5×10^{-4}	0.0298
Designed	Numerical simulation	-2.5×10^{-5}	-0.099×10^{-2}

TABLE 2.4 – *Shape factors of the semispherical, circular truncated cone and designed shield and associated Torque coefficient*

2.7 DISCUSSION

Torque direction and amplitude can be explained by a streamline curvature method and a wind separation. Fig. 2.13 and 2.14 are streamlines, seen from the top and the side view. Fig. 2.15 shows velocity vectors at just leeward from the shields (25cm far from the center of the shields; the red line in Fig. 2.14). I can see vortexes and turbulent separated flow in these 3 figures (Fig. 2.13 to 2.14).

In addition, these 3 figures and Fig. 2.15 show vertical profiles of the stream wire velocity. A turbulent flow and a flow separation occur where stream direction velocity has a negative value (the area surrounded in the green line). Bending of a streamline occurs at the edge of the shield's top, so from the law of streamline curva-

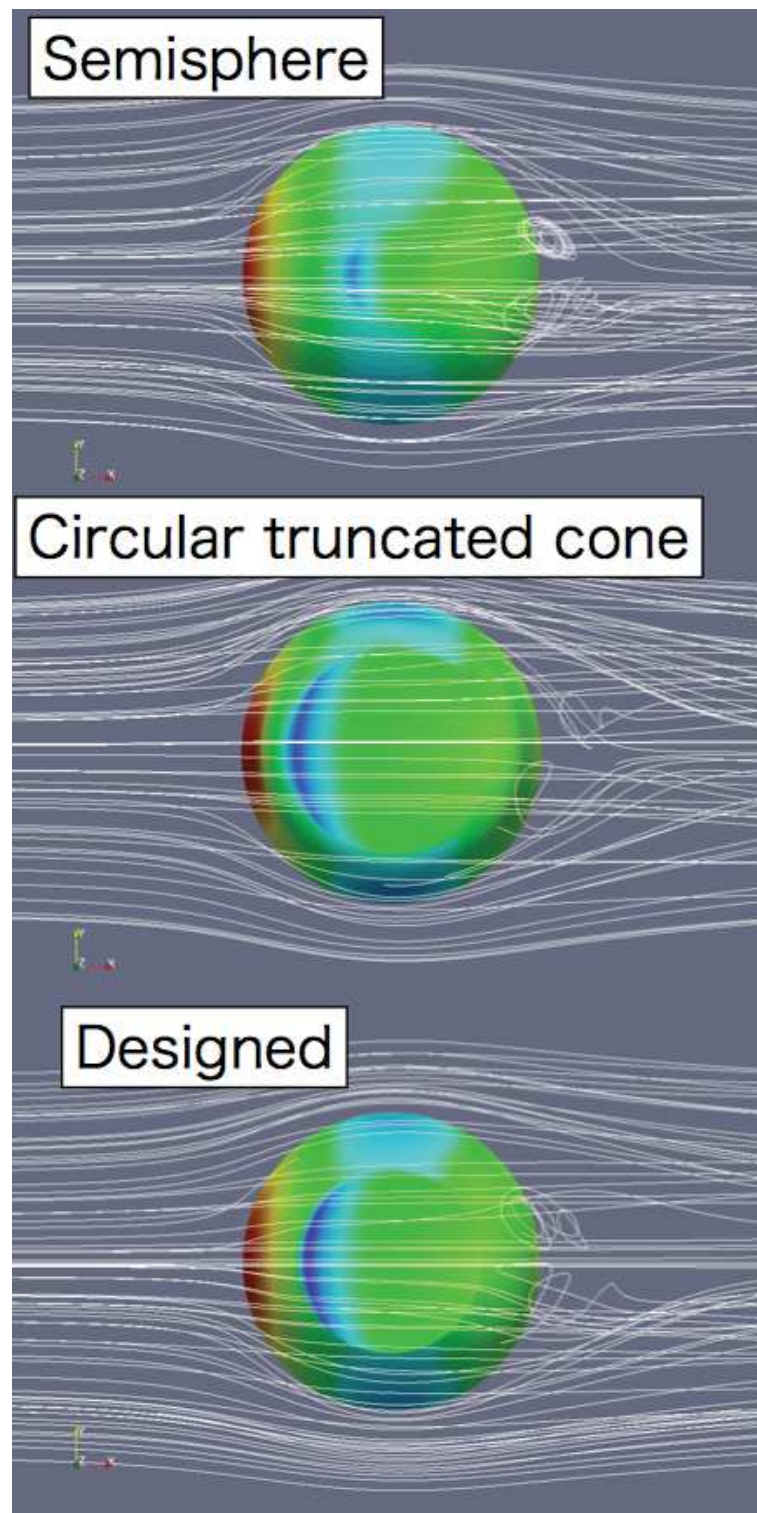


FIGURE 2.13 – Stream lines seen from the top. Red and blue color show positive and negative pressure respectively. Torque direction is explained by the balance between the positive and negative pressure.

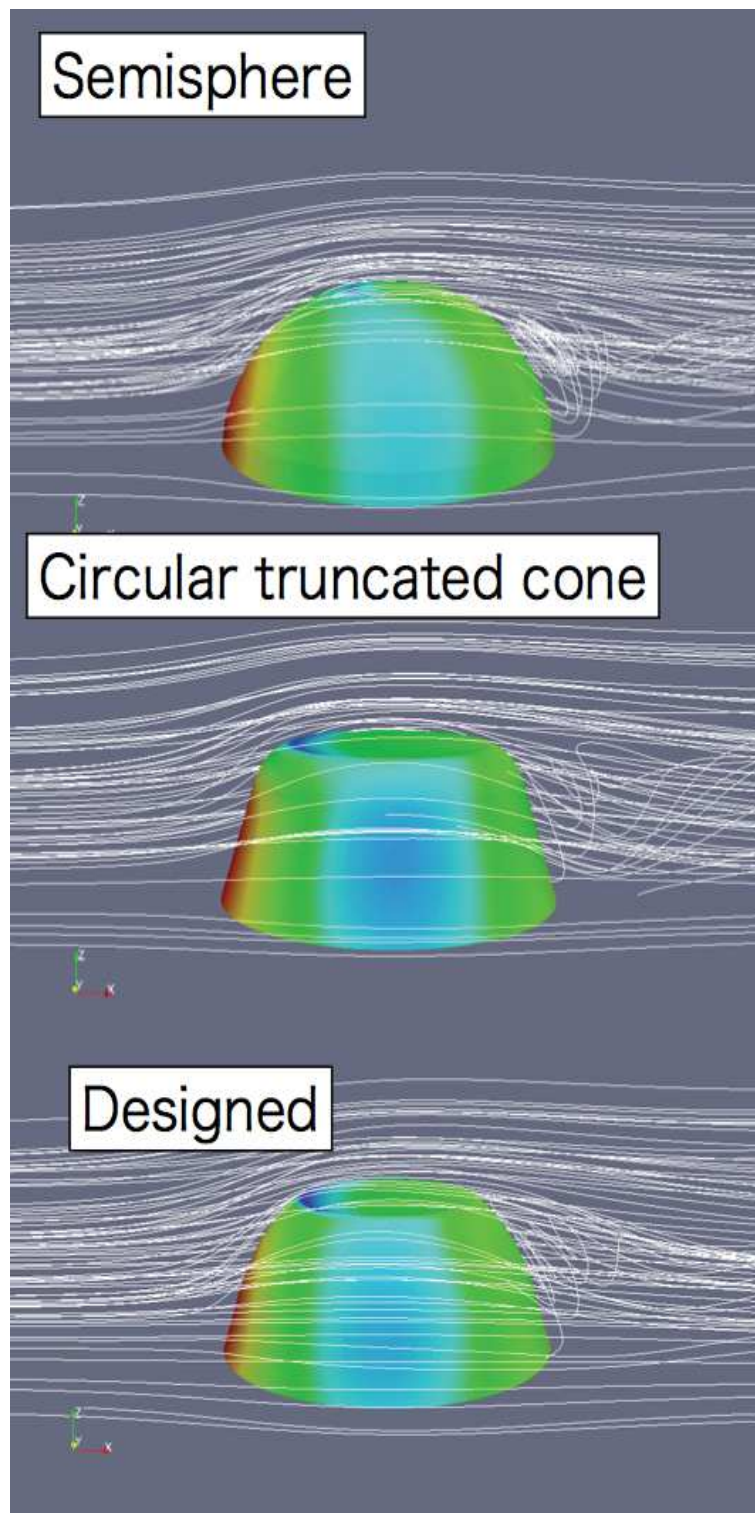


FIGURE 2.14 – *Stream lines seen from the side*

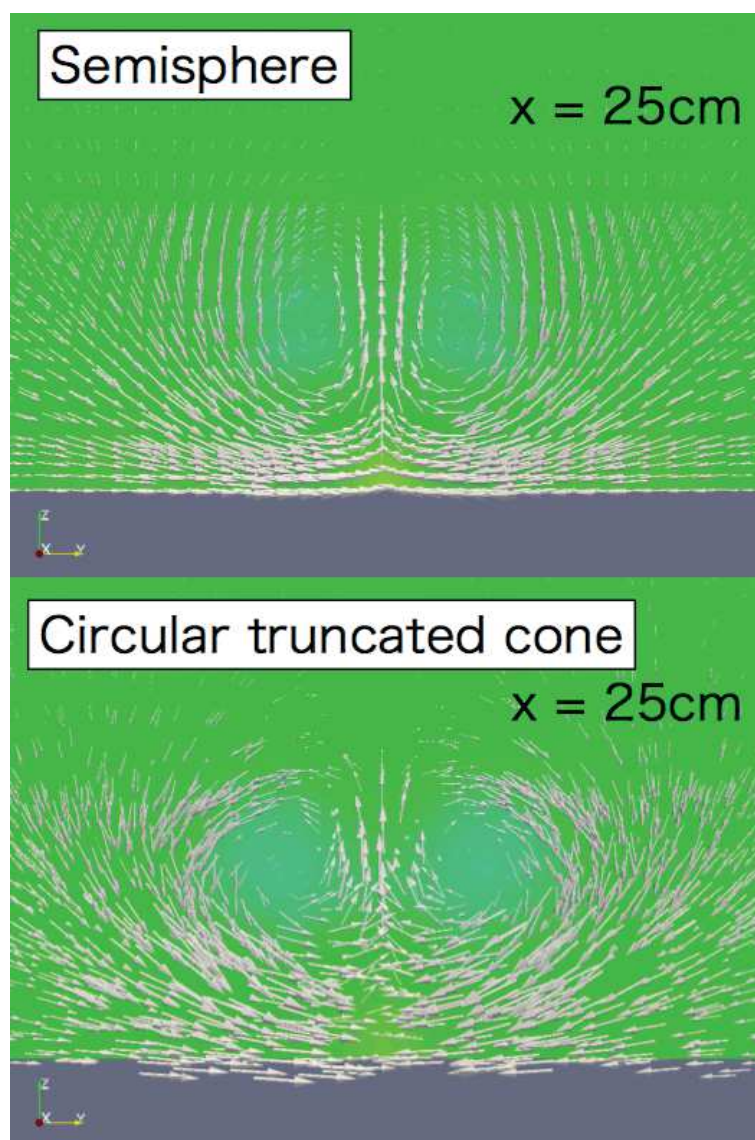


FIGURE 2.15 – Velocity vectors at just leeward from the shields (at the red line of Fig. 2.16). Arrows show wind vectors. We can see the Eddies have been developed at this area.

ture, shields are pulled outside in the area were surrounded by a red circle.

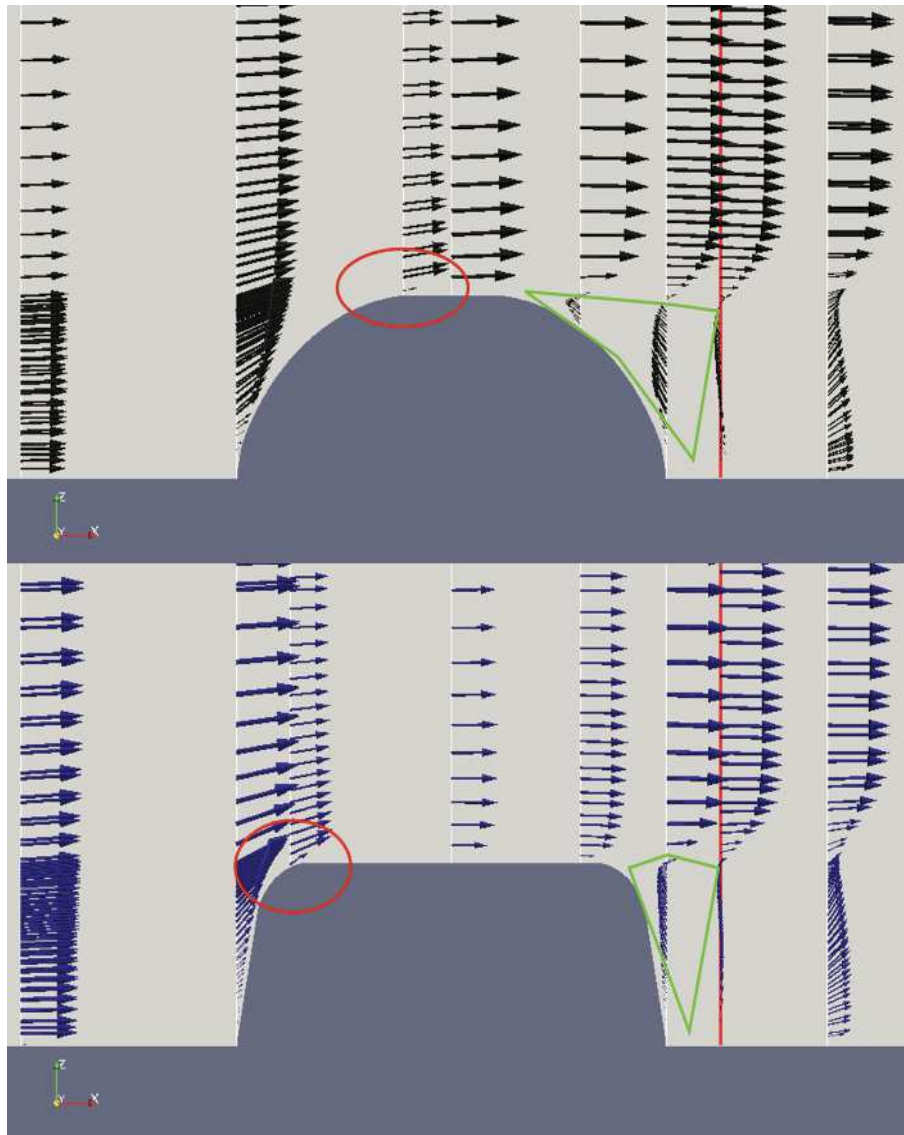


FIGURE 2.16 – *Streamwire velocity and turbulent and stream bending areas. The turbulence (green area) pulls the wind shields to upward. The bending wind (red area) generates torque to roll the windshield.*

In Fig. 2.16, the green area is the area of strong lift force, while the red area at distance from the center is the area of strong torque. Because of these 2 reasons, the semispherical shield is better than the circular truncated cone from a viewpoint of torque, but the circular truncated cone shield is better than the semispherical shield from a viewpoint of lift force.

2.7.1 Stability of the wind shield

I evaluated the stability of the shield in the following steps. First, I calculated slide force

$$F_x = \int p \vec{e}_x \cdot d\vec{S}, \quad (2.20)$$

where F_x is horizontal force which pushes the wind shield in horizontal direction, \vec{e}_x is unit vector parallel to the wind flow direction. If F_x is larger than μN , the shield would move (μ is coefficient of static friction, N is normal force). N is obtained from the differences in shield's weight (M) and lift force (L).

$$N = M \times g' - L, \quad (2.21)$$

where g' is gravity on Mars ($3.71m/s^2$). The results of numerical simulation for the designed shield were

$$F_x = S_x \times \rho U^2, \quad (2.22)$$

$$L = S_L \times \rho U^2, \quad (2.23)$$

where S_x is shape factor of horizontal direction force. So, the stability will be given as below

$$F_x < \mu N = \mu(Mg' - L). \quad (2.24)$$

The stability of the wind shield depends on wind velocity, the weight of the wind shield, and the static frictional coefficient. I took Pavonis Mons on Mars, which is one of the windiest places on the planet, as an example. The wind speed can be as high as 50 m/s (Toyota et al., 2011). I calculated the static frictional coefficient of martian soil from Martian regolith properties (Golombek et al., 2008). This gives me $\mu = 0.42 \pm 0.15$, if I assume these values as typical Martian properties. The maximum wind speed that meets the stability criteria is $U < 67.5 \pm 8.7m/s$. The speed is about the same as the strongest winds speed on the surface of Mars.

2.7.2 Tilt noise

I estimated ground tilt imposed by the torque on the designed shield. I assumed Martian ground as a semi-infinite elastic body to

calculate ground strain. I calculate settlement of the shield as :

$$\Delta H_E = I_G \frac{1 - \nu^2}{E} \Delta q B, \quad (2.25)$$

where H_E is ground settlement (deformation of the ground surface), I_G is settlement factor (Enkhtur *et al.*, 2013), ν is Poisson's ratio of the ground, E is Young's modulus of the ground, q is stress from feet of a wind shield and B is diameter of the legs. In this paper, I assume Martian ground as a semi-infinite elastic body with Young's modulus of $E = 9.5 \times 10^7 \text{ N/m}^2$ and Poisson's ratio of $\nu = 0.22$ (Delage *et al.*, 2017). Three circular feet of 4cm diameter support the wind shield (settlement factor is $I_G = 1.0$ for circular ground contact area). With eq(2.27), I get differential stress Δq :

$$\begin{aligned} \Delta q &= \frac{\Delta F}{S} \\ &= \frac{S_T \cdot \rho U^2}{D} \frac{1}{(B/2)^2 \pi}, \end{aligned} \quad (2.26)$$

where S is are of ground contact area of the leg and D is diameter of wind shield. I obtain tilt noise N_{tilt} :

$$\begin{aligned} N_{\text{tilt}} &= g_{\text{Mars}} \Delta \theta \\ &= g_{\text{Mars}} \frac{\Delta H_E}{D} \\ &= \frac{I_G g_{\text{Mars}} (1 - \nu^2) S_T \cdot \rho U^2 B}{D^2 \times E (B/2)^2 \pi}. \end{aligned} \quad (2.27)$$

So far, I calculated these lift forces torques and shape factors in constant velocity. In the case of ground tilt noise, I should estimate them as a function of frequency. First, I verified the frequency response of the wind shields. I did not find any frequency dependences in the 0.01Hz to 10Hz range. I estimate the efficiency of the wind shields by comparing seismometer sensitivity with tilt noise. If the expected tilt noise is higher than the sensitivity of the seismometer, the tilt noise would be detected as noise. Thus, I need martian wind spectrum data to calculate the tilt noise as a function of fre-

quency. I used observed wind data by Phoenix (Fig.2.17). I calculated the tilt noise with 3 wind models. One is observed wind data by Phoenix and the others are models based on the observation data. One is a windy situation and another is a stormy situation (average wind velocities are 20 m/s and 50 m/s (ref :MCD, Mars Climate Database (<http://www-mars.lmd.jussieu.fr>)). Finally, we plot the expected tilt noise and martian seismometer sensitivity requirement of the InSight mission at the windy site and stormy site (Fig. 2.18). Only designed shield's noise is lower than threshold detection of InSight seismometer requirement in the windy situation (Fig. 2.18 left). Even for the stormy situation, the tilt noise is almost lower than the threshold requirement (Fig. 2.18 right). When the ground tilt noise level is lower than the threshold level of seismometer sensitivity, I called this period a noise-free period. I estimated the tilt noise-free periods realized with our optimized wind shield. I made a simple wind model by Weibull distribution (Lorenz, 1996). The probability of wind velocity for each average wind velocity is given by the equation

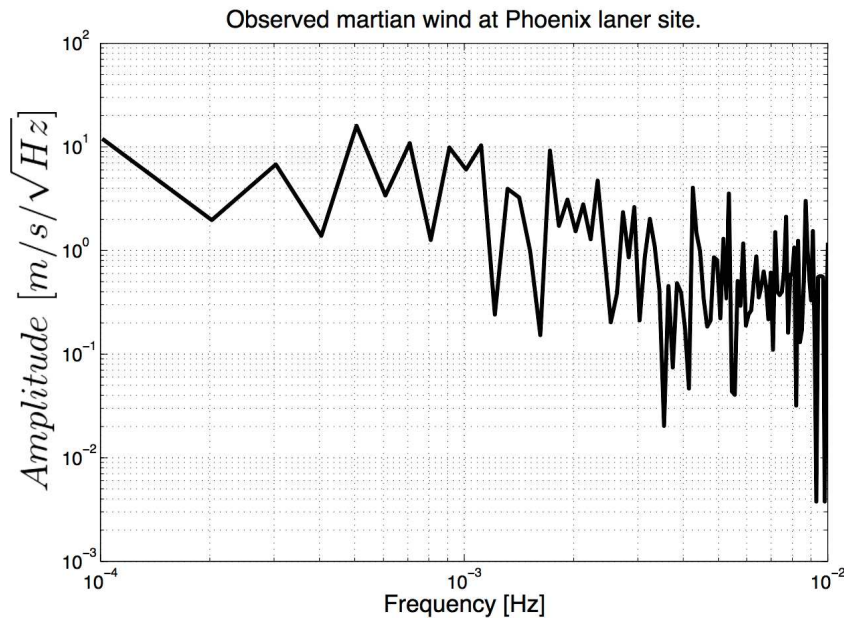


FIGURE 2.17 – *Martian wind data at Phoenix landing site. Location : E-125.7 N68.2, Sampling : 50 s, Local time : daytime of Mars, Average velocity : 5.1 m/s. The observation data has high amplitude in the range of around 10^{-3} Hz .*

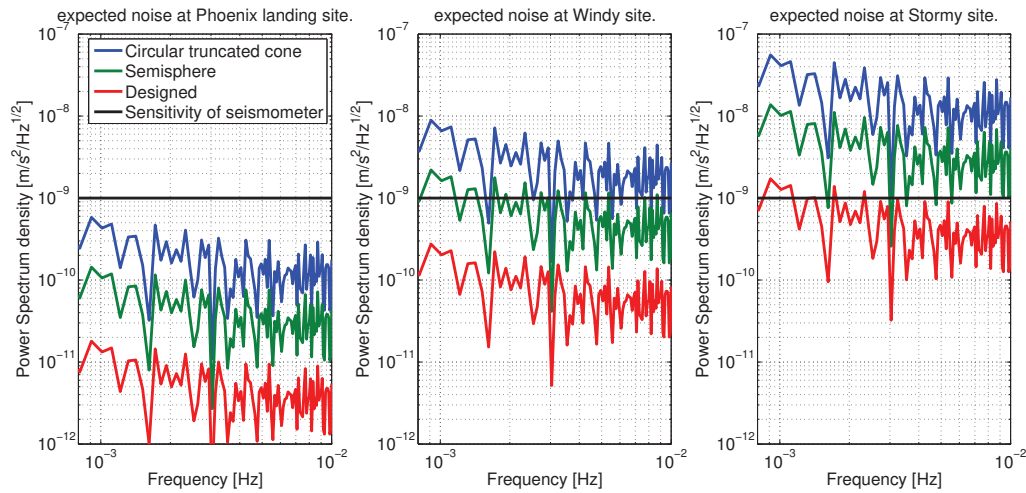


FIGURE 2.18 – Expected noise and sensitivity of the seismometer. The sensitivity of the seismometer is a requirement of the InSight mission seismometer. The ground tilt would be a noise source if the expected noise rises the sensitivity. The average of the wind velocities is 5 m/s, 20 m/s, and 50 m/s at Phoenix landing site, windy site, and stormy site respectively. In windy and stormy conditions, only the designed shield is effective to protect the seismometer.

$$f(V) = \left(\frac{k}{c}\right) \left(\frac{V}{c}\right)^{k-1} \exp\left\{-\left(\frac{V}{c}\right)^k\right\}, \quad (2.28)$$

where $f(V)$ is probability of wind velocity at V m/s, c is scale parameter and k is shape parameter. Scale parameter c is calculated by following expression

$$c = \frac{\bar{V}}{\Gamma\left(1 + \frac{1}{k}\right)}. \quad (2.29)$$

\bar{V} is average wind velocity, k is shape parameter and Γ is gamma function.

The tilt noise is depending on k value and average wind velocity. In this paper k is fixed to 1.5 (Lorenz, 1996). I referred to the MCD and found that global surface wind velocity can be as high as 20 m/s. Thus I set V as 5, 10, 20 m/s as calm, normal, and windy case respectively. Noise will not affect the observation if the noise drop below a threshold level (the level is the sensitivity of the InSight

mission seismometer), I consider the term as a noise-free period. Then I integrated the probability of noise-free periods, I got the ratio of the noise-free period (Tab. 2.5).

Average wind velocity (m/s)	5	10	20
Circular (%)	75.2	39.4	16.4
Semisphere (%)	97.9	75.5	39.6
Designed (%)	99.9	99.8	90.0

TABLE 2.5 – *Ratio of noise free period with respect to the whole observation period. The ratio indicates the efficiency of the wind shields. The improvement introduced by the new design is particularly significant for higher-wind environments.*

In this way, I evaluate the efficiency of the wind shields. The results suggest that only the designed wind shield can reduce tilt noise smaller than the sensitivity of the seismometer. For the long-term observation, the designed wind shield will realize more than 90% of noise-free periods even for the stormy condition. This shows clearly the efficiency of the designed wind shield compared to other designs.

2.8 CONCLUSION

In this study, I designed a torque-less wind shield for broadband seismic observations through wind tunnel tests and CFD simulations. I focused on lift force and torque as important factors for the design of the wind shield for Martian broadband seismic observations. I conducted wind tunnel tests and numerical simulations to evaluate the lift forces and the torques as a function of wind speed and air density. I found the proportional relationships where the lift forces and the torques change linearly with the dynamic pressure. I confirmed the numerical simulations with the results of wind tunnel tests.

I combined circular truncated cone shield and semispherical shield for optimization of the wind shield. I designed an effective torque-less wind shield for broadband seismic observation in windy environments on Mars and decrease the seismic noise caused by martian

wind. The designed torque-less wind shield keeps a stable position even for the strongest wind environment on Mars. It will also enable the noise-free periods of the designed wind shield longer than that of a typical wind shield. Finally, the ground noiseless period became more than twice in a windy environment.

NORMAL MODE PROPAGATION AND COUPLING WITH THE ATMOSPHERE AND GROUND.

SOMMAIRE

3.1	NORMAL MODE WITH ATMOSPHERE	55
3.2	SIMPLIFIED NORMAL MODE COMPUTATION	58
3.2.1	Approximation of the excitation force terms	63
3.2.2	Moment tensor of the excitation.	66
3.3	SOLUTIONS FOR THE NORMAL MODES	69
3.3.1	Strain and Stress	69
3.3.2	Normal modes properties	69

ACOUSTIC coupling between solid Mars and atmosphere is important for the calculation of Mars background free oscillation. This coupling leads to continuous excitation of Rayleigh waves and associated normal modes by atmospheric winds and pressure fluctuations. The normal modes are affected by many factors, but the effects are not same. In some cases, I can neglect such a complex effect and use a simple normal mode. The simple normal modes save computation time and let us take into account time variations of the atmosphere. In this chapter, I will show a new calculation method of normal mode in the atmosphere and Rayleigh waves excited by atmospheric sources.

3.1 NORMAL MODE WITH ATMOSPHERE

Atmospheric normal modes are affected by many factors; viscosity, radiative boundary, sound velocity, and relaxation. Viscosity and relaxation attenuate the amplitude of waves, radiative boundary changes resonance frequencies of waves, and sound velocity changes the length of waves. The precise normal modes are calculated by *Lognonné (2005); Lognonné and Johnson (2007)*. In these papers, they assumed a symmetrical atmosphere. While they succeeded in precisely evaluating the effects of the atmospheric layers, the evaluation required some expensive calculation. Such an expensive calculation prevents us from taking into account the lateral variation of the atmosphere and lets us study normal mode excitation with a 3D atmospheric model. Thus, we need some simplified modelization to decrease the calculation cost so that I can take into account the lateral variations. First, I evaluate the contribution from the high altitude atmosphere. While they do contribute to the normal mode excitation, their effect can be small due to the small air density of Mars. The lateral variation of the atmosphere is more important in normal mode excitation on Mars than on the Earth due to the larger atmospheric pressure variation on Mars. The main driver of the atmospheric variation is temperature. On Mars, the temperature variation is much larger than that of the Earth, because of the low atmospheric inertia. Because of the large temperature variation, the Marian atmospheric scale height changes $\pm 20\%$ in a day Fig. 3.1 which means the atmospheric structure differs significantly on the dayside and night side, thus lateral variation needs to take into account in MBF calculations.

In this study, I propose to compute the amplitude of the atmospheric normal modes by propagating the normal mode amplitude at the surface into the atmosphere. In other words, instead of directly calculating normal modes in the atmosphere, I extrapolate the modes calculated for the solid part of the planet into the atmosphere. For this purpose, I make the following assumptions :

- the normal mode phase velocity is much greater than acoustic-

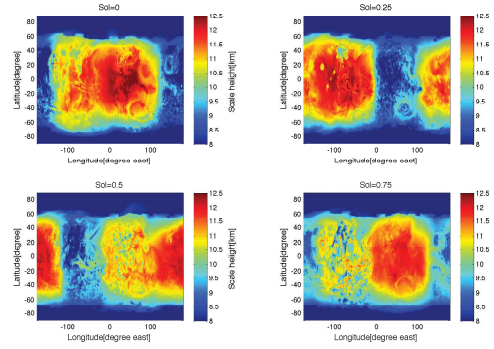


FIGURE 3.1 – Variation of atmospheric scale height in a day. The red area is hot and blue is the opposite. Because of the big temperature variation, the scale height changes from 8 to 12 km thickness in a day. During day time, the atmosphere expands to 12 km height, during night time it is opposite, it shrinks to 8 km height. The scale height variation affects normal mode structure directly. The iso-sphere model cannot describe this lateral effect.

wave velocity, leading to a vertically longitudinal upward-moving acoustic wave (Acoustic wave velocity is several hundred meters per second. Rayleigh wave velocity is a few kilometers per second.);

$$k_z z = \frac{\omega}{c_{acoustic}} > k_x x = \frac{\omega}{c_{Rayleigh}}$$

$$u_k^z(0) > u_k^x(0),$$

where $k_x = \frac{\omega}{c}$ is a horizontal wave number, x is the horizontal axis, $k_z = \frac{\omega}{c}$ is a vertical wave number, z is the altitude above the ground, c is wave velocity.

- the normal modes interact asymptotically with the atmosphere and without significant resonance between solid and atmosphere, which limits this approach to normal modes above the atmospheric cutoff frequency (Lognonné and Johnson, 2007).

Given these two assumptions, and assuming continuity of the vertical displacement and conservation of energy during the upward propagation. I can neglect horizontal propagation effect,

$$\begin{aligned} \nabla \vec{u}_k &= u_k^x(0)(-ik_x x)e^{-i(k_x x + k_z z)} + u_k^z(0)(-ik_z z)e^{-i(k_x x + k_z z)}, \\ &= u_k^z(0)(-ik_z z)e^{-i(k_z z)}, \end{aligned}$$

The wave-propagating normal mode vertical component is

$$u_k(z) = u_k(0) \cdot e^{-ik_z z} \times \sqrt{\frac{\rho(0)c(0)}{\rho(z)c(z)}} , \quad (3.1)$$

where $\rho(z)c(z)$ is the acoustic impedance, with $\rho(z)$ and $c(z)$ being the density and sound speed respectively and ω the angular frequency of the mode. The first factor on the right side of the equation is the wave-propagation factor and the second factor is the wave transmission ratio. Note here that the amplitude of the mode, even if complex in the solid part, is imaginary. With the wave-propagation method, I can describe the local time lateral variation of density and sound speed and, more generally, how the normal mode amplitude in the atmosphere depends on geography.

I compare the resulting amplitudes with those computed by using the more precise model of *Lognonné et al.* (2016). For angular orders, $\ell \geq 10$, the difference is less than the effect of the lateral variation (see Fig. 3.2) especially for the first 10 km of altitudes, where most of the excitation sources are expected. As I will see later, the normal mode amplitudes are requested only where the modes are observed (i.e. at the surface) and where the modes are excited. The lack of good modeling at altitudes larger than 10 km is therefore not an issue for my goal. This is of course very different for a study aiming to model the normal modes in the ionosphere, for which accurate modeling is requesting up the atmospheric height (*Lognonné* (2008)). However, for smaller angular orders and for modes with frequencies close to or below the atmospheric cutoff frequency, this simple propagation fails and large discrepancies appear because of acoustic-wave reflection and resonance in the atmosphere. Fig.3.4 shows the relative atmospheric energy for the fundamental spheroidal modes. The energy peaks around 2.2 mHz, which corresponds to the angular order $\ell=9$. This large coupling of the normal mode with angular order $\ell=9$ is normal if also seen on the mode amplitude (Fig. 3.3). Such modes, thus require exact computation. Note, however, that these modes are also difficult to observe because of the expected high very

low-frequency modes associated with temperature fluctuation below 5 mHz.

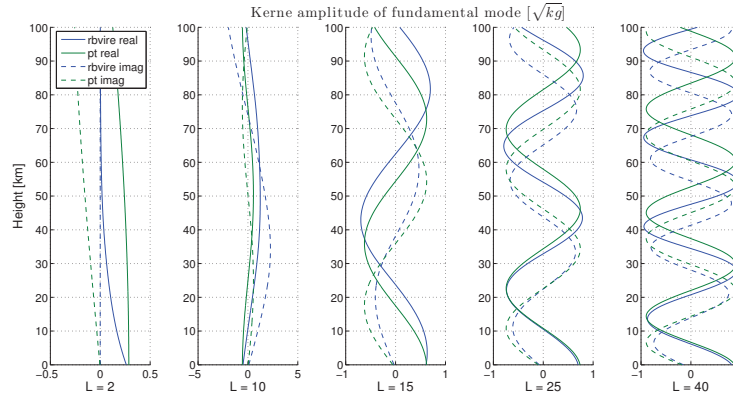


FIGURE 3.2 – Kernel sensitivity of normal modes in the air. Blue one includes radiative boundary, viscosity and relaxation. Green one consider only for wave propagation and transmission. Solid lines and dot lines are real part and imaginary part respectably. In $n \geq 10$ order, the gaps between 2 normal modes are small under scale height.

3.2 SIMPLIFIED NORMAL MODE COMPUTATION

I calculate the excitation force in the air f using by martian atmospheric model (Lognonné and Mosser, 1993). In the linearized Normal mode equation in the atmosphere is given by :

$$\rho_0 \frac{\partial \vec{v}_1}{\partial t} = -\nabla p_1 + \rho_0 \vec{g}_1 + \rho_1 \vec{g}_0 + \vec{f}, \quad (3.2)$$

where ρ , v , p , f and g are density, velocity, pressure, excitation force and gravity acceleration respectively. Subscript 0 and 1 equilibrium fields and perturbed fields. Non-subscripts are the full atmospheric fields. u and v represents displacement and velocity respectively. I describe the excitation force with fluid dynamics to estimate every term by GCM.

In the atmosphere, in general case, Navier-Stokes, mass conservation

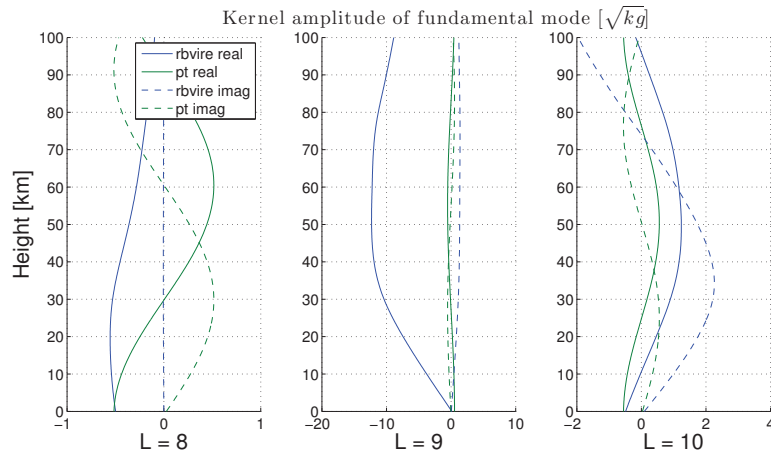


FIGURE 3.3 – Kernel sensitivity of normal modes in air. At the normal mode of angular order nine, the large gaps occur because of the resonance between the atmosphere and the solid part. The normal mode cannot describe this resonance, so the normal mode calculation only works for angular order 10. Below angular order 10, normal modes are hard to detect because of the low-frequency thermal noise.

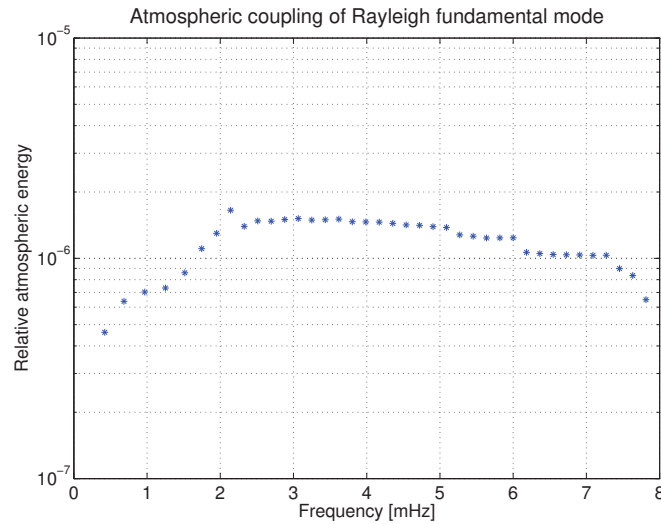


FIGURE 3.4 – Relative atmospheric energy of surface wave in the Mars atmosphere for Rayleigh surface waves. From left to right, the number of the angular order is 2,3,4 ... up to 39. The peak of the fraction is at angular order 9 (around 2.2 mHz). At the first peak, there is a strong resonance between atmosphere and solid part.

equations and parameter definitions are

$$\rho \left(\frac{\partial \vec{v}}{\partial t} + \vec{v} \cdot \nabla \vec{v} \right) = -\nabla p + \nabla \cdot (\rho \nu (\nabla \vec{v} + \nabla \vec{v}^T)) + \rho \vec{g}, \quad (3.3)$$

$$\frac{\partial \rho}{\partial t} = -\nabla \cdot (\rho \vec{v}), \quad (3.4)$$

$$\rho = \rho_0 + \rho_1,$$

$$p = p_0 + p_1,$$

$$\vec{g} = \vec{g}_0 + \vec{g}_1,$$

$$= \vec{g}_0 - \nabla \Psi_1,$$

where ν and Ψ are kinematic viscosity and mass redistribution potential. The left hand equation of the Navier-Stokes is inertia term (1st term is time variation and 2nd term is advection (convection)), the right hand is divergence of stress and external force (1st term is pressure, 2nd is viscosity, the 3rd is gravitational force).

I will neglect the viscosity terms in what follows, as I focus on my work to very long period signals associated to normal modes. From eq(3.4), the time derivative of the kinetic momentum is calculated as follow,

$$\begin{aligned} \frac{\partial}{\partial t}(\rho \vec{v}) &= \vec{v} \frac{\partial \rho}{\partial t} + \rho \frac{\partial \vec{v}}{\partial t}, \\ &= -[\nabla \cdot (\rho \vec{v})] \vec{v} - \nabla p + \rho \vec{g} - \rho (\vec{v} \cdot \nabla) \vec{v}, \\ &= -\nabla p + \rho \vec{g} - \nabla \cdot (\rho \vec{v} \vec{v}). \end{aligned} \quad (3.5)$$

I substitute the equation (3.5) into the normal mode equation (3.2) to describe the excitation force in the air,

$$\vec{f} = \nabla p_1 - \rho_1 \vec{g}_0 - \rho_0 \vec{g}_1 + \rho_0 \frac{\partial \vec{v}}{\partial t} - \nabla p + \rho \vec{g} - \nabla \cdot (\rho \vec{v} \vec{v}) - \vec{v} \frac{\partial \rho}{\partial t} - \rho \frac{\partial \vec{v}}{\partial t}.$$

This is the computation of excitation force. The excitation force will be calculated by atmospheric values calculated by GCM. Thus, the fluid is non viscos and incompressible. The viscosity and gravity terms are small. In this thesis, the viscosity and gravity terms are neglectable because the fluid is non viscos and incompressible. With the equilibrium equation, I can then rewrite the equation and get :

$$\vec{f} = -(\rho_0 - \rho) \frac{\partial \vec{v}}{\partial t} - \frac{\partial \rho}{\partial t} \vec{v} + \rho_1 \vec{g}_1 + \nabla (p_1 - \Delta p) - \nabla \cdot (\rho \vec{v} \vec{v}). \quad (3.6)$$

where the differential pressure $\Delta p = p - p_0$ is the excess pressure with respect to equilibrium when computed by the Navier-Stoke equation and will be now written as p_{true} . The elastic pressure

$$p_1 = -\vec{u} \cdot \nabla p_0 + p_{Hooke}, \quad (3.7)$$

$$p_{Hooke} = -\rho c^2 \nabla \vec{u}; \quad (3.8)$$

The mass conservation

$$\rho_1 = -\nabla \cdot (\rho_0 \vec{u}), \quad (3.9)$$

where p_{Hooke} and c are Hooke's pressure and sound speed. I substitute eq(3.7), (3.8) and (3.9) into (3.6) and neglect the non-linear term related to gravity, which gives :

$$\begin{aligned} \vec{f} = & \nabla \cdot (\rho_0 \vec{u}) \frac{\partial \vec{v}}{\partial t} - \frac{\partial \rho_1}{\partial t} \vec{v} - \nabla \cdot (\rho \vec{v} \vec{v}) \\ & - \nabla (p_{true} + \vec{u} \cdot \nabla p_0 + \rho c^2 \nabla \vec{u}). \end{aligned} \quad (3.10)$$

GCM gives us p_{true} , v and ρ . I will define later the difference between p_{true} and p_1 as the pressure glut :

$$p_{glut} = p_{true} - p_1 = p_{true} + \vec{u} \cdot \nabla p_0 + \rho c^2 \nabla \vec{u}. \quad (3.11)$$

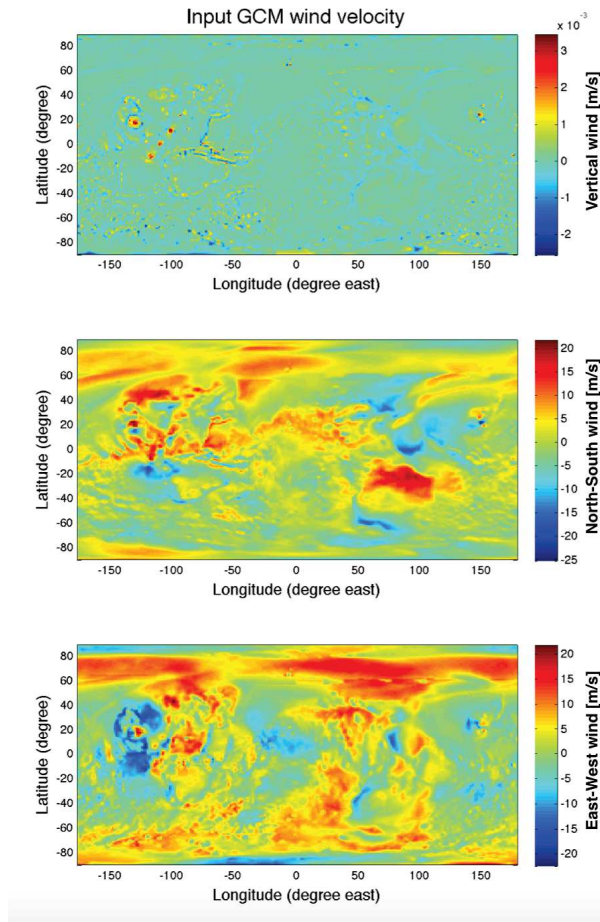


FIGURE 3.5 – GCM wind velocity field. Horizontal winds (North-South and East-West winds) are much faster than vertical wind. Thus the main contribution of reynolds stress of excitation force ($\rho v v$ in eq 3.12 is composed by horizontal winds.

3.2.1 Approximation of the excitation force terms

If I take the time derivative of the excitation force with respect to time, I can calculate magnitude relation between atmospheric pressure \dot{p} and elastic pressure $(\vec{v} \cdot \nabla p_0 + \rho c^2 \nabla \vec{v})$. I assumed that the time difference of air density and sound velocity are smaller than wind velocity. The amplitudes of elastic terms, estimated from GCM results, is about $10^{-7} Pa \cdot s^{-1}$ (Fig. 3.6). The values are as small as they can be ignored compare to the time differentiated atmospheric pressure $10^{-3} Pa \cdot s^{-1}$ (Fig 3.7). Note that in addition, GCM are known to filter the acoustic waves in their time propagation scheme, which is an additional reason to consider that the GCM field is free of acoustic waves.

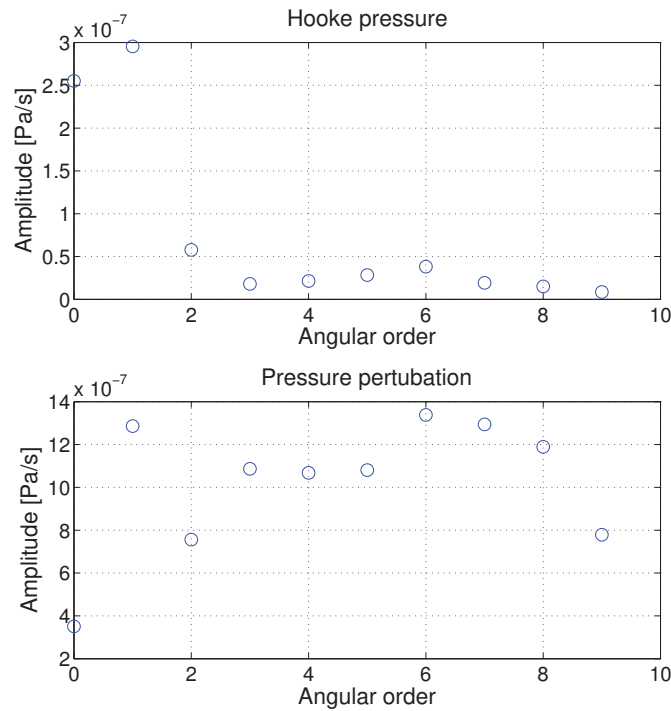


FIGURE 3.6 – The derivative of elastic pressure in the air. The magnitude of the amplitudes are $\approx 10^{-7} Pa \cdot s^{-1}$. They are enough small compare to the derivative of static pressure.

The time variation of the air density is about $10^{-3} [kg \cdot m^{-3}]$ in a day and its time differentiated value is about $10^{-7} [Pa \cdot s^{-1}]$ (Fig. 3.8). The effect of air density variation is small enough compare to the variation of the atmospheric pressure. It means that the air density

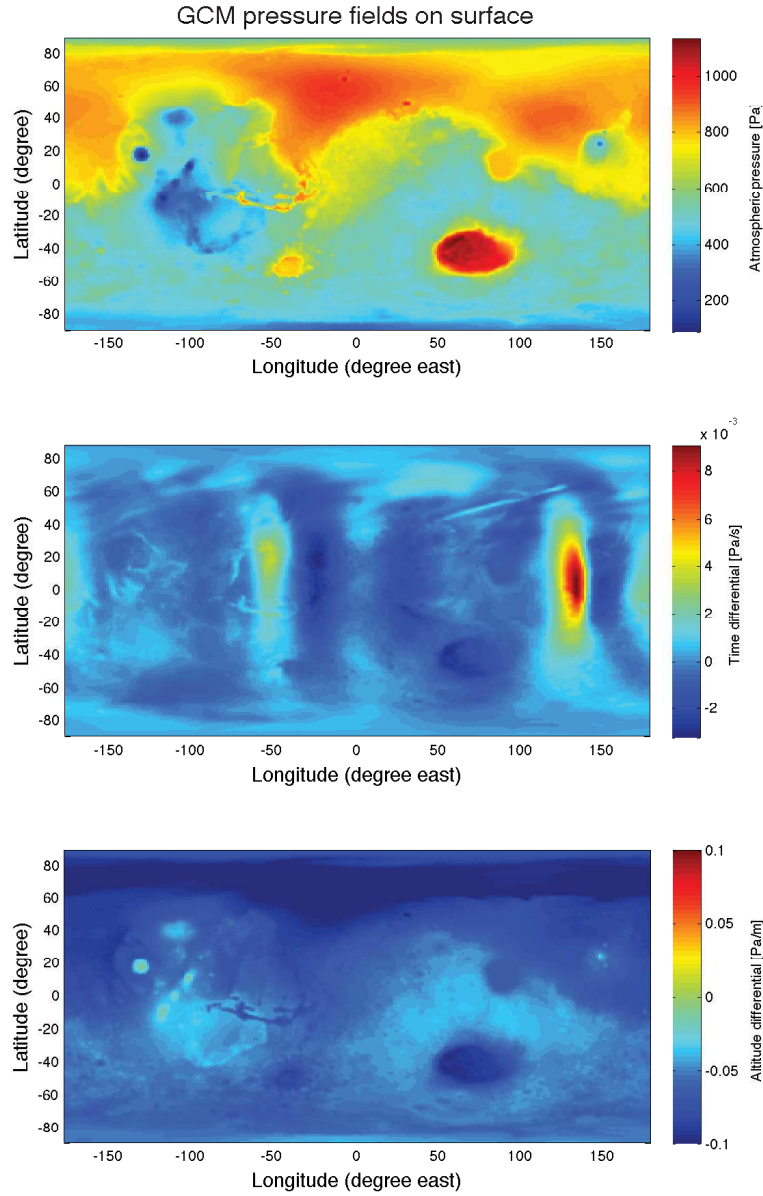


FIGURE 3.7 – Pressure fields at 4.5[m] height. The upper figure is atmospheric pressure field. The middle figure is time differentiated atmospheric pressure. The middle figure is height differentiated atmospheric pressure. Amplitude of the time differentiated pressure is $\approx 10^{-3} \text{ Pa} \cdot \text{s}^{-1}$. This time differentiated pressure is significantly larger compare to the derivative of elastic pressures $\approx 10^{-7} \text{ Pa} \cdot \text{s}^{-1}$.

variation term $\frac{\partial \rho}{\partial t} \vec{v}$ can be ignored.

I have shown the magnitude relationship between hydro static

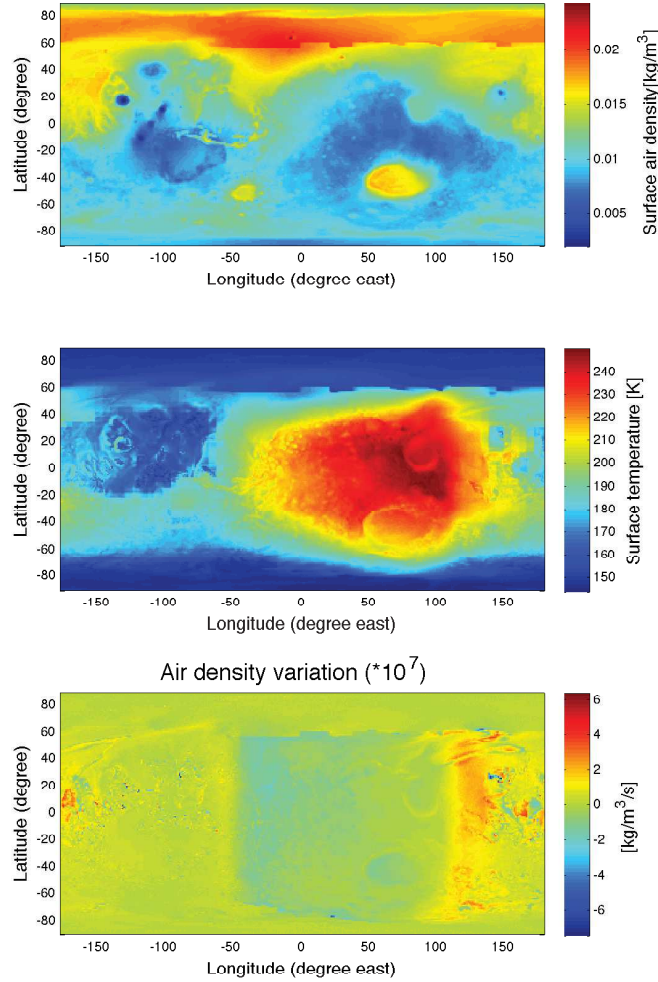


FIGURE 3.8 – Air density, temperature and time differentiated air density at the surface. The air density varies about 10^{-3}kg m^{-3} between day time and night time. The amplitude of the time differentiated air density is about $10^{-7} \text{kg m}^{-3} \text{s}^{-1}$.

pressure and elastic pressure in the air is

$$|\vec{u} \cdot \nabla p_0 + \rho c^2 \nabla \vec{u}| = p_1 \ll p_{\text{true}},$$

with the equation, the magnitude relation ship between $\nabla \cdot (\rho \vec{u}) \frac{\partial \vec{v}}{\partial t}$

and ∇p is given by

$$\begin{aligned}
 \rho_1 &= \int \frac{\partial \rho_1}{\partial t} dt = \int \nabla \cdot (\rho_0 \vec{v}) dt, \\
 &= \nabla \cdot \rho_0 \int \vec{v} dt, \\
 &= \nabla \cdot (\rho_0 \vec{u}), \\
 \rho_1 \frac{\partial \vec{v}}{\partial t} &= \nabla \cdot (\rho_0 \vec{u}) \frac{\partial \vec{v}}{\partial t}, \\
 \rho \frac{\partial \vec{v}}{\partial t} &\gg \rho_1 \frac{\partial \vec{v}}{\partial t}, \\
 \nabla p_{true} &\gg \nabla \cdot (\rho_0 \vec{u}) \frac{\partial \vec{v}}{\partial t},
 \end{aligned}$$

and $\nabla \cdot (\rho_0 \vec{u} \frac{\partial \vec{v}}{\partial t})$ term is negligible.

Finally, the excitation force is :

$$\vec{f} = -\nabla \cdot (\rho \vec{v} \vec{v}) - \nabla p_{glut}. \quad (3.12)$$

3.2.2 Moment tensor of the excitation.

I can therefore identify the second terms of eq(3.12) as the excitation coefficient, and the latter can be furthermore rewritten by using a generalization of the moment tensor, introduced by *Backus and Mulcahy* (1976a,b) for a quake, as noted by *Lognonné and Mosser* (1993). I then finally have

$$\Psi_k(t) = - \int_V dV \vec{u}_k \cdot [\nabla p_{glut} + \nabla \cdot (\rho \vec{v} \vec{v})] = \int_V dV \epsilon_k : \mathbf{m} - \int_S dS \vec{n} \cdot (\vec{u}_k : \mathbf{m}), \quad (3.13)$$

where I define the moment flux-glut tensor by :

$$m^{ij} = (p_{true} + \kappa \nabla \cdot \vec{u}) \delta^{ij} + \rho v^i v^j, \quad (3.14)$$

and where ϵ_k is the strain tensor of the normal mode k .

The surface integral terms can be re-written as

$$\int_S dS \vec{n} \cdot (\vec{u}_k : \mathbf{m}) = \sum_d \int_{S_d} dS [\vec{n} \cdot (\vec{u}_k : \mathbf{m})]_{-,d}^{+,d}, \quad (3.15)$$

where d are all the discontinuities in the solid planet, including the one between the surface and atmosphere (and for the Earth between

oceanic bottom and ocean) and when I assume that excitation occurs at the top of the atmosphere. In this expression, the difference of the field above and below each discontinuity is taken and represented by the brackets. I will limit myself to only the discontinuity between surface and atmosphere and will only consider the case of a spherical surface, even if asphericity, such as surface topography, can lead to specific excitations. In this hypothesis, the vertical wind cancel at the surface and the surface equation can be rewritten as

$$\int_S dS \vec{n} \cdot (\vec{u}_k : \mathbf{m}) = \int_S dS [u_k^0 m_{00}]_{-,s}^{+,s}, \quad (3.16)$$

where s denotes the surface. I furthermore assume that the surface pressure variations are such that the surface and subsurface is accomodating these pressure variation in the elastic regime. Although such a hypothesis could be discutable for the bottom of Earth's oceans, it seems very valid for Mars typical pressure fluctuation and is furthermore confirmed by observation of ground deformation from pressure drops (*Lognonné et al., 2020; Banerdt et al., 2020*). Consequently, the pressure glut cancels at the solid part of the surface (in fact, due to the solid character, these are the stress glut in the solid part). Due to the continuity of the vertical projected stress, this implies the cancellation of the pressure glut surface contribution. As no vertical flow occurs furthermore at the surface and as the vertical component of modes is continuous, the surface term cancels. Note that another approach needs to be used when normal modes are limited to the solid part and when computed assuming a free surface. In this case, indeed, a surface force needs to be used, to account for the pressure variation at the surface. In addition, this approach will not be able to integrate the acoustic emission generated by non-linearities in the atmosphere, unless the surface pressure is integrating the acoustic pressure fluctuations, which is not made by GCM pressure. :

With this moment flux-glut tensor, the normal mode excitation force are given by

$$s_k(t) = \int_V dV D_i u_k^j(\vec{r}) M_j^i, \quad (3.17)$$

where D_i denotes the covariant derivative and M_j^i is the source moment tensor density components. The trace of the source moment tensor density is simply :

$$\sum_{i,j} m_j^i \delta_j^i = 3p + \rho v^2. \quad (3.18)$$

For spheroidal normal mode which strain amplitude is vertical in the atmosphere, the important term for the source moment tensor is M_0^0 . My normal mode excitation can be approximated from eq(3.17) as

$$\begin{aligned} s_k(t) &= - \int_V dV \vec{u}_k \cdot \vec{F}_k, \\ &= - \int_V dV \vec{u}_k \cdot (\nabla \cdot M), \\ &= \int_V dV (\nabla \cdot \vec{u}_k) : M \\ &= - \int_V dV (p_{glut} + \rho v^0 v^0) \nabla_r u_k^r, \end{aligned} \quad (3.19)$$

where $\nabla_r u_k^r$ is the vertical strain terms ϵ_{00} , index 0 being used also for r . In case of the Earth, the normal mode in the atmosphere u_k are computed by several method (e.g. Lognonné *et al.* (1998b); Watada and Kanamori (2010)). I defined martian atmospheric normal mode (3.1)

$$\begin{aligned} u_k^r(z) &= u_k^r(0) \cdot e^{ik_z z} \times T(z), \\ T(z) &= \sqrt{\frac{\rho(0)c(0)}{\rho(z)c(z)}}, \end{aligned} \quad (3.20)$$

where c is acoustic speed, T is amplitude transmission ratio, ρ is air density, z is altitude from ground surface, k_z is wave number of z direction. If I assume the atmosphere to be locally isotherm, the sound speed does not change with altitude and I have then :

$$T(z) = \exp \frac{z}{2H_\rho}, \quad (3.21)$$

where H_ρ is the scale height for atmosphere density.

3.3 SOLUTIONS FOR THE NORMAL MODES

3.3.1 Strain and Stress

I introduce the stress $\tau^{\alpha\beta}$ and the strain $\epsilon^{\alpha\beta}$. The stress is related to the pressure field and the strain is :

$$\epsilon^{\alpha\beta} = \frac{1}{2} (\partial_\beta u^\alpha + \partial_\alpha u^\beta). \quad (3.22)$$

In spherical geometry I write these two tensors :

$$\begin{cases} \epsilon^{\alpha\beta}(r, \theta, \phi) = E^{\alpha\beta}(r) Y_l^{(\alpha+\beta)m}(\theta, \phi), \\ \tau^{\alpha\beta}(r, \theta, \phi) = T^{\alpha\beta}(r) Y_l^{(\alpha+\beta)m}(\theta, \phi). \end{cases} \quad (3.23)$$

where E and T are radial functions of strain and stress respectably.

3.3.2 Normal modes properties

Equation of motion is

$$\begin{cases} \rho \frac{\partial^2 |u\rangle}{\partial t^2} = A |u\rangle + |f\rangle, \\ \rho \frac{\partial^2 \vec{u}}{\partial t^2} = \vec{A}(\vec{u}) + \vec{f}, \end{cases} \quad (3.24)$$

where $|u\rangle$ is displacement, ρ is density, A is elastodynamic operator and $|f\rangle$ is external force per volume. The eigenvalues of A are ω_k and eigenvectors are $|u_k\rangle$, where k represents every multiplet (n, l, m) . Thus :

$$A |u_k\rangle = \omega_k^2 |u_k\rangle. \quad (3.25)$$

Let me suppose that the external force is a point source, so it is applied as a spatial δ -function, acting at the source : $\vec{r}_0 = (r_0, \theta_0, \phi_0)$. The external force \vec{f} is normal to the surface ground (atmospheric pressure perturbation and fluid dynamic pressure), I can express it :

$$\vec{f} = p\delta(r - r_0)\vec{e}_r, \quad (3.26)$$

where $p(= F/\Delta S)$ is atmospheric pressure field at ground surface, F is force and S is area.

If the external force $\vec{f}(\vec{r}, t) = \vec{f}(\vec{r})H(t)$ is applied as a step function time, where $H(t)$ is a step function. *Backus and Gilbert (1970)* showed that the excitation is

$$\vec{u}(r, t) = \sum_{n, l, m} ({}_n\Psi_l^m)_n \vec{u}_l^m(r, \theta, \phi) \frac{1 - e^{-i_n\omega_l t}}{n\omega_l^2}, \quad (3.27)$$

where ${}_n\Psi_l^m$ is excitation coefficient for each mode, be defined as

$$\Psi_k = \langle u_k | \frac{f}{\rho} \rangle = \int_V \vec{f}(\vec{r}) \cdot \vec{u}_k^*(\vec{r}) dV. \quad (3.28)$$

In these calculations, I use orthogonal and normalization relationship,

$$\langle u_{k'} | u_k \rangle = \iiint_V \rho \vec{u}_k^* \cdot \vec{u}_{k'} = \delta_{kk'}. \quad (3.29)$$

I describe excitation of normal modes ${}_n\Psi_l^m$ using in (A.18) as :

$$\begin{aligned} {}_n\Psi_l^m &= \int_V (u^\alpha)^* f^\alpha dV, \\ &= \int_V f^\alpha {}_nU_l^\alpha Y_l^{\alpha m*} dV. \end{aligned} \quad (3.30)$$

In this section, $f^+ = f^- = 0$ because I consider atmospheric pressure as the external force. I replace external force (3.26) in (3.30) :

$$\begin{aligned} {}_n\Psi_l^m &= \iiint dV p(\theta, \phi, t) \delta(r - r_0) {}_nU_l^{0m*}(r, \theta, \phi), \\ &= \iiint r_0^2 \sin \theta d\theta d\phi dr p(\theta, \phi, t) \\ &\quad \delta(r - r_0) {}_nU_l^{0m*}(r, \theta, \phi). \end{aligned} \quad (3.31)$$

Substitute (A.19) into (A.36) and by integration over r

$$\begin{aligned} {}_n\Psi_l^m &= r_0^2 {}_nU_l^0(r_0) \iint \sin \theta d\theta d\phi p(\theta, \phi, t) \bar{Y}_l^{0m}(\theta, \phi), \\ &= r_0^2 {}_nU_l^0(r_0) \iint d\Omega p(\theta, \phi, t) \bar{Y}_l^{0m}(\theta, \phi), \\ &= r_0^2 {}_nU_l^0(r_0) \kappa_l^m(t). \end{aligned} \quad (3.32)$$

As I supposed the planet has a spherical symmetry, I can move the source to the pole $(r_p, 0, 0)$ without changing the solution. Thus,

$$\begin{cases} P_l^{Nm} = 1 \text{ if } N = m, \\ P_l^{Nm} = 0 \text{ if } N \neq m. \end{cases} \quad (3.33)$$

Thus ${}_n\Psi_l^0$ becomes :

$${}_n\Psi_l^0 = f^0 {}_nU_l^0(r_p). \quad (3.34)$$

If $m \neq 0$, ${}_n\Psi_l^m$ is zero because f^- and f^+ are zero. Let's notice $r_0 = r_p$.

In this way, I can separate external force term into source spatial function term $r_0^2 {}_nU_l^0(r_0)$ and time function term $\kappa_l^m(t)$.

If basis is closed, I can always write $\forall |v\rangle, |v\rangle = \sum_k c_k |u_k\rangle$, where \forall is a universal quantification. I can describe the ground displacement $|u\rangle$ as summations of all normal modes displacements

$$\begin{aligned} \vec{u}(\vec{r}, t) &= \sum_n \sum_l \sum_m {}_n c_l^m(t) {}_n \vec{u}_l^m(\vec{r}_s), \\ &= \sum_k c_k(t) \vec{u}_k(\vec{r}_s), \end{aligned} \quad (3.35)$$

$$|u\rangle = \sum_k c_k |u_k\rangle, \quad (3.36)$$

$$I = \sum_k |u_k\rangle \langle u_k|. \quad (3.37)$$

I is unitary matrix. c_k is time and source function term and $|u_k\rangle$ is space function term. $|u_k\rangle$ is known. I have to solve c_k to find the displacement at the station $|u_s\rangle$.

I multiply $\langle u_k |$ by equation (3.24), and equation of motion becomes

$$\langle u_k | \frac{\partial^2}{\partial t^2} | u \rangle = - \langle u_k | A | u \rangle + \frac{\langle u_k | f \rangle}{\rho}, \quad (3.38)$$

$$\begin{aligned} \langle u_k | u \rangle &= \sum_{k'} c_{k'}(t) \langle u_k | u_{k'} \rangle, \\ &= \sum_{k'} c_{k'}(t) \delta_{k'k}, \\ &= c_k(t), \end{aligned} \quad (3.39)$$

$$\langle u_k | \frac{\partial^2}{\partial t^2} | u \rangle = \frac{\partial^2}{\partial t^2} \langle u_k | u \rangle = \frac{\partial^2 c_k(t)}{\partial t^2} \quad (3.40)$$

$$\begin{aligned} A | u \rangle &= \sum_{k'} A c_{k'} | u_{k'} \rangle, \\ &= \sum_{k'} c_{k'} \omega_{k'}^2 | u_{k'} \rangle, \quad (3.41) \\ - \langle u_k | A | u \rangle &= - \sum_{k'} c_{k'} \omega_{k'}^2 \langle u_k | u_{k'} \rangle, \\ &= - \sum_{k'} c_{k'} \omega_{k'}^2 \delta_{kk'}, \\ &= - \omega_k^2 c_k(t), \quad (3.42) \end{aligned}$$

where ω_k is eigenvalues. I can exchange the derivative and bracket in eq.(3.40), because normal modes are linear.

I get differential equation of c_k from eq. (3.30),(3.32),(3.38) and (3.42)

$$\frac{\partial^2 c_k(t)}{\partial t^2} + \omega_k^2 c_k(t) = r_0^2 {}_n U_l^0(r_0) \kappa_l^m(t). \quad (3.43)$$

Relationship between green function g_k and c_k is

$$c_k(t) = \int_{-\infty}^t g_k(t - \tau) {}_n \Psi_l^m(\tau) d\tau. \quad (3.44)$$

I developed the formalism, which can be either used for a pressure field acting on the surface or a pressure field acting in the Planetary Boundary Volume. This uses the same formalism as the more classical normal modes summation, but with all excitation coefficients or order m , while the summation request only $m=0$ for vertical point force and $m \leq 2$ for dislocation.

MARS BACKGROUND FREE OSCILLATIONS

4

SOMMAIRE

4.1	THE MARS GENERAL CIRCULATION MODEL	77
4.2	MARTIAN NORMAL MODES	80
4.2.1	The Martian Model	80
4.2.2	Normal Modes excitation	80
4.3	RESULTS AND DISCUSSION	84
4.3.1	Normal Modes Amplitude.	84
4.3.2	Normal Modes Detection and Seismometer Performances.	86
4.3.3	Internal model dependency.	88
4.3.4	Daily repetition of martian weather and spectral stacking method.	89
4.3.5	Estimation of the seismic magnitude of the MBF signal	90
4.4	CONCLUSION	93

This section is published in *Nishikawa et al. (2019)*. When a large earthquake occurs, seismic waves propagate around the whole planet for several 10s of hours after the event. These waves then generate standing oscillations which can estimate the boundary conditions for specific frequencies. Those standing modes are referred to as the Earth's free seismic oscillations and their associated frequencies are known as the Earth's seismic eigenfrequencies. It is highly possible that similar free oscillations occur on Mars.

In this chapter, I calculate MBFs signal using higher resolution GCM, developed recently by the LMD team (e.g. *Forget and Lebonnois (2013)*). These GCMs have the capability to resolve all the large-scale Martian atmospheric processes and variability : thermal tides, baroclinic waves, planetary-scale waves (*Haberle et al., 1999; Forget et al., 1999*). Turbulent motions in the PBL are, by design, left unresolved in GCMs and requires other numerical models such as Large-Eddy Simulation (*Spiga et al., 2010*), which is more suitable to simulate

smaller and local atmospheric perturbations. The atmospheric excitation by small-scale turbulence in the PBL is studied by *Kenda et al. (2017); Murdoch et al. (2017)*.

The amplitudes of normal modes are computed from GCM results by normal mode summation. This provides an estimate of the signals potentially recorded by the InSight SEIS VBB seismometer (*Lognonné et al., 2015*). Compared to previous studies, this thesis provides not only a better estimation of the normal modes MBFs and extension to higher frequencies as compared to *Lognonné and Johnson (2007, 2015)* but also provides pathways for the future processing of InSight measurements. My synthetic signals will be compared to the expected noise and will be used to test stacking strategies, with a special emphasis on daily repetition of Martian weather processes and resulting coherent seismic signal which significantly enhance the efficiency of the stacking method. Pressure fluctuation is strongly related to solar flux on the surface, especially daybreak and sunset time, big temperature variation generates pressure fluctuation (Fig. 4.1).

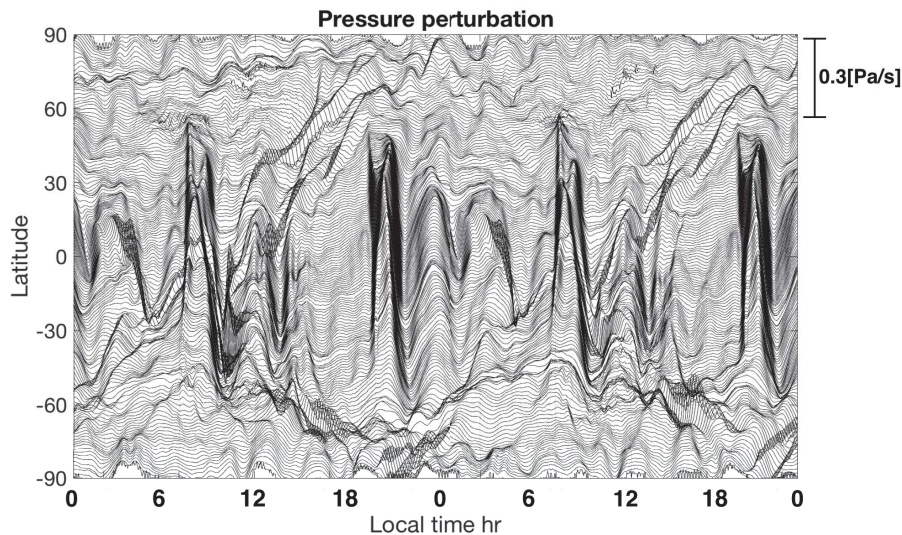


FIGURE 4.1 – Martian atmospheric pressure fluctuations as are simulated by the LMD GCM for the Mars meridian of longitude 0° . All pressure records have been demeaned and only the variation of pressure is shown. The vertical axis is latitude, the horizontal axis is local time hr. The large pressure fluctuations occur at sunrise and sunset. The shape of the pressure fluctuations repeats very similarly day after day. This strong daily repetition is not common on Earth.

The daily repetition is particularly notable in normal mode band (Fig. 4.2 and Fig. 4.3).

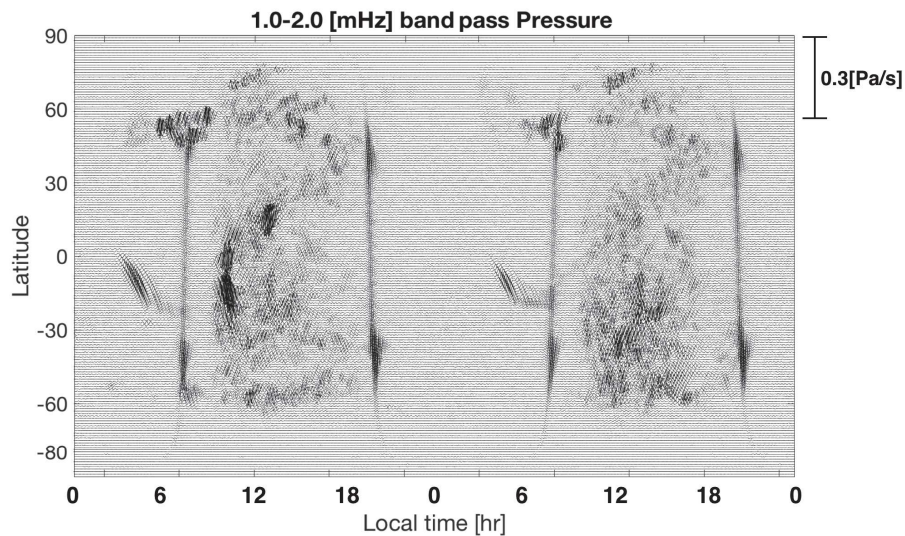


FIGURE 4.2 – *Martian atmospheric pressure fluctuation in the frequency band where normal modes concentrate. I applied a band-pass filter between 1.0 and 2.0 mHz to the raw pressure data (shown in Fig. 4.1). The daily repetition of Martian weather processes is clearly shown in the pattern. The band of the pattern 1.0 - 2.0 mHz corresponds to low degree (angular order 2-8) MBFs frequencies. The pressure fluctuations in the atmosphere excite daily coherent MBFs.*

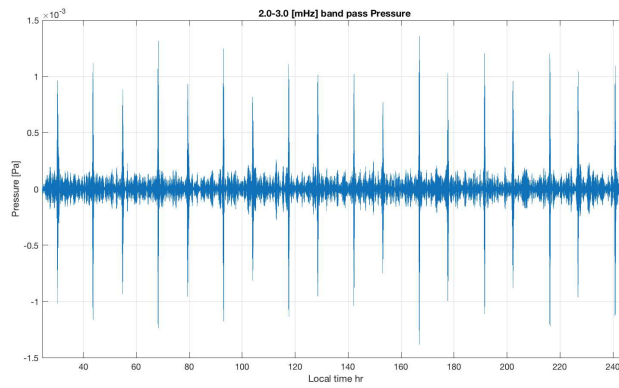


FIGURE 4.3 – *Martian atmospheric pressure fluctuation at frequency band where normal modes concentrate. I applied a band-pass filter between 2.0 and 3.0 mHz to the raw pressure data (shown in 4.1). Big pressure fluctuations at this band occur 2 times a day (at sunrise and sunset). The frequency band corresponds with middle degree (angular order 9-15) MBFs. Normal modes at this frequency are sensitive to upper mantle (see Fig. 4.5).*

4.1 THE MARS GENERAL CIRCULATION MODEL

The difficulties of normal mode computations by Global Circulation Models (GCMs) are related to the gaps between the temporal and spatial scale of normal mode and those of GCMs. Normal mode calculations require space and time scale resolutions that correspond with Mars' eigenfrequencies and corresponding wavelengths. Only the spatial resolution of Large Eddy Simulation (LES) matches the resolutions that correspond with Mars' eigenfrequencies and corresponding wavelengths but it can be made only on local scales.

Normal mode computations require a GCM simulation that is able to characterize the temporal variation of the Martian atmosphere down to a frequency of 0.01 Hz. And at least with a spatial resolution of 10 degrees latitude/longitude. Those requirements, dictated by seismic computations, are somewhat paradoxical from a meteorological point of view. Atmospheric activities with a typical time scale of 100 seconds correspond with some local to regional atmospheric circulation with a spatial scale of tens to hundreds of meters. Such a small scale atmospheric circulation will be challenging to resolve with GCMs, even with the best available supercomputing cluster. Most of the 100 second variation of Martian atmosphere is instead captured with the model with limited-area such as Large-Eddy Simulations *Spiga et al.* (2010)). Local seismic signature excited with such turbulence-resolving modeling is discussed in *Kenda et al.* (2017) and *Murdoch et al.* (2017). The remainder of this variability (i.e. the contribution that is not caused by microscale turbulence) is associated with mid-latitude baroclinic fronts and regional slope winds. The impact on global dynamics can be satisfyingly simulated through GCMs with a horizontal resolution of 1 degree. Conversely, nearly three decades of Mars GCM studies consistently demonstrate that the global dynamics (at spatial scales of about 10 degree latitude/longitude) are well simulated using a typical time step of 925 seconds (a quarter of a Martian hour) by the GCM. Taking into account such trade-off with the temporal and spatial resolution, the LMD team ran GCM simulations tailored for the seismic compu-

tations with the following settings. The simulations are performed with a time step of 60 s using 360 longitude grid points and 180 latitude grid points, corresponding to a mesh spacing of 1 degree and a horizontal resolution of 60 km. In the vertical, 25 levels are used with most of the levels located in the first 15 km to ensure a suitable resolution in the lower troposphere and in the boundary layer. Above 10 km, the vertical resolution is about one scale height and the altitude of the top level is about 60 km, which corresponds to 6 scale heights. This vertical grid thus features both the refined near-surface resolution and the accounting for the vast majority of the atmospheric mass, which enables to deal with all possible seismic coupling in subsequent computations.

Typical GCM simulations of the Martian climate are needed so that the resulting analysis of normal modes applies to the conditions met during the InSight mission. This does not require, however, as many simulations as would be expected from equivalent terrestrial studies. Both the low thermal inertia of the Martian surface and the fast radiative timescale of the thin Martian atmosphere imply that the Martian climate inter-annual variability is very low (except during the dust storm season, but InSight will land in 2018 at the end of this season) (*Read and Lewis, 2004*). Furthermore, given the key role played by the atmospheric dust loading in driving the Martian climate, and the small inter-annual variability of this parameter in the first half of a Martian year (*Montabone et al., 2015*), when the InSight operation will take place, running one GCM simulation in a given Martian year is providing predictions satisfactory for all Martian years outside the dust storm season. The dust scenario used thus corresponds to the Martian Year 27 which is a typical clear atmosphere scenario (dust visible opacity around 0.2) with no impact of the global dust storm. GCM simulations start at $L_s = 0$ degree (northern spring), which corresponds to the first months of the InSight mission on Mars, and are performed for 20 martian sols with a fixed dust profile. Given that gravity waves are partly resolved in my 1 degree \times 1 degree GCM simulation, I do not use the subgrid-scale scheme modeling the effect of those waves on the large-scale flow.

The outputs of the model used as inputs for the seismic modeling are surface pressure, temperature, atmospheric density, temperature, and winds.

As I mentioned above, this is a challenging problem for GCMs. While GCMs can accurately model the energy at low frequency, it loses energy at Martian normal mode frequencies, depending (Fig. 4.4). The discrepancy between the simulation and the observation depends on the observation environment, season, and other factors. Thus, the results from this study should be understood as the lower limit of the possible atmospheric excitations.

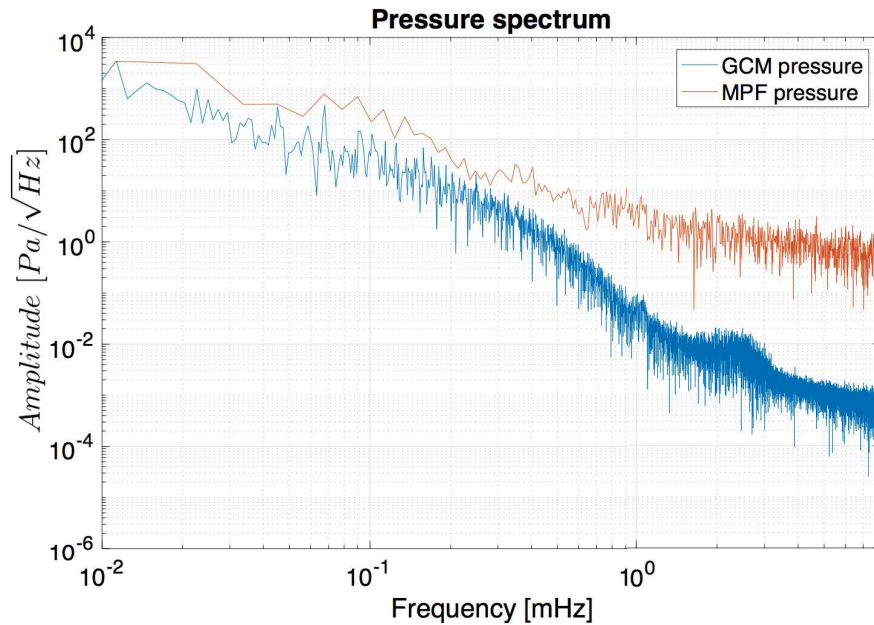


FIGURE 4.4 – Pressure spectrum of GCMs' pressure and observed pressure. The observation data is measured by Mars Pathfinder (LS=170 degree). The spectrum of GCMs is computed at the same location as the observation data of Mars Pathfinder (LS=0 degree). GCMs lose some energy in this frequency period. But the MBFs calculations using GCMs are useful as lower limit estimations.

4.2 MARTIAN NORMAL MODES

4.2.1 The Martian Model

The martian internal models have been discussed by many researchers. The first estimation is based on observation and laboratory experiments. Our current knowledge of the inner structure of Mars depends on gravitational observations and surface soil property data. From the mean density, gravity, and the moment of inertia of Mars, the core radius was estimated to be 1600 ± 200 km with 400 km of uncertainties (*Khan and Connolly, 2007; Sohl and Spohn, 1997; Spohn et al., 2001; Rivoldini et al., 2011; Smrekar et al., 2019*). The differences of the martian core status are reflected in the eigenfrequencies of low angular order normal modes (hundreds to thousands of seconds). In this paper, I use the Sohl model as a reference internal structure. I calculate seismic waves with a period longer than 120s. The period corresponds with normal modes of angular orders between 2 and 39. These modes represent the core and middle to deep mantle structure (Fig. 4.5).

4.2.2 Normal Modes excitation

The theory of normal mode excitation and of normal mode summation has been described in several studies (e.g. *Lognonné (1991); Dahlen and Tromp (1998); Lognonné et al. (1998b); Lognonné and Clévéché (2002)* among others) and I summarize here the approach. Martian global oscillations are the solution of the gravito-elastic equation (when attenuation is neglected) or gravito-anelastic equation when anelastic processes are considered. *Lognonné et al. (2016)* studied the effect of the attenuation processes in the Mars' atmosphere due to both the viscosity and CO₂ molecular relaxation and lead to the conclusion that at a long period (e.g. $T > 50$ sec), no significant atmospheric attenuation is expected in the lower atmosphere and where therefore most of the excitation will be generated, suggesting that an adiabatic approximation in the atmosphere is good enough for my modeling. The starting equations can be expressed as :

$$-\omega^2 \rho_0 \vec{u} = -\mathbf{A}(\vec{u}) + \vec{f}, \quad (4.1)$$

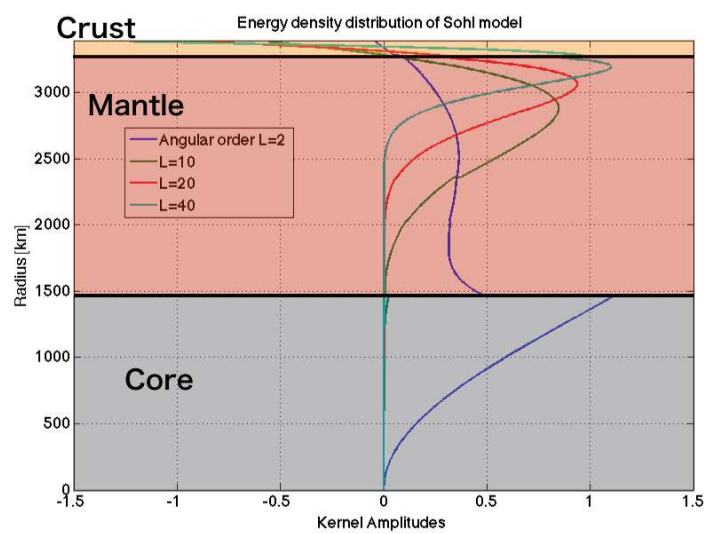


FIGURE 4.5 – Vertical amplitude of spheroidal fundamental normal modes in the solid part of Mars. Low degree normal modes are low frequency. Large amplitude area concentrate the mode's energy and sensitivity. Low degree waves (angular order 2-9) have sensitivities at core and deep mantle. High degree waves (angular order 10-39) have sensitivities at middle and shallow part of mantle. Each mode has sensitivity at a different depth.

and

$$\omega_k^2 \rho_0 \vec{u}_k = \mathbf{A}(\vec{u}_k), \quad (4.2)$$

where for the first equation, \mathbf{A} is the gravito-elastic operator (or gravito-anelasto one when attenuation is integrated), ρ_0 is the unperturbed density, \vec{f} is external force, ω is the angular frequency, \vec{u} is the displacement field responding to the force, and where the second equation is the one related to the normal modes, where ω_k is the normal mode angular frequency, \vec{u}_k is the associated displacement eigenfunction and subscript k includes 3 orders, n (radial order), l (angular order) and m (azimuthal order). Note that we corrected here a few typos made in *Nishikawa et al.* (2019). \mathbf{A} is defined for an internal structure model following *Lognonné and Clévéde* (2002) and given by :

$$\mathbf{A}(\vec{u}) = -\vec{\nabla}(\delta \vec{T}_{elastic} - \vec{u} \cdot \vec{\nabla} \vec{T}_0) + \vec{g}_0 \nabla \cdot (\rho_0 \vec{u}) + \rho_0 \vec{\nabla} \Phi, \quad (4.3)$$

for the solid part, where Φ is mass redistribution potential such that $\vec{g}_1 = -\vec{\nabla} \Phi$, \vec{g}_0 is unperturbed gravity acceleration, \vec{T}_0 the initial-stress and $\delta \vec{T}_{elastic}$ the elastic stresses, while the operator in the atmospheric part can be written by using $\mathbf{T}_0 = -p_0 \mathbf{I}$ and

$$\mathbf{T}_{elastic} = -p_{Hooke} \mathbf{I} = \kappa \nabla \cdot \mathbf{u} \mathbf{I}, \quad (4.4)$$

where \mathbf{I} is identity tensor, as :

$$\mathbf{A}(\vec{u}) = -\vec{\nabla}(\kappa \nabla \cdot \vec{u} + \vec{u} \cdot \vec{\nabla} p_0) + \vec{g}_0 \nabla \cdot (\rho_0 \vec{u}) + \rho_0 \vec{\nabla} \Phi, \quad (4.5)$$

where κ is bulk modulus and p_0 the equilibrium pressure. Following *Lognonné et al.* (1994), I can write momentum density field $\rho \vec{v}$ in the form

$$\rho(\vec{r}, t) \vec{v}(\vec{r}, t) = \rho_0(\vec{r}) \sum_k \dot{c}_k(t) \vec{u}_k(\vec{r}). \quad (4.6)$$

which provides the displacement \mathbf{u} field, which can be expressed to first order (and therefore on location far enough from the sources) as :

$$\vec{u} = \sum_k c_k(t) \vec{u}_k(\vec{r}). \quad (4.7)$$

I get differential equation of time and source function as

$$\frac{\partial^2 c_k(t)}{\partial t^2} + \omega_k^2 c_k(t) = \Psi_k(t), \quad (4.8)$$

where Ψ_k is the excitation force for each mode.

As seen in section 3, the equivalent force can be written as

$$\begin{aligned} \vec{f} = & \nabla \cdot (\rho_0 \vec{u}) \frac{\partial \vec{v}}{\partial t} - \frac{\partial \rho}{\partial t} \vec{v} - \nabla \cdot (\rho \vec{v} \vec{v}) \\ & - \nabla (p_{true} + \vec{u} \cdot \nabla p_0 + \kappa \nabla \vec{u}), \end{aligned} \quad (4.9)$$

and can be furthermore approximated by taking only the last terms, so that

$$\vec{f} = -\nabla (p_{true} + \vec{u} \cdot \nabla p_0 + \kappa \nabla \vec{u}) - \nabla \cdot (\rho \vec{v} \cdot \vec{v}) \quad (4.10)$$

$$= -\nabla \cdot [(p_{true} + \vec{u} \cdot \nabla p_0 + \kappa \nabla \vec{u}) \mathbf{I} + \rho \vec{v} \cdot \vec{v}] \quad (4.11)$$

$$= -\nabla \cdot \mathbf{m} \quad (4.12)$$

where we have the source tensor :

$$\mathbf{m} = (p_{true} + \vec{u} \cdot \nabla p_0 + \kappa \nabla \vec{u}) \mathbf{I} + \rho \vec{v} \cdot \vec{v} \quad (4.13)$$

The excitation force for each mode Ψ_k can therefore be written as

$$\int_V dV \vec{u}_k \cdot \vec{f} = - \int_V dV \vec{u}_k \cdot \nabla \cdot \mathbf{m} = \int_V dV \mathbf{E}_k \cdot \mathbf{m}, \quad (4.14)$$

when an integration by part is made over all the source domain and where \mathbf{E}_k is the strain tensor of the eigen mode k. We retrieve the expression proposed for non-gravitational operator by Lognonné et al. (1993) which generalized the concept of moment tensor of the excitation force introduced by *Backus and Mulcahy* (1976a,b) :

$$m^{ij} = (p + \kappa \nabla \cdot \vec{u}) \delta^{ij} + \rho v^i v^j. \quad (4.15)$$

The first term is practically dominated by the GCM pressure while the second part are the Reynold stresses. Fig. 4.6 (right) shows the spectrum of the pressure and Reynold stress on an arbitrary point at the surface of Mars, as obtained by the GCM. I found a spectrum with amplitudes decreasing as $1/f$. Most of the variability in the bandwidth of normal modes will be associated to the Reynolds stresses. All the terms in eq (4.15) can be derived from the values calculated by GCM, thus giving us a full description of the moment tensor with GCM results.

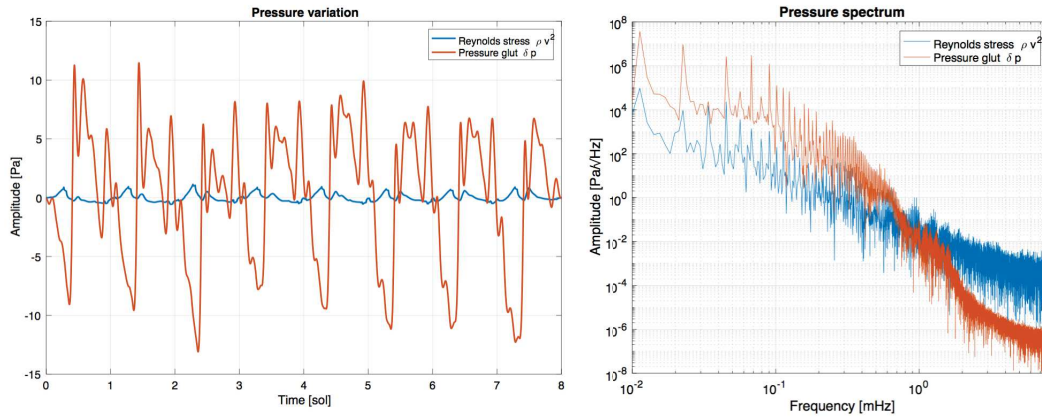


FIGURE 4.6 – Pressure glut and reynolds stress of GCM. Variation of pressure amplitude of pressure glut is stronger than reynolds stress (in left figure). Pressure glut is stronger than reynolds stress at low frequency and it is reversed at high frequency. At the high frequency, main contribution of the pressure variation is eddies. The eddies generate reynolds stress by its wind variations. GCM loses energy of eddies at low frequency.

4.3 RESULTS AND DISCUSSION

4.3.1 Normal Modes Amplitude.

The MBF is summation of all degree normal modes. In this study I calculate fundamental normal mode degree from 2 to 39. The MBF signal is orders of nanogals ($10^{-11}m/s^2$) (Fig. 4.7). This amplitude is larger than *Lognonné and Johnson* (2007, 2015). This is likely resulting from the larger angular orders and therefore frequencies. Since the signal is the summation of all normal mode, specific peak amplitudes are better observed in the spectrum (Fig. 4.8). The lowest frequency peak (0.4 mHz) is angular order 2 normal mode, the highest peak (8.3 mHz) is angular order 39 normal mode, but note that the amplitudes are well modeled only for frequencies bigger than 2 mHz. I do observe a gradual increase of the amplitude with frequency up to 5 mHz, after which the amplitude of peaks is almost constant.

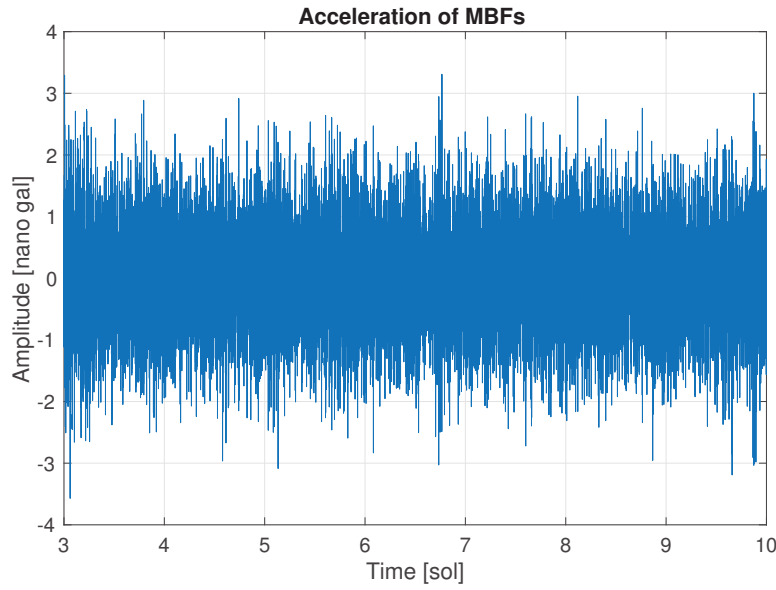


FIGURE 4.7 – 7 martian days MBF acceleration. The MBF is sum of angular order 2 to 39 fundamental normal modes. The amplitude is nanogals ($10^{-11}m/s^2$). The MBF continues for days since the normal modes are excited by continuous atmospheric activities. The first 3 sols data is meaningless results in a boundary condition of GCMs and stability of MBFs.

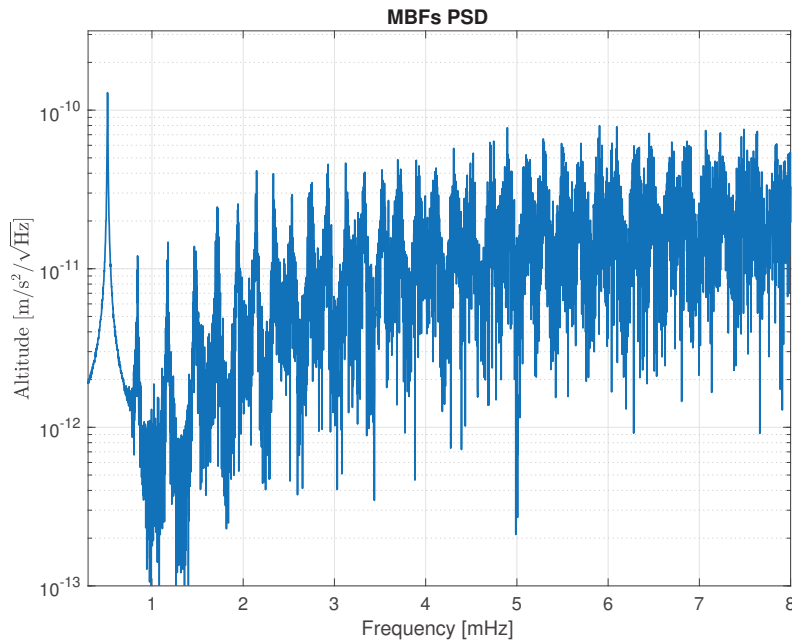


FIGURE 4.8 – Acceleration power spectrum density of MBF. Each peak shows its normal mode. There is 38 peaks in this figure from angular order 2 to 39 respectably. The time step of GCM is $61.5s (=8.13 \text{ mHz})$. I cannot calculate MBFs above 39th angular order.

4.3.2 Normal Modes Detection and Seismometer Performances.

MBFs amplitudes remain quite small and in order to be detected, the instrument must not only have a high sensitivity but in addition, must have low noise. Let me consider if these modes can be detected by the SEIS VBB sensors on their POS output, which has a flat acceleration gain in the frequency bandwidth of normal modes.

The LSB (Least Significant Bit) of SEIS seismometer for the differential outputs is given by

$$LSB = \frac{2 \times Voltage}{Gain}. \quad (4.16)$$

The voltage of the seismometer is ± 25 V, the acquisition dynamics is 24 Bit and gain is $\approx 10^4$ V/DU for low gain mode and about 4.5 times larger for high gain mode. The LSBs are therefore :

$$\begin{aligned} LSB_{LG} &= \frac{2 \times 25}{10^4 \times 2^{24}} = 30nGal, \\ LSB_{HG} &= \frac{2 \times 25}{4.5 \times 10^4 \times 2^{24}} = 6.6nGal. \end{aligned} \quad (4.17)$$

The amplitude of MBFs is a few nanogals only and the LSBs are therefore larger. The real ground acceleration signal contains not only MBF but also thermal drift, thermal and instrument noise, and possibly seismic signal. To carry out a more realistic evaluation, I approximate the daily temperature variation associated with the temperature sensitivity of the sensors with an ideal sinusoidal curve and superpose it on MBFs. Since this drift is much larger than 1 LSB, it enhances the MBFs up to a detectable level. The sinusoidal thermal noise model is given by

$$A_{temp}(t) = \gamma \delta T \left(1 - \cos \frac{2\pi t}{D_{sol}} \right), \quad (4.18)$$

where A_{temp} is the equivalent acceleration of temperature variations, t is the local time, D_{sol} is martian day duration, γ is the sensitivity of the VBB in acceleration unit per degree and δT is the temperature variation in one martian day. The temperature sensitivity γ is set to $10^{-5} m/s^2/K$ and daily temperature variation δT is 4 K, corresponding to expected variations during winter (Lognonné et al., 2019;

Mimoun et al., 2016). The amplitude of this thermal daily variation is, therefore, 4.0×10^6 nanogal, one million times larger than MBF signals.

I then simulate the signals by adding the MBF signal to the thermal drift and then simulate the digitization by converting this acceleration signal into bits. Data processing is then again simulated, by subtracting from the signal a sol-periodic sin wave with amplitudes computed by least square. For both the low-gain and high-gain, clear MBFs signal are then retrieved in the residual, demonstrating the capability of the acquisition to detect signals smaller than LSB due to the stochastic amplification of noise.

The signal remains much smaller than the expected instrument noise, which will be the superposition of the instrument self noise and of the residual of both the temperature drift subtraction and of potential pressure decorrelation (*Murdoch et al., 2017*). This is illustrated by Fig. 4.9 which compares the MBFs spectrum to the self noise of the instrument, in both LG and HG and to the expected thermal drift signal. In the bandwidth 5 mHz-10 mHz, the longer part of the target bandwidth for Martian Hum search (5mHz-20 mHz) and the bandwidth for which our modeling hypothesis and the GCMs have acceptable errors, the MBFs signal is expected to be 5-10 below the instrument self noise, depending on its gain. Only stacking of this signal over the mission duration will therefore allow a successful detection.

The amplitude of the ideal thermal noise model is $4.0 \times 10^6 nGal$. The acceleration is $0.4 \times 10^6 DU$ in low-gain mode or $1.4 \times 10^6 DU$ in high gain mode. The thermal noise acceleration is far larger compared to the MBF signal. No signal is caught by low-gain mode of the SEIS seismometer. Even high-gain mode can observe 1 DU signal several times in a half Martian day. However, ideal thermal noise can kick up after the decimal point values to 1 DU. The acquisition method is that I put known noise on MBF signal to make realistic ground acceleration, then digitize the ground acceleration, after that take digitized thermal noise from the digitized ground acceleration. After the subtraction of digitized thermal noise, more MBF

signals are caught by SEIS seismometer in both low-gain and high-gain mode. MBF signal is hidden by big thermal noise but after subtraction of digitized thermal noise, I get more MBF signals to compare with pure MBF signal.

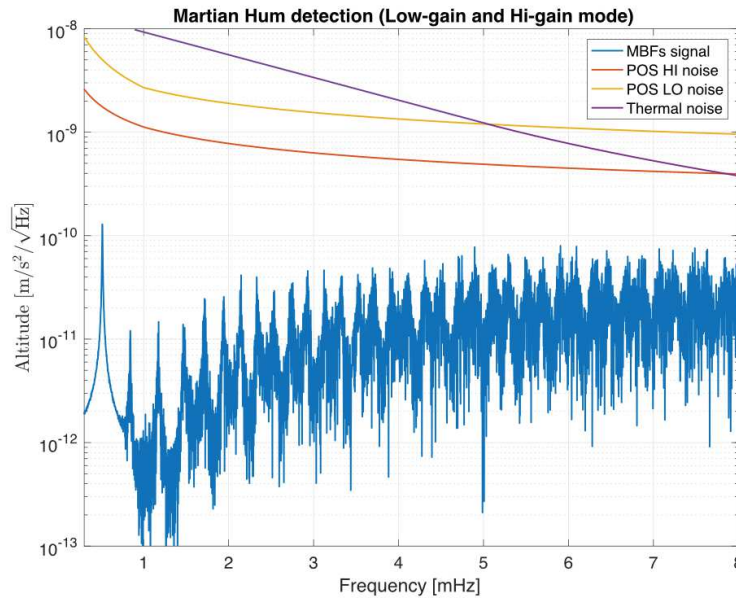


FIGURE 4.9 – Power spectrum acceleration density of MBF and instrumental, environmental noise. Above 5 mHz (angular order 22), thermal noise is much larger than signals. Below 6.5 mHz (angular order 30), the MBF signal overcome both instrumental and thermal noise. The signal may be detected MBF by high gain mode SEIS seismometer during night time. The overcome signals have sensitivities at middle and shallow part of mantle.

4.3.3 Internal model dependency.

The detection of the frequencies of the Normal modes will allow the inversion of the Mars upper mantle, as already illustrated by Panning *et al.* (2017). The position of the normal mode peaks depends on the internal structure, as shown in Fig. 4.10. These simulations have been done with two different internal structure models of Mars. This figure shows that the position of peaks strongly depends on the internal structure.

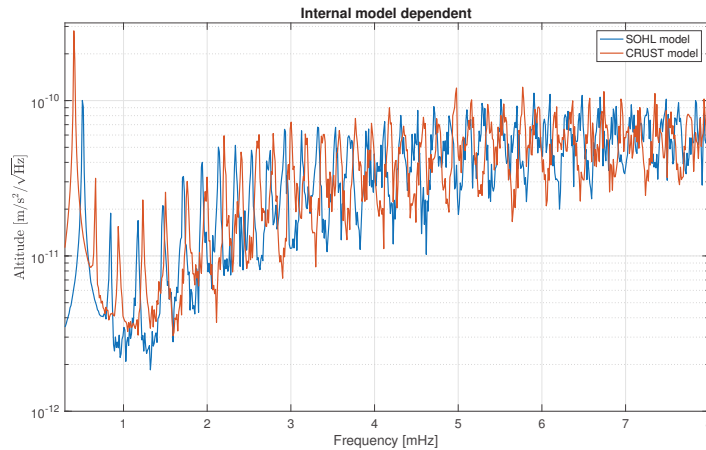


FIGURE 4.10 – Example of difference in MBF spectra from different Martian inner structure. I use two internal models of Mars. These two models have different mantle thicknesses. The position of peaks is different. The figure clearly shows different peak positions for different mars models. The difference in peak positions is about 0.1 mHz, which will be the frequency resolution required to discriminate between the 2 models.

4.3.4 Daily repetition of martian weather and spectral stacking method.

The thermal inertia of the Martian soil is low, due to its thin atmosphere. Thus the diurnal cycle of surface temperature is very large. This makes thermal tides a prominent factor of diurnal variability on Mars. This is further reinforced at the equatorial location of In-Sight. Mars has a clear dichotomy where the southern hemisphere is dominated by low lands and the northern hemisphere is dominated by highlands. The boundary of the dichotomy lays close to the equator and such dichotomy should contribute to the diurnal cycle through slope-induced circulations and the day-to-day variability associated with baroclinic waves is small (Spiga *et al.*, 2018). Thus, given that I consider atmospheric variability within a given season, there exists a significant daily repetition of atmospheric temperature, wind, pressure. This causes strong correlations in the diurnal range in our seismic computations derived from GCM simulations (Fig. 4.12). This makes stacking likely to be efficient to increase the MBFs up to the level above the self noise or other source of the noise.

On Mars, there is no water, no cloud, and the thermal inertia of

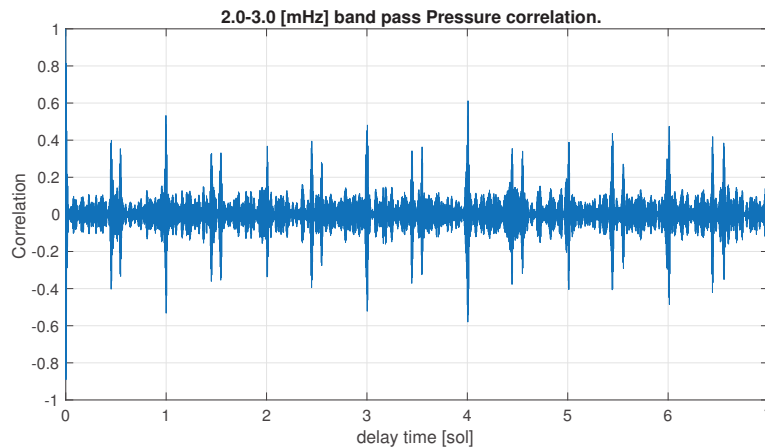


FIGURE 4.11 – *Pressure correlations at normal mode band frequency. High correlations are in exactly day and semi-diurnal. One day high correlations are sunrise - sunrise and sunset - sunset correlation. Semi-diurnal correlations are sunrise - sunset and sunset - sunrise correlations (semi-diurnal thermal tide). The periodic excitation force generates high efficiency of stacking. This precise phenomenon occurs on Mars but not on Earth.*

the soil is low. The solar flux reaches the ground surface, the solar flux generates heat on the surface, the heat will be transported to the atmosphere easily, and the heat will be the trigger of atmospheric activities. Thus the trigger of martian atmosphere activity is strongly dominated by solar flux. In other words, Martian weather is a strong function of local time. During night time, the place is calm while when the sun rises, eddies start to be driven on the surface. It means that the weather is very similar to the weather just one day after. The strong correlations are generated by daily similarity (Fig. 4.12). High correlations are in exactly daily. This is evidence of daily repetition and strong stacking effect of MBFs (4.13).

4.3.5 Estimation of the seismic magnitude of the MBF signal

Let me now estimate not only the amplitude of the MBFs in terms of seismic magnitude but check that our estimation in the MBFs is comparable to the one obtained by a simple energetic budget, following the approach of *Kobayashi and Nishida (1998a)*.

A first estimate is to assume that the release of acoustic and seismic energy in the atmosphere activities is driven by solar flux and that

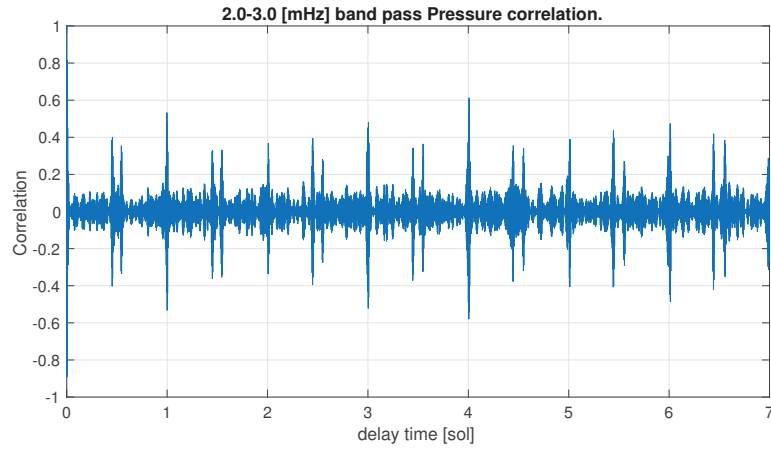


FIGURE 4.12 – *Pressure correlations at normal mode band. High correlations are exactly in a day and semi-diurnal period. One day high correlations are sunrise - sunrise and sunset - sunset correlation. Semi-diurnal correlations are sunrise - sunset and sunset - sunrise correlations (semi-diurnal thermal tide).*

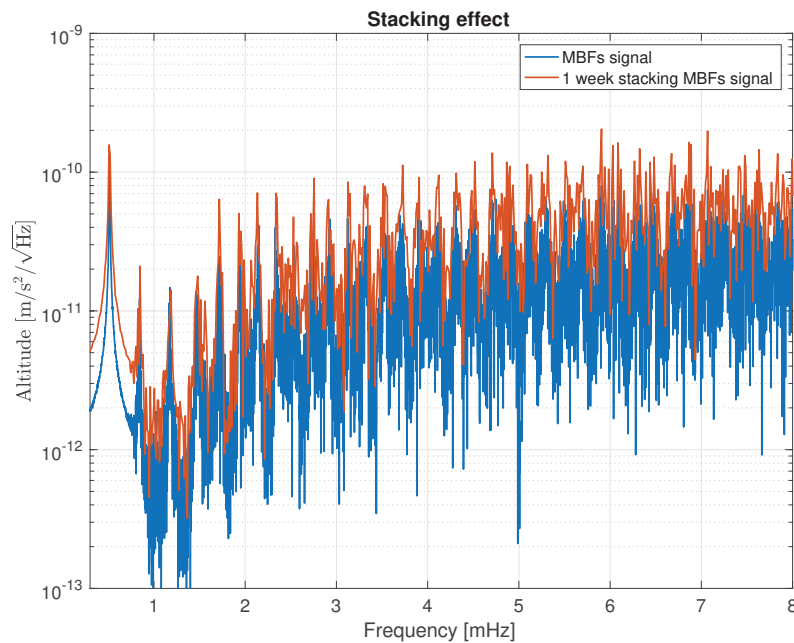


FIGURE 4.13 – *One week stacking effect. The daily stacking makes large and clear peaks. When MBFs are stacked more and more, the normal mode peaks become bigger and sharper.*

furthermore all the energy of planetary background free oscillations come from solar flux. This maximum energy can be expressed as

$$W_M = F_E \times \left(\frac{D_E}{D_M} \right)^2 \times (1 - A_M) \times \pi R_M^2, \quad (4.19)$$

where W_M is the solar flux deposited on Mars surface, F is solar flux above Earth atmosphere ($F_E = 1360 \text{ W/m}^2$), D is distance from the Sun ($D_M = 1.52 D_E$), A is the bound albedo ($A_M = 0.25$), subscript E and M are Earth and Mars case and R is radius. This solar energy is converted to seismic energy, with a coherency duration of $T\sqrt{Q}$, where Q is the quality coefficient of the mode and T is its period. Thus the MBFs energy (E_{MBF}) is given by

$$E_{MBF} = W_M \times s \times \sqrt{Q} \times T \times C, \quad (4.20)$$

where s is a acoustic efficiency of 1% (which can be achieved for high altitude wind of 40-50 m/s assuming an efficiency depending on M^3 , where M is the mach number, e.g. Goldreich & Kumar, 1988) C is the energy coupling ratio between atmosphere and solid part of Mars (typical value $C = 5 \times 10^{-6}$, (e.g. Lognonné and Johnson, 2015)), Q is seismic attenuation of MBFs (typical value $Q = 100$), T period of MBFs (typical value $T = 200$ sec). I use then the energy-magnitude relation of (Gutenberg and Richter, 1956) :

$$\log E = 4.8 + 1.5M, \quad (4.21)$$

where M is the magnitude of the seismic event. As the result, the rough estimation of MBF magnitude is $M=4.9$.

Let me now compare the amplitude obtained by our modeling with GCM with those excited by seismic activities. This is made by comparing the spectrum of the MBFs with those of quakes, occurring at an epicentral distance of 90 degrees. I find amplitudes of MBFs close to those generated by a $M_{5.0}$ seismic event (Fig. 4.14). The two estimations, either based on the GCM calculation or on solar flux estimations are consistent. These are also consistent with those estimated from Earth hum, which has been estimated as equivalent to an earthquake of magnitude 5.75-6 (Rhie and Romanowicz, 2004). For an Earth bound albedo of 0.306, the solar flux between

the two planets is indeed larger by a factor of almost 8 for the Earth as compared to Mars. This corresponds to magnitude 0.6 larger and therefore extrapolation of 5.3. Nevertheless, all these magnitudes estimations, although comparable, are smaller by one to the magnitude of 5.9 (e.g. 10^{18} Nm) which has been considered by several studies as required for the detection of Normal modes. For these reasons, I focused our next analysis on the possibility of coherent stacking for MBFs. My results showed that the coherency is maintain at least for 1 week with correlation over 0.4. Further correlation is yet to be confirmed. On the other hand, this assumes that we can stack a week of data to improve and by restacking such weekly stack of spectra over a full martian year, I can further improve the signal-noise ration.

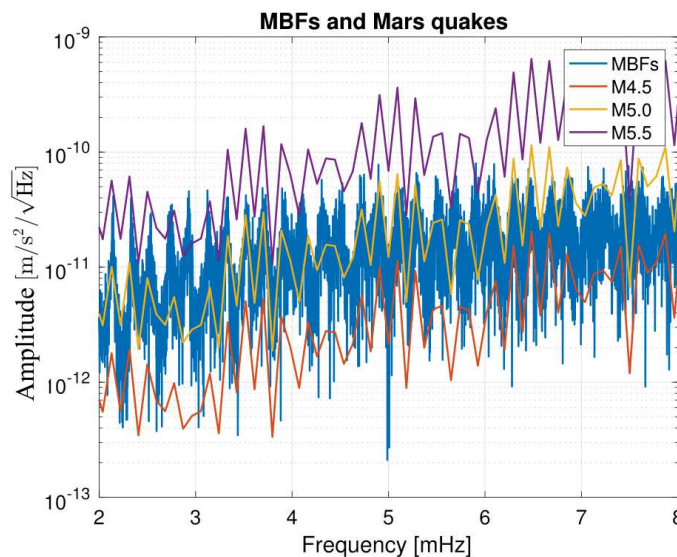


FIGURE 4.14 – Acceleration spectral density of MBF and free oscillations. The MBFs are excited by Martian atmosphere and others are theoretical spectra assuming seismic excitations of seismic events. The magnitudes of the events are M4.5, 5.0 and 5.5. MBFs is close to M5.0 oscillations. This result is consistent with estimations made with different approaches.

4.4 CONCLUSION

In this chapter, I evaluated the signal level of Mars' background free oscillations with high precision GCMs. Given the model limitation of GCMs, the obtained values should be regarded as a lower

limit of the possible amplitude of background free oscillations expected on Mars.

For the realistic evaluation, I introduced several assumptions which are based on observations and theories to simplify the model and took into account the 3D atmospheric structure.

With these models and assumptions, I obtained that the amplitudes of MBFs are likely to be orders of nanogals. This is consistent with previous studies such as *Kobayashi and Nishida (1998a)*; *Lognonné and Johnson (2007)*. I also confirmed that the obtained values are consistent with solar flux, which is the dominant source of energy for Martian atmospheric activities and MBFs. These results imply that the obtained values represent the typical signal level of MBFs though the amplitudes may differ with assumptions I adopt, such as the internal structure and atmospheric model.

Given the signal level of MBFs and the noise level of InSight SEIS instruments, it is difficult to detect the signal of MBFs by SEIS instruments. However, I found that stacking methods will be a powerful tool to overcome the problem. I took advantage of the daily repetition of martian atmosphere. The results may be the minimum estimate of MBF detection by the SEIS seismometer. They will enable us to estimate the deep internal structure of Mars and can be one of the successes of the InSight mission.

LOVE NUMBERS AND DEEP INTERNAL STRUCTURE.

5

SOMMAIRE

5.1	Q AND K2 OBSERVATION.	96
5.2	RHEOLOGY	99
5.2.1	On Theory	101
5.3	BENCH MARK TEST BY MOON.	102
5.3.1	Comparison with observation data.	103
5.4	IMPLICATION FOR INSIGHT	106
5.5	CONCLUSION	108

Observation of tidal parameters (Love numbers, tidal deformation, Q values) is one of the successful approaches to explore the deep internal structure of planets and satellites. I showed normal mode sensitivity with depth and discussed the detectability of MBFs in the previous chapter. From the results, I found that it is difficult to detect the MBFs at low angular order. The thermal noise increases exponentially and the noise will be dominant at low frequencies. It means that only MBFs observation is not enough to estimate deep martian internal structure. The MBFs observation would not be able to resolve the deep interior of the planet such as core size, core status, and deep mantle status. Tidal parameters have sensitivity at the blank region and thus provides me with complementary information. Thus, I can fill the gap with the observation of tidal parameters, such as Love numbers. In this chapter, I will show the mechanism of tidal deformation of a celestial body and the method to calculate the Love number for a given internal structure. I will theoretically evaluate how the deep internal structure of Mars affects the Love numbers. To validate my methodologies, I will use the Moon as a

Planetary deformation delay

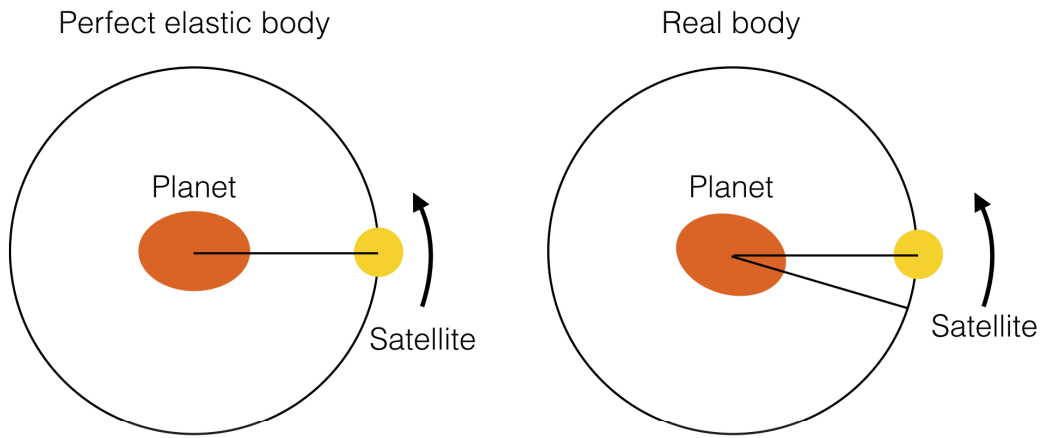


FIGURE 5.1 – *Deformation mechanism of planets and satellites. In case of perfect elastic body planet, its major axis points exactly toward the satellite. The direction of the major axis delays because of its friction. Torque resulting from the delay changes planet and satellite orbits and dissipates planetary energy.*

benchmark. Since the Moon has a large geodesic and seismic dataset, my results can be immediately compared with the observation. The comparison is useful as a benchmark for preparation for the InSight mission. The theory used in this section was also used to complete a seismic analysis of the deep moonquakes stress-drop and has lead to a joint inversion of the deep moon temperature, by using both the brittle-ductile constraints and those provided by the lunar tidal stresses and k_2 measurements (Nakamura et al., 2017, see Annexe 4).

5.1 Q AND k_2 OBSERVATION.

If the planet is a perfectly elastic body, deformation response occurs immediately and there are no energy dissipations. The reality is different and deformation delays are observed by telescopes and orbiters (Fig. 5.1). In other words, these energy dissipations and elastic modulus are observed as planetary deformation and delay of angular velocity. Q is energy dissipation ratio. The definition is described

by

$$Q^{-1} = \frac{1}{2\pi E_p} \oint \frac{dE}{dt} dt, \quad (5.1)$$

where E_p is peak energy of the system, $\oint \frac{dE}{dt} dt$ is energy dissipation during one cycle and E is wave energy of the system. The equation shows that a low Q system is dissipative and easy to lose energy (high Q is the opposite). Low Q means hot active interior and on the contrary high Q means cold nonactive interior. The Q value is proportional to satellite time-lag (Δt) and the tidal bulge angle ($\Delta\theta$) (Fig. 5.2). The tidal deformation is considered as vibration for a long period. The potential of the tidal acceleration on a point on a planet (U) can be described as

$$U = U_0 \cos(\omega t), \quad (5.2)$$

where ω is the angular frequency of the tide ($\omega = 2|\Omega - n|$) and time-lag (Δt) is

$$\epsilon = |\Omega - n| \Delta t, \quad (5.3)$$

where Ω and n are angular velocity of a planet and satellite (Fig. 5.2). In this case, the displacement (ξ) and velocity (u) of arbitrary position of the planet is described by

$$\xi = \frac{U_0}{g} \cos[\omega(t - \Delta t)], \quad (5.4)$$

$$= \frac{U_0}{g} \cos[(\omega t - 2\epsilon)], \quad (5.5)$$

$$u = \dot{\xi} = -\omega \frac{U_0}{g} \sin(\omega t - 2\epsilon). \quad (5.6)$$

where g is the gravity of the planet. Substitute eq (5.6) for eq (5.1).

$$\oint \frac{dE}{dt} dt = \int_0^T u \left(-\frac{\partial U}{\partial r} \right) dt \quad (5.7)$$

$$= -\frac{U_0}{g} \frac{\partial U_0}{\partial r} \pi \sin 2\epsilon \quad (5.8)$$

$$E_p = \int_0^{\frac{T}{4}} u \left(-\frac{\partial U}{\partial r} \right) dt \quad (5.9)$$

$$= \frac{U_0}{g} \frac{\partial U_0}{\partial r} \left(\frac{1}{2} \cos 2\epsilon - \frac{\pi}{4} \sin 2\epsilon \right) \quad (5.10)$$

Thus Q value is described by

$$Q^{-1} = \frac{1}{2\pi E_p} \oint \frac{dE}{dt} dt \approx \tan 2\epsilon \approx \sin 2\epsilon. \quad (5.11)$$

Energy dissipation rate (Q) is a function of observation value (ϵ).

Redmond and Fish (1964) mentioned relationship between bulge angle ($\Delta\theta$) and angular velocity of satellite (n) Fig. (5.2) as

$$\frac{dn}{dt} = -3n^2 \frac{m}{M} \sum_{j=2} \left(\frac{dP_j(\cos \Delta\theta)}{d\Delta\theta} \right) \left(\frac{a}{R} \right)^{2j+1}, \quad (5.12)$$

$$= \frac{9n^2 m}{8M} \left(\frac{a}{R} \right)^5 \left[4k_2 \sin 2\epsilon + k_3 \left(\frac{a}{R} \right)^2 (5 \sin 3\epsilon + \sin \epsilon) \right]. \quad (5.13)$$

where R is radius of the planet, a is semi-major axis of the satellite, m and M are mass of the satellite and planet. This equation is composed by observation values (R, a, n, m, M, ϵ) and k_2, k_3 . These k values are Love numbers which are dependences of shear modulus. The subscript indicates the degree. As a result of the equations, observations enable me to estimate Q and Love numbers.

Principle of measurement

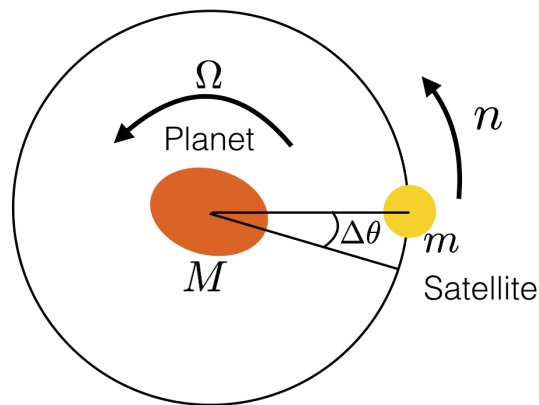


FIGURE 5.2 – *Principle of measurement.* If the planet is perfect elastic body, deformation response occurs immediately and the bulge angle $\Delta\theta$ is 0. Actual value of the bulge angle is not 0. The bulge angle and deformation delay are generated by friction inside planet. In conversely, observation of the bulge angle enables me to estimate internal structure of the celestial body.

5.2 RHEOLOGY

I discussed Love number estimation from observation in the previous chapter. Next, I will discuss the relationship between Love numbers and an internal structure. Love numbers are related to the rheological feature of a celestial body. Thus, I will first define the rheological model the I will be using in my discussion. Mainly rheological deformation has 2 types, one is solid, elastic deformation, and the other one is liquid deformation. In both cases, I can have attenuation, which is associated with viscosity for liquids (Fig. 5.3). Elastic deformation is described as spring and the stress(σ) is $\sigma = \mu\epsilon$, where μ is rigidity and ϵ is strain. Anelastic deformation is described as a damper and the stress is $\sigma = \eta\dot{\epsilon}$, where η is viscosity. Elastic deformation is reversible and anelasticity is non reversible.

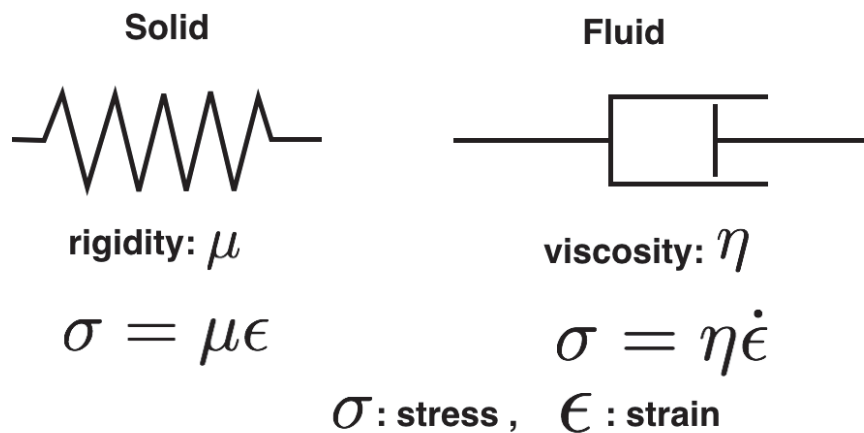


FIGURE 5.3 – Basic stress models. Basically, materials can be divided into two groups according to the rheological reaction. The solid group is elastic and reversible deformation. The liquid group is plasticity and irreversible deformation. This stress is described by its rigidity and viscosity respectively. Viscoelastic materials are composed of these 2 types of rheology.

Rocks and ice deformations act, however, as viscoelastic materials. Thus the Earth and planetary systems which consist of rocks and ice are modeled by a combination of springs and dampers. The most simple viscoelastic model is the Maxwell model. The model is

composed of one spring and one damper. The Maxwell model well explains the rheological behavior around Maxwell time (τ). The time scale (τ) is calculated by rigidity (μ) and viscosity (ν).

$$\tau = \frac{\eta}{\mu}, \quad (5.14)$$

$$\left\{ \begin{array}{l} T < \tau : \text{elastic,} \\ T > \tau : \text{plasticity} \end{array} \right\} \quad (5.15)$$

Response of the model is

$$\dot{\sigma}_{ij} + \frac{\mu}{\eta} \left(\sigma_{ij} - \frac{1}{3} \sigma_{kk} \delta_{ij} \right) = 2\mu \dot{\epsilon}_{ij} + \left(K_E - \frac{2}{3}\mu \right) \epsilon_{kk} \delta_{ij}, \quad (5.16)$$

where K_E is Bulk modulus. I perform Fourier transformation and obtain

$$\tilde{\sigma}_{ij} = 2\tilde{\mu}_M(\omega) \tilde{\epsilon}_{ij} + \left(K_E - \frac{2}{3}\tilde{\mu}_M(\omega) \right) \tilde{\epsilon}_{kk} \delta_{ij}, \quad (5.17)$$

$$\tilde{\mu}_M(\omega) = \frac{\mu\omega^2\eta^2}{\mu^2 + \omega^2\eta^2} + i \frac{\mu\omega^2\eta^2}{\mu^2 + \omega^2\eta^2}. \quad (5.18)$$

Eq (5.17) is the same as Hooke's law (elastic equation), eq (5.18) is complex shear modulus. The important thing is that this spring-damper model is able to calculate like elastic model eq (5.17) by introducing complex shear modulus. Long scale frequency as like tide is described well by the simple viscoelastic model. The simple Maxwell model cannot cover a wide frequency and is not suitable for the benchmark test. For the purpose of the broadband calculations, 2 classical models are suitable. One is Burgers model and another one is Andrade model (Fig. 5.4). Burgers model has 2 springs and 2 dampers, Andrade model has many springs and dampers. Burgers model is extended model of Maxwell model for broadband calculations. Andrade model is experimental model which has many parameters obtained by experimental test (*Castillo-Rogez, 2006*). I do not have enough experimental parameters Mars thus using Andrade model for Mars would be challenging. In the case of the benchmark test, I choose Burgers model.

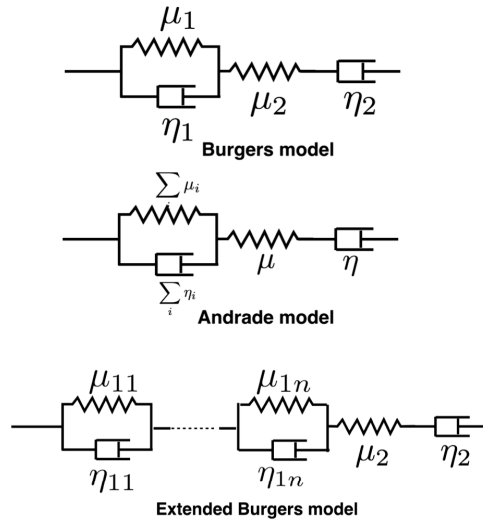


FIGURE 5.4 – *Viscoelastic models. These models are more complex than Maxwell model (simple viscoelastic model). More parameters and equations are required for these models than Maxwell model. These models, however, can calculate broadband phenomenon as like both tidal and seismic reaction of celestial body. Burgers is theoretical, Andrade is experimental model respectively.*

5.2.1 On Theory

I can get precise seismic Q number for shallow part of celestial bodies by seismological approaches (Garcia *et al.* (2011)). On the other hand, I have large error bars in the deep part because of a lack of observation for long seismic waves. Nimmo *et al.* (2012), calculated viscoelastic dissipation of lunar mantle using simple equations and extended Burgers model. The complex shear modulus is written $G^* = 1/J^*$, $J^* = J_r + J_i$, where J_r and J_i are real and imaginary part. Dissipation factors are give by Jackson and Faul (2010)

$$Q(\omega) = \frac{J_r(\omega)}{J_i(\omega)} = \frac{1 + J_{Br} + J_{Pr}}{(J_{Bi} + J_{Pi}) + \frac{1}{\omega\tau_M}}, \quad (5.19)$$

thus

$$J_r(\omega) = \frac{1}{G_U} \left[1 + \Delta \int_{\tau_L}^{\tau_H} \frac{D(\tau)d\tau}{(1 + \omega^2\tau^2)} \right] \quad (5.20)$$

and

$$J_i(\omega) = \frac{1}{G_U} \left[\omega \Delta \int_{\tau_L}^{\tau_H} \frac{\tau D(\tau) d\tau}{(1 + \omega^2 \tau^2)} + \frac{1}{\omega \tau_M} \right]. \quad (5.21)$$

$$G^{-1} = \sqrt{J_r^2 + J_i^2} \quad (5.22)$$

where G_U is the infinite-frequency shear modulus, τ is a dummy variable with units of time, D is relaxation time, Δ describes the strength of the relevant relaxation mechanism, ω is the angular frequency.

In the nature of the Burgers model, it has 2 relaxation times (Burgers model is a combination of the Maxwell model and Kelvin model or elastic and viscoelastic part) $D_B(\tau)$ and $D_P(\tau)$. $D_B(\tau)$ is under high-temperature ground or long timescale.

$$D_B(\tau) = \frac{\alpha \tau^{\alpha-1}}{\tau_H^\alpha - \tau_L^\alpha} \quad (5.23)$$

$D_P(\tau)$ is under relatively low-temperature or short timescale.

$$D_P(\tau) = \frac{1}{\tau \sigma \sqrt{2\pi}} \exp \left[-\frac{(\ln(\tau/\tau_p)\sigma)^2}{2} \right]. \quad (5.24)$$

These relaxation times are calculated by

$$\tau_i(P, T, d) = \tau_{iR} \left(\frac{d}{d_R} \right)^m \exp \left[\left(\frac{E}{R} \right) \left(\frac{1}{T} - \frac{1}{T_R} \right) \right] \exp \left[\left(\frac{V}{R} \right) \left(\frac{P}{T} - \frac{P_R}{T_R} \right) \right]. \quad (5.25)$$

where d is grain-size, P is pressure, T is temperature, V is volume per mol, E is energy per mol, and subscript R means reference. In this equation, I have 2 grain-size exponent : one for an elastic process and one for long-term viscous creep. This τ is dominated by value of $E + PV$. And the magnitude relationship is $E \gg PV$. Thus thermal state is more effective on the mechanism. In this way, I can calculate Q number as a function of ω, P, T, d .

5.3 BENCH MARK TEST BY MOON.

I will develop the theory more in detail in this section. Theoretical methods of dissipations are reviewed in the previous section(5.2).

The next step is the validation of the theory by seismic and geodetic observations. But I still lack information on seismic and geodetic data of Mars. In this section, I will show the validation of the k_2 method by seismic and geodetic data of the Moon instead of Mars. Moon is well observed celestial body by Apollo and other projects thus rich in geophysical observations capable of testing our approach (e.g *Nakamura (1982)*; *Vondrak et al. (2010)*; *Williams et al. (2014)*)).

5.3.1 Comparison with observation data.

The seismic velocity enables us to calculate Love numbers and vice versa. Love numbers are a function of seismic wave velocity, and the seismic velocity is a function of bulk modulus, temperature, density, and frequency. *Nimmo et al. (2012)* calculated Love numbers with many factors. In his paper, wave frequency and heat flux from the lunar core are important factors of the Love number. The wave frequency and heat flux change rigidity and seismic wave velocity as written in eq (5.21) and eq (5.25). The differences of lunar dissipation are big at the tidal frequency of the Moon (Fig. 5.5). In other words, Q and k_2 have high sensitivity at tidal frequency.

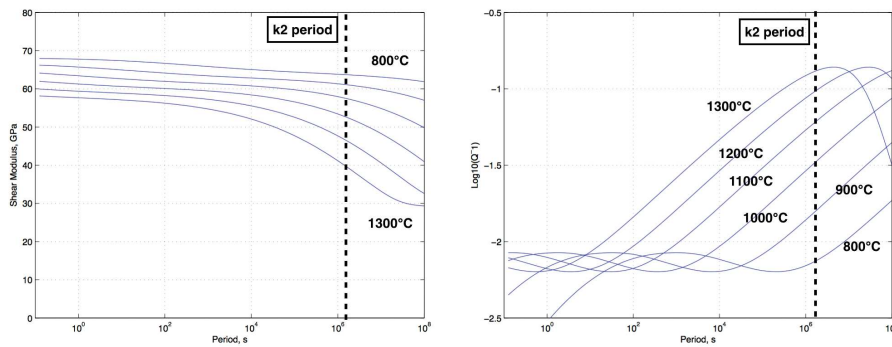


FIGURE 5.5 – Left figure shows shear modulus as a function of temperature and period. High temperature gives low shear modulus, but the differences are big at k_2 period. Right figure shows dissipation as a function of temperature and period. Low Q value (above of the figure) means more dissipative, the differences are big at tidal frequency of the Moon.

I need some input information to calculate the Love numbers. From eq (5.25), eq (5.27) and eq (5.26), I find that I need tempera-

ture, grain size, seismic wave velocity and tidal frequency for the calculation. These parameters affect significantly the Love number estimation, which will be further discussed in the following section.

Generally, wave delay by frequency is negligibly small. But in the case of the tide, the tidal period is huge compared to the seismic period (1.17×10^6 s and 1 s) and the delay will not be negligible. Fig. 5.6 shows the difference in wave velocity by frequency. Seismic wave velocities are based on the estimation by *Gagnepain-Beyneix et al.* (2006). The solid lines are wave velocities at the seismic frequency and the dot lines are wave velocities at tidal frequency. The difference between wave velocities is about 10 %. The difference in the wave velocities at tidal frequency changes the calculation result of Love numbers.

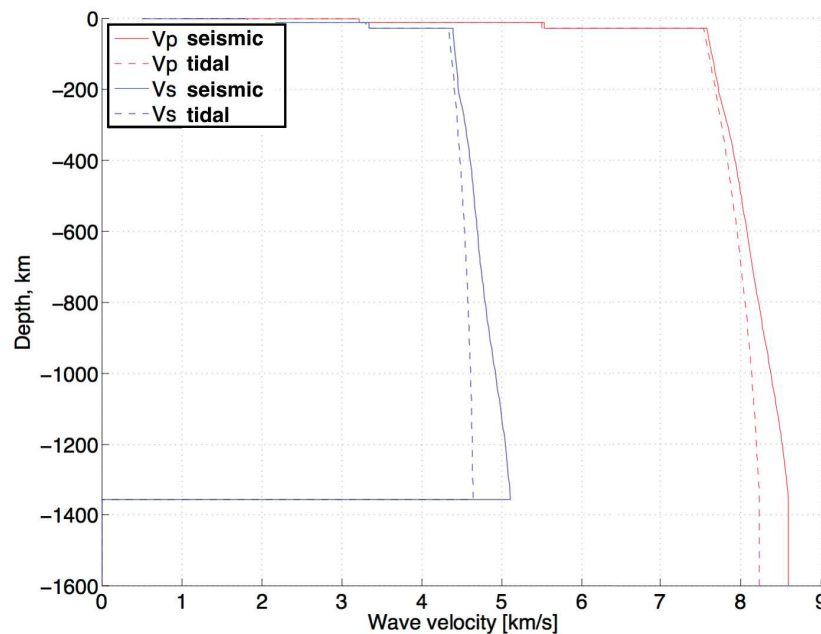


FIGURE 5.6 – Wave velocity in seismic frequency and tidal frequency. Wave velocity changes with frequencies. In the case shown in the figure, wave velocity at seismic frequency is 10 percentage faster than tidal frequency. The difference affects Love number calculations and estimations of internal structure.

In Fig. 5.7 and Fig. 5.8, I used 5 temperature models. 3 models are from *Nimmo et al.* (2012) (H values show mantle heating rate nWm^3). 1 model is from *Gagnepain-Beyneix et al.* (2006) (JGB06). 1 model is from

Kawamura et al. (2017)(TK17). Upper 2 figures are input information which are the same in both Fig. 5.7 and Fig. 5.8. The input information is based on seismic observations. 3rd and 4th figures (bottom figures) are wave velocity profiles and Q value profiles which are calculated from the input information. Wave velocity and Q value profiles are different between seismic frequency and tidal frequency. Seismic Q values are 100 - 150, tidal Q values are 10 - 50, tidal Q values are smaller than seismic Q values. This is the effect of wave frequency.

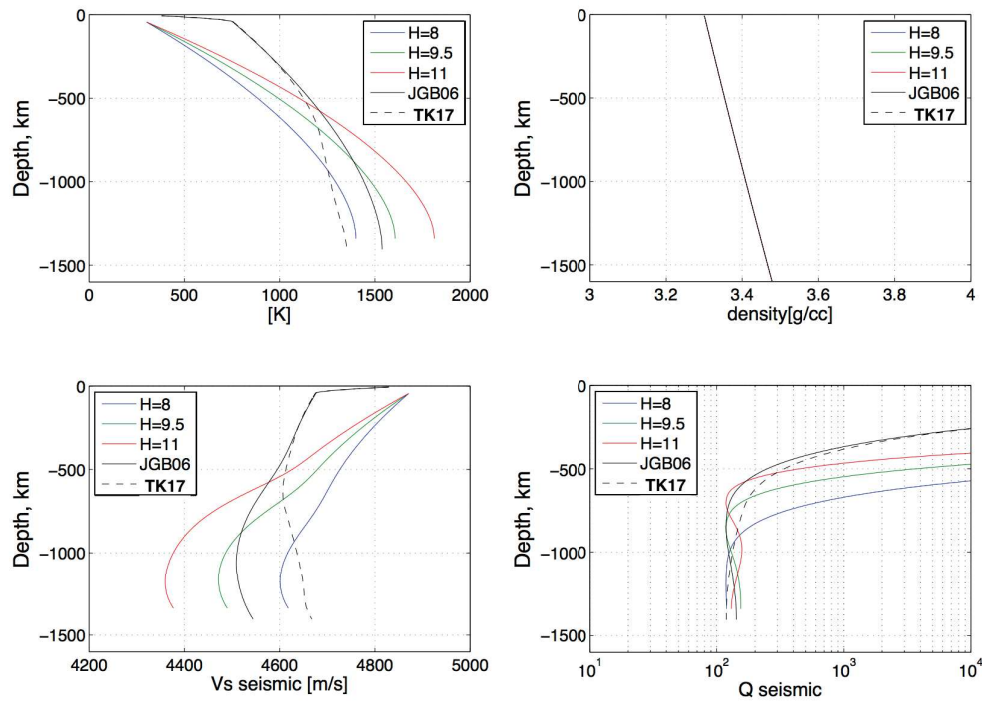


FIGURE 5.7 – Q calculation results at seismic frequency. Temperature and density profiles are input information. The profiles are estimated by observation and assumption of heat flux. Bottom left figure shows obtained wave velocity profile at seismic frequency. Wave velocity becomes slow when temperature becomes high. Bottom right is Q profile, the Q value is 100-150 at deep mantle.

Grain size is an important factor for the calculation of the Q value. Eq (5.25) is equation of relaxation time. The relaxation time is a function of pressure (obtained as a mass load from density profile), temperature, and grain size. The grain size is directly related to friction and dissipations. Fig. 5.9 shows input information and the

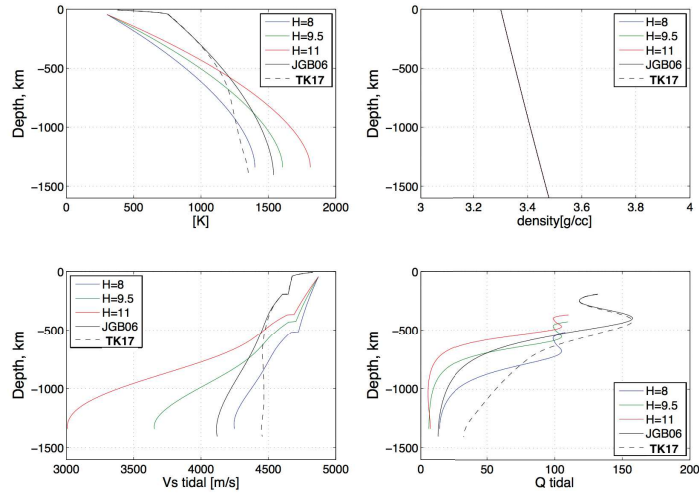


FIGURE 5.8 – Q calculation results at tidal frequency. Temperature and density profiles are same as the seismic frequency case. Bottom left figure shows obtained wave velocity profile at seismic frequency. Wave velocity becomes slow when temperature becomes high. Bottom right is Q profile, the Q value is less than 50 at deep mantle. The Q values are smaller than seismic frequency case.

calculation result of Q . In the calculations, I used the same temperature and seismic velocity profile, I only changed grain size from 1 mm to 1 cm. Calculation results of Q are different (red and black lines in Fig. 5.9). Net Q values are $Q_{1mm} = 39.8$, $Q_{1cm} = 74.8$.

I've already mentioned previously that Love numbers are functions of temperature, wave velocity, frequency, and grain size. The grain size is still uncertain property, but in this study, I use 1mm as grain size. This information will enable me to estimate the deep internal structure. Fig. 5.10 is the benchmark test of the estimation method. I fixed crust and mantle properties, and I varied the thickness of the outer core layer from 20 to 150 km. The k_2 value changes from 0.02389 to 0.02455. Observed k_2 is 0.02422 ± 0.00022 . As a result of the calculations, the thickness of the outer core is 50 to 130 km.

5.4 IMPLICATION FOR INSIGHT

Following the discussion I made on the Moon, I will further investigate possible implications for InSight observations. I have some

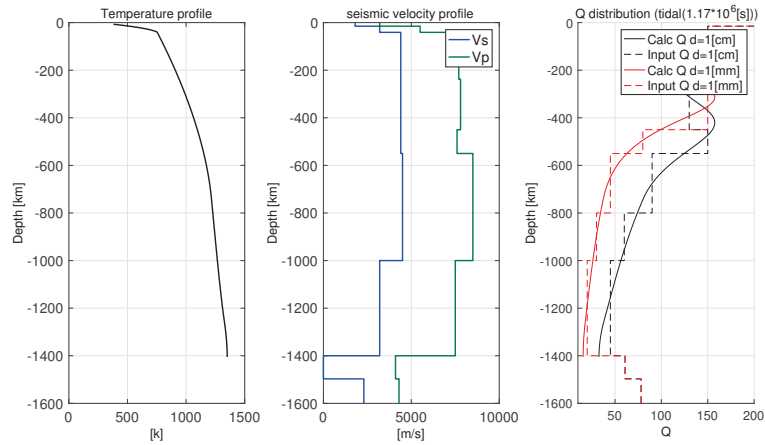


FIGURE 5.9 – Different results of Q value. Left and center figures are input temperature and seismic velocity (Kawamura et al. (2017)). Solid lines of right figure shows Q calculation results. Lines are input Q value to calculate net Q value. Calculation results of this model are $k_2 = 0.0257$ and $Q_{1mm} = 39.8$, $Q_{1cm} = 74.8$ ($k_2 = 0.02416 \pm 0.00022$ and $Q = 37.5 \pm 4$ Williams et al. (2014)). Grain size is important factor of Q value (eq (5.25)).

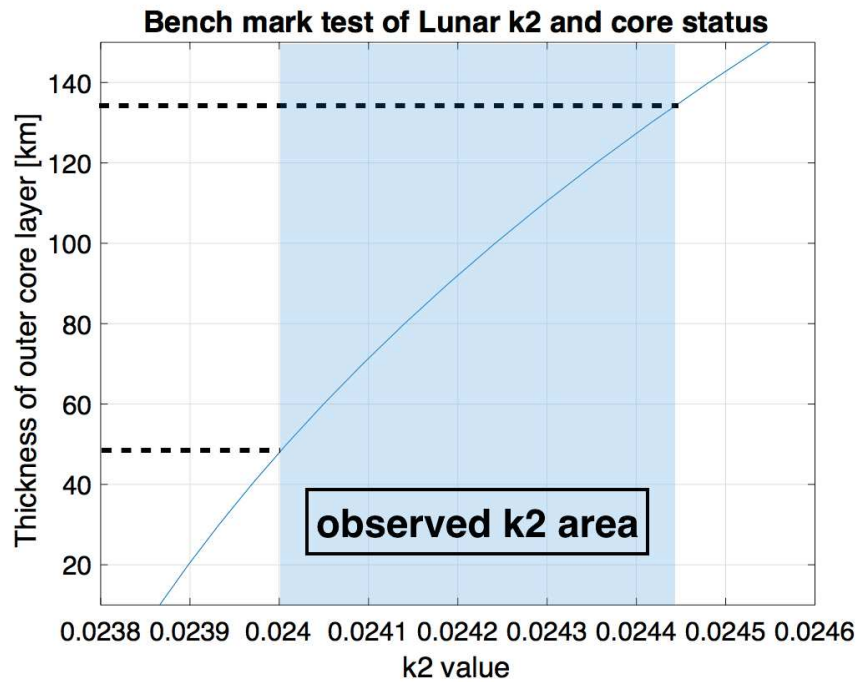


FIGURE 5.10 – Bench mark test of lunar k_2 and core status. Blue curve is k_2 and blue area is observed k_2 area. I fixed crust and mantle status (these status are determined by seismic observations). I changed thickness of outer core from 20 to 150 km to estimate the possible thickness. In this case, possible thickness of outer core is 50 to 130 km.

seismic V_s and V_p models (e.g. *Sohl and Spohn (1997)*). I can calculate seismic μ and tidal μ by eq (5.20) and eq (5.21). Thus, tidal wave velocities are

$$V_s^2(\omega_t) = V_s^2(\omega_s) \times \frac{J_R(\omega_t)}{J_R(\omega_s)}, \quad (5.26)$$

$$V_p^2(\omega_t) = \frac{K(\omega_s) + \frac{4}{3}\mu(\omega_t)}{\rho}, \quad (5.27)$$

where ω_s , ω_t , V_p and V_s are seismic frequency, tidal frequency, P-wave velocity and S-wave velocity. With these values, I evaluated Love numbers for Mars. As it was discussed in the previous chapter, upper and middle mantle structure will be defined by MBF observations. Thus I fixed crust and mantle status (from surface to 1820 km depth). Then, core radius was searched as a free parameter so that the obtained geodetic parameters match the observation. I calculated k_2 of 3 models. First model is Sohl model. The other 2 models are modified Sohl Model with the core size 100 km larger or smaller than the original model (Fig. 5.11). I fixed the mass, radius, and the crust/mantle composition. I changed only the core size. The ± 100 km error bar is close to InSight's capability.

By the calculations, k_2 of Sohl model, large core model and small core model are 0.167, 0.189, 0.151 in table(5.1). InSight enables us to distinguish the differential of them. I can estimate Love numbers as a function of core mantle boundary and vice versa.

	Sohl model	large core +100km	small core -100km
k_2	0.167	0.189	0.151

TABLE 5.1 – k_2 numbers calculated by input models. Calculation results of 3 models. 1st model is Sohl model, 2nd model has same internal structure from surface to bottom of mantle, but the core is 100 km larger than Sohl model. 3rd one is similar with 2nd one, but the core is 100 km smaller than Sohl model.

5.5 CONCLUSION

I showed deep internal structure estimation using tidal parameters with a special focus on Love numbers. To test this approach, I used

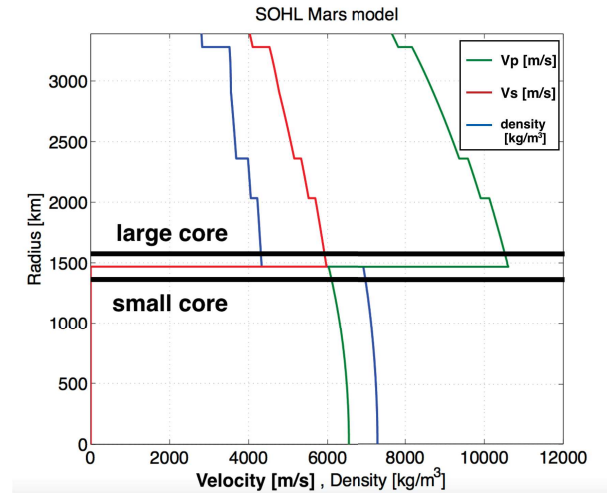


FIGURE 5.11 – Sohl internal structure model and ± 100 km core lines. Seismic observations (MBFs observations) can estimate crust and shallow middle mantle structure, in other words, core and deep mantle structures are not observable in this case. 2 degree Love numbers (Tidal deformations) work as low degree normal mode. The Love numbers will provide information to distinguish between the 3 core sizes (sohl core, large core and small core) and fill-in the blank of internal structure estimation of seismic observations.

lunar observation which includes seismic and geodetic data. This is a preparation for InSight observation, which also includes seismic and geodetic observations. I successfully showed here that observation of k_2 Love number enables us to constrain the deep internal structure of the Moon, such as the radius of the core. This strongly implies that by combining seismic and MBF observation, which has a high sensitivity to the shallower structure down to the upper mantle, and tidal observation, I can have a complete view of the internal structure from shallow to deep region.

The InSight will give us some temperature profile (by HP3), seismic wave velocity (by SEIS), and Love numbers (by RISE). As it was shown in the lunar example, this will provide us with full information to study the internal structure of Mars with its thermal states. In this study, I focus on MBF and Love number observation and demonstrated how I can benefit from such complementary observations. My results show that InSight will surely provide unique datasets to uncover the full internal structure of Mars.

CONCLUSION GÉNÉRALE

In this study, I established methodology to estimate mantle and core status of Mars to be ready for inSight mission by using seismology at long wavelength. I showed 3 methods, wind shield development, calculations of MBFs and Love number.

I designed torque-less wind shield for broadband seismic observations by wind tunnel tests and CFD simulations. I focused on lift force and torque as important factors for the design of wind shield for martian broadband seismic observations. I conducted wind tunnel tests and numerical simulations to evaluate the lift forces and the torques as a function of wind speed and air density. I confirmed the numerical simulations in the results of wind tunnel tests. I designed effective torque-less wind shield for broadband seismic observation in windy environments on Mars and improved the expected noise level for observation of broadband marsquakes caused by martian wind. The designed torque-less wind shield keeps a stable position even for the strongest wind environment on Mars, and the noise free periods of the designed wind shield is longer than typical wind shield's noise by one order of magnitude. In the results, the ground noiseless period became more than twice on windy environment.

I evaluated the signal level of Mars' background free oscillations with high resolution GCMs. Given the model limitation of GCMs, the obtained values should be regarded as a lower limit of possible amplitude of background free oscillations expected on Mars. For the realistic evaluation, I introduced several assumptions which are based on observations and theories to simplify the model to reduce the calculation cost and introduced 3D atmospheric structure. With these models and assumptions, I obtained that the amplitudes of MBFs are likely to be orders of nanogals. This is consistent with previous studies such as *Kobayashi and Nishida (1998a)*; *Lognonné and Johnson*

(2007). I also confirmed that the obtained values are consistent with energy budget with solar flux. After a series of discussions, I am confident that the obtained values represents the typical signal level of MBFs though the amplitudes may differ with assumptions I adopt, such as the internal structure and atmospheric model. Given the signal level of MBFs and noise level of InSight SEIS instruments, it is difficult to detect the signal of MBFs by SEIS instruments. The actual noise observed was about 30 nanogal (Fig. 5.12), which is about two orders of magnitude larger than the signal. The stacking in this study is about an order of magnitude more accurate, but the signal may be observed by a very detailed understanding of the noise using decorrelation and deglitch method (Lognonné *et al.* (2020)).

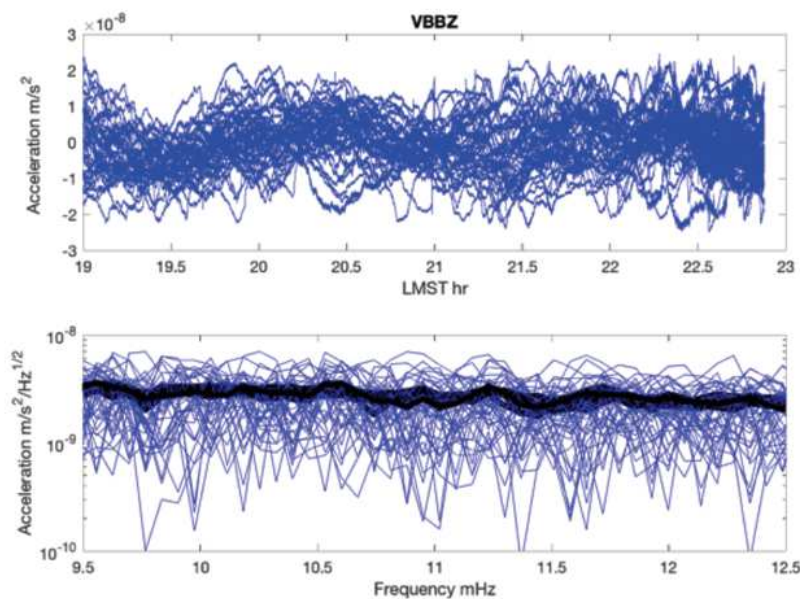


FIGURE 5.12 – Simple sensitivity tests of InSight observation data. The tests provide a detection threshold of about 30 nanogal, likely about 100 times larger than the expected MBFs.

I calculated Love numbers of Mars using possible internal structures to show the effectiveness of the Love number method which is based on rheology. I demonstrated from test calculation for the Moon that by using the Love number, I can discriminate between different core structure and have sensitivity to deep region of the body. This was a very promising results where seismic and geodetic observa-

tion can be combined to provide full view of the internal structure, which would also be the case for InSight. I evaluated how k_2 Love number will vary with different core size for Mars and showed that InSight will be capable of discriminating this.

In this study, I investigated the long period in several different points of view. First, I studied the noise reduction for optimized observation from engineering point of view. Secondly, I studied atmospheric excitation of MBFs and discussed its detectability by comparing the signal amplitude with the noise. MBFs were also discussed with a special interest in probing the relatively shallow structure, such as the mantle structure. Finally I investigated tidal deformation, which is the longest period studied in seismology. This was investigated as observations complementary to MBF observations since they are sensitive to deeper structure such as the core size. Through out this study I have studied the way to uncover the internal structure of Mars both from theoretical and observational point of view. Given that InSight have successfully landed on Mars and carrying out observations, I am fully convinced from my results that InSight will successfully reveal the Mars' inner structure and open a new window for Mars science in the near future.

ANNEXES



SOMMAIRE

A.1	CANONICAL BASIS AND GENERALIZED SPHERICAL HARMONICS	119
A.1.1	Spherical basis	120
A.1.2	Canonical basis	120
A.1.3	Passage from the spherical basis to canonical	120
A.1.4	generalized spherical harmonics	122
A.2	DATA INTERPOLATION.	123
A.2.1	Linear interpolation	123
A.2.2	Spline interpolation	124

annexe

ANNEXE

A.1 CANONICAL BASIS AND GENERALIZED SPHERICAL HARMONICS

I will introduce the canonical basis developed in *Phinney and Burridge* (1973). In order to simplify the Navier-Stokes equation (eq. 3.3). Indeed if I use the canonical I don't need to calculate second-order partial derivatives of Laplacian $\frac{\partial^2}{\partial \theta^2}$. This was then further developed by *Unno et al.* (1979); *Watada* (1995); *Lognonné et al.* (1998b) to include the coupling between the atmosphere and terrestrial body. I assume Earth is a radial symmetric system. This leads to use the spherical coordinate (r, θ, ϕ) . Thus I introduce a basis where the solution is the multiplication of a radial function and angular function. This basis is called the canonical basis. In this thesis, I consider the station has the location (r_s, θ_s, ϕ_s) and the source has the location (r_0, θ_0, ϕ_0) , I describe displacement in spherical basis as u_i (u with $i, j, k...$ in the subscript) and in canonical basis as u^α (u with $\alpha, \beta, \gamma...$ in the superscript).

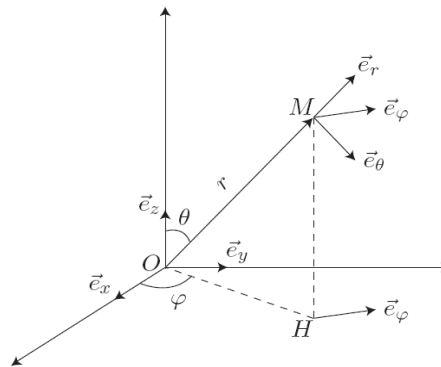


FIGURE A.1 – Spherical basis

A.1.1 Spherical basis

The unit vectors are \vec{e}_r , \vec{e}_θ and \vec{e}_ϕ . There is a representation of the spherical basis on Fig. A.1. A vector \vec{u} is written in the spherical basis :

$$\vec{u} = u_i \vec{e}_i = u_r \vec{e}_r + u_\theta \vec{e}_\theta + u_\phi \vec{e}_\phi. \quad (\text{A.1})$$

The scalar product is note $e_{ij} = \delta_{ij}$ with δ_{ij} the Kronecker symbol.

$$\begin{cases} \delta_{ij} = 1 & \text{if } i = j, \\ \delta_{ij} = 0 & \text{if } i \neq j. \end{cases} \quad (\text{A.2})$$

A.1.2 Canonical basis

A vector \vec{u} is written :

$$\vec{u} = u^\alpha \vec{e}_\alpha = u^0 \vec{e}_0 + u^+ \vec{e}_+ + u^- \vec{e}_-. \quad (\text{A.3})$$

I define the components as :

$$\begin{cases} u^0 = u_r, \\ u^+ = \frac{1}{\sqrt{2}}(-u_\theta + iu_\phi), \\ u^- = \frac{1}{\sqrt{2}}(u_\theta + iu_\phi). \end{cases} \quad (\text{A.4})$$

Thus for the unit vectors of the basis, I must have :

$$\begin{cases} \vec{e}_0 = \vec{e}_r, \\ \vec{e}_+ = \frac{1}{\sqrt{2}}(-\vec{e}_\theta - i\vec{e}_\phi), \\ \vec{e}_- = \frac{1}{\sqrt{2}}(\vec{e}_\theta - i\vec{e}_\phi). \end{cases} \quad (\text{A.5})$$

A.1.3 Passage from the spherical basis to canonical

From the eq. (A.10), the passage matrix $C_{i\alpha}$ from spherical basis to canonical basis reads :

$$C_{i\alpha} = \begin{pmatrix} \frac{1}{\sqrt{2}} & 0 & \frac{-1}{\sqrt{2}} \\ \frac{-i}{\sqrt{2}} & 0 & \frac{-i}{\sqrt{2}} \\ 0 & 1 & 0 \end{pmatrix} \quad (\text{A.6})$$

For a tensor M of any rank we write

$$m^{\alpha\beta\gamma\dots} = C_{\alpha i}^\dagger C_{\beta j}^\dagger C_{\gamma k}^\dagger \dots m_{ijk\dots}, \quad (\text{A.7})$$

where \dagger denotes Hermitian conjugation.

And I have the following relation :

$$C_{i\alpha} C_{\alpha j}^\dagger = \delta_{ij}, \quad (\text{A.8})$$

The contravariant canonical components of displacement is obtained :

$$u^\alpha = C_{\alpha i}^\dagger u_i. \quad (\text{A.9})$$

Any tensor m_{ij} in the spherical basis is written in canonical basis :

$$m^{\alpha\beta} = C_{i\alpha}^* C_{j\beta}^* m_{ij} = C_{\alpha i}^\dagger C_{\beta j}^\dagger m_{ij}, \quad (\text{A.10})$$

where $*$ denotes complex conjugation.

From eq (A.8) I have :

$$m_{ij} = C_{i\alpha} C_{j\beta} m^{\alpha\beta}. \quad (\text{A.11})$$

This is valid for the vector too. With the use of eq (A.2) and eq (A.10)

$$e_{\alpha\beta} = C_{i\alpha} C_{i\beta}. \quad (\text{A.12})$$

The equation (A.6) gives us :

$$e_{00} = 1, e_{-+} = e_{+-} = -1, e_{\alpha\beta} = 0 \text{ if } \alpha + \beta \neq 0. \quad (\text{A.13})$$

The scalar product in canonical basis is :

$$\vec{u} \cdot \vec{v} = e_{\alpha\beta} u^\alpha v^\beta. \quad (\text{A.14})$$

For a real basis (for example spherical), I have :

$$(u^*)_i = (u_i)^*. \quad (\text{A.15})$$

I can write

$$\begin{cases} (u_i)^* = C_{i\alpha}^* (u^\alpha)^*, \\ (u^*)_i = C_{i\alpha} (u^*)^\alpha. \end{cases} \quad (\text{A.16})$$

In multiplying eq (A.16) by $C_{i\beta}^*$ I obtain :

$$(u^*)^\beta = \delta_{\alpha\beta}(u^*)^\alpha = e_{\alpha\beta}(u^\alpha)^*. \quad (\text{A.17})$$

And finally :

$$\vec{u} \cdot \vec{v}^* = u^\alpha (v^*)^\beta e_{\alpha\beta} = u^\alpha (v^\gamma)^* e_{\alpha\beta} e_{\gamma\beta} = u^\alpha (v^\gamma)^* \delta_{\gamma\alpha}. \quad (\text{A.18})$$

A.1.4 generalized spherical harmonics

I assume the planet has a spherical symmetry (for example *Sohl and Spohn* (1997)), which means there is no lateral variation. Therefore in the canonical basis, I can write the components u^α of \vec{u}

$$u^\alpha(r, \theta, \phi) = \sum_n \sum_{l=0}^{\infty} \sum_{m=-l}^l {}_n U_l^{\alpha m}(r) Y_l^{\alpha m}(\theta, \phi), \quad (\text{A.19})$$

where n is radial order, l is angular order and m is azimuthal order. If I use a spherical basis, I cannot separate radial order from the angular ones.

For a tensor rank 2, I write the components $m^{\alpha\beta}$ of \vec{m} is the same as :

$$m^{\alpha\beta}(r, \theta, \phi) = \sum_n \sum_{l=0}^{\infty} \sum_{m=-l}^l {}_n M_l^{(\alpha+\beta)m}(r) Y_l^{(\alpha+\beta)m}(\theta, \phi). \quad (\text{A.20})$$

In this case I have $\alpha, \beta = -1, 0, 1$. In order to simplify the writing, I will remove n in U and M .

The angular part is given by the generalized spherical harmonics :

$$Y_l^{Nm}(\theta, \phi) = P_l^{Nm}(\cos \theta) e^{im\phi}, \quad (\text{A.21})$$

P_l^{Nm} is the generalized Legendre Polynomial. Let us notice $\alpha = 0$ is for a scalar.

$$P_l^{Nm}(\mu) = \frac{(-1)^{l-N}}{2^l (l-N)!} \sqrt{\frac{(l-N)!(l+m)!}{l! (l+N)! (l-m)!}} (1-\mu)^{-\frac{1}{2}(m-N)} (1+\mu)^{-\frac{1}{2}(m+N)} \\ \times \frac{d^{l-m}}{d\mu^{l-m}} [(1-\mu)^{l-N} (1+\mu)^{l+N}]. \quad (\text{A.22})$$

A.2 DATA INTERPOLATION.

Equation (3.44) is depending on both an oscillating term related to the normal mode and of potentially oscillating source terms, associated to the pressure. Let us consider for sake of facility that the input pressure is also sinusoidal, with angular frequency ω_0 , starting at time 0. This can be rewritten as

$$\kappa(t) = H(t - t_0) \cdot e^{i\omega_0(t-t_0)}, \quad (A.23)$$

$$p_k(t) = \int_{-\infty}^t d\tau \kappa(\tau) e^{i\sigma_k(t-\tau-t_0)}, \quad (A.24)$$

where p_k , κ , σ_k , ω_0 , t_0 and H are excitation, excitation pressure, normal mode angular velocity, excitation pressure angular velocity, integration start time and Heavyside function. If $t_0 = 0$, analytical solution of $p_k(t)$ is

$$\begin{aligned} p_{k_theory}(t) &= \int_0^t d\tau \kappa(\tau) e^{i\sigma_k(t-\tau)}, \\ &= e^{i\sigma_k t} \int_0^t d\tau e^{i(\omega_0 - \sigma_k)\tau}, \\ &= \frac{1}{i(\omega_0 - \sigma_k)} \cdot (e^{i\omega_0 t} - e^{i\sigma_k t}). \end{aligned} \quad (A.25)$$

A.2.1 Linear interpolation

I linear interpolate the sampled pressure variation

$$\kappa(\tau) = \kappa(t - \Delta t) + \frac{\tau - (t - \Delta t)}{\Delta t} [\kappa(t) - \kappa(t - \Delta t)]. \quad (A.26)$$

I calculate $p_k(t)$ by recurrence formula.

$$\begin{aligned} p_{k_linear}(t) &= \int_{-\infty}^{t-\Delta t} d\tau \kappa(\tau) e^{i\sigma_k(t-\tau)} + \int_{t-\Delta t}^t d\tau \kappa(\tau) \\ &= e^{i\sigma_k \Delta t} p_k(t - \Delta t) + \int_{t-\Delta t}^t d\tau \kappa(\tau) e^{i\sigma_k(t-\tau)}, \\ &= e^{i\sigma_k \Delta t} p_k(t - \Delta t) \\ &\quad + \Delta t \cdot (\kappa(t) + \kappa(t - \Delta t)) \cdot e^{i\sigma_k \Delta t}, \end{aligned} \quad (A.27)$$

$e^{i\sigma_k \Delta t} p_k(t - \Delta t)$ is past excitation with attenuation, and $\int_{t-\Delta t}^t d\tau \kappa(\tau) e^{i\sigma_k(t-\tau)}$ is new excitation between $t - \Delta t$ and t .

I calculate eq(A.25) and eq(A.27) by Matlab and Fortran. The differences between Matlab and Fortran are negligibly small (magnitude 10^{-14}) compare to the amplitude of calculation results (Fig.A.2). Thus, the difference of result is compiler error. Fig.A.3 shows p_{k_linear} and p_{k_theory} , p_{k_linear} and $p_{k_linear} - p_{k_theory}$. The error value of our interpolation is $11 \sim 13$ %.

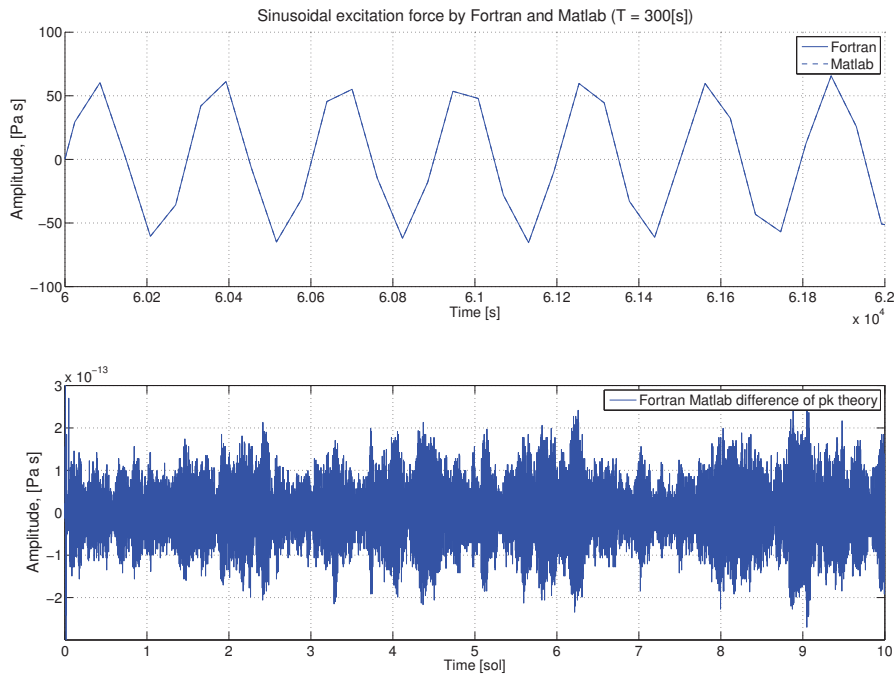


FIGURE A.2 – Difference between the excitation calculated by Fortran and Matlab, sinusoidal excitation pressure and force. The magnitudes of the difference are 10^{-14} smaller than the signals.

A.2.2 Spline interpolation

In the same way, I calculate $p_k(t)$ by 3 degree spline interpolation. Linear interpolation is a very simple method. By the interpolation, I can get only discontinuous results. In this section, I calculate continuous excitation force p_k using 3 degree spline interpolation.

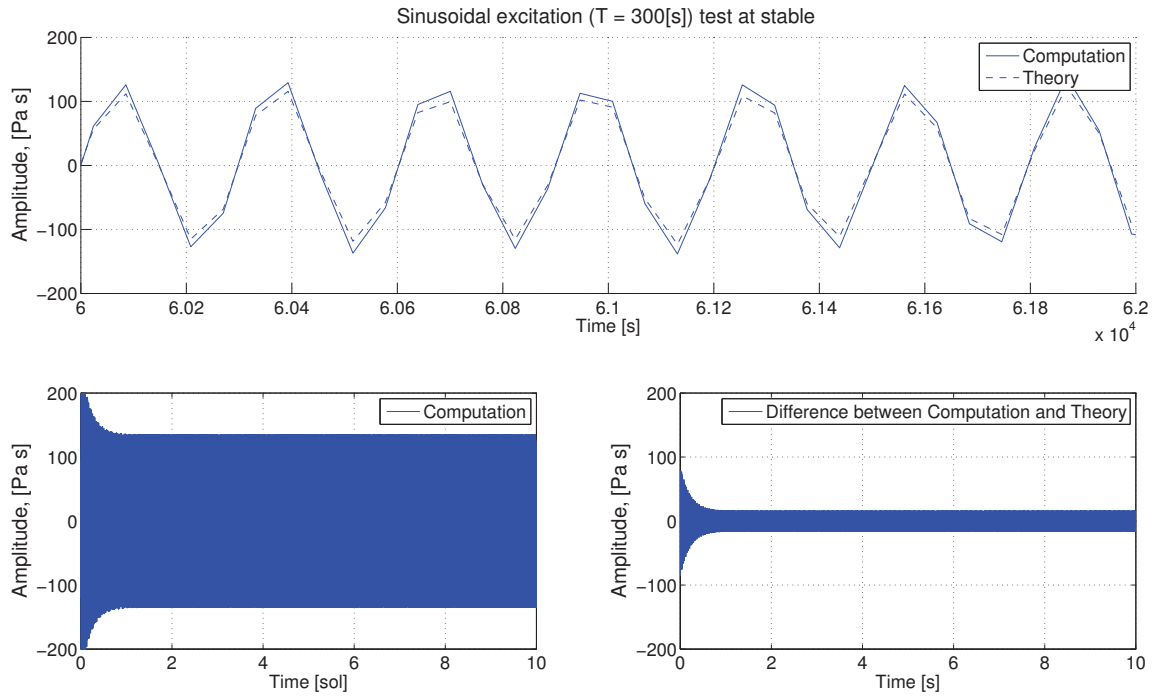


FIGURE A.3 – Top 2 $p_k(t)$ s (excitations) are calculated by analytic and linear interpolation method (p_{k_linear} and p_{k_theory}). Bottom left figure is the $p_k(t)$ by linear interpolation (p_{k_linear}). Bottom right figure is the difference between p_{k_linear} and p_{k_theory} . This ratio of p_k signal and p_k difference is the error (precision) of our linear interpolation.

$$\begin{aligned}
\kappa(t) &= \kappa(n) + \sum_{k=1}^3 x^k Q(n, k), \\
x &= t - t_n, \\
&= \frac{\tau - t_{n-1}}{t_n - t_{n-1}},
\end{aligned} \tag{A.28}$$

where n is number of data, and x is time of the spline. I substitute x into A ,

$$\begin{aligned}
A &= \int_{t_{n-1}}^{t_n} d\tau \kappa(\tau) e^{i\sigma_k(t_n - \tau)}, \\
&= e^{i\sigma_k \Delta t} \int_{x_1}^{x_2} dx \kappa(x) e^{i\sigma_k x}.
\end{aligned} \tag{A.29}$$

Thus, new continuous excitation force A is

$$\begin{aligned}
A &= \kappa(n) \times A_0 + Q(n, 1) \times A_1 + Q(n, 2) \times A_2 + Q(n, 3) \times A_3, \\
A_n &= e^{-i\sigma_k \Delta x} \int_{x_1}^{x_2} dx x^n e^{-i\sigma_k x},
\end{aligned} \tag{A.30}$$

where $\Delta x = x_2 - x_1$. I calculate A_n by partial integration.

$$\begin{aligned}
A_0 &= e^{-i\sigma_k \Delta x} \int_{x_1}^{x_2} dx e^{-i\sigma_k x}, \\
&= e^{-i\sigma_k \Delta x} \left[\frac{e^{i\sigma_k x}}{-i\sigma_k} \right]_{x_1}^{x_2}, \\
A_n &= e^{-i\sigma_k \Delta x} \int_{x_1}^{x_2} dx x^n e^{-i\sigma_k x}, \\
&= e^{-i\sigma_k \Delta x} \int_{x_1}^{x_2} dx x^n \left(\frac{e^{-i\sigma_k x}}{-i\sigma_k} \right)', \\
&= e^{-i\sigma_k \Delta x} \left(\left[x^n \cdot \frac{e^{-i\sigma_k x}}{-i\sigma_k} \right]_{x_1}^{x_2} - \int_{x_1}^{x_2} dx nx^{n-1} \cdot \frac{e^{-i\sigma_k x}}{-i\sigma_k} \right), \\
&= e^{-i\sigma_k \Delta x} \left[\frac{e^{-i\sigma_k x}}{-i\sigma_k} \cdot x^n \right]_{x_1}^{x_2} + \frac{n}{i\sigma_k} A_{n-1}, \\
&= e^{-i\sigma_k \Delta x} \left[\frac{e^{-i\sigma_k x}}{i\sigma_k} \sum_{k=0}^n \frac{n!}{k!} \frac{x^k}{(i\sigma_k)^{n-k}} \right]_{x_1}^{x_2}, \\
A_1 &= e^{-i\sigma_k \Delta x} \left[\frac{e^{-i\sigma_k x}}{i\sigma_k} \left(x + \frac{1}{i\sigma_k} \right) \right]_{x_1}^{x_2}, \\
A_2 &= e^{-i\sigma_k \Delta x} \left[\frac{e^{-i\sigma_k x}}{i\sigma_k} \left(x^2 + \frac{2x}{i\sigma_k} + \frac{2}{(i\sigma_k)^2} \right) \right]_{x_1}^{x_2}, \\
A_3 &= e^{-i\sigma_k \Delta x} \left[\frac{e^{-i\sigma_k x}}{i\sigma_k} \left(x^3 + \frac{3x^2}{i\sigma_k} + \frac{6x}{(i\sigma_k)^2} + \frac{6}{(i\sigma_k)^3} \right) \right]_{x_1}^{x_2},
\end{aligned} \tag{A.31}$$

Finally, I get continuous excitation force p_k as

$$p_k(t_n) = p_k(t_{n-1})e^{i\sigma_k \Delta x} + \kappa(n) \times A_0 + \sum_{k=1}^3 Q(n, k) \times A_k. \tag{A.32}$$

With this cubic spline interpolation, interpolation error decreases to 3 ~ 5 %

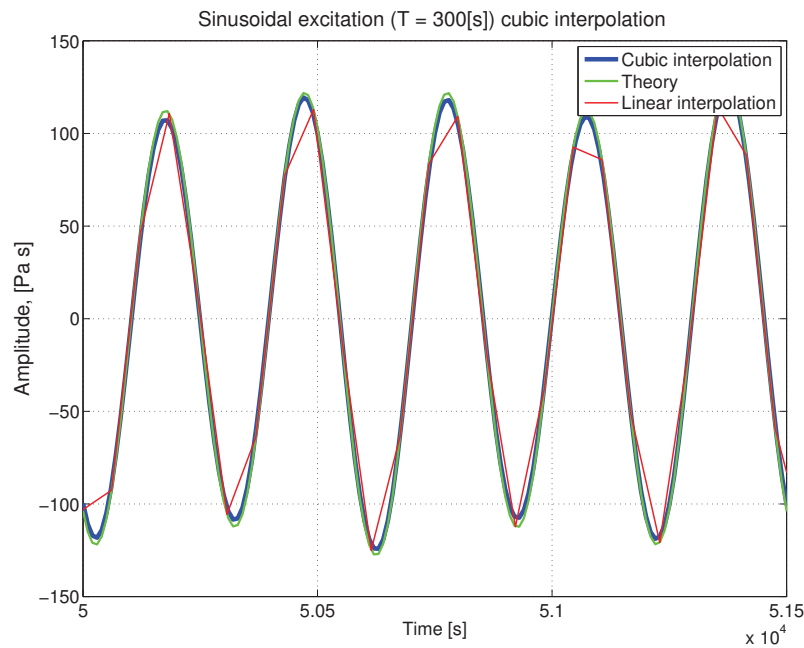


FIGURE A.4 – These lines are computation of 3 degree interpolation, analytic and linear interpolation results. Time step of cubic interpolation is 10[s], linear interpolation one is 61.5 s. The differences are error of interpolation method.

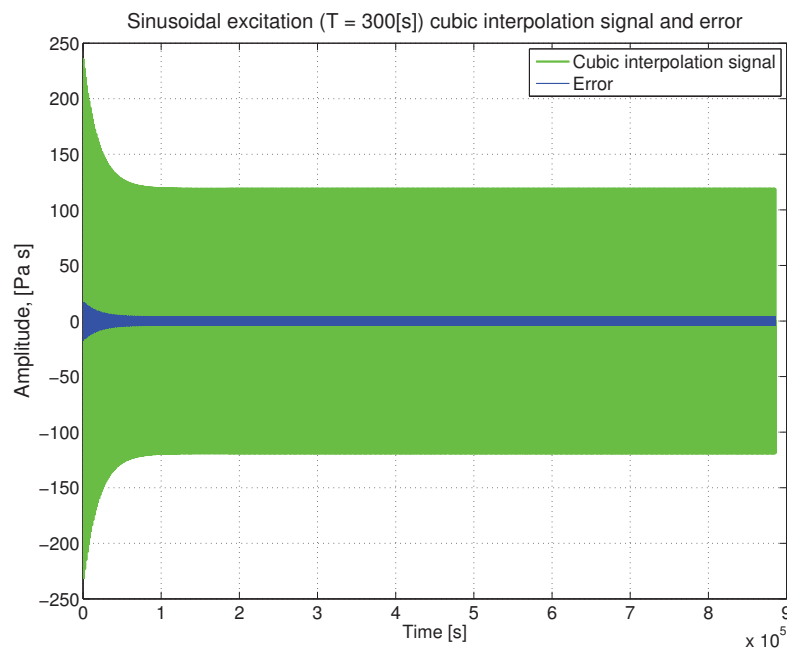


FIGURE A.5 – This figure shows spline interpolated p_k and its error. The error value is about 3%

PHINNEY-BURRIDGE NOTATION

The excitation force in canonical basis has been described by *Phinney and Burridge* (1973). A stress is applied at the point source $\vec{r} = \vec{r}_0$ at time $t = 0$.

$$\tau^{\alpha\beta} = M^{\alpha\beta} \delta(\vec{r} - \vec{r}_0) H(t) \quad (\text{A.33})$$

So the force is here $\vec{f} = \vec{\nabla} \cdot \vec{\tau}$. I can deduce the excitation :

$${}_n\psi_l^m = \int_V (\vec{\nabla} \cdot \vec{\tau}) \cdot {}_n\vec{u}_l^{m*} dV \quad (\text{A.34})$$

If I apply the gauss theorem and the boundary condition, I finally find :

$${}_n\psi_l^m = - \int \vec{M} : {}_n\vec{\epsilon}_l^{m*} \delta(\vec{r} - \vec{r}_0) dV \quad (\text{A.35})$$

In canonical components with the computation of the double product, I have :

$$\begin{aligned} {}_n\psi_l^m &= - \int M^{\alpha\beta} : {}_n\epsilon_l^{\alpha\beta*} \delta_{\alpha\beta} \delta_{\gamma\delta} \delta(\vec{r} - \vec{r}_0) dV, \\ &= M^{\alpha\beta} : {}_n\epsilon_l^{\alpha\beta*}(\vec{r}_0) \delta_{\alpha\beta} \delta_{\gamma\delta}. \end{aligned}$$

I obtain :

$$\begin{cases} {}_n\psi_l^0 = - (M^{00} {}_nE_l^{00} + 2M^{+-} {}_nE_l^{+-}) (r_0) \\ {}_n\psi_l^{\pm} = -2M^{0\pm} {}_nE_l^{0\pm}(r_0) \\ {}_n\psi_l^{\pm 2} = -M^{\pm\pm} {}_nE_l^{\pm\pm}(r_0) \end{cases} \quad (\text{A.36})$$

where super scripts o+- are canonical axis. I have the following relation :

$$\begin{cases} E^{0+} = E^{0-} \\ E^{++} = E^{--} \end{cases} \quad (\text{A.37})$$

When I sum the normal modes, I will sum only for $m = \pm 2, \pm 1, 0$ because the rest of the terms give ${}_n\psi_l^m = 0$. I can write the moment tensor from spherical to canonical :

$$\begin{cases} M^{00} = M_{rr} \\ M^{+-} = \frac{1}{2} (M_{\theta\theta} + M_{\phi\phi}) \\ M^{0\pm} = \frac{1}{\sqrt{2}} (M_{r\theta} + iM_{r\phi}) \\ M^{\pm\pm} = \frac{1}{2} (M_{\theta\theta} - M_{\phi\phi}) \mp iM_{\theta\phi} \end{cases} \quad (\text{A.38})$$

Then I write the displacement :

$$u(r_s, \theta_s, \phi_s, t) = \sum_n \sum_l \frac{1 - e^{i_n \omega_l t}}{n \omega_l^2} {}_n U_l^{Nm} \left(\sum_{m=-2}^2 {}_n \psi_l^{Nm} P_l^{Nm}(\cos \theta_s) e^{im\phi_s} \right) \quad (\text{A.39})$$

In this paper, I use N=0 order excitation force (first line of eq(A.36)). N=0 order excitation is

$$\begin{aligned} {}_n \psi_l^{0m} &= -(M^{00} {}_n E_l^{00} + 2M^{+-} {}_n E_l^{+-}), \\ &= \frac{dU^0(r)}{dr} (p + \rho v_r v_r) {}_n Y_l^{0m} + \frac{1}{r} \left[\sqrt{\frac{l(l+1)}{2}} U^+ - U^0 \right] [2p + \rho(v_\theta v_\theta + v_\phi v_\phi)] \end{aligned}$$

ANNEXE2

DESIGNING A TORQUE-LESS WIND SHIELD FOR BROADBAND OBSERVATION
OF MARSQUAKES



Designing a torque-less wind shield for broadband observation of marsquakes

Y. Nishikawa^{a,b,c,*}, A. Araya^b, K. Kurita^b, N. Kobayashi^d, T. Kawamura^c

^a Department of Earth and Planetary Science, The University of Tokyo, 7-3-1 Hongo Bunkyo-ku, Tokyo 113-0033, Japan

^b Earthquake Research Institute, The University of Tokyo, Japan

^c Institut de Physique du Globe de Paris, France

^d Institute of Space and Astronomical Science, Japan Aerospace Exploration Agency, Sagami-hara, Japan

ARTICLE INFO

Article history:

Received 3 April 2014

Received in revised form

9 October 2014

Accepted 24 October 2014

Available online 31 October 2014

Keywords:

Mars

Marsquake

Wind

Wind shield

Seismometer

Background noise

ABSTRACT

To perform seismic observations on Mars, reduction of the surface wind effect is necessary. In particular, ground tilt causes a serious problem for broadband seismic observations. Ground tilt is a seismic noise source, and it can be attributed to the torque of the wind shield. The torque brings about a difference in ground strain. Here, we report on an optimized torque-less wind shield to protect a seismometer from the wind, the design method, and an evaluation method for the background noise level. We have conducted wind tunnel tests and numerical simulations with several types of designs and obtained an effective shape to minimize the torque from the wind. The designed torque-less wind shield has lower ground tilt noise than typical-shape wind shields by one order of magnitude. This will enable us to achieve a more than 90% noise-free condition during an observation span, even for the most windy conditions on the Martian surface.

© 2014 Elsevier Ltd. All rights reserved.

1. Introduction

Seismic observations on other planets are expected to greatly expand our knowledge of their structure and tectonic activity as well as their thermochemical evolution. Even though Mars is one of the richest celestial bodies in terms of exploration data among the solar system (except for the Earth), most of the data are related to the surface composition. A large amount of information is available for the deep inner structure based on gravity observations and surface soil property data. With the constraints of mean density, gravity, and moment of inertia data, the inferred radius of the core has an ambiguity of 400 km, and the size is estimated as 1600 ± 200 km (Khan and Connolly, 2007; Sohl and Spohn, 1997; Spohn et al., 2001; Rivoldini et al., 2011). The differences in the Martian core state are reflected in long-period (dozens of seconds to thousands of seconds) seismic waves. Seismic observation of the planet is considered to be an effective way of providing constraints and insights into the planet's interior and dynamics. Through the NASA Apollo project, the first extraterrestrial seismic observation was achieved on the Moon. The Apollo installed five seismometers

on the Moon. As a result of the observations, we have a detailed lunar interior diagram (e.g. Nakamura, 1982; Lognonné et al., 2003). To further constrain the interior of Mars, seismic observation on Mars is important research (Khan and Connolly, 2007).

For seismometer observation on Mars, there exist several difficult technical problems to overcome. They are mostly due to the severe environments of Mars such as an extremely wide range of temperature variation, high-intensity cosmic ray radiation, ultraviolet irradiation, and strong surface wind. The wind period can be dozens of seconds to thousands of seconds. The long period corresponds to the seismic wave period for the Martian core. Thus, the strong wind on Mars causes serious problems in seismic observations, in particular for long-period wave observation.

Mars is known to have windy environments. The maximum Martian wind speed was calculated up to 80 m/s by cloud tracking at an altitude above 30 km (Kaydash et al., 2006), while the surface wind was measured by the landers Viking (Murphy et al., 1990) and Phoenix. Sandstorms called “dust devils” occur periodically, which is also a feature of Mars (Lorenz, 2013). These data show that the Martian surface wind has a regular daily variation in speed and direction. A maximum average wind speed of 16 m/s during the daytime at the Phoenix Lander site was reported (Holstein-Rathlou et al., 2010). On the surface of Mars, many aeolian features have been identified in high-resolution images, such as dunes, yardangs, streaks, sand sheets, and dust devil tracks

* Corresponding author at: Department of Earth and Planetary Science, The University of Tokyo, 7-3-1 Hongo Bunkyo-ku, Tokyo 113-0033, Japan.
Tel.: +81 3 5841 5666.

E-mail address: akasa@eri.u-tokyo.ac.jp (Y. Nishikawa).

(Fenton et al., 2005; Hayward et al., 2009). Fenton et al. estimated that the potential sand transports on the floor of the Proctor Crater are indicative of surface winds over 20 m/s. On the surface of sloped ground, a much higher wind velocity is estimated (Toyota et al., 2011). They simulated Martian surface winds from the distribution and time-variation of the specific dark wind streaks at Pavonis Mons. They concluded that the velocity can reach values of 40–50 m/s.

As discussed previously, the effect of wind is not negligible for broadband seismic observations on Mars. The Viking seismometer could not detect marsquakes because of the location of the seismometer and the strong Martian winds. It was placed on top of the lander, and the lander was shaken by the winds. Thus, the seismometer had not worked as a seismometer but much as a wind sensor (Anderson and Miller, 1977; Lorenz, 2012). The failure of the Viking seismic observation should be an important lesson for us. We are facing an urgent need to protect Martian seismometers from wind. Even if we put the seismometer directly on the ground, the effects of wind still exist. The best way to protect a seismometer from winds and extreme temperatures is to locate the seismometer in a calm place like a vault. If possible, we would locate the seismometer in a seismic vault, but it is technologically difficult. We investigated a realistic suggestion to protect the seismometer. Covering the seismometer with a wind shield is a very simple and powerful way to protect the seismometer from winds. The InSight mission uses a wind shield too (Yana et al., 2014). A wind shield over the seismometer would be indispensable to reducing the effect of wind if we install the sensor on the surface (Lognonné et al., 1996). In order to evaluate the effectiveness of the wind shield, they performed three tests. They deployed a seismometer in a seismic vault and another outside of the seismic vault on the ground surface, both utilizing a simplified prototype of the wind shield. A third seismometer was deployed directly on the surface (without a shield). They measured the seismic noise in these three situations. The seismic noise under the shield was one digit smaller than that without the shield. The noise spectral amplitude on the vertical component reached a level less than $2 \times 10^{-9} \text{ m/s}^{-2}/\text{Hz}^{1/2}$, which is very close to the Martian expected Low Noise Model (mentioned in Lognonné et al., 1996). The wind shield prevented the seismometer from shaking due to surface winds. They used only a simplified prototype of the wind shield, but the flow-induced effect depends on the shape of the wind shield. In particular, dynamic pressure on the wind shield generates torque, and the ground is pushed and inclined by the torque. This inclination potentially influences the observation results for marsquakes. We should optimize the size, shape, and weight of the wind shield to fit the seismometer and mission payload.

This paper focuses on the efficiency of the shape of the wind shield; thus, we fixed the size and weight of the wind shield. We report wind forces acting on the wind shields by using wind tunnel tests and CFD (computational fluid dynamics) simulations under limited conditions (low atmospheric pressure and high wind speed). First, we conducted a wind tunnel test under atmospheric pressure, which is relatively high compared to Martian pressure ($\sim 0.2 \text{ atm}$), for two extreme cases in terms of the wind shield shape. This was done to study the behavior of the wind shields against wind and pressure variations. Then, we ran numerical simulations under the same conditions as the wind tunnel tests using CFD to test the consistency between the numerical simulations and the experiments. Though CFD is a well-accepted method of simulating fluid behaviors, this is usually used for higher pressures compared to our settings, and we need to verify its capability to simulate low atmospheric pressure. Next, we used CFD to simulate the low atmospheric pressure of Mars to search in the parameter space to design an efficient shape for the wind shield. Finally, we tested our designed wind shield in a wind

tunnel test to evaluate its efficiency, again in a $\sim 0.2 \text{ atm}$ condition. On the basis of the results, we present an effective shape for the wind shield of the seismometer.

2. Wind shield development

2.1. Design principles

The wind shield for the Martian seismometer was designed according to the following steps. We fixed the size: 40 cm in diameter, 16 cm in height, and 1 kg in weight (without seismometer). The size is sufficient to contain the Martian seismometer that is under development based on the high-sensitivity borehole seismometer (one vertical axis seismometer 14 cm in diameter and 12 cm in height, Araya et al., 2007). We assumed the weight of the wind shield as 1 kg; a robotic arm from a Martian rover can carry this payload (Trebi-Ollennu et al., 2005). We selected an effective design for the shield so as to minimize wind effects. Wind tunnel tests and numerical simulations have been adopted in this research. The validity of our numerical simulation is ensured by the wind tunnel tests results (although the parameters of the wind tunnel are limited). Conducting many wind tunnel tests to optimize the wind shield would not be very efficient. Because of the validation, we can design the wind shield easily under more realistic Martian environments.

We focused on the lift force and torque generated by the wind because a large lift force and torque can slide the shield and strain the ground, respectively, which will be a main source of noise for seismometers (Fig. 1).

2.2. Wind tunnel test

We used a planetary environment wind tunnel facility at JAXA/ISAS in Sagami-hara. The wind tunnel generates high-speed winds under various atmospheric pressures: 10–30 m/s, 0.1–1.0 atm (Mars: 0–50 m/s, 0.005–0.01 atm). With the representative dimension of the wind shield being 40 cm, the corresponding Reynolds number is less than 4000. In the wind tunnel, we put a wind shield on a table and measured the weight with three sets of load cells (Fig. 2) by changing the atmospheric pressure from 0.1 to 0.3 atm and the wind velocity from 13 to 27 m/s. Note that this test does not represent the Martian condition. The wind tunnel we used was not capable of injecting winds at low atmospheric pressure. Thus, the tests were run to understand the behavior of the wind shields against wind and pressure variations, which will then be used to extrapolate the Martian conditions through numerical simulations. The lift force was calculated from the difference in the original weight and the sum of the three loads. The torque is calculated from the difference between the two front loads and the back loads (a negative torque value means a roll over to the upflow direction).

We conducted wind tunnel tests to evaluate the lift force and the torque as a function of the wind speed. We measured the

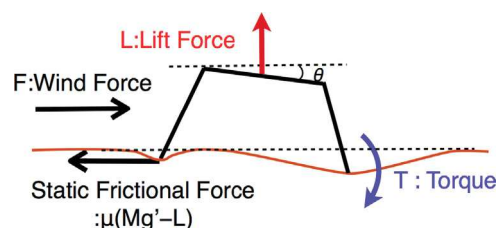


Fig. 1. Forces related to wind shield design. The lift force reduces the static frictional force. Large wind forces and small static frictional forces slide the wind shield. The torques strain the ground. Large strains generate ground tilt, which creates noise in seismic observations.

output of the load cells with 100 Hz sampling and 16-bit resolution. We used two typical designs for the shields: one is a semispherical shield (Fig. 3) and the other is a circular truncated cone (Fig. 4).

The results of the wind tunnel test are shown in Tables 1 and 2. The errors (σ) are estimated by the standard deviation of 200 samples (root of variance).

The lift forces and the torques are plotted in Figs. 5 and 6, respectively, as functions of the dynamic pressure $\frac{1}{2}\rho U^2$, where ρ is the atmospheric density (calculated by the equation of state for an ideal gas), and U is the wind velocity. Both of them seem to change proportionally to $\frac{1}{2}\rho U^2$. We fitted the observed lift forces and torques by using the least square method. We determined the proportional coefficient in this relation, and we found the lift force and the torque coefficient C (C_L and C_T are the coefficients for the

lift force and torque, respectively):

$$L \text{ (N)} = \frac{1}{2}\rho U^2 \times S \times C_L, \quad (1)$$

$$T \text{ (N m)} = \frac{1}{2}\rho U^2 \times S \times D \times C_T, \quad (2)$$

where L is the lift force, T is the torque, S is the circular area of the shield, and D is the diameter of the shield. As a result of the fitting, we obtained $C_{L(\text{semi})} = 3.2 \times 10^{-1}$ for the semispherical wind shield and $C_{L(\text{trun})} = 2.1 \times 10^{-1}$ for the truncated circular cone wind shield, whereas $C_{T(\text{semi})} = -0.80 \times 10^{-2}$ for the semisphere and $C_{T(\text{trun})} = 3.2 \times 10^{-2}$ for the truncated circular cone. We could evaluate the performance of these wind shields by comparing these coefficients C (Table 3).

2.3. Numerical simulation

We also evaluated the effect of wind on the shields by numerical simulation. We calculated the incompressible flow with the finite volume method by OpenFOAM, which is a free, open-source CFD software (www.openfoam.com/). We calculated the surface pressure on the wind shields with the same parameters that represent the wind tunnel test we performed. The torque (T) is equal to the sum of the outer product of p and d :

$$T = \int (p \vec{n}) \times \vec{d} dS, \quad (3)$$

where p , \vec{n} , and \vec{d} are the surface pressure of the shield, the unit normal vector to the surface of the wind shield, and the positional vector, respectively. Figs. 7 and 8 show the differential pressure between the average atmospheric pressure in the tunnel and the surface pressure on the wind shield. The shield's surface has a -30 to 20 Pa differential pressure. Negative pressure means that the shield is pulled by the wind, and positive pressure means that the shield is pushed by the wind. The negative pressure is distributed at the upstream side of the shield top and side flanks. These correspond to the locations where aim flow separation from the surface occurs.

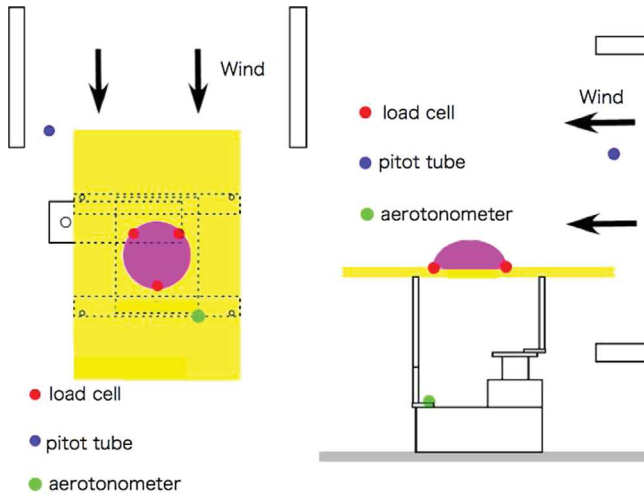


Fig. 2. Geometry of the wind tunnel facility: (left) top view above and (right) side view. The size of the table is 1 by 1.5 m. The diameter of the wind tunnel is 2 m. We measured the weight of the wind shield at the three points. They are arranged in a equilateral triangle.



Fig. 3. Semisphere wind shield: (left) top view and (right) side view. This stainless-steel wind shield is 40 cm in diameter and 16 cm in height.



Fig. 4. Truncated circular cone wind shield from (left) above and (right) side. This stainless-steel wind shield is 40 cm in diameter and 16 cm in height.

Table 1

Semispherical shield's wind tunnel test results (average lift force and torque) with errors. These values are proportional to the pressure and the square of the wind velocity.

Test conditions		Lift force (N)	Torque (N m)
Pressure (atm)	Wind velocity (m/s)		
0.1	13	0.38 ± 0.15	-0.014 ± 0.006
	20	0.93 ± 0.34	-0.010 ± 0.016
	27	1.82 ± 0.18	-0.015 ± 0.009
0.2	13	0.65 ± 0.12	-0.008 ± 0.006
	20	1.74 ± 0.31	-0.012 ± 0.017
	27	3.60 ± 0.18	-0.034 ± 0.009
0.3	13	0.90 ± 0.20	-0.016 ± 0.010
	20	2.81 ± 0.21	-0.026 ± 0.011

Table 2

Circular truncated cone shield's wind tunnel test results (average lift force and torque) with errors. These values are proportional to the pressure and the square of the wind velocity.

Test conditions		Lift force (N)	Torque (N m)
Pressure (atm)	Wind velocity (m/s)		
0.1	13	0.28 ± 0.27	0.024 ± 0.005
	20	0.77 ± 0.23	0.052 ± 0.009
	27	1.18 ± 0.18	0.077 ± 0.013
0.2	13	0.42 ± 0.31	0.033 ± 0.005
	20	1.09 ± 0.34	0.070 ± 0.030
	27	2.47 ± 0.17	0.140 ± 0.020
0.3	13	0.61 ± 0.21	0.047 ± 0.006
	20	1.72 ± 0.20	0.102 ± 0.013

The torque coefficient of the semispherical shield $C_{T(semi)}$ is -0.68×10^{-2} , whereas the coefficient of the circular truncated cone shield $C_{T(trun)}$ is 2.98×10^{-2} . These are nearly equal to those obtained in the wind tunnel tests ($-0.80 \pm 0.08 \times 10^{-2}$ and $3.23 \pm 0.12 \times 10^{-2}$, respectively, as in Table 3). This means that these numerical simulations are valid in these situations. We expanded these situations to the Martian situation by using the validated numerical simulation to design an effective wind shield.

2.4. Designing an effective wind shield

Under our size-fixed condition, the maximum horizontal noise is about $2 \times 10^{-10} \text{ m/s}^2/\text{Hz}^{1/2}$ in a stormy situation (we describe the situation below). Even in the stormy situation, the horizontal noise is smaller than the seismometer sensitivity ($2.0 \times 10^{-9} \text{ m/s}^2/\text{Hz}^{1/2}$) by one order of magnitude. Furthermore, the horizontal drag force is a proportional value of the dynamic pressure and the wind shield's impact area. Under our condition, the impact area changes by only 25%. This means that the horizontal noises differ due to not the wind shield shape but its scale. The torque coefficient changes by more than 400% because of its shape dependence. Therefore, in this paper, we focus on and estimate only vertical ground tilt noise. The difference in the torque direction is evident between the two designs. The semispherical shield rolled over to the upstream direction, while the circular truncated cone shield rolled over to the downstream direction. Therefore, a combination of these designs is expected to minimize the torque and the vertical noise. We combined two shapes in various proportions in the numerical simulations. Finally, we obtained a wind shield with almost zero torque (Figs. 9 and 10). The side from the bottom to 6 cm in height is made up of the circular truncated cone, and from 6 cm in height to the top (16 cm height) is made up of the semisphere. The diameters of the bottom and the top are 40 cm and 21.5 cm, respectively. $C_{T(costume)}$ for this designed shield is -1.0×10^{-3} (Table 3). The designed shape is eight times

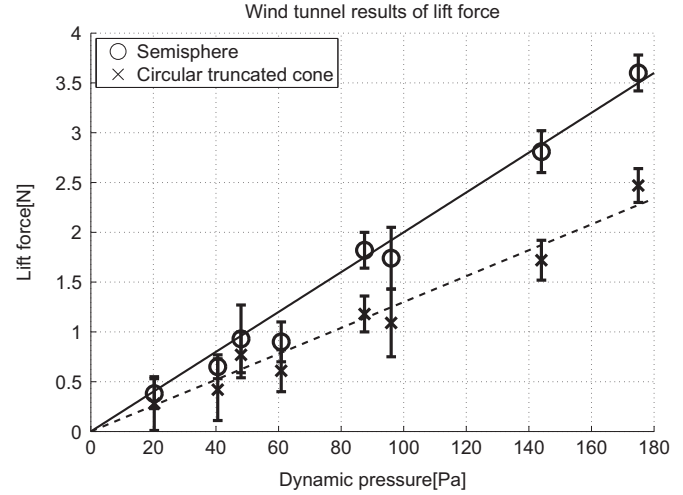


Fig. 5. Wind tunnel results for the lift forces. Using the least square method, we find the proportional relationship between the lift force and dynamic pressure. The lift forces increase with increasing dynamic pressure. Thus, the large dynamic pressure reduces the weight of the wind shield and moves the wind shield.

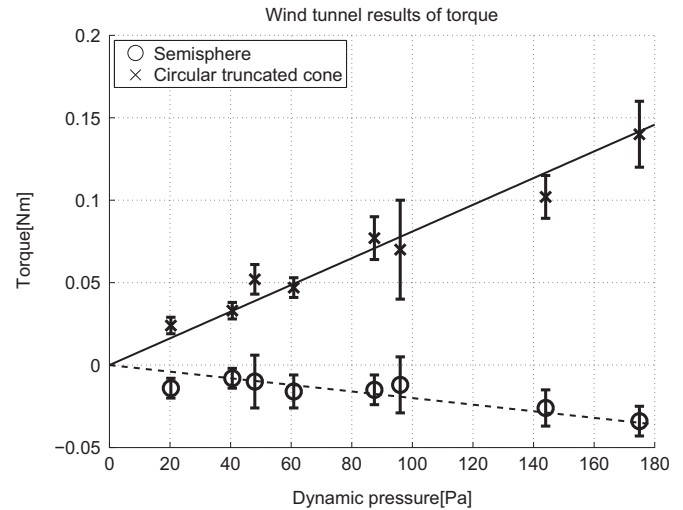


Fig. 6. Wind tunnel results for the torques. Using the least square method, we find the proportional relationship between the torque and dynamic pressure. Though both torques are proportional to the dynamic pressure, the torque directions are opposite. The semispherical wind shield is rolled up to the upstream direction, but the circular truncated cone wind shield is rolled up to the downstream direction.

more efficient than the semispherical shield and 30 times more efficient compared to the circular truncated cone shield based on the numerical simulation.

2.5. Discussion

2.5.1. Stability of the wind shield

We checked the absolute stability for the designed shield on Mars. First, we calculated the slide force

$$F_x = \int p \vec{e}_x \cdot d\vec{S}, \quad (4)$$

where F_x is the horizontal force that pushes the wind shield in the horizontal direction, and \vec{e}_x is the unit vector parallel to the wind flow direction. If F_x is larger than μN , the shield could move (μ is the coefficient of static friction, and N is the normal force). N is obtained from the difference between the shield weight (M) and

Table 3

Torque coefficients of the semispherical, circular truncated cone, and combined torque-less shields. The absolute value of the coefficient indicates the efficiency of the wind shield.

Shape	Condition	Torque coefficient (C_T)
Semisphere	Wind tunnel test	$-0.80 \pm 0.08 \times 10^{-2}$
	Numerical simulation	-0.68×10^{-2}
Circular truncated cone	Wind tunnel test	$3.23 \pm 0.12 \times 10^{-2}$
	Numerical simulation	2.98×10^{-2}
Designed torque-less	Wind tunnel test	$-0.19 \pm 0.10 \times 10^{-2}$
	Numerical simulation	-0.099×10^{-2}

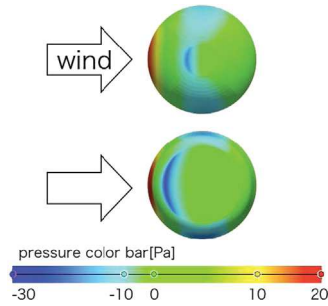


Fig. 7. Differential pressure distributions of the semisphere and truncated circular cone wind shield view from the top. These differential pressures are calculated under 0.1 atm and 20 m/s conditions.

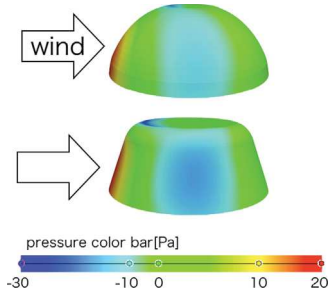


Fig. 8. Differential pressure distributions of the semisphere and truncated circular cone wind shield view from the side. These distributions are calculated under 0.1 atm and 20 m/s conditions.

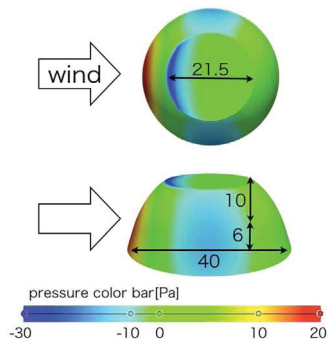


Fig. 9. Differential pressure distribution of the designed wind shield. The size is the same as the typical wind shield (40 cm in diameter and 16 cm in height). We shaped the lower 6 cm as a circular truncated cone, and the upper 10 cm is semispherical. This differential pressure distribution cancels the torques and reduces ground tilt.

lift force (L):

$$N = M \times g' - L, \quad (5)$$



Fig. 10. We conducted a wind tunnel test with the designed wind shield designed by combining the semisphere and the truncated circular cone wind shields. The results are consistent with the simulation results.

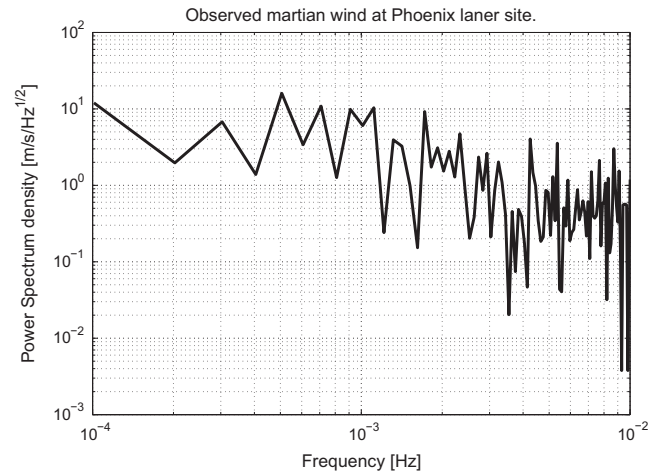


Fig. 11. Martian wind data at Phoenix landing site (location: E125.7 N68.2, sampling: 50 s, local time: daytime on Mars, average velocity: 5.1 m/s). The observation data has a high amplitude in the range around 10^{-3} Hz.

where g' is the gravity on Mars (3.71 m/s^2). The results of the numerical simulation for the designed shield were

$$F_x = \frac{1}{2} \rho U^2 \times S \times C_d, \quad (6)$$

$$L = \frac{1}{2} \rho U^2 \times S \times C_L, \quad (7)$$

where C_d is the drag coefficient of the horizontal direction force. Therefore, the stability condition is given as follows:

$$F_x < \mu N = \mu(Mg' - L). \quad (8)$$

The stability of the wind shield depends on the wind velocity, the weight of the wind shield, and the static frictional coefficient. One of the windy places is Pavonis Mons because of its slope wind. The strong wind speed is up to 50 m/s (Toyota et al., 2011). We calculated the static frictional coefficient of Martian soil from Martian regolith properties (Golombek et al., 2008) as $\mu = 0.42 \pm 0.15$; if we assume these values as typical Martian properties, the maximum wind speed to meet this stability condition is $U < 67.5 \pm 8.7 \text{ m/s}$. The speed is comparable to the strongest wind speed on the surface of Mars.

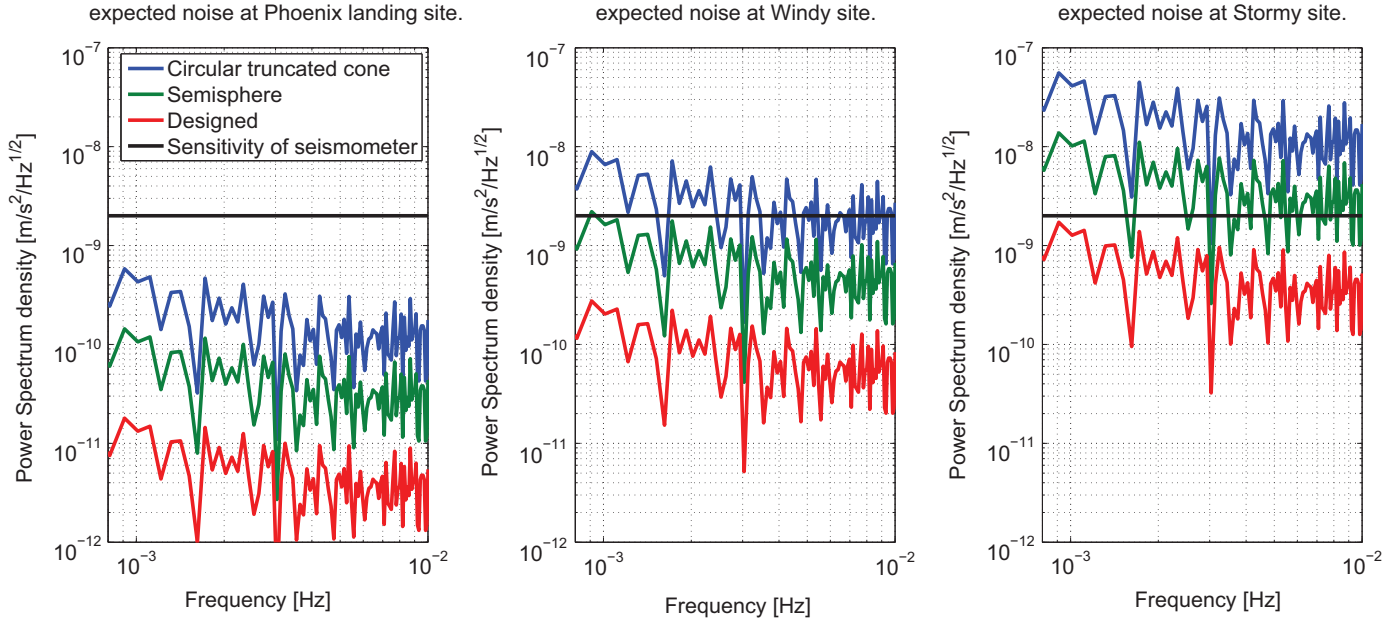


Fig. 12. Expected noise and sensitivity of the seismometer. The sensitivity of the seismometer is a requirement of the InSight mission seismometer. The ground tilt would be a noise source if the expected noise exceeds the sensitivity. The average wind velocities are 5.1 m/s, 20 m/s, and 50 m/s at the Phoenix landing site, the windy site, and the stormy site, respectively. In the windy and stormy conditions, only the designed shield is effective for protecting the seismometer.

2.5.2. Tilt noise

We estimated the ground tilt imposed by the torque on the designed shield. We assumed the Martian ground to be a semi-infinite elastic body to calculate the ground strain. We have many possibilities of noise on Mars, but in this research, we focus on only one vertical component. We calculate the settlement of the shelter as

$$\Delta H_E = I_G \frac{1-\nu^2}{E} \Delta q B, \quad (9)$$

where H_E is the ground settlement (deformation of the surface ground), I_G is the settlement factor, ν is Poisson's ratio of the ground, E is Young's modulus of the ground, q is the stress from the feet of the wind shield, and B is the diameter of the legs. In this paper, we assume the Martian ground to be a semi-infinite elastic body with Young's modulus of $E = 9.5 \times 10^7$ N/m² and Poisson's ratio of $\nu = 0.264$ (ref: P. Lognonné and F. Karakostas, personal communication). Three circular feet 4 cm in diameter support the wind shield (settlement factor is $I_G = 1.0$ for a circular ground contact area). Using Eq. (2), we get the differential stress Δq :

$$\Delta q = \frac{\Delta F}{S_c} = \frac{C_T \cdot \frac{1}{2} \rho U^2 \cdot S}{D} \frac{1}{(B/2)^2 \pi}, \quad (10)$$

where S_c is the ground contact area of the leg. We obtain the tilt noise N_{tilt} as follows:

$$\begin{aligned} N_{\text{tilt}} &= g_{\text{Mars}} \Delta \theta \\ &= g_{\text{Mars}} \frac{\Delta H_E}{D} \\ &= \frac{I_G g_{\text{Mars}} (1-\nu^2) C_T \cdot \frac{1}{2} \rho U^2 \cdot S \cdot B}{D^2 \times E (B/2)^2 \pi}. \end{aligned} \quad (11)$$

So far, we have calculated these lift forces, torques, and torque coefficients for a constant velocity. In the case of ground tilt noise, we should estimate them as a function of frequency. We probed the frequency response of the wind shields, and we did not find

any frequency dependences in the 0.01–10 Hz range. We estimate the efficiency of the wind shields by comparing the seismometer sensitivity with the tilt noise. If the expected tilt noise is higher than the sensitivity of the seismometer, the tilt noise would be recorded as an observation noise. Thus, we need Martian wind spectrum data to calculate the tilt noise as a function of frequency. We used observed wind data from Phoenix (Fig. 11). We calculated the tilt noise using three wind models. One is the observed wind data from Phoenix, and the others are models based on the observation data; one is for a windy situation, and another is for a stormy situation [average wind velocities are 20 m/s and 50 m/s (ref: MCD, Mars Climate Database, <http://www-mars.lmd.jussieu.fr>)]. Finally, we plot the expected tilt noise and Martian seismometer sensitivity requirement for the InSight mission (Mimoun et al., 2012) at the windy site and the stormy site (Fig. 12). Only the designed shield's noise is lower than the threshold detection of the InSight seismometer requirement in the windy situation (Fig. 12, left); even in a stormy situation, the tilt noise is almost lower than the threshold requirement (Fig. 12, right). When the ground tilt noise level is lower than the threshold level of the seismometer sensitivity, we call the span a noise-free period. We estimated the tilt-noise-free periods realized with our optimized wind shield. We made a simple wind model using a Weibull distribution. The probability of wind velocity for each average wind velocity is given by the equation

$$f(V) = \left(\frac{k}{c}\right) \left(\frac{V}{c}\right)^{k-1} \exp\left\{-\left(\frac{V}{c}\right)^k\right\}, \quad (12)$$

where $f(V)$ is the probability of the wind velocity V (m/s), c is a scale parameter, and k is a shape parameter. The scale parameter c is calculated from the average wind velocity \bar{V} , shape parameter k , and gamma function Γ :

$$c = \frac{\bar{V}}{\Gamma\left(1 + \frac{1}{k}\right)}. \quad (13)$$

The tilt noise is dependent on the k value and the average wind velocity. In this paper, k is 1.5 (Lorenz, 1996). Because of the

Table 4

Ratio of noise-free period. This ratio indicates the efficiency of the wind shields. The improvement introduced by the new design is particularly significant for higher-wind environments.

Average wind velocity (m/s)	5	10	20
Circular (%)	75.2	39.4	16.4
Semisphere (%)	97.9	75.5	39.6
Designed (%)	99.9	99.8	90.0

evaluation on the MCD, the average global surface wind velocity is around 20 m/s, so \bar{V} is assumed to be 5, 10, and 20 m/s for the calm, normal, and windy cases, respectively. We cannot detect noise if it drops below a threshold level (the level is based on the sensitivity of the InSight mission seismometer), and we consider the term as a noise-free period. Then, we integrated the probability of a noise-free period situation, and we got the ratio of the noise-free period (Table 4).

In this way, we evaluate the efficiency of the wind shields. The results suggest that the designed wind shield is efficient, especially in windy situations.

3. Conclusion

We designed a torque-less wind shield for broadband seismic observations using wind tunnel tests and CFD simulations. We focused on the lift force and torque as important factors for designing the wind shield for Martian broadband seismic observations. We conducted wind tunnel tests and numerical simulations to evaluate the lift forces and torques as functions of wind speed and air density. We found that the proportional relationship, lift forces, and torques change linearly with the dynamic pressure. We confirmed the numerical simulations in the wind tunnel test results. We combined a circular truncated cone shield and a semispherical shield for optimizing the wind shield under our fixed conditions. We designed an effective torque-less wind shield for broadband seismic observation in windy environments on Mars and decreased the noise level for the observation of broadband marsquakes caused by Martian wind. The designed torque-less wind shield keeps a stable position in the strongest wind environment on Mars, and the noise-free periods of the designed wind shield are smaller than a typical wind shield's noise by one order of magnitude. In the results, the ground noiseless span more than doubled in a windy environment. We also developed a new evaluation method for the background noise level excited by wind.

Acknowledgments

We would like to thank Mr. S. Nonaka, M. Anyouji, and W. Fukuda for supporting our wind tunnel tests at JAXA/ISAS. Also, we wish to thank Dr. T. Hirobe for performing the CFD simulations. Lastly, we thank Dr. H. Shiraishi for helpful discussions. This research was

supported by a Grant for the Global COE program “From the Earth to ‘Earths’” from the Ministry of Education, Culture, Sports, Science and Technology of Japan.

References

- Anderson, D., Miller, W., 1977. Seismology on Mars. *J. Geophys. Res.* 82 (28), 4524–4546.
- Araya, A., Sekiya, K., Shindo, Y., 2007. Laser-interferometric broadband seismometer for ocean borehole observations. In: *Proceedings of International Symposium on Underwater Technology*. IEEE, Tokyo, pp. 245–248.
- Fenton, L.K., Toigo, A.D., Richardson, M.L., 2005. Aeolian processes in proctor crater on mars: Mesoscale modeling of dune-forming winds. *J. Geophys. Res.: Planets* (1991–2012) 110(E6).
- Golombek, M., Haldemann, A., Simpson, R., Fergason, R., Putzig, N., Arvidson, R., Bell III, J., Mellon, M., 2008. Martian surface properties from joint analysis of orbital, earthbased, and surface observations. In: *The Martian Surface-Composition, Mineralogy, and Physical Properties*, vol. 1, p. 468.
- Hayward, R.K., Titus, T.N., Michaels, T.L., Fenton, L.K., Colaprete, A., Christensen, P.R., 2009. Aeolian dunes as ground truth for atmospheric modeling on mars. *J. Geophys. Res.: Planets* (1991–2012) 114 (E11).
- Holstein-Rathlou, C., Gunnlaugsson, H.P., Merrison, J.P., Bean, K., Cantor, B., Davis, J., Davy, R., Drake, N., Ellehoj, M., Goetz, W., et al., 2010. Winds at the phoenix landing site. *J. Geophys. Res.: Planets* (1991–2012) 115(E5).
- Kaydash, V., Kreslavsky, M., Shkuratov, Y.G., Videen, G., Bell III, J., Wolff, M., 2006. Measurements of winds on mars with hubble space telescope images in 2003 opposition. *Icarus* 185 (1), 97–101.
- Khan, A., Connolly, J., 2007. Constraining the composition and thermal state of mars from inversion of geophysical data. *LPI Contrib.* 1353, 3013.
- Lognonné, P., Beyneix, J., Banerdt, W., 1996. Ultra broad band seismology on InterMarsNet. *Planet. Space Sci.* 44 (11), 1237–1249.
- Lognonné, P., Gagnepain-Beyneix, J., Chenet, H., 2003. A new seismic model of the moon: implications for structure, thermal evolution and formation of the moon. *Earth Planet. Sci. Lett.* 211 (1), 27–44.
- Lorenz, R.D., 1996. Martian surface wind speeds described by the weibull distribution. *J. Spacecr. Rockets* 33 (5), 754–756.
- Lorenz, R.D., 2012. Planetary seismology expectations for lander and wind noise with application to venus. *Planet. Space Sci.* 62 (1), 86–96.
- Lorenz, R., 2013. The longevity and aspect ratio of dust devils: effects on detection efficiencies and comparison of landed and orbital imaging at mars. *Icarus* 226 (1), 964–970.
- Mimoun, D., Lognonné, P., Banerdt, W.B., Hurst, K., Deraucourt, S., Gagnepain-Beyneix, J., Pike, T., Calcutt, S., Bierwirth, M., Roll, R., Zweifel, P., Mance, D., Robert, O., Nbut, T., Tillier, S., Gabsi, T., Laudet, Ph., Kerjean, L., Perez, R., Giardini, D., Christensen, U., Garcia, R., 2012. the SEIS Team, The insight SEIS experiment. In: *The 43rd Lunar and Planetary Science Conference Abstract* 1493.
- Murphy, J.R., Leovy, C.B., Tillman, J.E., 1990. Observations of martian surface winds at the viking lander 1 site. *J. Geophys. Res.: Solid Earth* (1978–2012) 95 (B9), 14555–14576.
- Nakamura, Y., 1982. Apollo lunar seismic experiment: final summary. *J. Geophys. Res.* 87 (2), A117–A123.
- Rivoldini, A., VanHoolst, T., Verhoeven, O., Mocquet, A., Dehant, V., 2011. Geodesy constraints on the interior structure and composition of mars. *Icarus* 213 (2), 451–472.
- Sohl, F., Spohn, T., 1997. The interior structure of Mars: implications from SNC meteorites. *J. Geophys. Res.: Planets* 102, 1613–1635.
- Spohn, T., Acuña, M., Breuer, D., 2001. Geophysical constraints on the evolution of mars. *Space Sci. Rev.* 96, 231–262.
- Toyota, T., Kurita, K., Spiga, A., 2011. Distribution and time-variation of spire streaks at Pavonis mons on mars. *Planet. Space Sci.* 59 (8), 672–682.
- Trebi-Ollennu, A., Baumgartner, E.T., Leger, P.C., Bonitz, R.G., 2005. Robotic arm in-situ operations for the mars exploration rovers surface mission. In: 2005 IEEE International Conference on Systems, Man and Cybernetics, vol. 2. IEEE, Hilton Hotel, Waikoloa, HI, USA, pp. 1799–1806.
- Yana, C., Kerjean, L., Sylvestre-Baron, A., Baroukh, J., Nonon, M., Laudet, P., Weinstein-Weiss, S., Morales, L., Aguinaldo, A.M., Dubon, L., et al., 2014. Operations of the SEIS Seismometer Onboard the 2016 Insight Mission.

ANNEXE3

MARS' BACKGROUND FREE OSCILLATIONS

Mars' Background Free Oscillations

Y. Nishikawa¹ · P. Lognonné¹ · T. Kawamura¹ ·
A. Spiga² · E. Stutzmann³ · M. Schimmel⁴ ·
T. Bertrand⁵ · F. Forget² · K. Kurita⁶

Received: 18 June 2018 / Accepted: 7 January 2019
© Springer Nature B.V. 2019

Abstract Observations and inversion of the eigenfrequencies of free oscillations constitute powerful tools to investigate the internal structure of a planet. On Mars, such free oscillations can be excited by atmospheric pressure and wind stresses from the Martian atmosphere, analogous to what occurs on Earth. Over long periods and on a global scale, this phenomenon may continuously excite Mars' background free oscillations (MBFs), which constitute the so-called Martian hum. However, the source exciting MBFs is related both to the global-scale atmospheric circulation on Mars and to the variations in pressure and wind at the planetary boundary layer, for which no data are available.

To overcome this drawback, we focus herein on a global-scale source and use results of simulations based on General Circular Models (GCMs). GCMs can predict and reproduce long-term, global-scale Martian pressure and wind variations and suggest that, contrary to what happens on Earth, daily correlations in the Martian hum might be generated by the solar-driven GCM. After recalling the excitation terms, we calculate MBFs by using GCM computations and estimate the contribution to the hum made by the global atmospheric circulation. Although we work at the lower limit of MBF signals, the results indicate that the signal is likely to be periodic, which would allow us to use more efficient stacking theories than can be applied to Earth's hum. We conclude by discussing the perspectives for the In-

The InSight Mission to Mars II
Edited by William B. Banerdt and Christopher T. Russell

✉ Y. Nishikawa
nishikawa@ipgp.fr

- ¹ Institut de Physique du Globe de Paris, Sorbonne Paris Cité, Université Paris Diderot, Paris, France
- ² Laboratoire de Météorologie Dynamique (LMD/IPSL), Sorbonne Université, Centre National de la Recherche Scientifique, École Polytechnique, École Normale Supérieure, Paris, France
- ³ Institut de Physique du Globe de Paris, CNRS-UMR 7580, University Paris 7, Paris, France
- ⁴ Institute of Earth Sciences Jaume Almera – CSIC, Barcelona, Spain
- ⁵ Ames Research Center, National Aeronautics and Space Administration (NASA), Mountain View, CA, USA
- ⁶ Earthquake Research Institute, The University of Tokyo, Tokyo, Japan

Sight SEIS instrument to detect the Martian hum. The amplitude of the MBF signal is on the order of nanogals and is therefore hidden by instrumental and thermal noise, which implies that, provided the predicted daily coherence in hum excitation is present, the InSight SEIS seismometer should be capable of detecting the Martian hum after monthly to yearly stacks.

Keywords Mars · Planetary free oscillation · GCM · Seismometer · Normal mode · InSight

1 Introduction

When a large earthquake occurs, seismic waves propagate around the entire planet for tens of hours following the event. These waves can generate standing oscillations if they fulfill the boundary conditions for specific frequencies; the standing modes are referred to as Earth's free seismic oscillations and their associated frequencies are called Earth's seismic eigenfrequencies.

The first search for Earth's free oscillations started in the late 1950 (Benioff et al. 1959) these oscillations were first observed following the great Chilean earthquake of May 1960 (Benioff et al. 1961). Further developments in long-period seismometers and global networks then allowed the normal mode frequencies to be determined, and this information was used to invert the structure models of Earth's interior, including the famous Preliminary Earth Reference Model (Dziewonski and Anderson 1981). Further inversions were done by using the splitting properties of the normal modes, which provided three-dimensional models of the Earth's structure. Woodhouse and Deuss (2015); Laske and Widmer-Schmidrig (2015); Montagner (2015) and Romanowicz and Mitchell (2015), provide an extensive description of observations of Earth's normal modes and their use in determining Earth's interior structure, while Dahlen and Tromp (1998) and Millot-Langet et al. (2002) provide a theoretical description of the same.

Thus, determining Mars' normal modes has been proposed as one of the overarching goals of a seismological mission to Mars from the early times of space exploration (Kovach and Anderson 1965; Bolt and Derr 1969) to Viking (Okal and Anderson 1978) as well as the more recent projects such as Mesur (Solomon et al. 1991), Intermarsnet (Lognonné et al. 1996) and NetLander (Lognonné and Giardini 2000). Several papers detail detection techniques have been detailed in several papers (Lognonné and Mosser 1993; Zharkov and Gudkova 1997; Gudkova and Zharkov 2004; Lognonné 2005; Lognonné and Johnson 2007, 2015). The detection of the normal modes of Mars is one of the goals of the upcoming seismic monitoring mission "InSight" which should land and deployment in 2019 and of the SEIS experiment (Tong and García 2015; Lognonné et al. 2019).

Planetary free oscillations constitute a powerful tool to investigate the internal structure of planets, as illustrated by Panning et al. (2017) with the synthetic inversion of the structure of the fundamental spheroidal normal modes. However making such long-term seismic observations on Mars obliges us to overcome several difficult problems.

One issue is related to Mars itself, which lacks plate tectonics and therefore is devoid of the large-magnitude quakes ($M > 7$) the type of which are generally used on the Earth to analyze the normal modes. All seismicity models of Mars (Phillips and Grimm 1991; Golombek et al. 1992; Knapmeyer et al. 2006) suggest that the largest quake annually is in the moment-magnitude range of 5.2–6 (i.e., 10^{17} to 10^{18} Nm). Larger quakes, although very rare, cannot be excluded.

The second difficulty is the seismic noise expected on the Martian surface, which is known to be subject to large variations in temperature and wind that generate long-period

noise much greater than anything measured in Earth's seismic vaults, where Earth's normal modes are typically observed. The InSight SEIS noise model, described in detail by Mismoun et al. (2016), suggests that, over long periods, most of the SEIS instrument noise will be related to the thermal noise, which is expected to grow below 10 mHz as $f^{-2.5}$, with amplitude at 10 mHz in the range of 1 to $2.5 \times 10^{-9} \text{ m s}^{-2} \text{ Hz}^{-1/2}$ depending on the local time. As shown by Lognonne et al. (2006), seismic signals would have larger amplitudes globally were a quake with a moment larger than $2 \times 10^{17} \text{ Nm}$ to occur on Mars. Even if such a moment corresponds to the upper limit of the annual predicted seismicity, the Poisson statistics of such a rare event suggests that several years of operation are required to attain a significant occurrence probability. Therefore, we consider herein the nonseismogenic sources of normal mode excitation.

One possible source of normal mode excitation comes from atmospheric phenomena (see Spiga et al. 2018, for a detailed review). Mars has a very active atmosphere, with weather processes generating high winds, dust devils, and storms (Read and Lewis 2004; Spiga and Forget 2009). Cloud tracking shows that Martian wind speeds easily reach 80 m/s above 30 km (Kaydash et al. 2006), whereas surface wind can be as high as 20 m/s, according to measurements by the Viking landers (e.g., Murphy et al. 1990). Measurements by the Martian landers also show that the Martian atmosphere has a regular diurnal cycle of wind and pressure (Schofield et al. 1997; Martínez et al. 2017).

The nonacoustic pressure variations associated with the global weather and the Reynolds stress associated with the wind, be it turbulent gusts in the planetary boundary layer (PBL) or high-altitude planetary-scale wind, all constitute forces to excite planetary free oscillations (Kobayashi and Nishida 1998b,a), with theoretical details in Tanimoto and Um (1999). Part of the excitation forces has frequencies within the bandwidth of the normal modes and that corresponds to the eigenfrequencies of Martian normal modes between 0.4 and 20 to 30 mHz. These particular excitation forces can globally and continuously excite the corresponding normal modes. This continuous excitation force is a possible source of Mars' background free oscillations (MBFs).

This idea for the observation of MBF was actually been suggested shortly after the first observation of Earth's background free oscillations (EBFs) (Suda et al. 1998). Oceanic excitation was initially proposed by Watada and Masters (2001). The first interpretations proposed that the entire excitation is produced by atmospheric turbulence in the Earth's PBL, which suggests that a simple scaling may exist between Earth and Mars (Kobayashi and Nishida 1998b,a). The seasonal variations in the continuous excitation later observed by Nishida et al. (2000) also support an atmospheric origin, while Tanimoto and Um (1999) proposed a simplified theory. However, the most recent studies show that the major source of continuous excitation on Earth is over the oceans (Tanimoto 2005; Rhie and Romanowicz 2004, 2006) and that, in this process, infragravity waves over the continental shelves are much more efficient seismic sources (Webb 2007) than atmospheric turbulence. However, excitation by atmospheric sources remains significantly below 5 mHz (Nishida 2013b). Note that coupled modes exist between the atmosphere and the solid earth (Lognonné et al. 1998b, 2016), and that pressure sources at the bottom of the ocean (Nishida 2014) cannot explain this larger excitation; instead, integrated atmospheric excitations at the base of Earth's atmosphere must be involved.

Observed EBFs are on the order of 0.5 nanogal ($1 \text{ nanogal} = 10^{-11} \text{ m s}^{-2}$) (Nishida 2013a) per individual mode. Stacking techniques can enhance the peak amplitude of normal modes to overcome instrument- and station-induced noise, which allows the mode eigenfrequencies to be determined. These eigenfrequencies may then be used to invert the internal structure as was done for quakes, as illustrated by Nishida et al. (2009). The same phenomenon should occur on Mars, meaning that the observation of MBFs should allow us to

determine the frequencies of fundamental spheroidal normal modes, which would constrain models for Mars' interior.

Kobayashi and Nishida (1998b) estimated the magnitude of MBFs by using a theoretical scaling based on the solar energy received by the planet (related to the planetary albedo and distance to Sun) and on the thickness of the PBL. They assumed that turbulence in the PBL provides the main excitation force for MBFs, which led them to estimate a free oscillation amplitude of several nanogals, a value quite close to that of Earth. Tanimoto (2001) estimated relative modal estimated the relative modal amplitude between Earth and Mars by using several parameters for the atmosphere and terrestrial part. Estimates of the MBF amplitude are about 30–50% of the EBFs. Lognonné (2005) and Lognonné and Johnson (2007) focused on very-long-period MBFs and, by using more realistic Martian-climate models and normal mode summations, produced MBF seismograms for periods ranging 300 to 400 s, which correspond to angular orders 12 to 15. This approach is based on the assumption that, for these very long periods and wavelengths, the major source of excitation is not Reynolds stresses or nonacoustic pressure related to the PBL, but the nonacoustic pressure related to global atmospheric circulation. They estimated the free-oscillation amplitude to be several hundredths of nanogals, which corresponds to amplitudes typically ten times smaller than those of EBFs of the same angular order.

The generation of seismic waves by atmospheric activity is not only associated with nonacoustic pressure acting on the surface, but also with the acoustic waves generated in the atmosphere and converted into seismic waves at the surface. Lognonné et al. (1998b), Watada and Kanamori (2010), and Lognonné et al. (2016) simplified this concept by demonstrating that the overall excitation in the atmosphere may be estimated based on the normal modes of the coupled solid-atmosphere system and on the atmospheric force volumetric density, which acts throughout the atmosphere and is subject to wind and nonacoustic pressure fluctuations. This approach requires integrating over the full atmospheric seismogenic volume to calculate the excitation force of the atmosphere. As shown more precisely by Lognonné et al. (1994) the latter is associated with seismic forces related to nonacoustic pressure and nonlinear Reynolds stresses in the atmosphere and can be expressed as

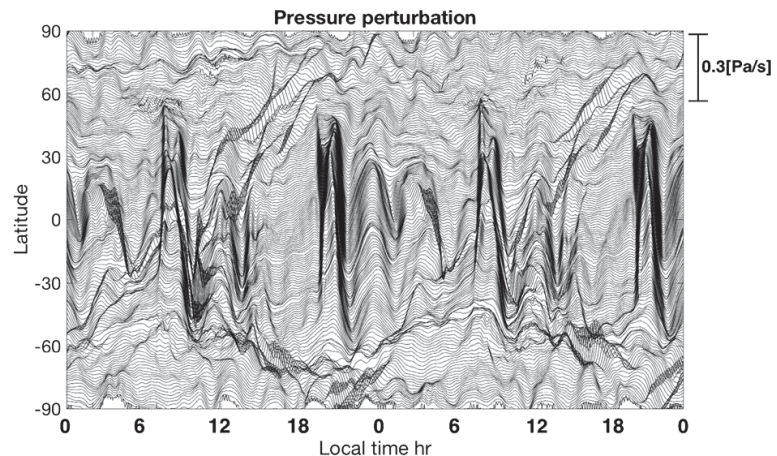
$$\Pi_i^j = -p_{glut}\delta_i^j - \rho v_i v^j, \quad (1)$$

where p_{glut} nonacoustic pressure, which is defined as $p_{glut} = p_{true} - p_{Hooke}$, where $p_{Hooke} = -\kappa \nabla \cdot \mathbf{v}$. \mathbf{v} is the atmospheric wind, ρ is atmospheric density, and p_{Hooke} is the pressure modeled by the Hooke pressure, which involves the linear model used in linear acoustics or seismology. Therefore, following the proposition made by Backus and Mulcahy (1976) for localized sources in Earth seismology and by Goldreich and Keeley (1977) for globally distributed sources in Solar seismology, we generalize here the concept of stress glut to the pressure induced by nonlinear Reynolds stresses that occur in the Martian PBL. This generalization considers that all true volumetric forces, apart from those generated by Hooke pressure, are source terms captured by the seismic moment of Eq. (1). Thus, we consider that the pressure glut and wind are respectively written as

$$p_{glut} = p_{glut,global} + p_{glut,PBL}, \quad \mathbf{v} = \mathbf{v}_{global} + \mathbf{v}_{PBL}. \quad (2)$$

Practically speaking, the wind and pressure glut associated with the PBL turbulence will be at much higher frequencies and on a smaller scale than those associated with the global circulation, but both will contribute to the overall excitation processes through Eq. (1). Therefore, the two estimates seem to provide the two end members of the general case, with

Fig. 1 Pressure fluctuations in Martian atmospheric simulated by LMD GCM for Mars meridian of longitude 0° . All pressure records are demeaned and only pressure variations are shown. Vertical axis is latitude; horizontal axis is local time [hr]. The largest pressure fluctuations occur at sunrise and sunset. The pressure fluctuations repeat to high-precision day after day. This strong daily repetition is not common on Earth



Lognonné and Johnson (2007) focusing on the global part of the excitation and Kobayashi and Nishida (1998b) focusing on the PBL part.

Major differences in PBL thickness exist between the Earth PBL, which ranges from 0.2 to 2 km and the Martian PBL, which is much thicker (about 5 to 6 km, typically) (Petrosyan et al. 2011; Spiga 2011). Because the speed of sound is less on Mars than on Earth (220 m/s compared with 340 m/s), the volumetric excitation is likely much more important on Mars than on Earth where, moreover, most of the energy of the atmospheric winds is transferred to oceanic waves, which then play a major role in the excitation of EBFs. In other words, the Earth view, where most EBF excitation may be modeled by invoking bottom-oceanic and near-surface forces, is not likely to be valid on Mars.

A first key difference is the important daily repetition of weather patterns on Mars, which is mostly related to the importance of solar flux and to the lack of a major source of other atmospheric energy, such as Earth's humidity and water. Although this initially appears in the temperature variations, which are fairly well represented by a Fourier series (see, e.g., Van Hoolst et al. 2003), it is also the case for the pressure field, as illustrated in Fig. 1, which shows the pressure variations at zero longitude as a function of local time and of latitude over two sols, as generated by a typical GCM. Such sol repetition also appears in the signal, when the latter is filtered in the frequency bandwidth of the normal modes. This is shown in Fig. 2, which corresponds to the signals of Fig. 1, but is filtered between 1 and 2 mHz (i.e., periods between 1000 and 500 s) and by Fig. 3, where the bandwidth is higher and corresponds to 2 to 3 mHz (i.e., periods between 330 and 500 s).

In this paper, we expand these past studies by using higher-resolution GCMs developed recently by the Laboratoire de Météorologie Dynamique (LMD) (see e.g., Forget and Lebonnois 2013) to better estimate normal mode amplitudes and to analyze whether the repeating atmospheric sources significantly impact the excitation of normal modes, including terms of stacking strategies. These GCMs can resolve all the large-scale Martian atmospheric processes and variabilities such as thermal tides, baroclinic waves, and planetary-scale waves (Haberle et al. 1999; Forget et al. 1999). Turbulent motions in the PBL are, by design, left unresolved in GCMs; their study requires large-eddy simulations (Spiga and Lewis 2010). This will not be included for the excitation force investigated herein [note that atmospheric excitation by small-scale turbulence in the PBL is addressed by Kenda et al. (2017) and Murdoch et al. (2017)].

Normal mode amplitudes are computed from GCM results by summing the normal modes, which estimates the signals that may be recorded by the InSight SEIS VBB seismometer (Lognonné et al. 2015; Lognonné et al. 2019). Compared with previous studies, the present study provides not only better lower estimates of MBF normal modes and ex-

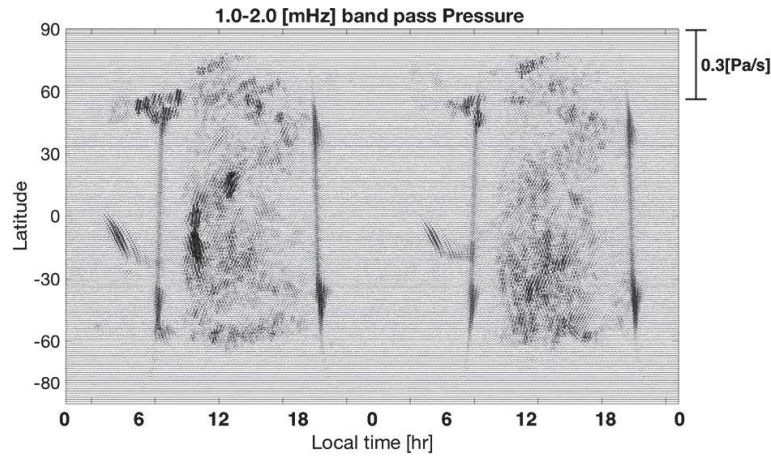


Fig. 2 Pressure fluctuations in Martian atmospheric in frequency band where normal modes concentrate in normal mode band. We applied a 1.0–2.0 mHz band-pass filter to the raw pressure data (shown in Fig. 1). The daily repetition of Martian weather processes appears clearly shown in the pattern. The band of the pattern at 1.0–2.0 mHz corresponds to low MBF frequencies (angular order 2 to 8) MBFs frequencies. The pressure fluctuations in the atmosphere excite daily coherent MBFs

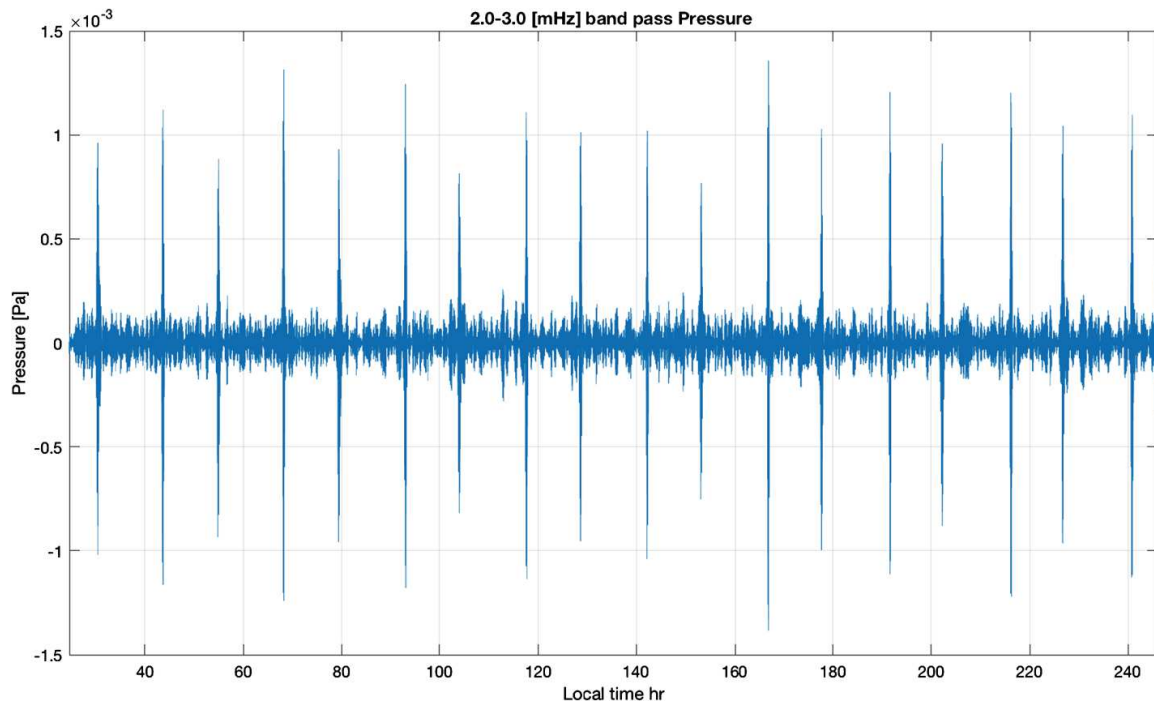


Fig. 3 Pressure fluctuations in Martian atmosphere at frequency band where normal modes concentrate at normal mode band. We applied a band-pass filter between 2.0 and 3.0 mHz to the raw pressure data (shown in Fig. 1). The large pressure fluctuations in this band occur twice a day (at sunrise and sunset). The frequency band corresponds to middle degree MBFs (angular order 9 to 15). Normal modes at this frequency are sensitive to the upper mantle (see Fig. 5)

tension to higher frequencies than Lognonné and Johnson (2007, 2015), but also pathways for the future processing of InSight measurements. Our synthetic signals will be compared with the expected noise and used to test stacking strategies, with a special emphasis on possible coherent stacking techniques made possible by the daily repetition of Martian weather. Finally, we conclude by estimating the probability of detecting MBFs with the SEIS seismometer.

2 Martian Global Climate Modeling for Normal Mode Computation

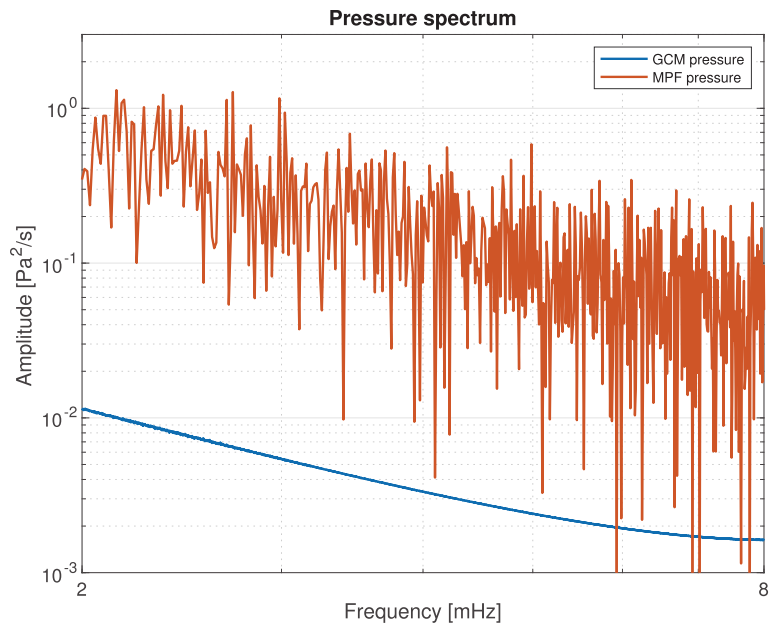
To predict the atmospheric excitation force, we used Mars Global Climate Model (GCM) which is designed to simulate large-scale atmospheric dynamics over an entire planetary sphere. The characteristics of the model are described in detail in Forget et al. (1999). We use the latest, most realistic, version of the model, which features interactive dust transport (Madeleine et al. 2011), radiatively active water and ice clouds (Navarro et al. 2014), and a thermal plume model for the boundary layer (Colaïtis et al. 2013).

Computing normal mode excitation requires a GCM simulation that is able to characterize the Martian atmospheric temporal variability of pressure and winds in the Martian atmosphere at 0.01 Hz (period 100 s), with a horizontal resolution suitable for normal modes, (i.e., 10° latitude and longitude). These requirements, dictated by seismic computations, are somewhat paradoxical from a meteorological point of view. A timescale of 100 s is associated with atmospheric circulations evolving over typical spatial scales of tens to hundreds of meters, which are challenging to resolve with GCMs, even with the best available supercomputing cluster. Most of the 100 s variability of the Martian atmosphere is instead captured through limited-area, turbulence-resolving modeling [large-eddy simulations; see, e.g., Spiga and Lewis (2010); see also Kenda et al. (2017), Murdoch et al. (2017) for a discussion of local seismic signature]. The remainder of this variability (i.e., the contribution that is not caused by microscale turbulence) is associated with mid-latitude baroclinic fronts and regional slope winds (which impact the global dynamics) and can be satisfactorily simulated through GCMs with a horizontal resolution of 1° . Conversely, nearly three decades of Mars GCM studies have consistently demonstrated that the global dynamics (at spatial scales of about 10° latitude and longitude) are well simulated by using a typical time step of 925 s in the GCM.

We also ran Martian GCM simulations specifically tailored for the seismic computations. The LMD GCM simulations used a 60 s time step, 360 longitude grid points, and 180 latitude grid points, corresponding to a mesh spacing of $1^\circ \times 1^\circ$ and a horizontal resolution of 60 km [in a setting akin to the GCM simulations described in Pottier et al. (2017)]. In the vertical direction, 25 levels are typically used with most of the levels located in the first 15 km to ensure a suitable resolution in the lower troposphere and in the boundary layer. Above 10 km, the vertical resolution is about one scale height and the altitude of the top level is about 60 km, which corresponds to about 6 scale heights. This vertical grid thus offers both the refined near-surface resolution and the accounts for the vast majority of the atmospheric mass, which allows us to deal with all possible seismic coupling in subsequent computations. It is important to note that turbulent motions developing at high frequency are not resolved by the GCM: the PBL mixing they cause is parameterized in the LMD GCM by dedicated schemes (Colaïtis et al. 2013). The GCM results used to compute normal modes thus only feature atmospheric variability at scales ranging from regional to global, and frequencies typically of the order 10^{-3} Hz (and below).

Typical GCM simulations of the Martian climate are needed so that the resulting analysis of normal modes applies to the conditions of the InSight mission. However, this does not require, however, as many simulations as would be expected from equivalent terrestrial studies. Both the low thermal inertia of the Martian surface and the fast radiative timescale of the thin Martian atmosphere imply a very low Martian-climate inter-annual variability (except during the dust storm season, but InSight will land in 2018 at the end of this season) (Read and Lewis 2004). Furthermore, given the key role played by the atmospheric-dust loading in driving the Martian climate as well as the small inter-annual variability of this parameter in the first half of the Martian year (Montabone et al. 2015) running one GCM

Fig. 4 Spectrum of GCM pressure and observed pressure. The observational data were acquired by Mars Pathfinder (LS = 170°). The GCM spectrum is computed for the same location as the observational data of Mars Pathfinder (LS = 0°). The results differ by an order of magnitude, implying that GCMs cannot fully explain the observed energy, which is likely due to inadequate modeling in GCMs of local-scale turbulences. Thus, MBFs calculated by using GCMs should be regarded as a lower limit of possible excitations



simulation for the year in which the InSight mission occurs will provide sufficiently accurate predictions for all Martian years (outside the dust storm season). The dust scenario used thus corresponds to the Martian Year 27 which is a typical clear atmosphere scenario (dust visible opacity around 0.2) with no effects from a global dust storm. GCM simulations start at $L_s = 0^\circ$ (northern spring), which corresponds to the first months of the InSight mission on Mars, and are performed for 20 Martian sols with a fixed dust profile. Given that gravity waves are partly resolved in our $1^\circ \times 1^\circ$ GCM simulation, we do not use the subgrid-scale scheme to model the effect of those waves on the large-scale flow. The outputs of the model, which are used as inputs for the modeling of the seismic moment density, as defined by relation Eq. (1), and are surface pressure and temperature, as well as atmospheric density, temperature, and winds.

The observed atmospheric status differs from that predicted by the GCM, despite the location being the same. This is illustrated in Fig. 4 for the Pathfinder location. Parts of these discrepancies are related to both the pitot pressure (associated with local wind) and to the local-scale eddies, which are not resolved by the GCM but are discussed above.

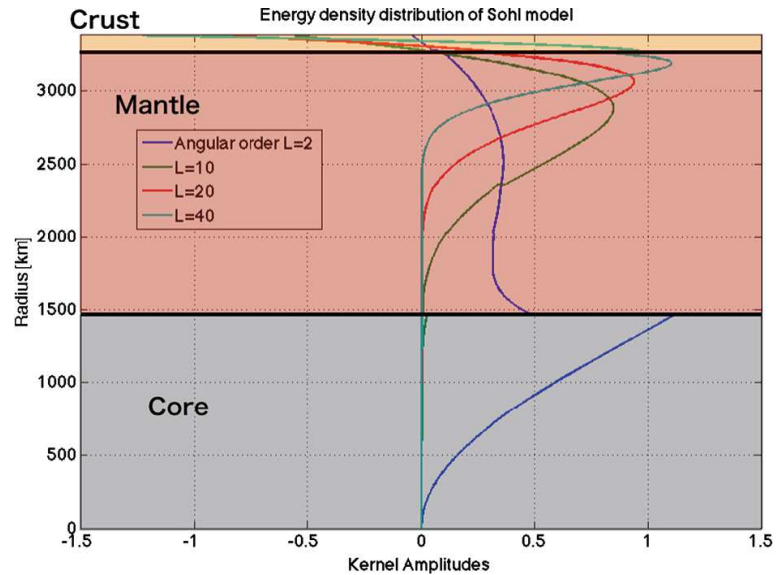
As we mentioned above, this is a challenging problem because our approach relies on GCMs. It is dependent on the environment in which the observation is made, the season, and other factors, notably, that GCMs lose energy at Martian normal mode frequencies (Fig. 4).

3 Estimating the Amplitude of Martian Normal Modes

3.1 Internal Structure Model

Martian internal models have been discussed by many researchers; please see Panning et al. (2017) and Smrekar et al. (2018) for further descriptions and review. The biggest differences between these models are in the crustal thickness and core radius. The first estimates are based on observation and laboratory experiments. A large amount of information about the inner structure is based on gravitational observations and data on surface-soil properties. With the constraints of mean density, moment of inertia, and k_2 Love number, the inferred radius of the core is estimated to be 1600 ± 200 km (Khan and Connolly 2007; Sohl and

Fig. 5 Vertical amplitude of spheroidal fundamental normal modes in solid part. Low-degree normal modes are low frequency. Large-amplitude areas concentrate the models energy and sensitivity. Low-degree waves (angular order 2 to 9) are sensitive at the core and deep mantle. High-degree waves (angular order 10 to 39) are sensitive at the middle and shallow part of the mantle. Each mode is sensitive at a different depth



Spohn 1997; Spohn et al. 2001; Rivoldini et al. 2011). However, only normal modes with very long periods are sensitive to the core size and, furthermore, their amplitude near the surface depends only weakly on core size. Consequently, the choice of internal model is not critical for our estimate of MBF amplitude, and all models will provide similar results. In the present work, we use the Sohl model to generate a reference internal structure. We calculate fundamental spheroidal normal modes longer than 120 s, and the limitation of the period is dictated by the GCM time step. This corresponds to calculating spheroidal normal modes of angular orders between $\ell = 2$ and $\ell = 39$ and of radial order $n = 0$ which constrains the core and the deep, middle mantle (Fig. 5).

3.2 Normal Modes Excitation

The theory of normal mode excitation and of normal mode summation is described in several papers (see, e.g., Lognonné 1991; Dahlen and Tromp 1998; Lognonné 2002) so we only briefly summarize the approach here. Martian global oscillations are governed by the gravito-elastic equation (when attenuation is neglected) or by the gravito-anelastic equation, when anelastic processes are considered. Atmospheric normal modes may also be computed by using the theory developed by Lognonné et al. (1998a). Lognonné et al. (2016) studied attenuation processes in the Mars atmosphere due to both the viscosity and CO₂ molecular relaxation. They concluded that, for long periods (e.g., $T \geq 50$ s), no significant atmospheric attenuation should be expected in the lower atmosphere where the greatest excitation force is concentrated, suggesting that an adiabatic approximation of the atmosphere suffices for our modeling. The starting equation is

$$-\omega_k^2 \rho_0 \mathbf{u}_k + \mathbf{A}(\mathbf{u}_k) = \mathbf{f}, \quad (3)$$

where ω_k is the angular eigenfrequency, \mathbf{u}_k is the associated displacement eigenfunction, \mathbf{A} is the gravito-elastic operator (or gravito-anelasto operator), ρ_0 is the unperturbed density and \mathbf{f} is the external force. The gravito-elastic operator \mathbf{A} is defined for the internal structure model and is given by:

$$\mathbf{A}(\mathbf{u}) = \nabla(\delta \mathbf{T}_{elastic} - \mathbf{u} \cdot \nabla \mathbf{T}_0) - \mathbf{g} \nabla \cdot (\rho_0 \mathbf{u}) + \rho_0 \nabla \Phi, \quad (4)$$

for the solid part, where Φ is the mass-redistribution potential, \mathbf{g} is the gravity acceleration due to gravity, \mathbf{T}_0 is the pre-stress and $\delta\mathbf{T}_{elastic}$ is the elastic stresses. The operator in the atmospheric part can be written by using $\mathbf{T}_0 = -p_0\mathbf{I}$ and

$$\mathbf{T}_{elastic} = -p_{Hooke}\mathbf{I} = \kappa\nabla\cdot\mathbf{u}\mathbf{I}, \quad (5)$$

where \mathbf{I} is the identity tensor. The result is

$$\mathbf{A}(\mathbf{u}) = \nabla(\kappa\nabla\cdot\mathbf{u} + \mathbf{u}\cdot\nabla p_0) - \mathbf{g}\nabla\cdot(\rho_0\mathbf{u}) + \rho_0\nabla\Phi, \quad (6)$$

where κ is the bulk modulus and p_0 is the equilibrium pressure. Following Lognonné et al. (1994), we can write the momentum-density field $\rho\mathbf{v}$ in the form

$$\rho(\mathbf{r}, t)\mathbf{v}(\mathbf{r}, t) = \rho_0(\mathbf{r}) \sum_k \dot{c}_k(t)\mathbf{u}_k(\mathbf{r}), \quad (7)$$

which provides the displacement field \mathbf{u} , which can be expressed to first order (and therefore sufficiently far enough from the sources when on location) as

$$\mathbf{u} = \sum_k c_k(t)\mathbf{u}_k(\mathbf{r}). \quad (8)$$

We get the differential equation with respect to time and the source function as

$$\frac{\partial^2 c_k(t)}{\partial t^2} + \omega_k^2 c_k(t) = \Psi_k(t), \quad (9)$$

where Ψ_k is the excitation force for each mode. To compute the normal mode excitation forces, we consider the nonlinear equation of momentum conservation,

$$\begin{aligned} \frac{\partial}{\partial t}(\rho\mathbf{v}) &= -\nabla p + \rho\mathbf{g} - \nabla\cdot(\rho\mathbf{v}\mathbf{v}), \\ &= -\nabla p_{Hooke} - \nabla\cdot(\rho\mathbf{u})\mathbf{g} - \nabla\delta p_{glut} - \nabla\cdot(\rho\mathbf{v}\mathbf{v}), \\ &= -\mathbf{A}(\mathbf{u}) - \nabla\delta p_{glut} - \nabla\cdot(\rho\mathbf{v}\mathbf{v}), \\ \delta p_{glut} &= p - p_0 + \kappa\nabla\cdot\mathbf{u} + \mathbf{u}\cdot\nabla p_0, \\ \delta p_{Hooke} &= -\kappa\nabla\cdot\mathbf{u} - \mathbf{u}\cdot\nabla p_0, \end{aligned} \quad (10)$$

where p_0 is the equilibrium pressure and $p_{glut} = p_0 + \delta p_{glut}$ is the GCM pressure as the GCM filter acoustic waves. We assume here that the gravity term is linear and therefore excluded from this term excitation processes associated with nonlinearity (Julián et al. 1998). If existing in the Martian atmosphere, (e.g., for atmospheric gravity waves), this might be therefore an additional excitation term for frequencies below the 2 mHz acoustic cutoff (Lognonné et al. 2016). However, transport terms are fully included in the Reynolds stress term $\rho\mathbf{v}\mathbf{v}$.

Note also that the GCM pressure variations are much greater than those generated by the flow, so that $\delta p_{glut} \approx p - p_0$. We project Eq. (10) onto a given normal mode, which gives

$$\begin{aligned} \int_V dV \mathbf{u}_k \cdot \frac{\partial}{\partial t}(\rho\mathbf{v}) &= \ddot{c}_k, \\ &= - \int_V dV \mathbf{u}_k \cdot \mathbf{A}(\mathbf{u}) - \int_V dV \mathbf{u}_k \cdot [\nabla\delta p_{glut} + \nabla\cdot(\rho\mathbf{v}\mathbf{v})], \end{aligned}$$

$$\begin{aligned} \int_V dV \mathbf{u}_k \cdot \frac{\partial}{\partial t} (\rho \mathbf{v}) &= \ddot{c}_k, \\ &= -\omega_k^2 c_k(t) - \int_V dV \mathbf{u}_k \cdot [\nabla \delta p_{glut} + \nabla \cdot (\rho \mathbf{v} \mathbf{v})]. \end{aligned} \quad (11)$$

Note that, in this projection, we shall decompose the volumetric integration for all partial volumes (in practical terms, the atmosphere and interior) i separated by discontinuities j , such that

$$\begin{aligned} &\int_V dV \mathbf{u}_k \cdot [\nabla \delta p_{glut} + \nabla \cdot (\rho \mathbf{v} \mathbf{v})] \\ &= \sum_i \left[\int_{S_i} dS [\delta p_{glut} \mathbf{u}_k \cdot \mathbf{n}_i + \rho \mathbf{u}_k \cdot \mathbf{v} \mathbf{v} \cdot \mathbf{n}_i] - \int_{V_i} dV \nabla \mathbf{u}_k \cdot \mathbf{m} \right] \\ &= - \int_V dV \nabla \mathbf{u}_k \cdot \mathbf{m} + \sum_j \int_{S_j} dS [\mathbf{u}_k \cdot \mathbf{n}_i \delta p_{glut}]_{-}^{+} \end{aligned} \quad (12)$$

where we assume no vertical winds at the interface. (Note that this approach is here limited to a spherical surface and that additional excitation terms could occur due to topography, in way similar to what occurs for Earth's hum [see, e.g., Nishida (2017)]. The vector \mathbf{n}_i is the normal to the surface, leaving the volume i , denoted $+$ and $-$ the volume against $+$, for which the normal vector is oriented in the opposite directions. Following Lognonné and Mosser (1993), we define here the flux-glut moment density tensor as

$$m^{ij} = (p + \kappa \nabla \cdot \mathbf{u}) \delta^{ij} + \rho v^i v^j. \quad (13)$$

Equation (12) simplifies further because we have not only continuity of pressure at the atmosphere-solid interface, but also continuity of the Hooke pressure and the vertical amplitude of modes across this interface. We therefore identify the second term as the excitation coefficient, which can be rewritten as

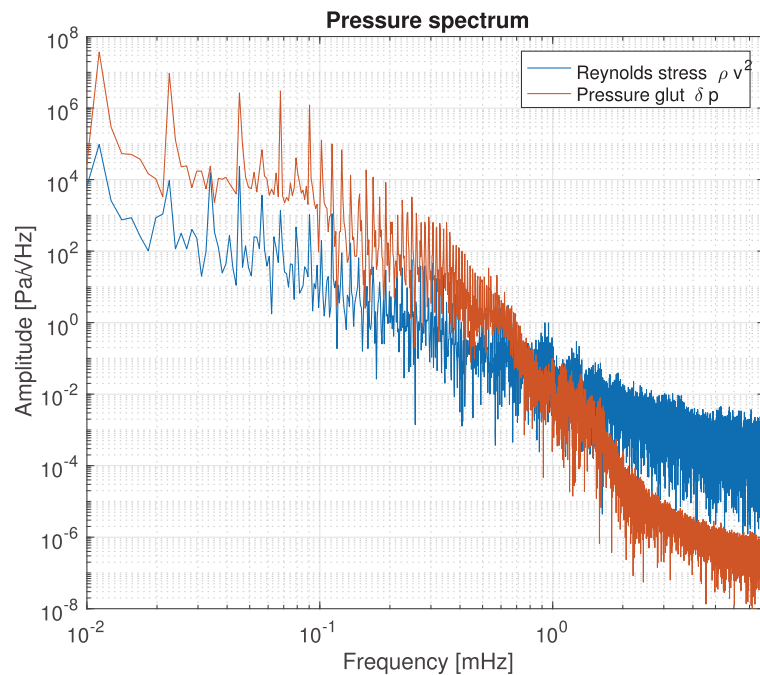
$$\Psi_k(t) = - \int_V dV \mathbf{u}_k \cdot \nabla [\delta p_{glut} + \cdot (\rho \mathbf{v} \mathbf{v})] = \int_V dV \epsilon_k : \mathbf{m}, \quad (14)$$

where ϵ_k is the strain tensor of the normal mode k . Figure 6 shows the pressure and Reynolds stress spectra for an arbitrary point on the surface of Mars, as calculated by the GCM. Note that the amplitudes decrease as $1/f$. Most of the variability in the normal mode bandwidth is associated with the Reynolds stress. All terms in Eq. (13) can be derived from the values calculated by the GCM, thereby giving us a full description of the moment tensor based on the GCM results.

3.3 Normal Modes Amplitudes in Atmosphere

Estimating the normal modes excitation coefficients $\Psi_k(t)$ requires knowledge of the normal mode amplitude in the atmosphere. Given the exponential decay of the density and the a priori thickness of the Martian boundary layer, most of the pressure glut release will occur in the first 10 km so we focus on computing the normal modes at these relatively low altitudes. Normal mode atmospheric amplitudes are affected by many factors, such as viscosity, radiative boundary, sound velocity, relaxation, resonance, etc. See Lognonné et al. (2016) for more details on the different parameters affecting the amplitude modeling. At low altitudes

Fig. 6 GCM pressure and Reynolds stress power spectrum. The pressure glut is stronger (weaker) than the Reynolds stress at low (high) frequencies. At high frequencies, the main contribution to the pressure variation is eddies, which generate Reynolds stress through wind variations



and in the bandwidth of normal modes, viscous and relaxation processes can be neglected, as done by Lognonné and Johnson (2007). However both Lognonné and Johnson (2007, 2015) and Lognonné et al. (2016) assume the atmosphere to be spherically, symmetric and rigorous. The three-dimensional computation of the normal modes requires a prohibitive amount of computing time. Although the interior structure of Mars can be considered spherically symmetric, the acoustic properties of the Martian atmosphere depend strongly on local time, with large variations between the night and day for the height scale, temperature, and density, and therefore for the sound speed and acoustic impedance as well as the coupling between ground and atmosphere. This is illustrated in Fig. 7, which shows the variation of atmospheric scale height. Relative variations of $\pm 20\%$ with LS (or during one day at the same longitude) are observed, which suggest that lateral variation of the atmospheric coupling should be accounted for in MBF calculations. Furthermore, Mars has larger lateral atmospheric variations than does Earth. The main driver of atmospheric variation is temperature: on Mars, temperature variations are much greater than on Earth because of the absence of oceans and atmospheric water vapor, which serve as effective thermal reservoirs and stabilize the temperature. Thus, the MBF with three-dimensional atmospheric structure must be estimated to better understand the signal levels of MBFs and perfect the simulations. However, to account for the lateral variation while maintaining a realistic calculation time requires some modeling and simplification. Thus we simplified the atmospheric structure by neglecting viscosity, radiative boundaries, relaxation, and resonance.

In this paper, we propose to compute the amplitude of the atmospheric normal modes by propagating the normal mode amplitude at the surface into the atmosphere. In other words, instead of directly calculating normal modes in the atmosphere, we extrapolate the modes calculated for the solid part of the planet into the atmosphere. For this purpose, we make the following assumptions:

- the normal mode phase velocity is much greater than acoustic-wave velocity, leading to a vertically longitudinal upward-moving acoustic wave;
- the normal modes interact asymptotically with the atmosphere and without significant resonance between solid and atmosphere, which limits this approach to normal modes above the atmospheric cutoff frequency.

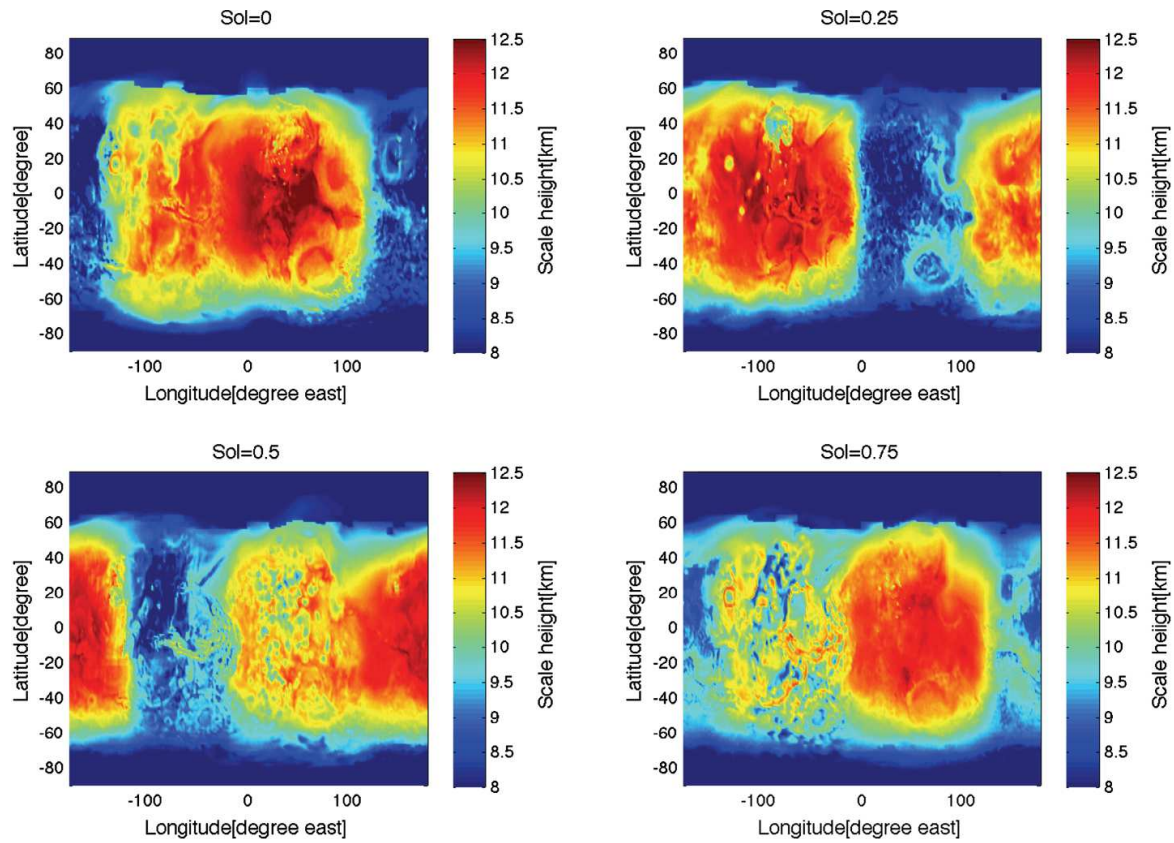


Fig. 7 Daily variation of atmospheric scale height. The red (blue) areas are thick (thin). Because of the large temperature variations, the scale height thickness changes from 8 to 12 km in one day. During the day, the atmosphere expands to 12 km height, whereas it shrinks to 8 km height at night. This variation in scale height directly affects the normal mode structure, and the isosphere model cannot describe this lateral effect

Given these two assumptions, the wave-propagation normal mode is

$$u_k(z) = u_k(0) \cdot e^{-ik_z z} \times \sqrt{\frac{\rho(0)c(0)}{\rho(z)c(z)}}, \quad (15)$$

where k_z is a vertical wave number and z is the altitude above the ground. The first factor on the right side of the equation is the wave-propagation factor and the second factor is the wave transmission ratio. With the wave-propagation method, we can describe the local time and, more generally, how the normal mode amplitude in the atmosphere depends on geography.

We compare the resulting amplitudes with those computed by using the more precise model of Lognonné et al. (2016). For angular orders $\ell \geq 10$, the difference is less than the effect of the lateral variation (see Fig. 8). However, for smaller angular orders and for modes with frequencies close to or below the atmospheric cutoff, this simple propagation fails and large discrepancies appear because of acoustic-wave reflection and resonance in the atmosphere. Figure 10 shows the relative atmospheric energy for the fundamental spheroidal modes. The energy peaks around 2.2 mHz, which corresponds to the angular order $\ell = 9$. This large coupling of the normal mode with angular order $\ell = 9$ is normal if also seen on the mode amplitude (Fig. 9).

Such modes, thus require exact computation. Note, however, that these modes are also difficult to observe because of the expected high very low-frequency modes associated with temperature fluctuation below 5 mHz.

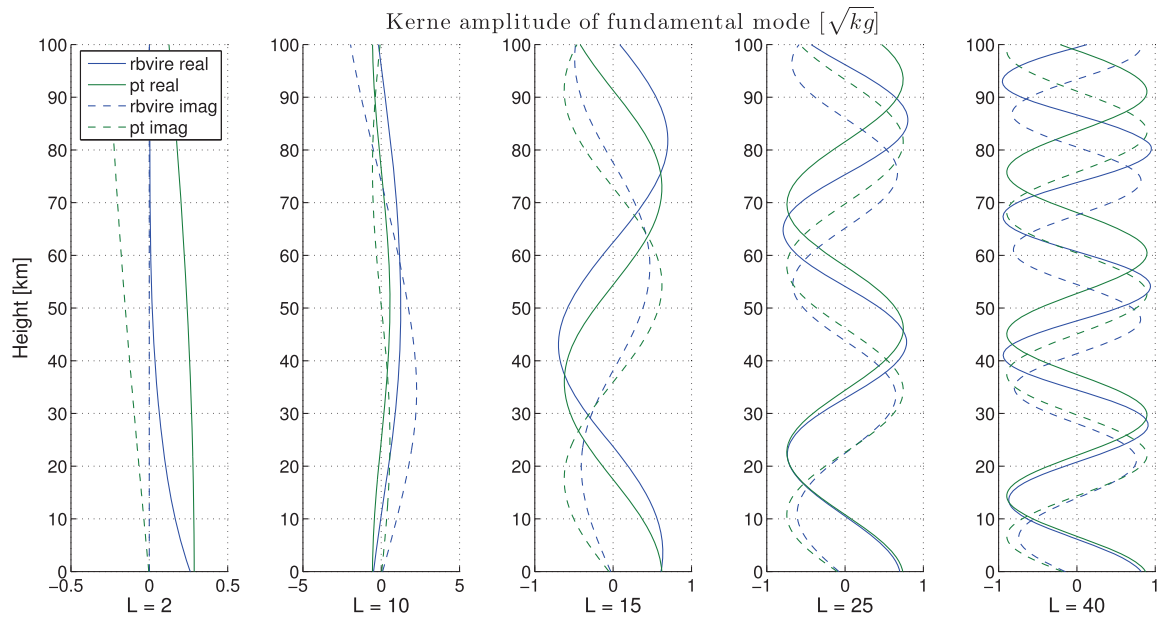


Fig. 8 Kernel sensitivity of normal modes in air. Blue curves include the radiative boundary, viscosity, and relaxation. Green curves include only wave propagation and transmission. Solid lines and dotted lines show the real part and imaginary parts, respectively. For order $n \Rightarrow 10$, the gaps between two adjacent normal modes are much less than the scale height

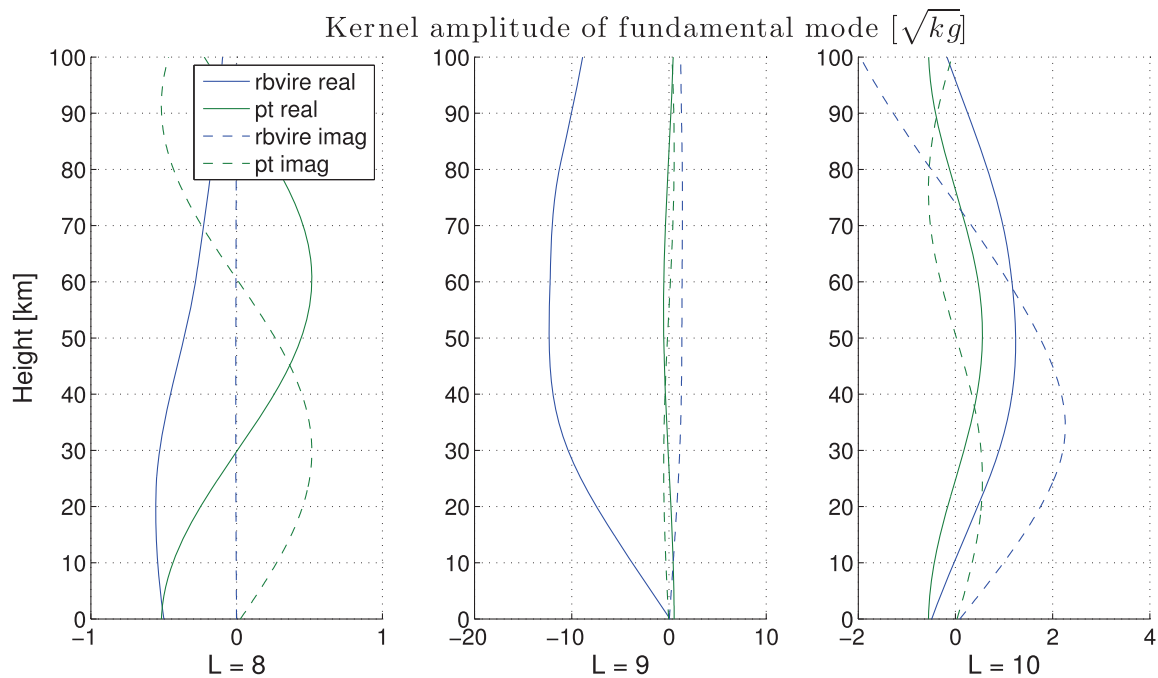


Fig. 9 Kernel sensitivity of normal modes in air. At the normal mode of angular order nine, the large gaps occur because of the resonance between the atmosphere and the solid part. The normal mode cannot describe this resonance, so the normal mode calculation only works for angular order 10. Below angular order 10, normal modes are hard to detect because of the low-frequency thermal noise (see Sect. 4.2)

Fig. 10 Relative atmospheric energy of surface wave in the Mars atmosphere for Rayleigh surface waves as a function of frequency. Associated angular order values range from $\ell = 2$ to $\ell = 39$. The peak of the fraction is at angular order 9 (near 2.2 mHz). At the first peak, a strong resonance appears between the atmosphere and the solid part

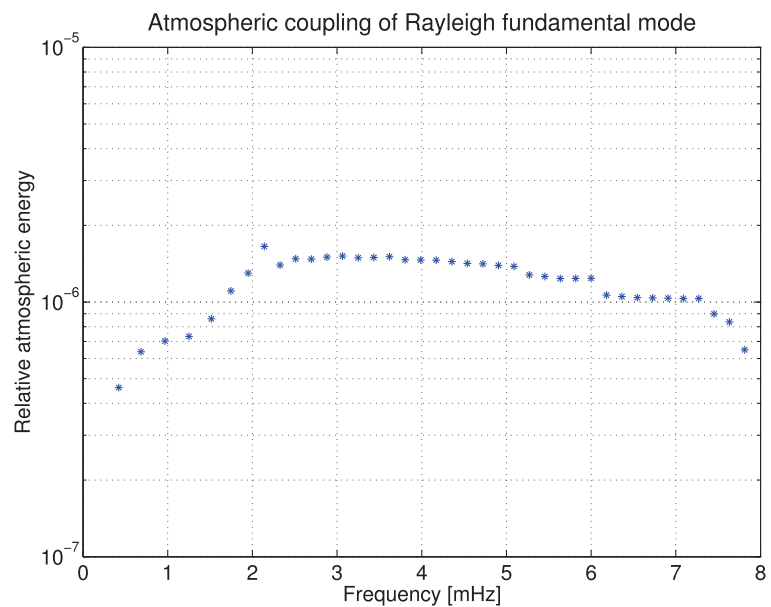
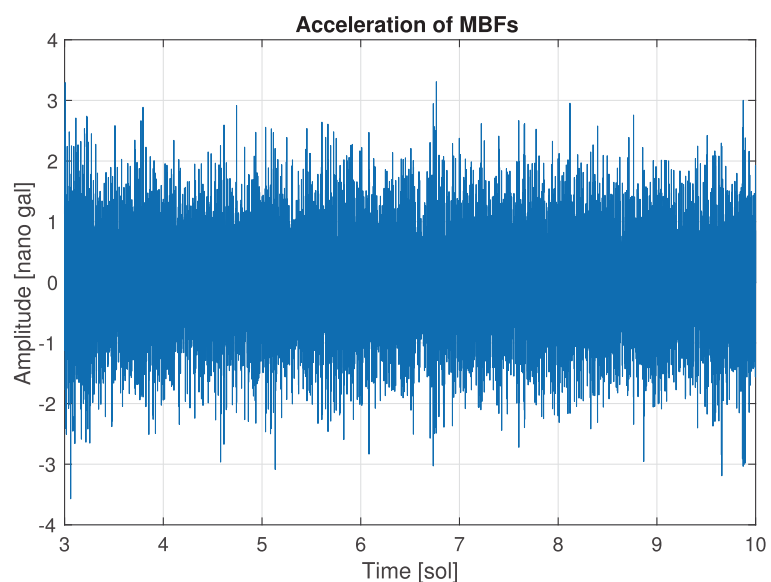


Fig. 11 7 MBF acceleration as a function of Martian days. The MBF is the sum of fundamental normal modes of angular order 2 to 39. The amplitude is given in nanogals (10^{-11} m/s^2). The MBF continues for days because the normal modes are excited by continuous atmospheric activities. The data for the first three sols are meaningless due to the GCM boundary conditions and the stability of MBFs

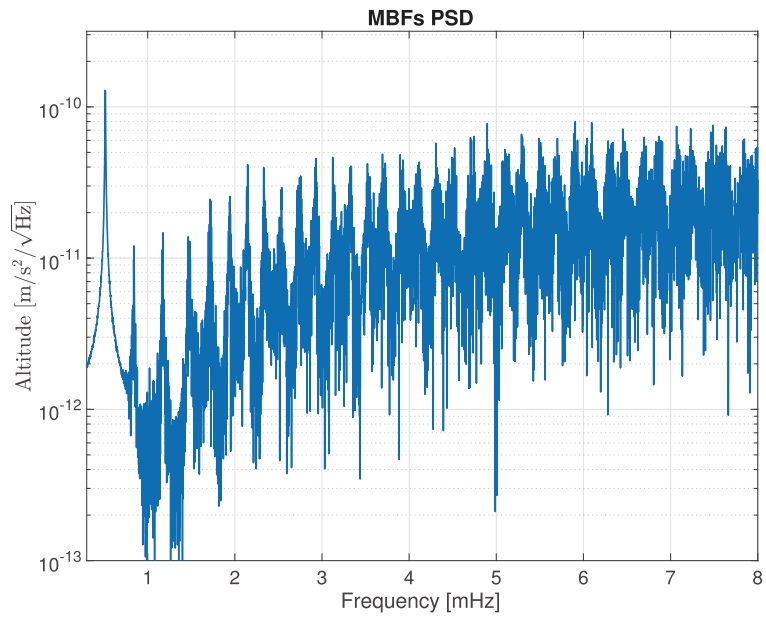


4 Results and Discussion

4.1 Normal Modes Amplitude

The MBF is obtained by summing the fundamental Rayleigh normal modes, with the amplitude of each computed by using Eqs. (8) and (11). For this study, we summed the fundamental normal mode for degrees $\ell = 2$ to $\ell = 39$. The amplitude of the MBF signal is a few nanogals (10^{-11} m/s^2), as shown in Fig. 11. This amplitude is greater than that reported by Lognonné and Johnson (2007, 2015), which is likely because of the larger angular orders and therefore larger frequencies that they used. Since the signal is the sum of all normal modes, specific peak amplitudes are more clearly shown in Fig. 12. The lowest-frequency peak (0.4 mHz) is a normal mode of angular order 2, whereas the highest-frequency peak (8.3 mHz) is a normal mode of angular order 39. Note, however, that the amplitudes are well modeled only for frequencies greater than 2 mHz. We also observe a gradual increase of the amplitude with frequency up to 5 mHz, after which the amplitude of the peaks remains constant.

Fig. 12 Calculated spectrum of acceleration power density of MBFs. The MBFs are estimated by using GCMs and the internal structure given by the Sohl model. The normal mode frequencies come from power spectral density calculations. Each peak is a normal mode; there are 38 peaks in this figure, ranging from angular order 2 to 39. The amplitude grows with frequency up to 5 mHz and is then remains constant for frequencies ≥ 5 mHz



4.2 Normal Modes: Detection and Seismometer Performance

MBF amplitudes are quite small and so can be detected only by using instruments with high sensitivity and low noise. Let us consider whether these modes can be detected in the POS output of the InSight SEIS VBB sensors. This output has a flat acceleration gain in the frequency bandwidth of normal modes (see Lognonné et al. 2019).

The least significant bit (LSB) of the InSight SEIS seismometer for differential output is

$$LSB = \frac{2 \times \text{Voltage}}{\text{Gain}}. \quad (16)$$

The seismometer voltage is ± 25 V, the acquisition dynamics is 24 bit, and the gain is $\approx 10^4$ V/DU for low gain mode and about 4.5 times greater for high gain mode. Therefore, the LSBs are

$$LSB_{LG} = \frac{2 \times 25}{10^4 \times 2^{24}} = 30 \text{ nanogal}, \quad (17)$$

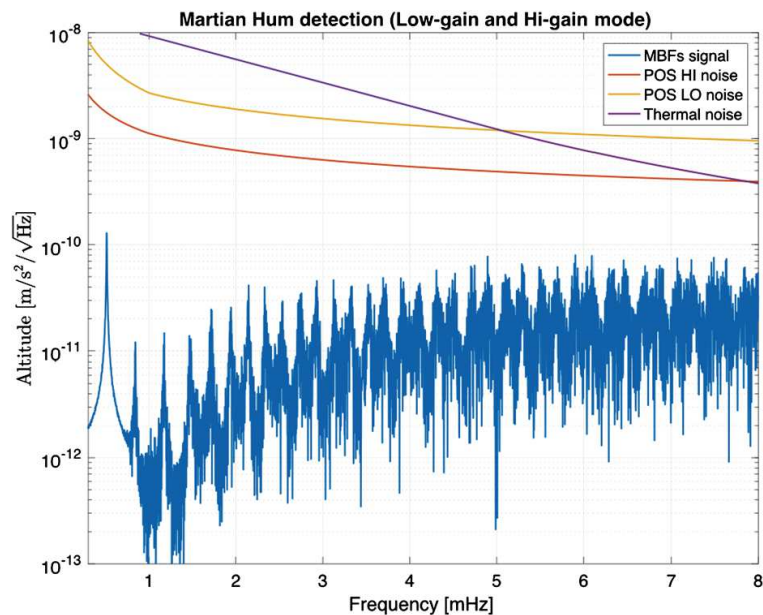
$$LSB_{HG} = \frac{2 \times 25}{4.5 \times 10^4 \times 2^{24}} = 6.6 \text{ nanogal}.$$

The amplitude of MBFs is only nanogals and the LSBs are therefore greater. The real ground acceleration signal contains MBF, as well as thermal drift, thermal and instrument noise, and possibly seismic signal. For a more realistic evaluation, we approximate the daily temperature variation associated with the temperature sensitivity of the sensors with an ideal sinusoidal curve and superpose it on the MBFs. Because this drift is much greater than 1 LSB, it enhances the MBFs up to a detectable level. The sinusoidal thermal-noise model is given by

$$A_{temp}(t) = \gamma \delta T \left(1 - \cos \frac{2\pi t}{D_{sol}} \right), \quad (18)$$

where A_{temp} is the equivalent acceleration of temperature variations, t is local time, D_{sol} is the duration of a Martian day, γ is the sensitivity per degree of the VBB in the acceleration

Fig. 13 Spectrum of power acceleration density of MBF, instrumental noise, and environmental noise. Above 5 mHz (angular order 22), thermal noise is much greater than the MBF signal. Below 6.5 mHz (angular order 30), the MBF signal overcomes both instrumental and thermal noise. During nighttime, the InSight SEIS seismometer in high-gain mode may detect the MBF signal. The MBF signals detected carry information about the middle, shallow part of the Martian mantle



unit, and δT is the temperature variation over one Martian day. The temperature sensitivity γ is set to 10^{-5} m/s²/K and daily temperature variation δT is 4 K, which corresponds to the variations expected during winter (Mimoun et al. 2016; Lognonné et al. 2019). The amplitude of this thermal daily variation is therefore 4.0×10^6 nanogal, which is six orders of magnitude greater than MBF signals.

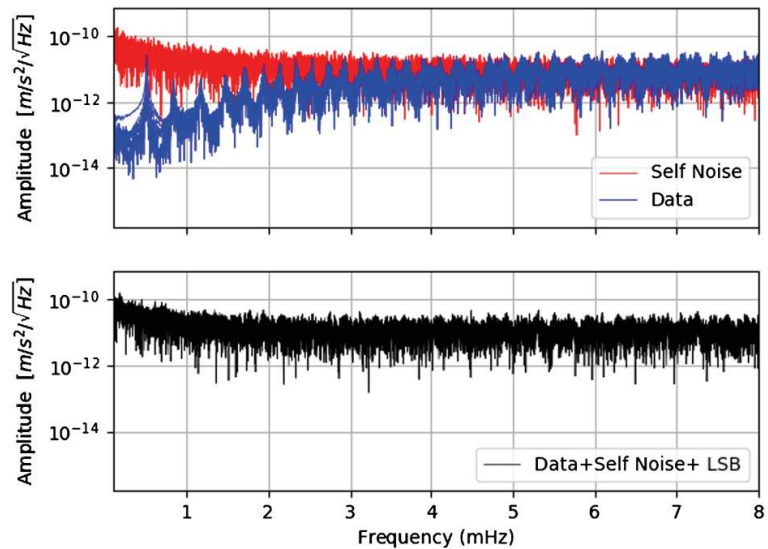
We simulate the signals by adding the MBF signal to the thermal drift, and then simulate the digitization by converting this acceleration signal into bits. Subtracting from the signal a sol-periodic sine wave with amplitudes computed by using the least-squares method simulates data processing. For both low gain and high gain, clear MBFs signal are retrieved from the residual, which demonstrates the capability of the acquisition system to use stochastic amplification of the noise to detect signals smaller than the LSB.

The signal remains much smaller than the expected instrument noise, which is the superposition of the instrument self-noise and of the residual of both the subtracted temperature drift and the potential pressure decorrelation (Murdoch et al. 2017). This is illustrated in Fig. 13, which compares the MBF spectrum to the instrument self-noise in both low gain and high gain and to the expected thermal-drift signal. In the 5 to 10 mHz band, which contains a large part of the target bandwidth for the Martian hum search (5 to 20 mHz) and the bandwidth in which our modeling hypothesis and the GCMs have acceptable errors, the MBF signal is expected to be 5 to 10 below the instrument self-noise, depending on the gain. Stacking this signal over the mission duration will then allow successful detection.

The amplitude of ideal thermal noise model is 4.0×10^6 nanogal. The acceleration is 0.4×10^6 DU in low-gain mode or 1.4×10^6 DU in high gain mode. The thermal noise acceleration is far greater than the MBF signal. Thus, no signal is detected by the InSight SEIS seismometer in low-gain mode. In high-gain mode, we can detect 1 DU signal several times per half Martian day. However, ideal thermal noise can kick up to 1 DU after the decimal point. After subtracting the digitized thermal noise, more MBF signals are detected using the InSight SEIS seismometer in both low- and high-gain mode. Although the MBF signal is hidden by the large thermal noise, after subtracting the digitized thermal noise, we capture a greater part of the MBF signal.

To improve the signal to noise ratio and detect the MBF normal modes, we further process data as follows. First, we create a trace that contains MBF signal and noise. As explained previously, noise can be decomposed as self-noise, thermal noise and LSB noise. We com-

Fig. 14 Spectrum amplitude of each two sol long segment for MBF traces (blue) and self-noise traces (red) in the top figure and for S4 traces (black) in the bottom figure



pute self-noise as the inverse Fourier transform of a spectrum whose amplitude follows the station sensitivity as a function of frequency and whose phase is random. This self-noise is added to the MBF seismogram to create a trace S1. Thermal noise is then computed as a sinus function over one sol with an amplitude of 10^{-4} m/s^2 to simulate the seismic acceleration generated by thermal drift. This thermal noise is added to trace S1 to create trace S2. LSB noise takes into account the least significant bit ($5.81/4 \times 10^{-11} \text{ m/s}^2$). Trace S2 is modified so that the only signal above the LSB is kept and this trace is called S3. Finally, we assume that the thermal drift is known and it is subtracted to trace S3 to generate the final trace S4.

The seismogram S4 is then cut into segments of two sols with one sol overlap, starting at sol 4. Figure 14 (top) displays spectra amplitude of each two sol-long segments for the MBF signal (blue lines) and self-noise (red lines) and confirms that the amplitude of the MBF normal modes is below the self-noise. Figure 14 (bottom) shows the spectra amplitude of each segments of trace S4 (black lines). Normal modes are not visible in the amplitude spectra of the different data segments.

Data are then processed as follows. Phase auto-correlation is computed for each segment and then stacked using the phase weighted stack method following the method developed in Schimmel et al. (2011), Ventosa et al. (2017), Schimmel et al. (2018). For comparison, we apply the same processing to MBF traces, S1 traces (MBF+self noise) and S4 traces (MBF+self noise+LSB). Figure 15 (top) show the amplitude spectra of each stack. Normal mode peaks are clearly visible for the MBF stack amplitude spectrum between 1.5 and 8 mHz. Some modes can also be detected for the stack of traces S4 at frequencies higher than 4 mHz.

In order to enhance the signal to noise ratio, we further select the Rayleigh wave train windows on the stack of auto-correlograms by setting to 0 the rest of the signal as in Deen et al. (2017). We keep signal around 0-time lag and around each surface wave train R1 to R3. We keep 6 minutes around 0 lag time and select R1 to R3 wave trains considering that their group velocities are between 3.8 and 5.7 km/s. Figure 15 (bottom) displays the new amplitude spectra, and we observe that the normal mode peaks are now clearly visible for frequencies above 2.5 mHz for the MBF stack and also for data with realistic noise (self-noise or MBF+self noise). Adding longer time series will improve the signal to noise ratio and therefore we expect that normal modes excited by the Mars atmosphere should be detectable.

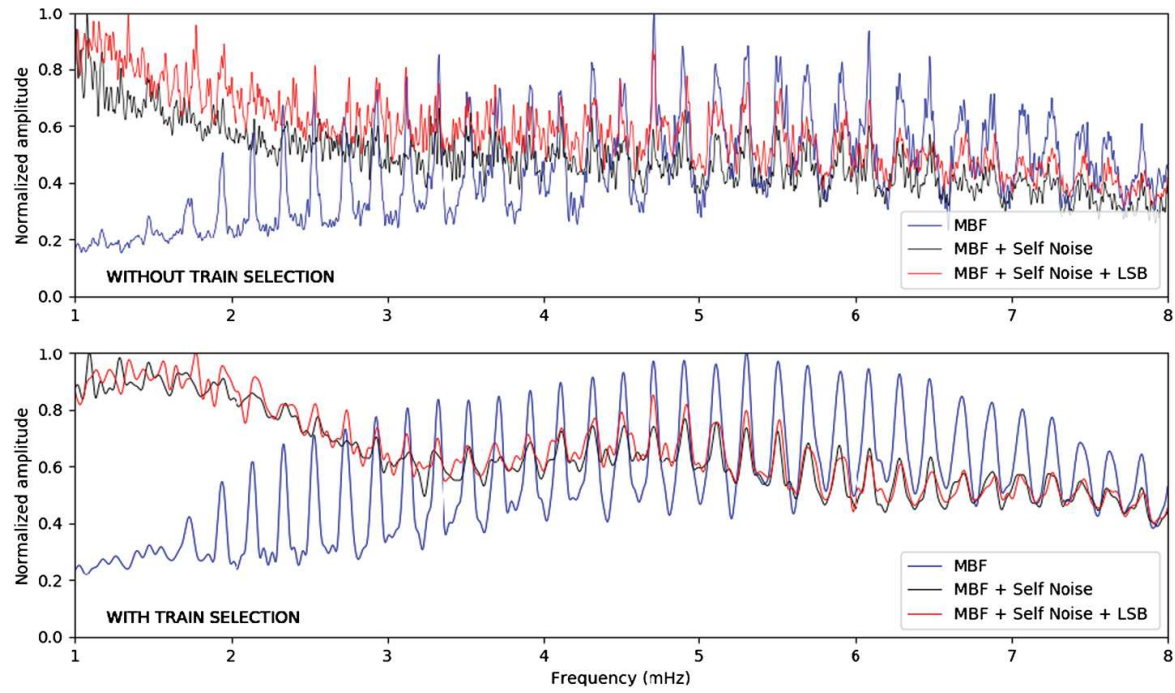


Fig. 15 Normalized spectrum amplitude of the stack of autocorrelograms without surface wave train selection (top) and after surface wave train selection (bottom). The blue, black and red curves correspond to MBF, MBF+self noise and MBF+self noise + LBS noise (S4) data respectively

4.3 Estimate of Seismic Magnitude of MBF Signal

We now not only estimate the MBF amplitude in terms of seismic magnitude, but also check that our estimate of the MBFs is comparable to that obtained by applying a simple energetic budget, following the approach of Kobayashi and Nishida (1998b).

For a first estimate, we assume that the release of acoustic and seismic energy into atmospheric activities is driven by solar flux and, furthermore, that all the energy of planetary background free oscillations comes from solar flux. This maximum energy may be expressed as

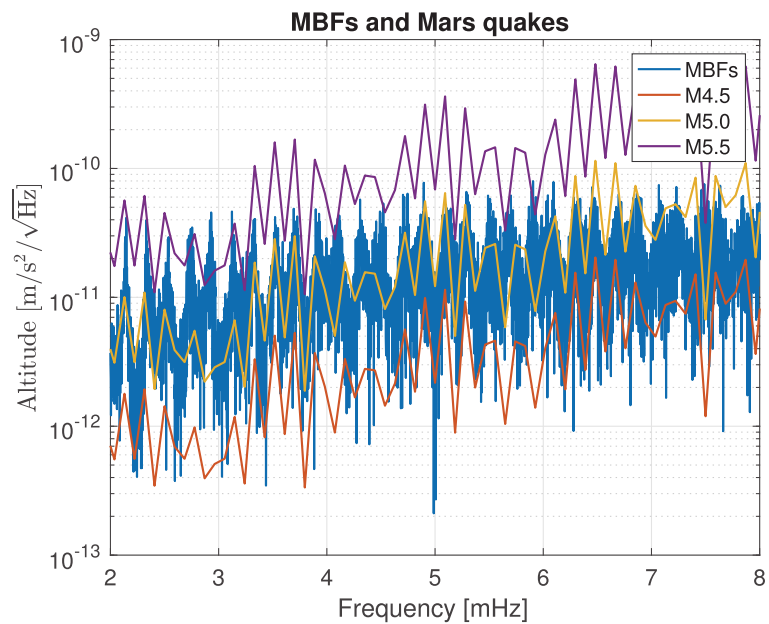
$$W_M = F_E \times \left(\frac{D_E}{D_M} \right)^2 \times (1 - A_M) \times \pi R_M^2, \quad (19)$$

where W_M is the rate at which the Sun transfers energy to the Mars surface, F is the solar flux above Earth's atmosphere ($F_E = 1360 \text{ W/m}^2$), D is the distance from the Sun ($D_M = 1.52D_E$), A is the bound albedo ($A_M = 0.25$), subscripts E and M refer to Earth and Mars, respectively, and R_M is the radius of Mars. This solar energy is converted to seismic energy, with a coherency duration of $T\sqrt{Q}$, where Q is the quality coefficient of the mode and T is its period. Thus the MBF's energy (E_{MBF}) is

$$E_{MBF} = W_M \times s \times \sqrt{Q} \times T \times C, \quad (20)$$

where $s = 0.01$ is an acoustic efficiency (which can be achieved for high-altitude winds of 40 to 50 m/s, assuming an efficiency depending on M^3 , where M is Mach number, [see, e.g., Goldreich and Kumar (1988)]). The constant C is the energy coupling ratio between the atmosphere and the solid part of Mars (a typical value is $C = 5 \times 10^{-6}$, (see, e.g., Lognonné and Johnson 2015)), Q is seismic attenuation of MBF's (typical value $Q = 100$), T is period

Fig. 16 Spectrum power acceleration density of MBF and free oscillations. The Martian atmosphere excites the MBFs and the free oscillations are excited by imaginary seismic events. The magnitude of the events are M4.5, 5.0, and 5.5. MBFs are close to M5.0 oscillations. This result is consistent with rough estimates



of MBFs (typical value $T = 200$ s). We then use the energy-magnitude relation of (Gutenberg and Richter 1956):

$$\log E = 4.8 + 1.5M, \quad (21)$$

where M is the magnitude of the seismic event. A rough estimation of the MBF magnitude gives $M = 4.9$.

We now compare the amplitude obtained by our GCM modeling with that excited by seismic activity. This is achieved by comparing the spectrum of the MBFs with those of quakes that occur at an epicentral distance of 90° . We find amplitudes of MBFs close to those generated by a M5.0 free oscillation (Fig. 16), while the estimates based on the GCM calculation are consistent with those based on solar flux. The results are also consistent with those estimated from Earth's hum, which has been estimated to be equivalent to a daily earthquake of magnitude 5.75–6 (Rhie and Romanowicz 2004). Given the earthbound albedo of 0.306, the solar flux for Earth is eightfold that of Mars, which corresponds to magnitude 0.6 greater and therefore an extrapolation of 5.3. Nevertheless, all these estimates of magnitudes, although comparable, are less than the magnitude of 5.9 (i.e., 10^{18} Nm) which is considered by several studies as a prerequisite for detecting normal modes. Therefore, we will focus our next analysis on the possibility of coherent stacking for MBFs, which, for a Mars year of 687 days, might lead to an increase in amplitudes by $\approx 26\epsilon$, where ϵ is the fraction of daily coherent hum. For a sol-to-sol coherency exceeding 0.4, this might lead to an order of magnitude increase in signal, allowing signals to possibly peak out of the noise after stacking data over a year.

4.4 Weather Correlation and Stacking Method

The Martian surface has low thermal inertia because it is devoid of oceans. Thus, the diurnal surface-temperature cycle is very large. Combined with the very thin atmosphere, this makes thermal tides a prominent element of diurnal variability on Mars. This is further reinforced by the equatorial location of InSight. Mars has a clear dichotomy whereby low lands dominate the southern hemisphere, while the northern hemisphere is dominated by highlands. The boundary of the dichotomy is close to the equator and this dichotomy contributes

Fig. 17 Pressure correlations in normal mode frequency band. Large correlations are diurnal and semi-diurnal. On a given day, the large correlations are the sunrise-sunrise and sunset-sunset correlations. Semi-diurnal correlations are sunrise-sunset and sunset-sunrise (semi-diurnal thermal tide). The periodic excitation force generates high-efficiency stacking. This precise phenomenon occurs on Mars but not on Earth

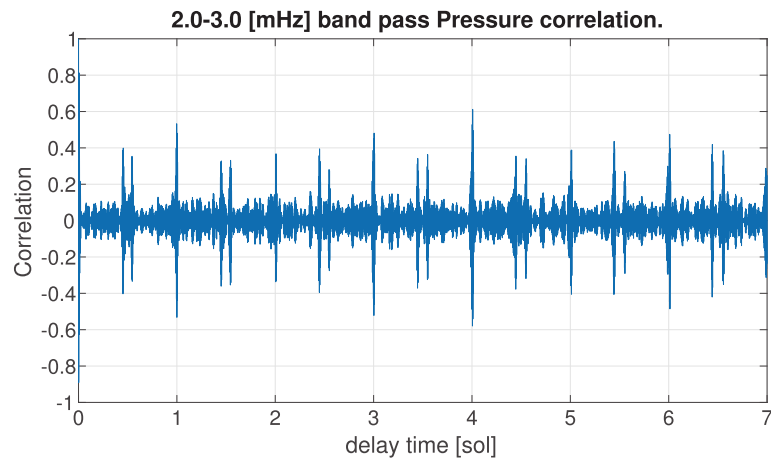
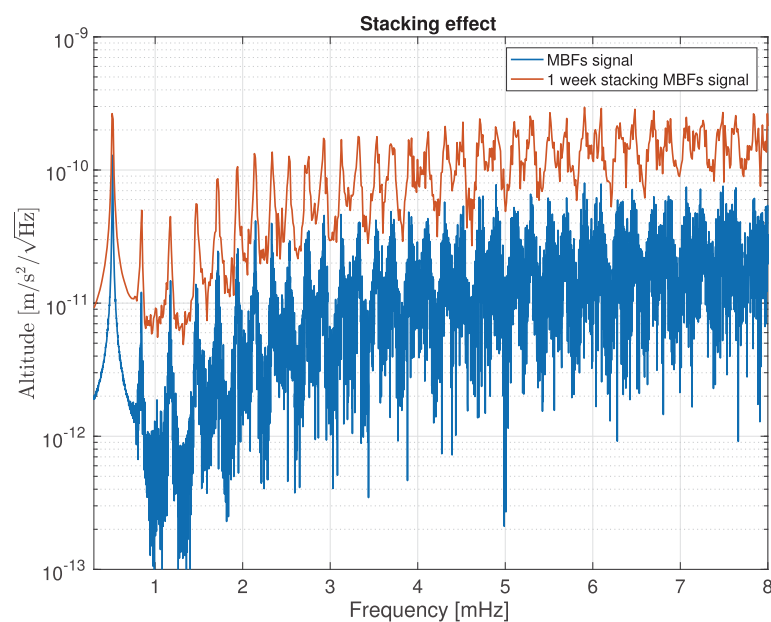


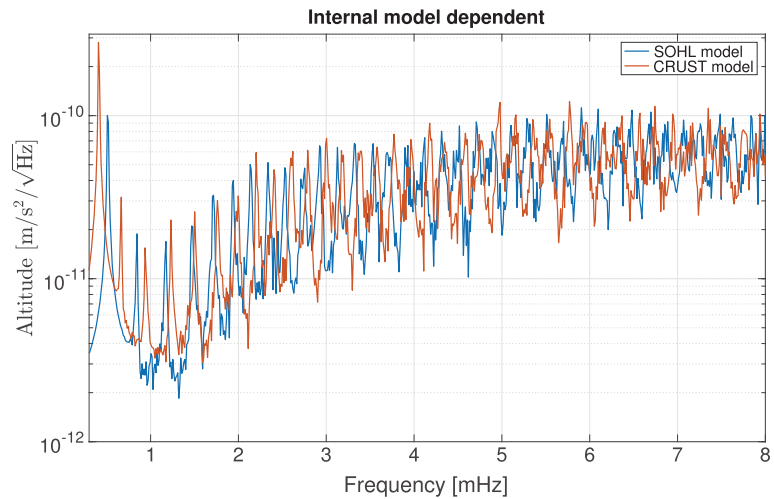
Fig. 18 Stacking efficiency for one week of data. Blue curve is MBF power density. Red line is MBF power density after one week of stacking. Daily stacking leads to large, clear peaks. The longer MBFs are stacked, the larger and sharper the normal mode peaks become. One week of stacking already leads to a significant improvement in the signal-to-noise ratio, which demonstrates that Martian stacking is far more effective than terrestrial stacking. As a result of such efficient stacking for Mars, some MBF peaks are likely to be detected by the InSight SEIS seismometer



to the diurnal cycle through slope-induced circulations, although the day-to-day variability associated with baroclinic waves is small (Spiga et al. 2018). Thus, provided we consider atmospheric variability within a given season, a significant daily repetition of atmospheric temperature, wind, and pressure should be the norm. This will correlate strongly with the diurnal range in our seismic computations derived from GCM simulations (Fig. 17), which means that stacking is likely to be an efficient way to increase the MBF amplitude above that of the self-noise or other noise sources. We tested this hypothesis with a one-week stack from the GCM simulation. The 7 sol-long data were divided into 7 time series of 24.6 hours. The results shown in Fig. 18 indicate a threefold increase in the amplitudes of stacks over 7 sols. Although extrapolation over a long period will require further GCM modeling, and because the sol-to-sol correlation might weaken over weeks, these preliminary results suggest that stacking the seismic signal over the sol time might enable significant to very significant amplification of the Mars hum. Furthermore, detecting the normal mode frequencies will allow the inversion of the Mars upper mantle, as already illustrated by Panning et al. (2017). The position of the normal mode peaks depends on the internal structure, as shown on Fig. 19. These simulations were done with two different internal structure models for Mars and the results show that the resolution after the stacking suffices to adequately shift associated with the structures.

Fig. 19

Internal-model-dependent MBFs. We use two internal models of Mars, which results in differing peak positions. The difference in peak positions corresponds to the difference in the internal structure of Mars, and the seismometer on InSight can detect this difference in frequencies. If we can detect these peaks, we can determine the internal structure of Mars



5 Conclusion

This study evaluates the magnitude of the signal of Mars' background free oscillations by using high-precision GCMs. Given the limitation of GCMs, the values obtained should be regarded as a lower limit of the possible amplitude of background free oscillations expected on Mars.

To obtain a realistic evaluation, we make several assumptions that are based on observations and theory to simplify the model and take into account the three-dimensional atmospheric structure of Mars.

Given these models and assumptions, the results indicate that MBF amplitudes are likely to be on the order of nanogals, which is consistent with previous studies, such as Kobayashi and Nishida (1998b), Lognonné and Johnson (2007). We also confirmed that the values obtained are consistent with solar flux. These results imply that the values obtained represent the typical strength of MBF signals, although the amplitudes may differ because of the assumptions used, such as those involving the internal structure and atmospheric model.

Given the level of MBF signal and the level of noise from the InSight SEIS instruments, detecting MBF signals with the InSight SEIS instruments will remain difficult. However, because the detection strategy exploits the daily repetition of the Martian atmosphere, stacking is found to be a powerful tool to overcome this problem.

The results should be viewed as a minimum estimate for MBF detection by the InSight SEIS seismometer. Knowledge of the Martian MBFs should allow us to estimate the deep internal structure of Mars and can be one of successes of the InSight mission.

Acknowledgements The authors are grateful for the support of CNES for the development of the SEIS experiment and its scientific support, and to the ANR for supporting the project through ANR SEISMARS. Y.K. acknowledges the support of the CNES and JSPC for his Ph.D. support. P.L. and A.S. acknowledge the support of IUF. This is IPGP contribution number 4010 and InSight contribution number 74.

Publisher's Note Springer Nature remains neutral with regard to jurisdictional claims in published maps and institutional affiliations.

References

- G. Backus, M. Mulcahy, Moment tensors and other phenomenological descriptions of seismic sources—I. Continuous displacements. *Geophys. J. Int.* **46**(2), 341–361 (1976)

- H. Benioff, J.C. Harrison, L. LaCoste, W.H. Munk, L.B. Slichter, Searching for the Earth's free oscillations. *J. Geophys. Res.* **64**(9), 1334–1337 (1959)
- H. Benioff, F. Press, S. Smith, Excitation of the free oscillations of the Earth by earthquakes. *J. Geophys. Res.* **66**(2), 605–619 (1961)
- B.A. Bolt, J.S. Derr, Free bodily vibrations of the terrestrial planets. *Vistas Astron.* **11**, 69–102 (1969)
- A. Colaitis, A. Spiga, F. Hourdin, C. Rio, F. Forget, E. Millour, A thermal plume model for the Martian convective boundary layer. *J. Geophys. Res., Planets* **118**(7), 1468–1487 (2013)
- F.A. Dahlen, J. Tromp, *Theoretical Global Seismology* (Princeton University Press, Princeton, 1998)
- M. Deen, E. Wielandt, E. Stutzmann, W. Crawford, G. Barruol, K. Sigloch, First observation of the Earth's permanent free oscillations on ocean bottom seismometers. *Geophys. Res. Lett.* **44**(21), 10,988–10,996 (2017). <https://doi.org/10.1002/2017GL074892>
- A.M. Dziewonski, D.L. Anderson, Preliminary reference Earth model. *Phys. Earth Planet. Inter.* **25**(4), 297–356 (1981)
- F. Forget, S. Lebonnois, Global climate models of the terrestrial planets. *Comp. Climatol. Terr. Planets* **1**, 213–229 (2013)
- F. Forget, F. Hourdin, R. Fournier, C. Hourdin, O. Talagrand, M. Collins, S.R. Lewis, P.L. Read, J-P. Huot, Improved general circulation models of the Martian atmosphere from the surface to above 80 km. *J. Geophys. Res., Planets* **104**(E10), 24155–24175 (1999)
- P. Goldreich, D.A. Keeley, Solar seismology. II. The stochastic excitation of the solar p-modes by turbulent convection. *Astrophys. J.* **212**, 243–251 (1977)
- P. Goldreich, P. Kumar, The interaction of acoustic radiation with turbulence. *Astrophys. J.* **326**(1), 462–478 (1988)
- M.P. Golombek, W.B. Banerdt, K.L. Tanaka, D.M. Tralli, A prediction of Mars seismicity from surface faulting. *Science* **258**(5084), 979–981 (1992)
- T.V. Gudkova, V.N. Zharkov, Mars: interior structure and excitation of free oscillations. *Phys. Earth Planet. Inter.* **142**(1–2), 1–22 (2004)
- B. Gutenberg, C.F. Richter, Earthquake magnitude, intensity, energy, and acceleration: (second paper). *Bull. Seismol. Soc. Am.* **46**(2), 105–145 (1956)
- R.M. Haberle, M.M. Joshi, J.R. Murphy, J.R. Barnes, J.T. Schofield, G. Wilson, M. Lopez-Valverde, J.L. Hollingsworth, A.F.C. Bridger, J. Schaeffer, General circulation model simulations of the Mars Pathfinder atmospheric structure investigation/meteorology data (1999)
- P. Julián, M. Jordán, A. Desages, Canonical piecewise-linear approximation of smooth functions. *IEEE Trans. Circuits Syst. I, Fundam. Theory Appl.* **45**(5), 567–571 (1998)
- V.G. Kaydash, M.A. Kreslavsky, Y.G. Shkuratov, G. Videen, J.F. Bell III., M. Wolff, Measurements of winds on Mars with Hubble Space Telescope images in 2003 opposition. *Icarus* **185**(1), 97–101 (2006)
- B. Kenda, P. Lognonné, A. Spiga, T. Kawamura, S. Kedar, W.B. Banerdt, R. Lorenz, D. Banfield, M. Golombek, Modeling of ground deformation and shallow surface waves generated by Martian dust devils and perspectives for near-surface structure inversion. *Space Sci. Rev.* **211**(1–4), 501–524 (2017)
- A. Khan, J.A.D. Connolly, Constraining the composition and thermal state of Mars from inversion of geophysical data. *LPI Contributions*, No. 1353 (2007), p. 3013
- M. Knapmeyer, J. Oberst, E. Hauber, M. Wählisch, C. Deuchler, R. Wagner, Working models for spatial distribution and level of Mars' seismicity. *J. Geophys. Res., Planets* **111**(E11) (2006)
- N. Kobayashi, K. Nishida, Atmospheric excitation of planetary free oscillations. *J. Phys. Condens. Matter* **10**(49), 11557 (1998a)
- N. Kobayashi, K. Nishida, Continuous excitation of planetary free oscillations by atmospheric disturbances. *Nature* **395**(6700), 357–360 (1998b)
- R.L. Kovach, D.L. Anderson, The interiors of the terrestrial planets. *J. Geophys. Res.* **70**(12), 2873–2882 (1965)
- G. Laske, R. Widmer-Schmidrig, *Treatise on Geophysics, Theory and Observations: Normal Mode and Surface Wave Observations*, vol. 1.04 (Elsevier, Amsterdam, 2015)
- P. Lognonné, Normal modes and seismograms in an anelastic rotating Earth. *J. Geophys. Res., Solid Earth* **96**(B12), 20309–20319 (1991)
- P. Lognonné, Normal modes of the Earth and planets, in *Handbook on Earthquake and Engineering Seismology* (2002), pp. 125–147
- P. Lognonné, Planetary seismology. *Annu. Rev. Earth Planet. Sci.* **33**, 571–604 (2005)
- P. Lognonné, D. Giardini, The NetLander very broad band seismometer. *Planet. Space Sci.* **48**, 1289–1302 (2000)
- P. Lognonné, C.L. Johnson, *Planetary Seismology*, vol. 10.03 (Elsevier, Amsterdam, 2007)
- P. Lognonné, C.L. Johnson, *Planetary Seismology*, vol. 10.03 (Elsevier, Amsterdam, 2015)
- P. Lognonné, B. Mosser, Planetary seismology. *Surv. Geophys.* **14**(3), 239–302 (1993)

- P. Lognonné, B. Mosser, F.A. Dahlen, Excitation of jovian seismic waves by the Shoemaker-Levy 9 cometary impact. *Icarus* **110**(2), 180–195 (1994)
- P. Lognonné, J.G. Beyneix, W.B. Banerdt, S. Cacho, J.F. Karczewski, M. Morand, Ultra broad band seismology on InterMarsNet. *Planet. Space Sci.* **44**(11), 1237–1249 (1996)
- P. Lognonné, E. Clévéde, H. Kanamori, Computation of seismograms and atmospheric oscillations by normal-mode summation for a spherical Earth model with realistic atmosphere. *Geophys. J. Int.* **135**(2), 388–406 (1998a)
- P. Lognonné, V.N. Zharkov, J.F. Karczewski, B. Romanowicz, M. Menvielle, G. Poupinet, B. Brient, C. Cavoit, A. Desautez, B. Dole et al., The seismic optimism experiment. *Planet. Space Sci.* **46**(6–7), 739–747 (1998b)
- P. Lognonné, T. Spohn, D. Mimoun, S. Ulamec, J. Biele, GEP-ExoMars: a geophysics and environment observatory on Mars, in *37th Annual Lunar and Planetary Science Conference*, vol. 37 (2006)
- P. Lognonné, W.T. Pike, V. Tong, R. Garcia, Planetary seismometry, in *Extraterrestrial Seismology* (2015), pp. 36–48
- P. Lognonné, F. Karakostas, L. Rolland, Y. Nishikawa, Modeling of atmospheric-coupled Rayleigh waves on planets with atmosphere: from Earth observation to Mars and Venus perspectives. *J. Acoust. Soc. Am.* **140**(2), 1447–1468 (2016)
- P. Lognonné, W.B. Banerdt, D. Giardini, W.T. Pike, U. Christensen, P. Laudet, S. de Raucourt, P. Zweifel, S. Calcutt, M. Bierwirth, K.J. Hurst, F. Ijpelaan, J.W. Umland, R. Llorca-Cejudo, S.A. Larson, R.F. Garcia, S. Kedar, B. Knapmeyer-Endrun, D. Mimoun, A. Mocquet, M.P. Panning, R.C. Weber, A. Sylvestre-Baron, G. Pont, N. Verdier, L. Kerjean, L.J. Facto, V. Gharakanian, J.E. Feldman, T.L. Hoffman, D.B. Klein, K. Klein, N.P. Onufer, J. Paredes-Garcia, M.P. Petkov, J.R. Willis, S.E. Smrekar, M. Drilleau, T. Gabsi, T. Nebut, O. Robert, S. Tillier, C. Moreau, M. Parise, G. Aveni, S. Ben Charef, Y. Bennour, T. Camus, P.A. Dandonneau, C. Desfoux, B. Lecomte, O. Pot, P. Revuz, D. Mance, J. tenPierick, N.E. Bowles, C. Charalambous, A.K. Delahunty, J. Hurley, R. Irshad, H. Liu, A.G. Mukherjee, I.M. Standley, A.E. Stott, J. Temple, T. Warren, M. Eberhardt, A. Kramer, W. Kühne, E.-P. Miettinen, M. Monecke, C. Aicardi, M. André, J. Baroukh, A. Borrien, A. Bouisset, P. Boutte, K. Brethomé, C. Brysbaert, T. Carlier, M. Deleuze, J.M. Desmarres, D. Dilhan, C. Doucet, D. Faye, N. Faye-Refalo, R. Gonzalez, C. Imbert, C. Larigauderie, E. Locatelli, L. Luno, J.-R. Meyer, F. Mialhe, J.M. Mouret, M. Nonon, Y. Pahn, A. Paillet, P. Pasquier, G. Perez, R. Perez, L. Perrin, B. Pouilloux, A. Rosak, I. Savin de Larclause, J. Sicre, M. Sodki, N. Toulemont, B. Vella, C. Yana, F. Alibay, O.M. Avalos, M.A. Balzer, P. Bhandari, E. Blanco, B.D. Bone, J.C. Bousman, P. Bruneau, F.J. Calef, R.J. Calvet, S.A. D’Agostino, G. de los Santos, R.G. Deen, R.W. Denise, J. Ervin, N.W. Ferraro, H.E. Gengl, F. Grinblat, D. Hernandez, M. Hetzel, M.E. Johnson, L. Khachikyan, J.Y. Lin, S.M. Madzunkov, S.L. Marshall, I.G. Mikellides, E.A. Miller, W. Raff, J.E. Singer, C.M. Sunday, J.F. Villalvazo, M.C. Wallace, D. Banfield, J.A. Rodriguez-Manfredi, C.T. Russell, A. Trebi-Ollennu, J.N. Maki, E. Beucler, M. Böse, C. Bonjour, J.L. Berenguer, S. Ceylan, J. Clinton, V. Conejero, I. Daubar, V. Dehant, P. Delage, F. Euchner, I. Estève, L. Fayon, L. Ferraioli, C.L. Johnson, J. Gagnepain-Beyneix, M. Golombek, A. Khan, T. Kawamura, B. Kenda, P. Labrot, N. Murdoch, C. Pardo, C. Perrin, L. Pou, A. Sauron, D. Savoie, S. Stähler, E. Stutzmann, N.A. Teanby, J. Tromp, M. van Driel, M. Wieczorek, R. Widmer-Schmidrig, J. Wookey, SEIS: Insight’s Seismic Experiment for Internal Structure of Mars. *Space Sci. Rev.* **215**(1), 12 (2019). <https://doi.org/10.1007/s11214-018-0574-6>
- J.-B. Madeleine, F. Forget, E. Millour, L. Montabone, M.J. Wolff, Revisiting the radiative impact of dust on Mars using the LMD global climate model. *J. Geophys. Res., Planets* **116**(E11) (2011)
- G.M. Martínez, C.N. Newman, A. De Vicente-Retortillo, E. Fischer, N.O. Renno, M.I. Richardson, A.G. Fairén, M. Genzer, S.D. Guzewich, R.M. Haberle, A.-M. Harri, O. Kemppinen, M.T. Lemmon, M.D. Smith, M. de la Torre-Juárez, A.R. Vasavada, The modern near-surface Martian climate: a review of in-situ meteorological data from viking to curiosity. *Space Sci. Rev.* **212**(1), 295–338 (2017). <https://doi.org/10.1007/s11214-017-0360-x>
- R. Millot-Langet, E. Clévéde, P. Lognonné, Realistic long period synthetic seismograms using normal modes of a 3d anelastic elliptic rotating Earth, in *EGS General Assembly Conference Abstracts*, vol. 27 (2002)
- D. Mimoun, N. Murdoch, P. Lognonné, T. Pike, K. Hurst et al. (SEIS Team), The seismic noise model of the InSight mission to Mars. *Space Sci. Rev.* (2016)
- L. Montabone, F. Forget, E. Millour, R.J. Wilson, S.R. Lewis, B. Cantor, D. Kass, A. Kleinböhl, M.T. Lemmon, M.D. Smith et al., Eight-year climatology of dust optical depth on Mars. *Icarus* **251**, 65–95 (2015)
- J.P. Montagner, *Treatise on Geophysics, Deep Earth Structure: Upper Mantle Structure: Global Isotropic and Anisotropic Elastic Tomography*, vol. 1.19 (Elsevier, Amsterdam, 2015)
- N. Murdoch, B. Kenda, T. Kawamura, A. Spiga, P. Lognonné, D. Mimoun, W.B. Banerdt, Estimations of the seismic pressure noise on Mars determined from Large Eddy Simulations and demonstration of pressure decorrelation techniques for the InSight mission. *Space Sci. Rev.* **211**(1–4), 457–483 (2017)

- J.R. Murphy, C.B. Leovy, J.E. Tillman, Observations of Martian surface winds at the Viking Lander 1 site. *J. Geophys. Res., Solid Earth* (1978–2012) **95**(B9), 14555–14576 (1990)
- T. Navarro, J.-B. Madeleine, F. Forget, A. Spiga, E. Millour, F. Montmessin, A. Määttänen, Global climate modeling of the Martian water cycle with improved microphysics and radiatively active water ice clouds. *J. Geophys. Res., Planets* **119**(7), 1479–1495 (2014)
- K. Nishida, Earth's background free oscillations. *Annu. Rev. Earth Planet. Sci.* **41**, 719–740 (2013a)
- K. Nishida, Global propagation of body waves revealed by cross-correlation analysis of seismic hum. *Geophys. Res. Lett.* **40**(9), 1691–1696 (2013b)
- K. Nishida, Source spectra of seismic hum. *Geophys. J. Int.* **199**(1), 416–429 (2014)
- K. Nishida, Ambient seismic wave field. *Proc. Jpn. Acad. Ser. B* **93**(7), 423–448 (2017)
- K. Nishida, N. Kobayashi, Y. Fukao, Resonant oscillations between the solid earth and the atmosphere. *Science* **287**(5461), 2244–2246 (2000)
- K. Nishida, J.-P. Montagner, H. Kawakatsu, Global surface wave tomography using seismic hum. *Science* **326**(5949), 112 (2009)
- E.A. Okal, D.L. Anderson, Theoretical models for Mars and their seismic properties. *Icarus* **33**(3), 514–528 (1978)
- M.P. Panning, P. Lognonné, W.B. Banerdt, R. García, M. Golombek, S. Kedar, B. Knapmeyer-Endrun, A. Mocquet, N.A. Teanby, J. Tromp et al., Planned products of the Mars structure service for the InSight mission to Mars. *Space Sci. Rev.* **211**(1–4), 611–650 (2017)
- A. Petrosyan, B. Galperin, S.E. Larsen, S.R. Lewis, A. Määttänen, P.L. Read, N. Renno, L.P.H.T. Rogberg, H. Savijärvi, T. Siili et al., The Martian atmospheric boundary layer. *Rev. Geophys.* **49**(3) (2011)
- R.J. Phillips, R.E. Grimm, Martian seismicity, in *Lunar and Planetary Science Conference*, vol. 22 (1991), pp. 1061–1062
- A. Pottier, F. Forget, F. Montmessin, T. Navarro, A. Spiga, E. Millour, A. Szantai, J.-B. Madeleine, Unraveling the Martian water cycle with high-resolution global climate simulations. *Icarus* (2017). <https://doi.org/10.1016/j.icarus.2017.02.016>
- P.L. Read, S.R. Lewis, *The Martian Climate Revisited: Atmosphere and Environment of a Desert Planet* (Springer, Berlin, 2004)
- J. Rhie, B. Romanowicz, Excitation of Earth's continuous free oscillations by atmosphere–ocean–seafloor coupling. *Nature* **431**(7008), 552 (2004)
- J. Rhie, B. Romanowicz, A study of the relation between ocean storms and the Earth's hum. *Geochem. Geophys. Geosyst.* **7**(10) (2006)
- A. Rivoldini, T. Van Hoolst, O. Verhoeven, A. Mocquet, V. Dehant, Geodesy constraints on the interior structure and composition of Mars. *Icarus* **213**(2), 451–472 (2011)
- B.A. Romanowicz, B.J. Mitchell, *Treatise on Geophysics, Deep Earth Structure: Q of the Earth from Crust to Core*, vol. 1.19 (Elsevier, Amsterdam, 2015)
- M. Schimmel, E. Stutzmann, J. Gallart, Using instantaneous phase coherence for signal extraction from ambient noise data at a local to a global scale. *Geophys. J. Int.* **184**(1), 494–506 (2011). <https://doi.org/10.1111/j.1365-246X.2010.04861.x>
- M. Schimmel, E. Stutzmann, S. Ventosa, Low-frequency ambient noise autocorrelations: waveforms and normal modes. *Seismol. Res. Lett.* **89**(4), 1488–1496 (2018). <https://doi.org/10.1785/0220180027>
- J.T. Schofield, J.R. Barnes, D. Crisp, R.M. Haberle, S. Larsen, J.A. Magalhaes, J.R. Murphy, A. Seiff, G. Wilson, The Mars Pathfinder atmospheric structure investigation/meteorology (ASI/MET) experiment. *Science* **278**(5344), 1752–1758 (1997)
- S.E. Smrekar, P. Lognonné, T. Spohn, W.B. Banerdt, D. Breuer, U. Christensen, V. Dehant, M. Drilleau, W. Folkner, N. Fuji, R.F. Garcia, D. Giardini, M. Golombek, M. Grott, T. Gudkova, C. Johnson, A. Khan, B. Langlais, A. Mittelholz, A. Mocquet, R. Myhill, M. Panning, C. Perrin, T. Pike, A.-C. Plesa, A. Rivoldini, H. Samuel, S.C. Stähler, M. van Driel, T. Van Hoolst, O. Verhoeven, R. Weber, M. Wieczorek, Pre-mission InSights on the Interior of Mars. *Space Sci. Rev.* **215**(1), 3 (2018). <https://doi.org/10.1007/s11214-018-0563-9>
- F. Sohl, T. Spohn, The interior structure of Mars: implications from SNC meteorites. *J. Geophys. Res., Planets* **102**, 1613–1635 (1997)
- S.C. Solomon, D.L. Anderson, W.B. Banerdt, R.G. Butler, P.M. Davis, F.K. Duennebier, Y. Nakamura, E.A. Okal, R.J. Phillips, Scientific rationale and requirements for a global seismic network on Mars (1991)
- A. Spiga, Elements of comparison between Martian and terrestrial mesoscale meteorological phenomena: katabatic winds and boundary layer convection. *Planet. Space Sci.* **59**(10), 915–922 (2011)
- A. Spiga, F. Forget, A new model to simulate the Martian mesoscale and microscale atmospheric circulation: validation and first results. *J. Geophys. Res., Planets* **114**(E2) (2009)
- A. Spiga, S.R. Lewis, Martian mesoscale and microscale wind variability of relevance for dust lifting. *Mars* **5**, 146–158 (2010)

- A. Spiga, D. Banfield, N.A. Teanby, F. Forget, A. Lucas, B. Kenda, J.A. Rodriguez Manfredi, R. Widmer-Schmidrig, N. Murdoch, M.T. Lemmon, R.F. Garcia, L. Martire, Ö. Karatekin, S. Le Maistre, B. Van Hove, V. Dehant, P. Lognonné, N. Mueller, R. Lorenz, D. Mimoun, S. Rodriguez, É. Beucler, I. Daubar, M.P. Golombek, T. Bertrand, Y. Nishikawa, E. Millour, L. Rolland, Q. Brissaud, T. Kawamura, A. Mocquet, R. Martin, J. Clinton, É. Stutzmann, T. Spohn, S. Smrekar, W.B. Banerdt, Atmospheric science with InSight. *Space Sci. Rev.* **214**, 109 (2018). <https://doi.org/10.1007/s11214-018-0543-0>
- T. Spohn, M.H. Acuña, D. Breuer, Geophysical constraints on the evolution of Mars. *Space Sci. Rev.* **96**, 231–262 (2001)
- N. Suda, K. Nawa, Y. Fukao, Earth's background free oscillations. *Science* **279**(5359), 2089–2091 (1998)
- T. Tanimoto, Continuous free oscillations: atmosphere-solid earth coupling. *Annu. Rev. Earth Planet. Sci.* **29**(1), 563–584 (2001)
- T. Tanimoto, The oceanic excitation hypothesis for the continuous oscillations of the Earth. *Geophys. J. Int.* **160**(1), 276–288 (2005)
- T. Tanimoto, J. Um, Cause of continuous oscillations of the Earth. *J. Geophys. Res., Solid Earth* **104**(B12), 28723–28739 (1999)
- V.C.H. Tong, R.A. García, *Extraterrestrial Seismology* (Cambridge University Press, Cambridge, 2015)
- T. Van Hoolst, V. Dehant, F. Roosbeek, P. Lognonné, Tidally induced surface displacements, external potential variations, and gravity variations on Mars. *Icarus* **161**(2), 281–296 (2003)
- S. Ventosa, M. Schimmel, E. Stutzmann, Extracting surface waves, hum and normal modes: time-scale phase-weighted stack and beyond. *Geophys. J. Int.* **211**(1), 30–44 (2017). <https://doi.org/10.1002/2017JB014354>
- S. Watada, H. Kanamori, Acoustic resonant oscillations between the atmosphere and the solid earth during the 1991 Mt. Pinatubo eruption. *J. Geophys. Res. Solid Earth* **115**(B12) (2010)
- S. Watada, G. Masters, Oceanic excitation of the continuous oscillations of the Earth, in *AGU Fall Meeting Abstracts* (2001), art. S32A-0620
- S.C. Webb, The Earth's hum is driven by ocean waves over the continental shelves. *Nature* **445**(7129), 754 (2007)
- J.H. Woodhouse, A. Deuss, *Theory and Observations – Earth's Free Oscillations*, vol. 1.03 (Elsevier, Amsterdam, 2015)
- V.N. Zharkov, T.V. Gudkova, On the dissipative factor of the Martian interiors. *Planet. Space Sci.* **45**(4), 401–407 (1997)

ANNEXE4

EVALUATION OF DEEP MOONQUAKE SOURCE PARAMETERS : IMPLICATION
FOR FAULT CHARACTERISTICS AND THERMAL STATE

RESEARCH ARTICLE

10.1002/2016JE005147

Key Points:

- Reevaluated source parameters of deep moonquakes through spectral analyses with combined spectra from long- and short-period seismic records of Apollo
- Deep moonquake faults are better explained with a self-affine model than a self-similar model and likely to be smoother than terrestrial faults
- Brittle-ductile transition temperature was reevaluated and was compared to temperature profiles of the Moon

Correspondence to:

T. Kawamura,
kawamura@ipgp.fr;
t.kawamura@nao.ac.jp

Citation:

Kawamura, T., P. Lognonné,
Y. Nishikawa, and S. Tanaka (2017),
Evaluation of deep moonquake source
parameters: Implication for fault
characteristics and thermal state,
J. Geophys. Res. Planets, 122, 1487–1504,
doi:10.1002/2016JE005147.

Received 1 AUG 2016

Accepted 16 JUN 2017

Accepted article online 22 JUN 2017

Published online 18 JUL 2017

Evaluation of deep moonquake source parameters: Implication for fault characteristics and thermal state

Taichi Kawamura^{1,2}, Philippe Lognonné¹, Yasuhiro Nishikawa^{1,3}, and Satoshi Tanaka⁴

¹Institut de Physique du Globe de Paris, Université Paris Diderot–Sorbonne Paris Cité, Paris, France, ²National Astronomical Observatory of Japan, Oshu City, Japan, ³Department of Earth and Planetary Science, The University of Tokyo, Bunkyo, Japan, ⁴Institute of Space and Astronautical Science, Japan Aerospace Exploration Agency, Sagami-hara, Japan

Abstract While deep moonquakes are seismic events commonly observed on the Moon, their source mechanism is still unexplained. The two main issues are poorly constrained source parameters and incompatibilities between the thermal profiles suggested by many studies and the apparent need for brittle properties at these depths. In this study, we reinvestigated the deep moonquake data to reestimate its source parameters and uncover the characteristics of deep moonquake faults that differ from those on Earth. We first improve the estimation of source parameters through spectral analysis using “new” broadband seismic records made by combining those of the Apollo long- and short-period seismometers. We use the broader frequency band of the combined spectra to estimate corner frequencies and DC values of spectra, which are important parameters to constrain the source parameters. We further use the spectral features to estimate seismic moments and stress drops for more than 100 deep moonquake events from three different source regions. This study revealed that deep moonquake faults are extremely smooth compared to terrestrial faults. Second, we reevaluate the brittle-ductile transition temperature that is consistent with the obtained source parameters. We show that the source parameters imply that the tidal stress is the main source of the stress glut causing deep moonquakes and the large strain rate from tides makes the brittle-ductile transition temperature higher. Higher transition temperatures open a new possibility to construct a thermal model that is consistent with deep moonquake occurrence and pressure condition and thereby improve our understandings of the deep moonquake source mechanism.

Plain Language Summary Apollo seismic observation discovered that the Moon is seismically active and the observation detected more than 13000 seismic events. Among the detected events, most frequently observed seismic events are deep moonquakes that occur at 800–1200 km depth in the Moon. Although intensive studies have been carried out for decades, why and how deep moonquakes occur are remaining mysteries. One of the reasons is that the magnitude of the deep moonquake fault and the speed of the seismic slip are unclear. In this study, we reinvestigated the deep moonquake data to reveal their fault characteristics. While previous studies mainly used the long-period seismometer records, we also used the short-period seismic records of Apollo to improve the estimation. This enabled us to study more than 100 deep moonquakes events while only one event was studied in the previous study. With 131 deep moonquakes, we carried out comparative and statistic study of the fault characteristics. Our study revealed that the deep moonquake faults are much smoother compared to the terrestrial counterparts and the stress release of the event is as low as the tidal stress between the Earth and the Moon. The correlation between the deep moonquake occurrence and tidal stress has been pointed out and our study supports the idea that the tidal stress is not only triggering the deep moonquakes but also responsible of the whole stress release of the seismic activity.

1. Introduction

Deep moonquakes are the most frequently observed seismic events on the Moon, and more than 7000 events were detected during the Apollo seismic experiment (July 1969 to September 1977) [Nakamura, 2003] (Figure 1). In spite of the many recorded deep moonquake events, the exact nature of deep moonquake occurrence remains to be understood. Understanding the source mechanisms of deep moonquakes will open a window on the mechanical and thermal conditions of the deep interior of the Moon and will provide a unique opportunity to observe active features of the deep interior of the Moon. Deep moonquake source

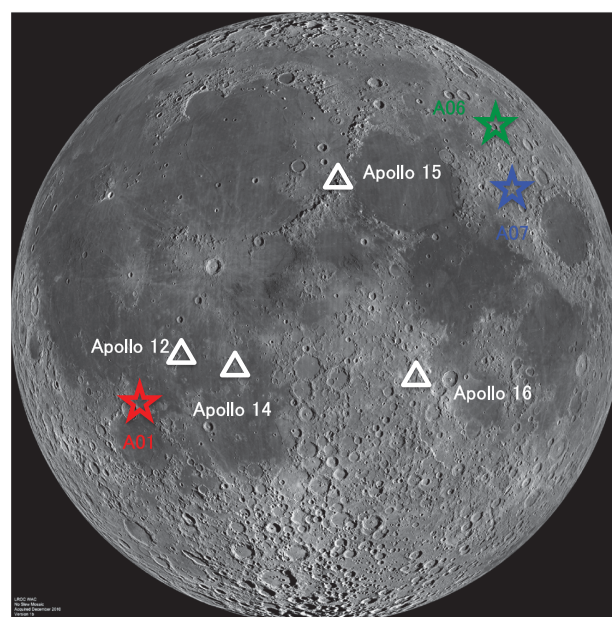


Figure 1. Geometric configuration of Apollo seismic stations and deep moonquake source regions. The lunar globe was taken from Lunar Reconnaissance Orbiter Camera (LROC) observation courtesy of NASA (<http://photojournal.jpl.nasa.gov/catalog/PIA14011>). Apollo stations and deep moonquake nests were added by the authors.

regions are located between depths of 750 and 1200 km in the most recent analyses [Khan and Mosegaard, 2002; Lognonné et al., 2003; Nakamura, 2003]. They occur periodically with the tides raised on the Moon by the Earth and the Sun at well-defined nests, suggesting their triggering by the terrestrial tide [e.g., Lammlein, 1977].

Various studies have evaluated the tidal stress acting on deep moonquake source regions [Toksöz et al., 1977; Cheng and Toksöz, 1978; Minshull and Goult, 1988; Weber et al., 2009]. While these studies succeeded in giving quantitative estimates of the tidal stress, they were not able to fully describe the source activity of deep moonquakes. Among the reasons for this are the poor constraints on the source parameters of deep moonquakes, such as seismic moment and stress drop that result from both the poor data quality of Apollo and the deep moonquakes' low magnitudes [Goins et al., 1981].

The aim of this study is to revisit the Apollo seismic data and carry out an improved estimation of seismic moments and stress drops of deep moonquakes, which will provide new constraints on the source mechanism including mechanical and thermal conditions at the depth of the deep moonquakes. Better understanding of the source mechanisms of deep moonquakes and comparison of the tidal strain/stress drop ratio with respect to the brittle-ductile transition are critical for understanding the lunar seismic activity.

1.1. Existing Problems of the Deep Moonquake Source Mechanism

Two major issues regarding the investigation of the deep moonquake source mechanism still exist. The first is the relation between stress drop, tidal stress, and lithostatic pressure. Only the study by Goins et al. [1981] quantitatively evaluated the source parameters of deep moonquakes and estimated the source parameters for the largest event from the A01 deep moonquake. They obtained a stress drop of approximately 0.01 MPa and a seismic moment of 5×10^{13} Nm. Although previous studies claim that the normal and shear tidal stress (0.1–0.01 MPa) [Toksöz et al., 1977; Cheng and Toksöz, 1978; Minshull and Goult, 1988; Weber et al., 2009] are in good agreement with such a stress drop, how such a slip with a small stress drop is triggered under high lithostatic pressure (~4 GPa) still remains unclear. Goins et al. [1981] considered only one deep moonquake event. Therefore, whether the values are representative of all deep moonquakes or they should be regarded as an outlier estimated with the largest event is unclear. To better understand the characteristics of deep moonquakes, providing estimates for a larger number of events and having a global and statistical view of the source parameters are important.

The second issue concerns the thermal conditions of the source region. Several studies have proposed thermal profiles of the Moon, suggesting that the temperature of the deep moonquake source region is too high for it to be in a brittle regime [e.g., Gagnepain-Beyneix et al., 2006; Khan et al., 2014]. The recent discovery of the liquid state of the lunar core [Weber et al., 2011; Garcia et al., 2011] and strong tidal heating and/or partial melting at the base of the mantle [Harada et al., 2014; Khan et al., 2014] also suggests high temperatures at the lunar core mantle boundary. At such temperatures (1500–1600 K) and pressures (~4 GPa), the source regions are likely to be in a ductile regime, and an ordinary brittle fracture is not likely to be possible.

Seismic activity in ductile conditions is also observed on Earth [e.g., Ye *et al.*, 2016; Frohlich and Nakamura, 2009]. Comparison between deep moonquakes and intermediate-depth earthquakes is discussed in detail in Frohlich and Nakamura [2009]. In terms of pressure, deep moonquakes correspond to intermediate-depth earthquakes at a depth of 100–135 km. Both cases occur at the pressure and temperature conditions wherein ordinary brittle fracture is unlikely. On Earth, these intermediate-depth earthquakes are now recognized as those occurring in the cold, stressed, subducting lithosphere [Frohlich and Nakamura, 2009]. Several models have been proposed for the possible source mechanisms for such intermediate-depth earthquakes. The first model is transformational faulting, which is related to the phase transition of minerals [Hacker *et al.*, 2003]. However, this model is not suitable for the mechanism of deep moonquakes because based on the pressure and temperature conditions of the source regions, any phase transformation is not likely to occur [e.g., Khan *et al.*, 2007; Kuskov and Kronrod, 2009]. The second is plastic or melt instabilities [Hacker *et al.*, 2003]. This model is mainly used to explain deep earthquakes at >300 km depth, where the pressure and temperature are higher than those of deep moonquake source regions. There is no clear evidence of its application to intermediate-depth earthquakes [Hacker *et al.*, 2003]. Whether this model can explain the source mechanism of deep earthquakes is not evident. Thus, its application to deep moonquakes also needs to be carefully considered. The third is dehydration embrittlement, which is expected to occur when minerals release a fluid that increases the pore pressure [Hacker *et al.*, 2003]. This is a widely accepted explanation for seismicity in a subduction zone, where water contents are 0.1–5 wt %. Recent discovery of water on the Moon [e.g., Saal *et al.*, 2008] questions whether the lunar interior is dry; however, the expected water content in the subduction zone is considerably lower than that in the terrestrial subduction zones wherein dehydration embrittlement plays a significant role. Thus, although several studies suggest possible explanations for intermediate-depth earthquakes, applying them to explain the seismicity of deep moonquakes is difficult.

1.2. Outline of This Study

In this study, we first perform spectral analysis of Apollo seismic data and use the obtained source parameters to reevaluate the thermal conditions of the source regions. The analysis method followed here is outlined in the scheme shown in Figure 2. First, spectral analyses of Apollo seismic data are performed for estimating the spectral features of deep moonquake spectra to constrain the source time function of deep moonquakes (section 2). Assuming that deep moonquakes are fault activities that can be expressed with double-coupled force, we estimate the stress drops of deep moonquakes from the source time functions (section 3). With the obtained stress, which is comparable to the tidal stress, we assume that the main source of stress glut, causing deep moonquakes, is tidal stress. Next, we estimate the brittle-ductile transition temperature for deep moonquakes using tidal strain rates (sections 4.1–4.3). Following the discussion in section 1.1 and with analogy to intermediate-depth earthquakes, we assume that deep moonquakes are triggered via brittle fractures in the source regions. To quantitatively compare the existing temperature models of the Moon and the brittle-ductile transition temperature, reevaluation of the transition temperature is essential. The obtained transition temperature will then be used to constrain the temperature profile inside the Moon (section 4.3). Assuming that deep moonquakes occur as a result of brittle fractures on faults, the temperature in the deep moonquake source regions is required to be lower than the transition temperature. We compared the obtained brittle-ductile temperature with several temperature profiles of the Moon proposed in previous studies to test whether the transition temperature is compatible with the existing models (section 4.4).

2. Data Processing

The rupture signature of deep moonquakes can be extracted from the source time function within seismic spectra. However, the limited frequency band and instrument sensitivity of the Apollo seismometers have prevented detailed spectral analysis. In addition to this, the spectral features are masked by the propagation and site reverberation effects, the latter being large on the Moon due to the high scattering and low attenuation. We overcome these difficulties by (1) combining Apollo long-period (LP) and short-period (SP) data to obtain the equivalent of broadband data, (2) stacking the signals for the same pair of stations and deep moonquake nests to evaluate the nonseismic source term within the spectra, and (3) applying a correction factor to account for the energy redistributed into the coda by the intense scattering [e.g., Goins *et al.*, 1981].

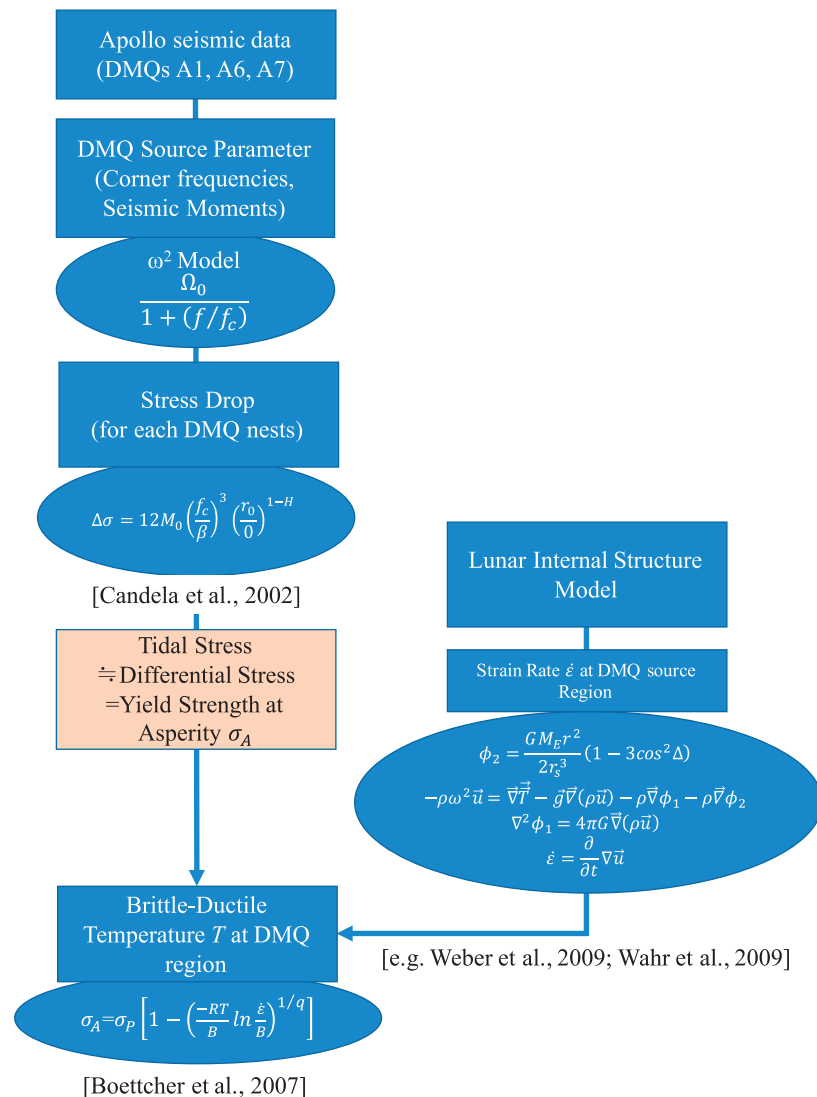


Figure 2. Flowchart of the data processing carried out in this study.

2.1. Recombination of Long-Period (LP) and Short-Period (SP) Seismic Data

While estimation of the source parameters through spectral analysis has already been performed by *Goins et al.* [1981], it suffered from the limited frequency band of the LP Apollo seismometer. The corner frequencies of seismic records are an important parameter that quantifies the source parameters such as slip time, seismic moment, and seismic energy release. *Goins et al.* [1981] evaluated the corner frequency of the largest deep moonquake with LP data and reported 1 Hz for the corner frequency. However, this value is close to the upper limit of the LP frequency band and may contain large uncertainties, especially when the true corner frequency is higher (Figure 3). Each Apollo Lunar Surface Experiment Package also contained one vertical SP seismometer, and the Apollo LP and SP seismometers cover different frequency bands with some overlap (Figure 3; LP: 0.1–1.5 Hz and SP: 1–10 Hz). Since stress drops of seismic activities are proportional to the corner frequency with a power of 3, a small difference in the corner frequencies can result in a large difference in the stress drops [e.g., *Aki and Richards*, 2002; *Goins et al.*, 1981]. We will take advantage of the overlap of LP and SP frequency band and numerically combine the two data streams to obtain a single broadband data stream and complete continuous spectra that cover both frequency bands of LP and SP data. This will enable us to carry out the spectral analysis with the wider frequency band necessary to improve the estimation of

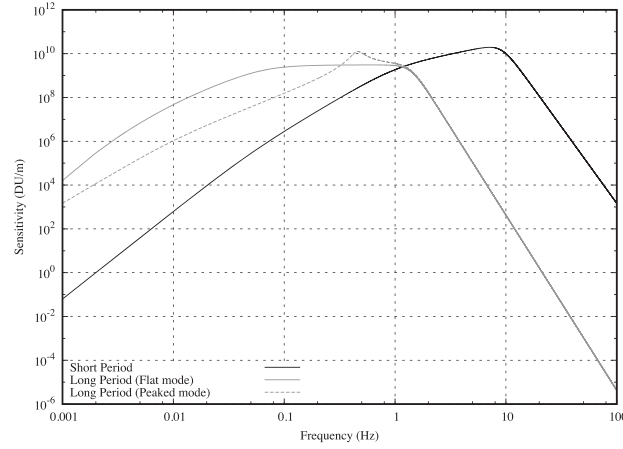


Figure 3. Instrument response of Apollo seismometers of long and short periods. The black curve refers to the short periods, and the gray curves refer to the long-period seismometer, respectively. Since the long-period seismometer had two observation modes (flat and peaked modes), two curves are shown for the long-period seismometer. The bold and dashed curves represent the flat and broad modes, respectively.

tra (typically 30–60 s) and data about 5–10 min before the signal was used for the noise evaluation (data without gaps, glitch, or spikes were chosen). We used signal arrival from the moonquake catalog on Nakamura [1992], and this was used as reference time throughout the analyses. For the best $S(\omega)$, we need $\frac{dI}{dS} = 0$.

$$\frac{dI}{dS} = \frac{d}{dS} \left\{ \frac{(d_{LP}(\omega) - T_{LP}(\omega)S(\omega)) - (d_{LP}(\omega) - T_{LP}(\omega)S(\omega))}{\sigma_{LP}^2(\omega)} + \frac{(d_{SP}(\omega) - T_{SP}(\omega)S(\omega)) - (d_{SP}(\omega) - T_{SP}(\omega)S(\omega))}{\sigma_{SP}^2(\omega)} \right\} \quad (2)$$

$$= \left(\frac{\|T_{LP}(\omega)\|^2}{\sigma_{LP}^2(\omega)} + \frac{\|T_{SP}(\omega)\|^2}{\sigma_{SP}^2(\omega)} \right) S(\omega) - \frac{T_{LP}(\omega) - d_{LP}(\omega)}{\sigma_{LP}^2(\omega)} - \frac{T_{SP}(\omega) - d_{SP}(\omega)}{\sigma_{SP}^2(\omega)}$$

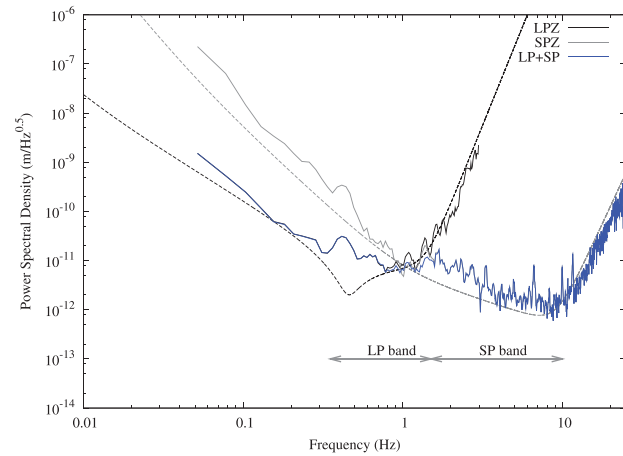


Figure 4. Example of the hybrid broadband spectrum composed of LP and SP combined data. The plot shows the combined spectrum from deep moonquake event A06 (20 May 1976, 17:35). Spectra from the LP and SP narrowband seismometers are shown together with the hybrid broadband spectrum for comparison. The dashed line shows the noise level of the seismometer. Outside the frequency bands, the obtained spectra are comparable to the instrumental noise and show similar trends.

corner frequency and seismic moment. We do this through a least squares method, by finding the best spectrum $S(\omega)$ that minimizes residual I ,

$$I = \frac{\|d_{LP}(\omega) - T_{LP}(\omega)S(\omega)\|^2}{\sigma_{LP}^2(\omega)} + \frac{\|d_{SP}(\omega) - T_{SP}(\omega)S(\omega)\|^2}{\sigma_{SP}^2(\omega)} \quad (1)$$

where $d_{LP}(\omega)$ and $d_{SP}(\omega)$ are the data from LP and SP seismometers, respectively; $T_{LP}(\omega)$ and $T_{SP}(\omega)$ are the transfer functions; σ_i^2 represents the instrument noise; ω is the frequency; and the $\| \cdot \|$ indicates the absolute value. The noise was estimated from the data with no seismic events, corresponding to the data just before the examined event. The time window was fixed to the same value as the window used to evaluate the signal spec-

The bar above $d_i(\omega)$, $T_i(\omega)$, and $S(\omega)$ refers to the complex conjugate. This gives us

$$S(\omega) = \frac{T_{LP}(\omega) - d_{LP}(\omega)/\sigma_{LP}^2(\omega) + T_{SP}(\omega) - d_{SP}(\omega)/\sigma_{SP}^2(\omega)}{\|T_{LP}(\omega)\|^2/\sigma_{LP}^2(\omega) + \|T_{SP}(\omega)\|^2/\sigma_{SP}^2(\omega)} \quad (3)$$

An example of a combined spectrum is shown in Figure 4. The high-frequency components and low-frequency components are mainly constrained with SP and LP spectra, respectively, and we can see that the combined spectrum covers the frequency band of the two seismometers. To run the combination, the LP and SP seismometers need to be aligned and be on the same axis. Since only the vertical (Z) axis is available for the SP, this approach is only possible on the vertical axis. Furthermore, since there were some malfunctions on SPZ and LPZ axes for station 12 and station 14, this processing is possible only with data from stations 15 and 16 (Figure 1).

2.2. Spectral Parameters and Source Time Function

For the source time function $A^{\text{source}}(f)$, we use ω^2 model, which is a well-accepted model in terrestrial seismology [Aki and Richards, 2002] expressed as

$$A^{\text{source}}(f) = \frac{\Omega_0}{1 + (f/f_c)^2} \quad (4)$$

where f_c is a corner frequency and Ω_0 is the DC value of the spectrum. This shows that the seismic spectra are flat up to the corner frequency and rolls-off by the power of 2 at higher frequencies. The ω^2 model was developed for far-field displacement excited by a slip on a fault, which assumes a double-couple force as the seismic source. The model adopts the Haskell fault model where a rupture is expressed as a boxcar function whose width is given by the risetime and the duration of the rupture. The simple fault model predicts a spectral feature as described in the ω^2 model and it explains terrestrial observations very well [see reviews, e.g., Aki and Richards, 2002; Shearer, 2009, and references therein]. In addition to the source time function, seismic spectra contain the information on the effects of propagation and site reverberation, which are observed in the form of intense scattering and a strong coda of the seismogram [Aki and Richards, 2002]. In order to account for these effects, we express the observed spectrum $A^{\text{source}}(f)$ based on a theoretical model as follows:

$$A(f) = A^{\text{source}}(f) \times \exp\left(-\frac{\pi ft}{Q}\right) \times R_{\text{local}} \times R_{\text{raypath}} + \text{noise} \quad (5)$$

The first term is the source time function described previously. The second term accounts for the anelastic attenuation, where Q is the attenuation factor and t is the travel time. R_{local} and R_{raypath} represent the local effect or station function and the effect depending on the raypath between the source and the station.

2.3. Spectral Stacking

For better estimation of the source parameters, the nonseismic source term should be well constrained. While the source time function varies for each event, the nonseismic source component can be regarded as being almost identical when we fix a pair of station and seismic sources. Since deep moonquakes occur repeatedly at certain nests, we were able to stack the data to evaluate the nonseismic source component. First, a tentative corner frequency f'_c and tentative DC value Ω'_0 are assigned to each event

$$A_i(f) = A_i^{\text{source}}(f; \Omega'_0, f'_c) \times \exp\left(-\frac{\pi ft}{Q}\right) \times R_{\text{local}} \times R_{\text{raypath}} + \text{noise} \quad (6)$$

where i represents the i th event for a station-seismic source pair. With the tentative value, we calculated the source time function and eliminate the term by dividing the spectrum with the source time function, leaving only the source-station-dependent term and the noise on the left hand.

$$\frac{A_i(f)}{A_i^{\text{source}}(f; \Omega'_0, f'_c)} = \exp\left(-\frac{\pi ft}{Q}\right) \times R_{\text{local}} \times R_{\text{raypath}} + \text{noise}/A_i^{\text{source}}(f; \Omega'_0, f'_c) \quad (7)$$

By stacking this for all events for a certain pair of source and station, we can extract the source-station-dependent term. Statistically speaking, we can expect that the noise will be reduced by the root square of the number of the events stacked, if we assume that the noise is purely random [e.g., Baker, 1999]. After stacking n events, we obtain

$$\frac{1}{n} \sum \frac{A_i(f)}{A_i^{\text{source}}(f; \Omega'_0, f'_c)} = \exp\left(-\frac{\pi ft}{Q}\right) \times R_{\text{local}} \times R_{\text{raypath}} + \frac{1}{n} \sum \text{noise}/A_i^{\text{source}}(f; \Omega'_0, f'_c) \quad (8)$$

where it is expected that $\frac{1}{n} \sum \text{noise}/A_i^{\text{source}}(f; \Omega'_0, f'_c) \ll \exp\left(-\frac{\pi ft}{Q}\right) \times R_{\text{local}} \times R_{\text{raypath}}$. The right-hand term can be regarded as the response between the source and the station including all the nonseismic source effects, such as local effects during the propagation or noise and spikes of instrumental origin. This response was used to correct the observed spectrum so that we can extract the source time function from the data. Using this corrected spectrum, we reestimate f_c and Ω_0 . By running this process iteratively, we can refine the estimation of f_c and Ω_0 . For the first iteration, we need to give some tentative values for f_c and Ω_0 as initial values, which were expressed as f'_c and Ω'_0 above.

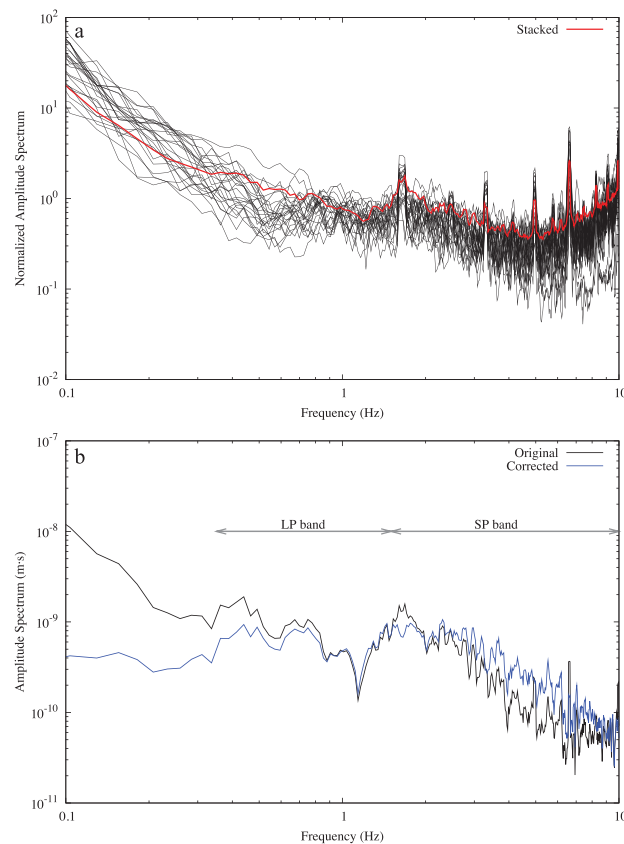


Figure 5. Stacking of background spectrum and background correction. (a) All the individual spectra (black) and the stacked spectrum (red). We see that peaks and spikes that are common among the spectra are also present in the stacked spectrum. (b) An example of the correction carried out for the seismic spectrum. Spikes (e.g., 1.5, 5, and 7 Hz) are removed by the correction and attenuation is also corrected with the data processing.

2.4. Correction of Scattering Effect

Intense scattering is one of the characteristic features of lunar seismograms, and a significant amount of energy is redistributed into its coda [Dainty *et al.*, 1974]. This point needs to be taken into account for estimation of the seismic moment. A previous study [Goins *et al.*, 1981] treated this problem by introducing a correction factor estimated from amplitude decay of coda. We took a similar approach and applied a correction factor to our estimation. Figure 6 shows the absolute value of the amplitude of the largest A06 event observed at the station 16. The blue shaded portion of the waveform refers to the time window we used to estimate f_c and Ω_0 . We expect that the signal is less contaminated by reflected and scattered signal at its first arrival. We therefore used the first data strip and correct for the redistribution of the energy using the following process. We divided the seismic signal into smaller segments with the same width as the reference time windows. Figure 6 demonstrates an example of data segments used in the analyses. The blue shaded segment of the data, which starts from the reported signal arrival [Nakamura, 1992], was first used to estimate f_c and Ω_0 . Then, a Fourier transform was applied on each data segment and the Ω_0 was estimated for each data segment. The time variation of Ω_0 is shown in Figure 6. This time variation of Ω_0 was used to correct the seismic moment that was evaluated with the first segment. The variation of Ω_0 shows good correlation with the amplitude of the waveform and the signal level exceeds the noise level 300–800 s after the signal start. We assume that Ω_0 degrades linearly and express the variation of Ω_0 with time with a linear function by fitting the data. We assume that the seismic energy is contained in the seismic signal until the Ω_0 reaches 0. In other words, we assume that the seismic energy is redistributed inside the triangle bounded by x axis, signal arrival, and the degrading function of Ω_0 estimated previously. This triangle is shown as a

We started the inversion with initial values f'_c and Ω'_0 , estimated with a fixed Q model given in the previous study [Nakamura and Koyama, 1982], which gives about $Q = 2000$ – 3000 . After the first iteration, we stack the spectra with the source time function component removed to estimate the background spectra as described previously (Figure 5 and equation (8)). We, in turn, take the original spectrum $A_i(f)$ and correct this with the background spectra obtained from the stack where we expect only the source time function to be contained in the corrected spectra (Figure 5). With the corrected spectra, we reestimate f_c and Ω_0 with the least squares fitting of the source time function $A^{\text{source}}(f)$. This will give us new sets of f_c and Ω_0 . With a new set of f_c and Ω_0 in hand, we reexecute the stack to improve the estimate for the background spectrum. The process will be iterated until the improvement of the iteration is smaller than the error bar. The iteration converges typically within 5–10 iterations. Figure 5 shows an example of spectral stacking and correction using the background spectrum.

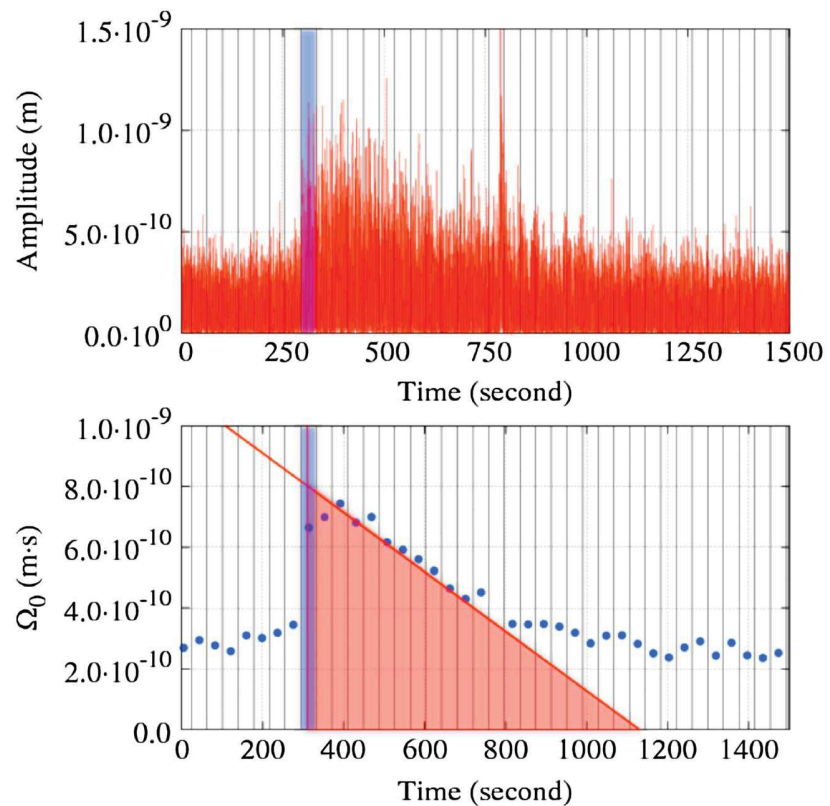


Figure 6. An example of (top) amplitude variation and the (bottom) time variation of Ω_0 , which is the DC value of the spectrum, for the A06 deep moonquake event. The blue shaded region shows the short time window used to estimate f_c and Ω_0 . The data were divided into short strips of data 40 s long. The data strip is divided by a black line in the figure. In the bottom plot, Ω_0 estimated for each data strip is shown in blue dots. The time variation of Ω_0 was fitted with the red line in the plot. The red triangle shows the portion of the signal carrying the scattered seismic energy. The plot uses an arbitrary time origin.

red triangle in Figure 6. By comparing the total energy within the triangle and energy within the first data segment of the seismic wave, we can evaluate the correction factor α . This can be expressed as

$$\alpha = \frac{\sqrt{\sum \Omega_{0,i}^2}}{\Omega_{0,1}} \quad (9)$$

where $\Omega_{0,1}$ refers to $\Omega_{0,i}$ of the i th data segment from the signal arrival. The characteristics of the coda or the degrading feature of the Ω_0 are expected to be dependent of the scattering feature near the station and the raypath between the source region and the station. This means that the correction factor is a raypath-dependent term (i.e., constant for a source region and station pair) and not an event-dependent term. Thus, we calculated the correction factor for each set of source region and station.

3. Estimation of Source Parameters

3.1. Spectral Fitting and Evaluation of Spectral Features

After having processed the series of data we expect that the spectra contain only the source time function and we fit the data to the ω^2 model described previously. Through the fitting, we obtain f_c and Ω_0 . For the events detected at multiple stations, we carry out the fitting for the two stations simultaneously since f_c and Ω_0 should be identical for the same event. We did the above analysis for 131 events from three deep moonquake nests A01, A06, and A07, which are some of the most active deep moonquake nests observed so far (Figures 1 and 7). While more than 100 source regions have been identified [Nakamura, 2003], we focus on the three active nests, which should give the best quality data set for our first attempt to carry out

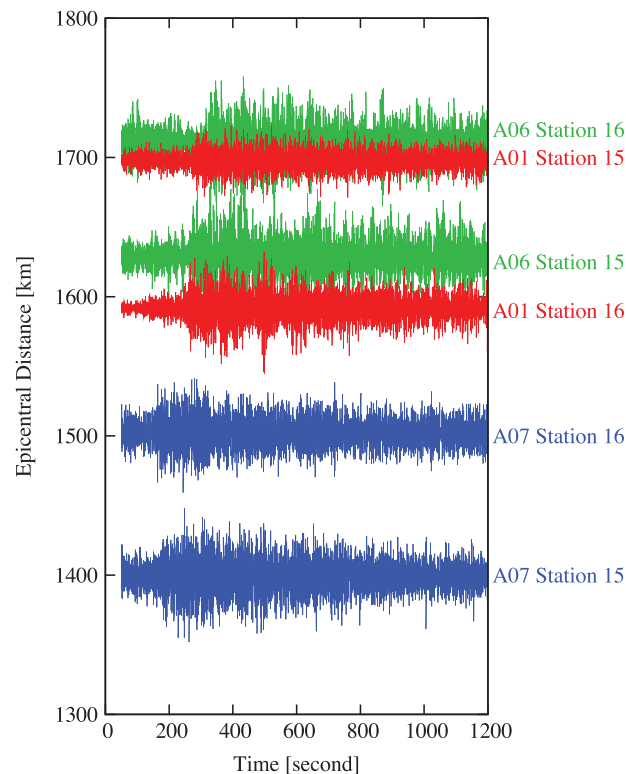


Figure 7. A01, A06, and A07 deep moonquake events. The figure shows the associated virtual broadband seismogram at each station for a single deep moonquake event, from each nest (A01: 27 March 1976, 18:48; A06: 25 November 1975, 23:20; and A07: 11 April 1976, 12:51). Note that since the seismograms refer to different events for different nests, the amplitude and arrival times are set with arbitrary offsets and amplifications are not to scale.

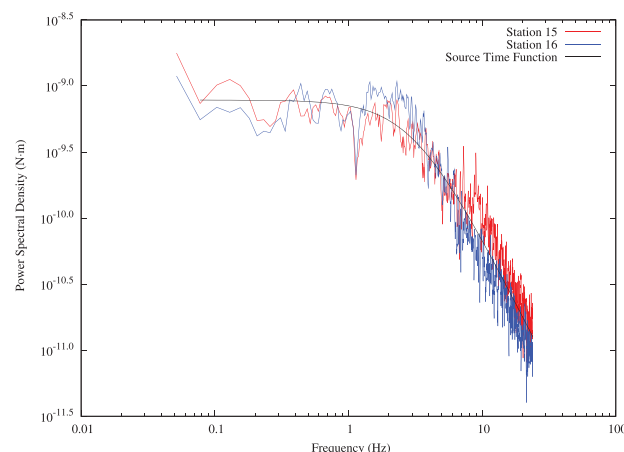


Figure 8. An example of a spectrum's fit for a seismic source function from A06 deep moonquake (20 May 1975, 17:35). The seismic spectra were corrected for attenuation and other nonseismic components (see text for details). The best fit model is shown in the plot and corresponds to a moment of $2.0 \pm 0.2 \times 10^{13}$ Nm (moment magnitude = 2.8) and a cutoff frequency of 3.5 Hz.

broadband spectral analysis on the Moon. The A01 nest is the most active deep moonquake source and A06 and A07 are sources that are located close to stations 15 and 16 (Figure 1). These data should be the best data set to carry out our first analysis since they have likely the best signal-to-noise ratio. Figure 8 shows the result of spectral fitting of the source time function to the data. We see that the model is in agreement with the observations and that the observations at two stations also compares favorably.

Figure 9 shows the estimated corner frequencies and seismic moments for all studied events from these three nests. By expanding the frequency range, we succeeded in estimating source parameters, not only for various nests but also over a wide range of seismic moments, ranging from $10^{12.5}$ Nm to almost 10^{14} Nm, which correspond to a moment magnitude from 2.3 to 3.3. The estimated corner frequencies are distributed within a wider range but we rejected the values outside the noise roll-off of the SP (8 Hz). While the previous study obtained 1 Hz for the corner frequency, most of our corner frequencies are distributed between 1 and 8 Hz, which is reasonable since we are investigating events of smaller magnitude.

3.2. Estimation of Stress Drops

Investigation of fault activities and source mechanisms in terrestrial seismology derived a scaling law between seismic moments, corner frequencies, and stress drops, which explains terrestrial observations well [Aki and Richards, 2002; Goins *et al.*, 1981]. This is expressed as

$$\Delta\sigma = 12M_0 \left(\frac{f_c}{\beta} \right)^3 \quad (10)$$

where $\Delta\sigma$ is the stress drop, M_0 is the seismic moment, and β is the shear velocity at the source region. Assuming that deep moonquakes are also fault activities that can be expressed with a double-couple force, which is supported by the clear appearance of P and S wave signals, the same scaling law should be applicable to deep moonquakes. This

was the same assumption made in the previous study [Goins *et al.*, 1981], and we will use the same approach to estimate the stress drops. Terrestrial observations suggest that the stress drop is independent of seismic moment and is almost constant over a wide range of seismic moments [Ide *et al.*, 2003]. This is known as the self-similarity of seismic events. Referring to the terrestrial examples and given that the deep moonquakes occur in relatively well-defined source regions, we assume that events from the same nest occur in very similar condition, possibly on the same fault plane. Thus, we assume that stress drop is constant within a nest. This allows us to estimate the stress drop for each deep moonquake nests from the sets of f_c and Ω_0 we obtained previously. The scaling law (equation (10)) was fitted to the f_c s and Ω_0 s to obtain the stress drop. The errors on stress drop will be evaluated through the misfit. The fit was weighted by estimation error of the corner frequencies. With this assumption, we estimated stress drops of the deep moonquake nests as follows: A01: 0.14 ± 0.01 MPa, A06: 0.09 ± 0.01 MPa, and A07: 0.09 ± 0.008 MPa. These stress drops are significantly larger than those estimated in the previous study [Goins *et al.*, 1981]. This discrepancy is retrieved for the single event used in the previous study, an A01 deep moonquake event on 29 October 1975. While both studies have similar seismic moments (6.8×10^{13} Nm in our study and 7.4×10^{13} Nm in the previous study), the corner frequency obtained here is higher (2.4 ± 0.1 Hz in our study and 1 Hz in the previous study) which resulted in a higher stress drop. This is reasonable since the seismic moment is mainly constrained by the long-period component of spectra while corner frequency is constrained by the high-frequency component where we see the improvement with our broadband data.

4. Discussion

4.1. Self-Similarity of Seismic Activities and Fault Roughness

While the least squares fit performed in the previous section enables us to estimate stress drops of deep moonquakes, the model did not result in a satisfactory fit especially at low and high frequencies. Indeed, the trend of the data appears to be smaller than the -3 slope, which has been suggested from traditional scaling laws for f_c , M_0 , and $\Delta\sigma$ [e.g., Aki and Richards, 2002; Goins *et al.*, 1981]. This implies that the deep moonquakes are not self-similar where stress drops are independent of seismic moments [Ide *et al.*, 2003] and stress drops show some moment dependency.

Self-similarity of quakes and moment dependency of stress drops have been debated for a long time [e.g., Ide *et al.*, 2003; Allmann and Shearer, 2009; Abercrombie, 2014]. While many studies claim that earthquake stress drops are independent of their seismic moments [e.g., Ide *et al.*, 2003], the estimated stress drops have a large scatter of 0.1–100 MPa. This scatter is interpreted as unmodeled sources of error such as near-surface attenuation or directivity effects [Candela *et al.*, 2011], but some studies claim that heterogeneous properties of faulting and fault surface influence the values of static stress drop [Allmann and Shearer, 2009; Mayeda and Walter, 1996].

One of the key properties affecting the moment dependency of stress drop is the fault roughness. The classical view of the fault roughness is that the fault roughness is also self-similar, where the vertical and horizontal dimension is amplified isotropically regardless of the scaling transformation. In other words, the roughness properties are the same for microscopic and macroscopic scales. Such self-similar faults result in self-similarity of quakes and stress drops are independent of seismic moments. Many studies regarded that the fault surface can be characterized by a self-similar roughness.

On the other hand, observations of actual fault surface imply that the fault roughness is better expressed as a self-affine surface rather than a self-similar surface [Schmittbuhl *et al.*, 1993; Candela *et al.*, 2012; Bistacchi *et al.*, 2011]. When the fault roughness is self-affine rather than self-similar, the vertical and horizontal dimension will not be amplified isotropically. In this case, the roughness defined at microscopic scale may be different at macroscopic scale. By applying a self-affine model, we would be able to take into account the evolution of fault roughness for different fault sizes. Since the seismic moment is a product of fault size, average slip, and shear modulus of the fault [Aki and Richards, 2002], self-affinity of fault and different roughness features at microscopic and macroscopic scales will have significant influence on the moment dependency of stress drops. Interestingly, while observations of faults surface exposed as an outcrop is better represented as a self-affine roughness, fault surface at seismogenic depth observed with radar sounder also supports the self-affine surface for seismic faults [Bistacchi *et al.*, 2011]. This implies that the self-affine geometrical model may represent a global feature of natural fault surfaces. Schmittbuhl *et al.* [2006] proposed a

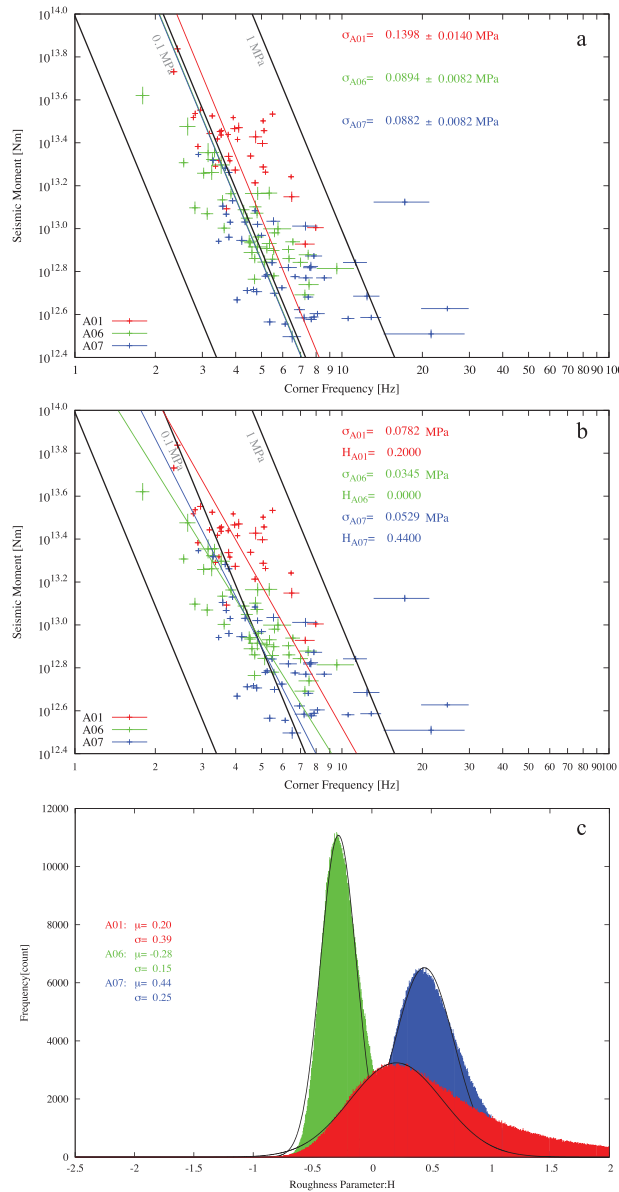


Figure 9. Source parameters estimated for A01, A06, and A07 deep moonquake nests. Corner frequencies and seismic moments estimated for each event from the three nests we investigated are shown in the plot as A01: red, A06: green, and A07: blue. The best fit model obtained and the corresponding stress drops are also shown. Figure 9a shows the results for a self-similar fault, and Figure 9b shows the results for a self-affine fault including effect of roughness. Figure 9c shows the distribution of roughness parameter H , as described in the text, obtained in each subset of bootstrap resampling. The black line refers to the Gaussian distribution that was fitted to each histogram whose expected values μ and standard deviations σ are also shown. The μ can be regarded as the most probable value of H with an error quantified by σ . For all nests, the fits prefer low H and low stress drops are preferred.

fault model taking into account the effect of such a self-affine fault surface. This model explains well the stress field observed before and after the Nojima Fault of Japan [Schmittbuhl *et al.*, 2006]. Candela *et al.* [2011] took this model to investigate the effect of a self-affine fault surface on stress drops and suggested that this will result in moment dependency of the stress drop.

4.2. Self-Affine Fault Roughness and Seismic Moment Dependency of Stress Drop

In the self-affine fault model, the fault's roughness can be smoother at large scale, while at small scale, there is a large variety of patterns of small-amplitude asperities [Candela *et al.*, 2011]. The affinity of the fault is expressed through the Hurst exponent H , which is also known as a roughness parameter. In the self-similar model, when the horizontal dimension is amplified from δx to $\lambda \delta x$, the vertical roughness will also be amplified from δy to $\lambda \delta y$. For a self-affine model, when the horizontal dimension is amplified from δx to $\lambda \delta x$, the vertical roughness will be amplified from δy to $\lambda^H \delta y$. Thus, when $H = 1$, it will be identical to be a self-similar model. On the other hand, for smaller H , the fault roughness flattens with increasing dimensions. Candela *et al.* [2011] claims that this will result in stress drop variation with fault size, $\Delta \sigma \propto r^{H-1}$, where r is the fault size [Candela *et al.*, 2011]. We follow their discussion and assume that $\Delta \sigma = \Delta \sigma_0 (r/r_0)^{H-1}$, where r_0 is a reference fault size where we define the reference stress drop.

Average stress drop and seismic moments are expressed as follows with the traditional model [Aki and Richards, 2002]:

$$\Delta \sigma = \frac{7\pi}{16} G \frac{a}{r} M_0 = GAa \quad (11)$$

where G is the shear modulus, a is an average slip, r is the size of fault, and A is an area of rupture. When we assume a circular fault, as is often the case for terrestrial seismology [Aki and Richards, 2002], we get

$$\Delta\sigma = \frac{7}{16} \frac{M_0}{r^3} = 12M_0 \left(\frac{f_c}{\beta}\right)^3 \Delta\sigma_0 \left(\frac{r}{r_0}\right)^{H-1} = 12M_0 \left(\frac{f_c}{\beta}\right)^3 \Delta\sigma = 12M_0 \left(\frac{f_c}{\beta}\right)^3 \left(\frac{r_0}{r}\right)^{1-H} \quad (12)$$

Introducing such relations, we are able to take into account the fault roughness and moment dependency of stress drop. The parameter used in this study refers to the values by *Goins et al.* [1981], which is $\beta = 4.2$ km/s. We referred to a previous study that estimated the size of the A01 deep moonquake nest [Nakamura, 1978] to define the reference fault size $r_0 \sim 1$ km. However, little is known about the fault size of deep moonquakes for the moment. The small seismic moment we obtained in this study implies either a small fault area and/or small slip. When we assume a shear modulus of ~ 60 GPa for the deep moonquake source regions and from the obtained seismic moment, which is 10^{12} – 10^{14} , we obtain a slip of 10^{-5} – 10^{-2} m for a 1 km circular fault. If the slip of deep moonquakes is larger, the fault size can be smaller, and the effective stress drop for each seismic event can be larger.

Figure 9 shows results obtained with the self-affine model. As was done for a self-similar model, we carried out least squares fitting with the self-affine model to estimate the stress drops. Here we used equation (12) instead of equation (10) for the fitting. As shown in Figure 9, the misfit of the least squares fit is improved by introducing roughness parameter H to the stress drop estimation. This implies that our data supports the self-affine fault model for deep moonquakes.

However, the small amplitudes of the recorded quakes lead to large scatters in the data set, leaving significant uncertainties in our estimation. Such scatters in the data may result in erroneous H value due to outliers that may not be suitable for use in the fitting. We therefore took a statistic approach to estimate H and its uncertainty. Instead of defining stress drops and H through single least squares fitting, we executed multiple runs of least squares fitting and studied the distribution of the H value we obtained from each fitting. Each least squares fit was carried out with a data set, which was resampled from the original data set. This was done with a statistical method known as bootstrapping [Efron, 1979]. This will enable us to avoid misinterpretation of the data from some outliers, since the random process will generate subsets with and without the outliers. If a few outliers were contaminating our least squares fit, it is more likely that the outliers will not be included in the resampled data set and the result with the outliers will be discarded in the following statistical analysis. The fit was weighted by estimation error of the corner frequencies. Statistically speaking, the distribution of H obtained from the multiple resampling and fitting should give us representative H values for the data set.

We carried out one million resamplings and fittings and studied the distribution of the resultant H values. From the histograms of the H values, the mode should be regarded as the representative H and the standard deviation can be regarded as the deviation of H value due to the scatter in the data set. Figure 9 also shows the histogram for H obtained for each bootstrapping subset. Assuming that the histogram follows a Gaussian distribution ($f(x) = 1/\sqrt{2\pi\sigma^2} \exp(-(x - \mu)^2/2\sigma^2)$), the mode (μ) will correspond to the H value and the standard deviation (σ) can be regarded as the estimation error. A similar statistic approach is also possible for the stress drop where we can define stress drop from the histogram. By definition, the stress drop we obtained here corresponds to the value that is obtained with the representative H value, which is also defined statistically. For all nests, we obtained H values that are significantly lower than 1, which implies that deep moonquake faults are better explained with a self-affine model. This means that the fault roughness flattens with fault size and the fault can be considered to be smooth in macroscopic scale. The sets of H and stress drop ($\Delta\sigma$) that give the best fit for each nest are as follows: A01: $H = 0.20 \pm 0.39$, $\Delta\sigma = 0.06 \pm 0.02$ MPa; A06: $H = -0.28 \pm 0.15$, $\Delta\sigma = 0.025 \pm 0.005$ MPa; and A07: $H = 0.44 \pm 0.25$, $\Delta\sigma = 0.04 \pm 0.01$ MPa. In the case of A06, the Hurst exponent attains negative values but this does not oppose the tendency that the deep moonquake faults are smooth with low H values. For the smooth faults, the stress drops are lower than for the self-similar model and are comparable to the tidal stress for all deep moonquake nests.

The range for the roughness H values of terrestrial faults is 0.5–0.8 [Candela et al., 2011; Candela et al., 2012]. Thus, our results imply that the deep moonquake faults are smoother compared to terrestrial faults in terms of the Hurst exponent. While studies suggest evolution of fault surface roughness with maturity, there has been no evidence of variation in H values with maturity [e.g., Brodsky et al., 2011; Brodsky et al., 2015]. Deep moonquake faults that have been active monthly since their formation can be regarded as very active faults compared to terrestrial faults. This major aging difference as compared to the Earth's much younger

faults support a very developed abrasion of the fault surface through the repeated quakes (A1 has typically a rate of about 80 events per year [Weber *et al.*, 2009]). Qualitatively speaking, it is reasonable to expect a very smooth fault for deep moonquakes but its implication for the Hurst exponent should be investigated more in detail in future work.

When applied to the deep moonquake faults, the self-affine fault model provides stress drops ranging from the maximum of the shear stresses generated by the tides to a fraction of these [Weber *et al.*, 2009] and supports the hypothesis that Earth tides not only trigger deep moonquakes but also provide most of the stress glut generating the quakes. This idea is also compatible with the polarization of deep moonquake signals [Frohlich and Nakamura, 2009], which is difficult to realize with unidirectional tectonic stress. The question remains whether the tidal stress will be able to trigger a slip under a pressure of ~4 GPa. Experimental studies show that the friction coefficient decreases drastically with lubrication from granular or fractured layer near fault boundary, which grows with fault activities [Collettini *et al.*, 2009; Reches and Lockner, 2010; Di Toro *et al.*, 2011; De Paola *et al.*, 2011]. While quantitative evaluation is yet to be investigated, an extremely smooth fault supports the idea that tides are the dominant source of excitation of deep moonquakes.

4.3. Brittle-Ductile Transition Temperature at Deep Moonquake Sources

The previous discussion suggests that the tidal stress is the main excitation force of deep moonquakes. This point needs to be taken into account in evaluating the brittle-ductile transition temperature. Notably, we need to take into account the strain rate from the tides and not the tectonic strain rate. This is likely to have a significant impact on the temperature since the tidal strain rate is about 3–4 magnitudes larger than the tectonic strain rate in terrestrial seismogenic regions. This is due to the monthly periodicity of the strain variation, in contrast to the secular-tectonic strain accumulation on Earth. As observed on the terrestrial outer trench high at subduction zones, which is regarded as a fast-moving tectonically active areas with a high strain rate, a larger temperature of the brittle-ductile transition is expected for deep moonquakes [McKenzie *et al.*, 2005].

Models were proposed to evaluate the brittle-ductile temperature for a given composition, and we are able to quantify this for a set of temperature, differential stress, and rheological parameters. The lower mantle where the deep moonquake source regions rest is likely to be an olivine-rich environment. Here we will use the model adopted in Boettcher *et al.* [2007] for a dry olivine single crystal, and correct it for the pressure range of the deep moonquakes. As discussed previously, the stress drop obtained from the spectral analyses implies that the tidal stress is the dominant stress source for deep moonquakes. Thus, we use parameters of tidal stress between the Earth and the Moon in the following discussion. Boettcher *et al.* [2007] showed that deformation of the asperities occurs according to flow laws determined from indentation creep tests on dry olivine single crystals. Following Boettcher *et al.* [2007], the strength of olivine σ_A can be expressed as

$$\sigma_A = \sigma_P \left[1 - \left(\frac{-RT}{H} \ln \frac{\dot{\epsilon}}{B} \right)^{1/q} \right] \quad (13)$$

where the Peierl's stress $\sigma_P = 8500$ MPa, the gas constant $R = 8.314$ J/mol/K, the activation enthalpy $H = 5.4 \times 10^5$ J/mol, the empirical constant $B = 5.7 \times 10^{11} \text{ s}^{-1}$, the exponent $q = 2$, and $\dot{\epsilon}$ is the strain rate at the source region. This will enable us to estimate olivine strength σ_A at a given temperature for a given strain rate.

Among the parameters, variables are strain rate, temperature, and strength of olivine. Since we assumed that deep moonquakes are excited by tides, strength should be comparable to tidal stress. Thus, if we can calculate the strain rate at deep moonquake regions, we can obtain the temperature and this correspond to the brittle-ductile transition temperature. Strain rate can be calculated from a given model of the interior structure. Here we used both integrated lunar structure models from Gagnepain-Beyneix *et al.* [2006] with the core proposed by Weber *et al.* [2011] and the model of Garcia *et al.* [2011]. We assumed the velocity structure of Gagnepain-Beyneix *et al.* [2006] down to the core-mantle boundary and added the core of either Weber *et al.* [2011] or Garcia *et al.* [2011] for comparison. Then we estimated the strain rate for the deep moonquake region following the discussion of Lognonné and Johnson [2007, 2015, section 10.03.2.3 and Appendix A]. A correction was made to account for the physical dispersion between wave velocities at seismic frequencies (~1 Hz) and the tidal frequencies (~1 μ Hz), leading to about 20% reduction of the shear modulus. This will be described in more detail later in the study. The homogenous model of Weber

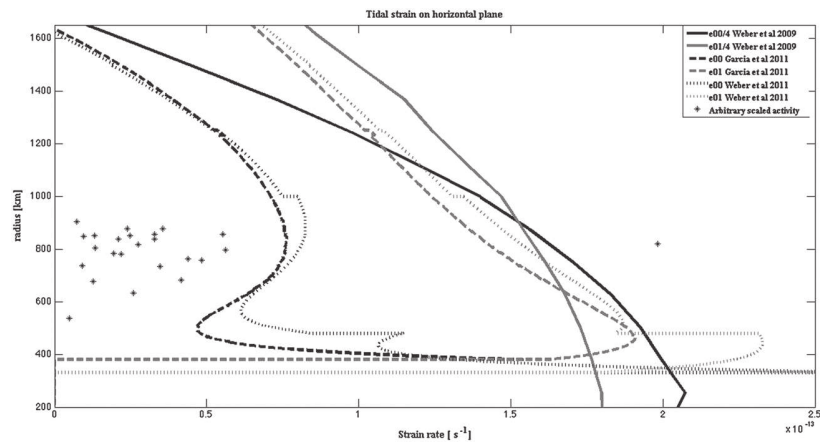


Figure 10. Comparison of two strain rate components associated with the projection of the strain tensor on a horizontal plane for the models from *Weber et al.* [2009], *Weber et al.* [2011], and *Garcia et al.* [2011]. The strain obtained with the model of *Weber et al.* [2009] has been divided by four and results from much lower values of the shear velocities than those of *Garcia et al.* [2011] and *Weber et al.* [2011]. In all cases, the strains are computed with resolution defined by the number of layers we define (512 layers, 3 km resolution), for the A01 deep moonquake location used by *Weber et al.* [2009], for an Earth location pointing toward the center of the near side of the Moon at a distance of 385,000 km. The tidal time variation potential has been scaled in order to provide 2.5 kPa/d and 1.8 kPa bar/d for the peak amplitude of the normal, respectively, shear stress variation at A1 on the horizontal plane, as illustrated by Figure 9 of *Weber et al.* [2009].

et al. [2009] has been also used, although the shear modulus is likely too low (10^{10} Pa), which is equivalent to shear velocities of 1.825 km/s. The strain was estimated with a simplified tidal model described in Appendix A and computed for all deep moonquakes. This results in a strain rate of about $1.5 \times 10^{-13} \text{ s}^{-1}$ for the shear strain and of about 10^{-13} s^{-1} for the normal strain for both models of *Weber et al.* [2011] and *Garcia et al.* [2011], with respect to the horizontal plane (Figure 10). In this figure, we used the average strain of all deep moonquakes. Strains are lower by a factor of 4 than those of the low-rigidity homogenous model of *Weber et al.* [2009]. Note that the models of *Garcia et al.* [2011] and *Weber et al.* [2011], because of the core, reshape the profile of the strain and provide a maximum strain at the depth where we have the maximum of deep moonquake activity, as already suggested by *Lognonné and Johnson* [2007, 2015]. Other published models for seismic and density models provide very comparable strain rate, as long as their core radius is similar.

For each deep moonquake source region, we used the depth and specific strain rate (associated with their location) to define the shear and normal strain rate at the source region. Then the transition temperature

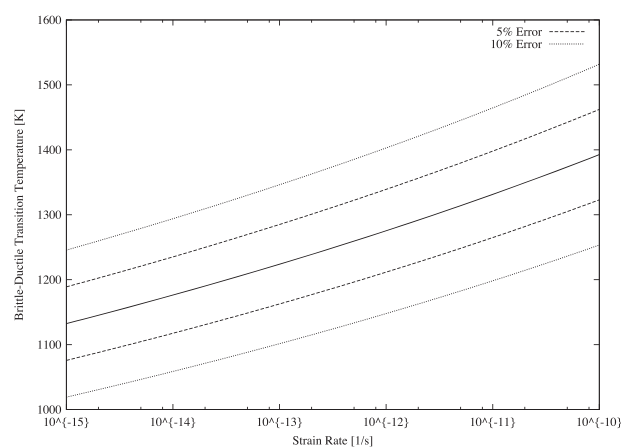


Figure 11. Variation of brittle-ductile transition temperature with strain rate and activation energy.

can be obtained according to the model described with equation (13). This will give us a transition temperature as a function of depth as shown in the black triangles in Figure 11. This results in brittle-ductile transition temperatures of about 1240–1275 K depending on the depth of each deep moonquake source region, which ranges from 835 to 1200 km. These values are likely to contain some errors due to the uncertainties on the parameters we used. The brittle-ductile transition temperature obtained here is an estimation based on given condition and subject to change depending on the

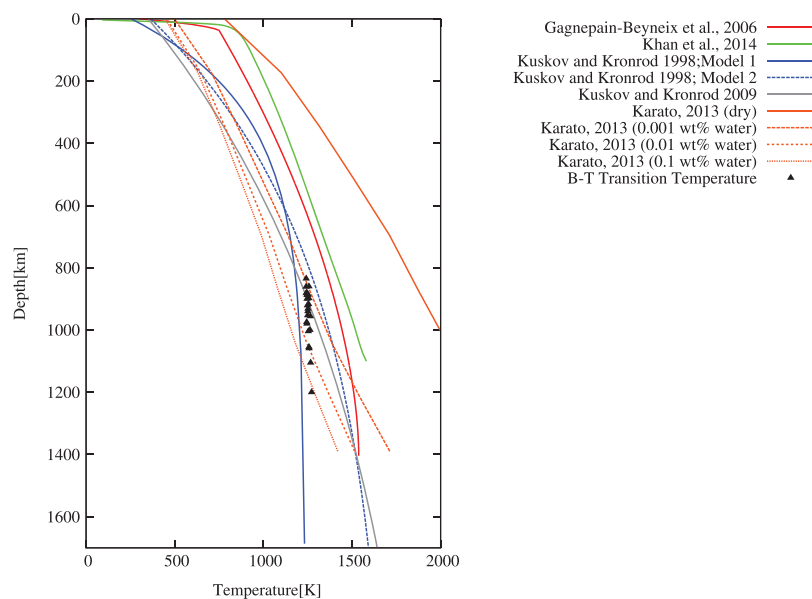


Figure 12. Comparison between temperature profiles from previous studies [Gagnepain-Beyneix *et al.*, 2006; Khan *et al.*, 2014; Kuskov and Kronrod, 1998; Kuskov and Kronrod, 2009; Karato, 2013] and the brittle-ductile transition temperature obtained in this study.

parameters we adopt. First, we assumed dry olivine which might be questioned given the recent discovery of water on the Moon. Studies suggest that the lunar mantle may contain about 100 ppm of water [e.g., Chen *et al.*, 2015; Elkins-Tanton and Grove, 2011]. Experimental study on single crystal olivine for wet and dry conditions shows that strength of olivine will be factor of 1.3–1.6 weaker with water supply at ~4GPa, 1200°C condition [Girard *et al.* 2013]. This implies that the effect of water of 100 ppm is not significant for evaluation of brittle-ductile transition, especially when the differential stress or strength is expected to be small compared to Peierl's stress. Second possible source of error is the activation energy H used in equation (13). Previous studies point out that activation energy of olivine has 5–10% of uncertainties [Ohuchi *et al.*, 2015]. This results in 50–100 K of error on the transition temperature (Figure 11). Finally, the influence of strain rate evaluation should be evaluated. Figure 11 shows the variation of brittle-ductile transition temperature with strain rate. The figure shows that replacing tectonic strain rate (10^{-15}) with tidal strain rate (10^{-13}) results in 100–150 K difference in the transition temperature. Figure 10 shows that different models result in 10^{-14} difference in strain rate, and this will result in tens of kelvin in the transition temperature. These are the possible source or errors and errors on the transition temperature.

4.4. Comparing the Brittle-Ductile Transition Temperature With Temperature Models of the Moon

The higher strain rate of tides resulted in a higher brittle-ductile transition temperature, and it is important to compare this with existing temperature profiles of the Moon. Here we referred to studies that provided temperature profile to depth of the deep moonquake source regions using variety of different approaches [Kuskov and Kronrod, 1998; Gagnepain-Beyneix *et al.*, 2006; Kuskov and Kronrod, 2009; Karato, 2013; Khan *et al.*, 2014]. Figure 12 shows a comparison between different temperature profiles and brittle-ductile transition temperatures obtained in the previous section. As mentioned previously, proposed temperatures in the deep moonquake source region are hotter than brittle-ductile temperatures even allowing for a higher brittle-ductile transition as temperature proposed in this study. There are two models that satisfy the temperature constraint in the deep moonquake source region. One is the Model 1 of Kuskov and Kronrod [1998]. Kuskov and Kronrod [1998] used thermodynamic and geochemical models with a seismic velocity model to construct the temperature profile. They used two different boundary conditions to construct two end-members for the temperature profiles, and Model 1 corresponds to the case where they assumed a lower limit of the density at the crust mantle boundary. Another model compatible with the brittle-ductile

transition temperature is the wet model with >0.1 wt % of water from *Karato* [2013]. As it was discussed before, under wet conditions, olivine strength will be lower by a factor of 1.3–1.6 [*Girard et al.*, 2013] and its impact on the brittle-ductile transition temperature in the deep moonquake source regions is small.

To conclude, the cold models proposed in previous studies are compatible with our estimation of the brittle-ductile transition. For these models, deep moonquakes can be understood as the brittle response of the Moon due to tidal stress accumulation.

5. Summary and Conclusion

In this study, we reevaluated source parameters of deep moonquakes through spectral analyses. To improve our estimation, we combined both LP and SP seismic records to obtain continuous spectra and carried out spectral analysis with a broader frequency band. This enabled us to study more than 100 deep moonquake events from three different source regions and to perform a statistical and comparative investigation of the source parameters.

We showed that a traditional self-similar fault model gives stress drops of ~ 0.1 MPa. Furthermore, our results support the self-affine fault model for deep moonquakes, also observed for terrestrial faults. Our results show that the roughness parameter (Hurst exponent) of the fault is significantly smaller compared to terrestrial faults, which implies that the deep moonquake faults are much smoother than the terrestrial counterparts. This results in stress drop of 0.05 MPa, which is comparable to shear tidal stress acting on deep moonquake faults. This suggests that the tidal stress not only triggers the deep moonquake activity but also acts as a dominant source of the excitation.

Assuming that the tidal stress is responsible for deep moonquake activity, we reevaluated the brittle-ductile transition temperature of deep moonquake source regions with tidal strain rate. This resulted in higher brittle-ductile transition temperature than the temperature previously proposed. Obtained transition temperatures were compared with temperature profiles proposed in previous studies. While most of the modeled temperature profiles are hotter than the transition temperature, cold temperature profiles model, such as the model with wet mantle from *Karato* [2013], are compatible with the brittle-ductile transition temperature obtained in this study.

Appendix A: Computation of the Strain Rate

We computed the strain rate at a given deep moonquake source with a simple model of the Earth tide, assuming a tidal potential of harmonic order 2 expressed as for *Weber et al.* [2009]:

$$\phi_2 = \frac{GM_E r^2}{2r_s^3} (1 - 3\cos^2 \Delta) \quad (A1)$$

where G , M_E , r , r_s , and Δ are the gravitational constant, Earth's mass, lunar radius, Earth to Moon distance, and angular distance between the Earth's nadir point on the Moon and the deep moonquake's epicenter. We first compute the vertical $U(r)$ and horizontal tidal displacement $V(r)$ from *Wahr et al.* [2009] software (<https://code.google.com/p/satstress/>) and then strain in spherical coordinate (see *Phinney and Burridge* [1973] for the strain and stress expressions). This consists in the resolution of the tide equation for a gravito-elastic lunar model, which can be rewritten as

$$-\rho\omega^2 \vec{u} = \vec{\nabla} \vec{T} - \vec{g} \vec{\nabla} (\rho \vec{u}) - \rho \vec{\nabla} \phi_1 - \rho \vec{\nabla} \phi_2 \nabla^2 \phi_1 = -4\pi G \vec{\nabla} (\rho \vec{u}) \quad (A2)$$

where \vec{T} is the stress tensor perturbation (depending linearly on \vec{u} and which includes elastic stress and displacement in the prestressed body), ϕ_1 is the mass redistribution potential, ρ is the density, g is the gravity, and ω is the tidal bulge angular frequency (in the lunar reference frame). See Lognonné and Clévéde for more details on the equation as well as associated boundary conditions.

We then decompose the angular term of equation (A1) in P20 and P22 harmonics, by using $\cos \Delta = \sin \theta \cos \phi$, such that

$$P_2^0(\cos \theta) = -\frac{1}{2} P_2^0(\cos \theta) + \sqrt{\frac{3}{2}} P_2^2(\cos \theta) \cos(2\phi) \quad (A2)$$

where θ and ϕ are the colatitude and longitude with respect to a spherical coordinate system whose vertical axis is perpendicular to the Earth's nadir point direction. We then compute the time evolution of θ and ϕ by

assuming a simple lunar orbit with semimajor great axis of 384,748 km, eccentricity of 0.059006, lunar radius of 1738 km, and lunar orbit period of $T = 27.555$ day, assuming that the r_s distance verifies Kepler law, Moon is in synchronous rotation, and a lunar rotation axis tilted by 6.68° with respect to the orbital plane and along the zero lunar meridian direction at the origin of time. The strain rate is computed numerically from the numerical expression with the time depending on radius, latitude, and longitude by time finite differences, and the maximum strain is then considered. For the Weber *et al.* [2009], the obtained strain is about $6.6 \times 10^{-13} \text{ s} = 5.7 \times 10^{-8} \text{ day}^{-1}$ for the horizontal shear strain, which leads, for the $\mu = 10^{10} \text{ Pa} = 10^5 \text{ bar}$ rigidity, to stress of 2μ times the shear strain, and therefore of about $0.011 \text{ bar/d} = 1.1 \text{ kPa/d}$, to be compared to Figure 9b of Weber *et al.* [2009], which suggests peak-to-peak stress of $2 \times 0.015 \text{ bar/d}$.

Acknowledgments

We would like to acknowledge the reviewers, especially A. Khan for the comments and discussion which was important to improve the manuscript. This work has been supported by CNES and by ANR SISMOMARS. Taichi Kawamura would like to acknowledge the ANR SISMOMARS for the additional support for his Postdoc position. This is IGP contribution 3865. The raw Apollo seismic data used in this study are available either through NASA Space Science Data Coordinate Archive (<http://nssdc.gsfc.nasa.gov/>; PSPG-00665, PSPG-00012, and PSPG-00738) or IGP Data Center (<http://datacenter.igpp.fr/metadata/XA/>).

References

- Aki, K., and P. G. Richards (2002), *Quantitative Seismology*, 2nd ed., chap. 10, pp. 491–536, Univ. Sci. Books, Sausalito, Calif.
- Allmann, B. B., and P. M. Shearer (2009), Global variations of stress drop for moderate to large earthquakes, *J. Geophys. Res.*, *114*, B01310, doi:10.1029/2009JB005821.
- Abercrombie, R. E. (2014), Stress drops of repeating earthquakes on the San Andreas Fault at Parkfield, *Geophys. Res. Lett.*, *41*, 8784–8791, doi:10.1002/2014GL062079.
- Baker, S. F. (1999), Processing near-surface seismic reflection data: A primer (Society of Exploration Geophysicists Course Notes Volume 9), *Soc. Explor. Geophys.*, doi:10.1190/1.9781560802020.
- Bistacchi, A., W. A. Griffith, S. A. F. Smith, G. Toro, R. Jones, and S. Nielsen (2011), Fault roughness at seismogenic depths from lidar and photogrammetric analysis, *Pure Appl. Geophys.*, doi:10.1007/s00024-011-0301-7.
- Boettcher, M. S., G. Hirth, and B. Evans (2007), Olivine friction at the base of oceanic seismogenic zones, *J. Geophys. Res.*, *112*, B01205, doi:10.1029/2006JB004301.
- Brodsky, E. E., J. J. Gilchrist, A. Sagi, and C. Collettini (2011), Faults smooth gradually as a function of slip, *Earth Planet. Sci. Lett.*, *302*, 185–193, doi:10.1016/j.epsl.2010.12.010.
- Brodsky, E. E., J. D. Kirkpatrick, and T. Candela (2015), Constraints from fault roughness on the scale-dependent strength of rocks, *Geology*, doi:10.1130/G37206.1.
- Candela, T., F. Renard, M. Bouchon, J. Schmittbuhl, and E. E. Brodsky (2011), Stress drop during earthquakes: Effect of fault roughness scaling, *Bull. Seismol. Soc. Am.*, *101*(5), 2369–2387.
- Candela, T., F. Renard, Y. Klinger, K. Mair, J. Schmittbuhl, and E. E. Brodsky (2012), Roughness of fault surfaces over nine decades of length scales, *J. Geophys. Res.*, *117*, B08409, doi:10.1029/2011JB009041.
- Chen, Y., Y. Zhang, Y. Liu, Y. Guan, J. Eiler, and E. M. Stolper (2015), Water, fluorine, and sulfur concentrations in the lunar mantle, *Earth Planet. Sci. Lett.*, *427*, 37–46.
- Cheng, C. H., and M. N. Toksöz (1978), Tidal stresses in the Moon, *J. Geophys. Res.*, *83*, 845–853, doi:10.1029/JB083iB02p00845.
- Collettini, C., A. Niemeijer, C. Viti, and C. Marone (2009), Fault zone fabric and fault weakness, *Nature*, *462*, 907–910, doi:10.1038/nature08585.
- Dainty, A. M., M. N. Toksöz, K. R. Anderson, P. J. Pines, Y. Nakamura, and G. Latham (1974), Seismic scattering and shallow structure of the Moon in oceanus procellarum, *Moon*, *9*, 11, doi:10.1007/BF00565388.
- De Paola, N., T. Hirose, T. Mitchell, G. Di Toro, C. Viti, and T. Shimamoto (2011), Fault lubrication and earthquake propagation in thermally unstable rocks, *Geology*, *39*(1), p35–p38, doi:10.1130/G31398.1.
- Di Toro, G., R. Han, T. Hirose, N. De Paola, S. Nielsen, K. Mizoguchi, F. Ferri, M. Cocco, and T. Shimamoto (2011), Fault lubrication during earthquakes, *Nature*, *471*, 494–498, doi:10.1038/nature09838.
- Efron, B. (1979), Bootstrap methods: Another look at the jackknife, *Ann. Stat.*, *7*(1), 1–26, doi:10.1214/aos/1176344552. [Available at <http://projecteuclid.org/euclid.aos/1176344552>.]
- Elkins-Tanton, L. T., and T. L. Grove (2011), Water (hydrogen) in the lunar mantle: Results from petrology and magma ocean modeling, *Earth Planet. Sci. Lett.*, *307*, 173–179.
- Frohlich, C., and Y. Nakamura (2009), The physical mechanisms of deep moonquakes and intermediate-depth earthquakes: How similar and how different?, *Phys. Earth Planet. Inter.*, *173*, 365–374.
- Gagnepain-Beyneix, J., P. Lognonné, H. Chenet, D. Lombardi, and T. Spohn (2006), A seismic model of the lunar mantle and constraints on temperature and mineralogy, *Phys. Earth Planet. Inter.*, *159*, 140–166.
- Garcia, R. F., J. Gagnepain-Beyneix, S. Chevrot, and P. Lognonné (2011), Very preliminary reference Moon model, *Phys. Earth Planet. Inter.*, *188*, 96–113.
- Girard, J., J. Chen, P. Raterron, and C. W. Holyoke III (2013), Hydrolytic weakening of olivine at mantle pressure: Evidence of [100](010) slip system softening from single-crystal deformation experiments, *Phys. Earth Planet. Inter.*, *216*, 12–20.
- Goins, N. R., A. M. Danity, and M. N. Toksöz (1981), Seismic energy release of the Moon, *J. Geophys. Res.*, *86*, 378–388, doi:10.1029/JB086iB01p00378.
- Harada, Y., S. Goossens, K. Matsumoto, J. Yan, J. Ping, H. Noda, and J. Haruyama (2014), Strong tidal heating in an ultralow-viscosity zone at the core–mantle boundary of the Moon, *Nat. Geosci.*, *7*, 569–572, doi:10.1038/ngeo2211.
- Hacker, B. R., S. M. Peacock, G. A. Abers, and S. D. Holloway (2003), Subduction factory, 2, are intermediate-depth earthquakes in subducting slabs linked to metamorphic dehydration reactions?, *J. Geophys. Res.*, *108*(B1), 2030, doi:10.1029/2001JB001129.
- Ide, S., G. C. Beroza, S. G. Prejean, and W. L. Ellsworth (2003), Apparent break in earthquake scaling due to path and site effects on deep borehole recordings, *J. Geophys. Res.*, *108*(B5), 2271, doi:10.1029/2001JB001617.
- Karato, S. (2013), Geophysical constraints on the water content of the lunar mantle and its implications for the origin of the Moon, *Earth Planet. Sci. Lett.*, *384*, 144–153.
- Khan, A., and K. J. Mosegaard (2002), An inquiry into the lunar interior: A non-linear inversion of the Apollo lunar seismic data, *J. Geophys. Res.*, *107*(E6), 5036, doi:10.1029/2001JE001658.
- Khan, A., J. A. D. Connolly, J. MacLennan, and K. Mosegaard (2007), Joint Inversion of Seismic and Gravity Data for Lunar Composition and Thermal State, *Geophys. J. Int.*, *168*, 243, doi:10.1111/j.1365-246X.2006.03200.x.
- Khan, A., J. A. D. Connolly, A. Pommier, and J. Noir (2014), Geophysical evidence for melt in the deep lunar interior and implications for lunar evolution, *J. Geophys. Res. Planets*, *119*, 2197–2221, doi:10.1002/2014JE004661.

- Kuskov, O. L., and V. A. Kronrod (1998), Constitution of the Moon 5. Constraints on composition, density, temperature and radius of a core, *Phys. Earth Planet. Inter.*, *107*, 285–306.
- Kuskov, O. L., and V. A. Kronrod (2009), Geochemical constraints on the model of the composition and thermal conditions of the Moon according to seismic data, *Izv., Phys. Solid Earth*, *45*, 753, doi:10.1134/S1069351309090043.
- Lammlein, D. R. (1977), Lunar seismicity and tectonics, *Phys. Earth Planet. Inter.*, *14*, 224–174.
- Lognonné P., and C. Johnson (2007), Planetary seismology, in *Treatise in Geophysics, Planets and Moons*, vol. 10, chap. 4, edited by G. Schubert, pp. 69–122, Elsevier, Amsterdam, Netherlands, doi:10.1016/B978-044452748-6.00154-1.
- Lognonné P., and C. Johnson (2015), Planetary seismology, in *Treatise in Geophysics, Planets and Moons*, vol. 10, 2nd ed., chap. 10.03, edited by G. Schubert, pp. 65–120, Elsevier, Amsterdam, Netherlands, doi:10.1016/B978-0-444-53802-4.00167-6.
- Lognonné, P., J. Gagnepain-Beyneix, and H. Chenet (2003), A new seismic model of the Moon: Implication in terms of structure, formation and evolution, *Earth Planet. Sci. Lett.*, *211*, 27–44.
- Mayeda, K., and R. W. Walter (1996), Moment, energy, stress drop, and source spectra of western United States earthquakes from regional coda envelopes, *J. Geophys. Res.*, *101*(B5), 11,195–11,208, doi:10.1029/96JB00112.
- McKenzie, D., J. Jackson, and K. Priestley (2005), Thermal structure of oceanic and continental lithosphere, *Earth Planet. Sci. Lett.*, *233*, 337–349.
- Minshull, T. A., and N. R. Gouly (1988), The influence of tidal stresses on deep moonquake activity, *Phys. Earth Planet. Inter.*, *52*, 41–55.
- Nakamura, Y. (1992), Lunar—Catalog for lunar seismic data from Apollo passive seismic experiment on 8-mm video cassette (EXABYTE) tapes (University of Texas Institute for Geophysics).
- Nakamura, Y. (1978), A1 moonquakes—Source distribution and mechanism, *Lunar and Planet. Sci. Conf.*, *9th*, Houston, Tex., 13–17 March.
- Nakamura, Y. (2003), New identification of deep moonquakes in the Apollo lunar seismic data, *Phys. Earth Planet. Inter.*, *139*, 197–205.
- Nakamura, Y. (2009), Farside deep moonquakes and deep interior of the Moon, *J. Geophys. Res.*, *110*, E01001, doi:10.1029/2004JE002332.
- Nakamura, Y., and J. Koyama (1982), Seismic Q of the lunar upper mantle, *J. Geophys. Res.*, *87*(B6), 4855–4861, doi:10.1029/JB087iB06p04855.
- Ohuchi, T., T. Kawazoe, Y. Higo, K. Funakoshi, A. Suzuki, T. Kikegawa, and T. Irifune (2015), Dislocation-accommodated grain boundary sliding as the major deformation mechanism of olivine in the Earth's upper mantle, *Sci. Adv.*, *1*, e1500360.
- Phinney, R. A., and R. Burridge (1973), Representation of the elastic-gravitational excitation of a spherical Earth model by generalized spherical harmonics, *Geophys. J. R. astr. Soc.*, *34*, 451–487.
- Reches, Z., and D. A. Lockner (2010), Fault weakening and earthquake instability by powder lubrication, *Nature*, *467*, 452–455, doi:10.1038/nature09348.
- Saal, A. E., E. H. Hauri, M. Lo Cascio, J. A. Van Orman, M. J. Rutherford, and R. F. Cooper (2008), Volatile content of lunar volcanic glasses and the presence of water in the Moon's interior, *Nature*, *454*, 193–195.
- Schmittbuhl, J., S. Gentier, and S. Roux (1993), Field measurements of the roughness of fault surfaces, *Geophys. Res. Lett.*, *20*, 639–641, doi:10.1029/93GL00170.
- Schmittbuhl, J., G. Chambon, A. Hansen, and M. Bouchon (2006), Are stress distributions along faults the signature of asperity squeeze?, *Geophys. Res. Lett.*, *33*, L13307, doi:10.1029/2006GL025952.
- Shearer, P. M. (2009), *Introduction to Seismology*, 2nd ed., chap. 9, pp. 241–300, Cambridge Univ. Press, U.K.
- Toksöz, M. N., N. R. Goins, and C. H. Cheng (1977), Moonquakes: Mechanisms and relation to tidal stresses, *Science*, *196*, 979–981.
- Wahr, J., Z. A. Selvens, M. E. Mullen, A. C. Barr, G. Collins, M. M. Selvens, and R. T. Pappalardo (2009), Modeling stresses on satellites due to non-synchronous rotation and orbital eccentricity using gravitational potential theory, *Icarus*, *200*, 188–206.
- Weber, R. C., B. G. Bills, and C. L. Johnson (2009), Constraints on deep moonquake focal mechanisms through analyses of tidal stress, *J. Geophys. Res.*, *114*, E05001, doi:10.1029/2008JE003286.
- Weber, R. C., P. Lin, E. J. Garnero, Q. Williams, and P. Lognonné (2011), Seismic detection of the lunar core, *Science*, *331*(6015), 309–312.
- Ye, L., T. Lay, H. Kanamori, Z. Zhan, and Z. Duputel (2016), Diverse rupture processes in the 2015 Peru deep earthquake doublet, *Sci. Adv.*, *2*(6), e1600581, doi:10.1126/sciadv.1600581.

BIBLIOGRAPHIE

- Anderson, D., and W. Miller (1977), Seismology on Mars, *Journal of Geophysical Research*, 82(28), 4524–4546. (Cité page 27.)
- Araya, A., K. Sekiya, and Y. Shindo (2007), Laser-Interferometric Broadband Seismometer for Ocean Borehole Observations, in Proc. of International Symposium on Underwater Technology, *IEEE*, pp. 245–248. (Cité page 29.)
- Backus, G., and F. Gilbert (1970), Uniqueness in the inversion of inaccurate gross earth data, *Philosophical Transactions of the Royal Society of London. Series A, Mathematical and Physical Sciences*, 266(1173), 123–192. (Cité page 69.)
- Backus, G., and M. Mulcahy (1976a), Moment tensors and other phenomenological descriptions of seismic sources-i. continuous displacements, *Geophysical Journal International*, 46(2), 341–361. (Cité pages 12, 66 et 83.)
- Backus, G., and M. Mulcahy (1976b), Moment tensors and other phenomenological descriptions of seismic sources-ii. discontinuous displacements, *Geophysical Journal International*, 47(2), 301–329. (Cité pages 66 et 83.)
- Banerdt, W. B., S. E. Smrekar, D. Banfield, D. Giardini, M. Golombek, C. L. Johnson, P. Lognonné, A. Spiga, T. Spohn, C. Perrin, et al. (2020), Initial results from the insight mission on mars, *Nature Geoscience*, pp. 1–7. (Cité pages 3 et 67.)
- Banfield, D., J. Rodriguez-Manfredi, C. Russell, K. Rowe, D. Lene-man, H. Lai, P. Cruce, J. Means, C. Johnson, A. Mittelholz, et al. (2019), Insight auxiliary payload sensor suite (apss), *Space Science Reviews*, 215(1), 4. (Cité page 4.)

- Benioff, H., J. Harrison, L. LaCoste, W. Munk, and L. Slichter (1959), Searching for the earth's free oscillations, *Journal of Geophysical Research*, 64(9), 1334–1337. (Cité page 7.)
- Benioff, H., F. Press, and S. Smith (1961), Excitation of the free oscillations of the earth by earthquakes, *Journal of Geophysical Research*, 66(2), 605–619. (Cité page 7.)
- Bolt, B. A., and J. S. Derr (1969), Free bodily vibrations of the terrestrial planets, *Vistas in astronomy*, 11, 69–102. (Cité page 8.)
- Castillo-Rogez, J. (2006), Internal structure of rhea, *Journal of Geophysical Research : Planets*, 111(E11). (Cité page 100.)
- Colaïtis, A., A. Spiga, F. Hourdin, C. Rio, F. Forget, and E. Millour (2013), A thermal plume model for the martian convective boundary layer, *Journal of Geophysical Research : Planets*, 118(7), 1468–1487. (Cité pages 15 et 18.)
- Crisp, J. A., M. Adler, J. R. Matijevic, S. W. Squyres, R. E. Arvidson, and D. M. Kass (2003), Mars exploration rover mission, *Journal of Geophysical Research : Planets*, 108(E12). (Cité page 1.)
- Dahlen, F., and J. Tromp (1998), *Theoretical global seismology*, Princeton university press. (Cité pages 8 et 80.)
- Delage, P., F. Karakostas, A. Dhemaied, M. Belmokhtar, P. Lognonné, M. Golombek, E. De Laure, K. Hurst, J.-C. Dupla, S. Kedar, et al. (2017), An investigation of the mechanical properties of some martian regolith simulants with respect to the surface properties at the insight mission landing site, *Space Science Reviews*, 211(1-4), 191–213. (Cité page 48.)
- Dreibus, G., and H. Wanke (1985), Mars, a volatile-rich planet, *Meteoritics*, 20, 367–381. (Cité page 2.)
- Dziewonski, A. M., and D. L. Anderson (1981), Preliminary reference earth model, *Physics of the earth and planetary interiors*, 25(4), 297–356. (Cité pages 4 et 7.)
- Enkhtur, O., T. D. Nguyen, J. M. Kim, and S. R. Kim (2013), Evaluation of the settlement influence factors of shallow foundation by

- numerical analyses, *KSCE Journal of Civil Engineering*, 17(1), 85–95. (Cité page 48.)
- Folkner, W. M., V. Dehant, S. Le Maistre, M. Yseboodt, A. Rivoldini, T. Van Hoolst, S. W. Asmar, and M. P. Golombek (2018), The rotation and interior structure experiment on the insight mission to mars, *Space Science Reviews*, 214(5), 100. (Cité page 3.)
- Forget, F., and S. Lebonnois (2013), Global climate models of the terrestrial planets, *Comparative Climatology of Terrestrial Planets*, 1, 213–229. (Cité page 73.)
- Forget, F., F. Hourdin, R. Fournier, C. Hourdin, O. Talagrand, M. Collins, S. R. Lewis, P. L. Read, and J.-P. Huot (1999), Improved general circulation models of the martian atmosphere from the surface to above 80 km, *Journal of Geophysical Research : Planets*, 104(E10), 24,155–24,175. (Cité pages 15 et 73.)
- Gagnepain-Beyneix, J., P. Lognonné, H. Chenet, D. Lombardi, and T. Spohn (2006), A seismic model of the lunar mantle and constraints on temperature and mineralogy, *Physics of the Earth and Planetary Interiors*, 159(3-4), 140–166. (Cité page 104.)
- Garcia, R. F., J. Gagnepain-Beyneix, S. Chevrot, and P. Lognonné (2011), Very preliminary reference moon model, *Physics of the Earth and Planetary Interiors*, 188(1-2), 96–113. (Cité page 101.)
- Garcia, R. F., B. Kenda, T. Kawamura, A. Spiga, N. Murdoch, P. H. Lognonné, R. Widmer-Schmidrig, N. Compaire, G. Orhand-Mainsant, D. Banfield, et al. (2020), Pressure effects on the seis-insight instrument, improvement of seismic records, and characterization of long period atmospheric waves from ground displacements, *Journal of Geophysical Research : Planets*, 125(7), e2019JE006,278. (Cité page 5.)
- Giardini, D., P. Lognonné, W. B. Banerdt, W. T. Pike, U. Christensen, S. Ceylan, J. F. Clinton, M. van Driel, S. C. Stähler, M. Böse, et al. (2020), The seismicity of mars, *Nature Geoscience*, 13(3), 205–212. (Cité page 9.)

- Goldreich, P., and D. Keeley (1977), Solar seismology. ii-the stochastic excitation of the solar p-modes by turbulent convection, *The Astrophysical Journal*, 212, 243–251. (Cité page 12.)
- Golombek, M., A. Haldemann, R. Simpson, R. Fergason, N. Putzig, R. Arvidson, J. Bell III, and M. Mellon (2008), Martian surface properties from joint analysis of orbital, earth-based, and surface observations, *The Martian Surface-Composition, Mineralogy, and Physical Properties*, 1, 468. (Cité page 47.)
- Golombek, M. P., W. B. Banerdt, K. L. Tanaka, and D. M. Tralli (1992), A prediction of mars seismicity from surface faulting, *Science*, 258(5084), 979–981. (Cité page 8.)
- Gómez-Elvira, J., C. Armiens, L. Castañer, M. Domínguez, M. Genzer, F. Gómez, R. Haberle, A.-M. Harri, V. Jiménez, H. Kahanpää, et al. (2012), Rems : The environmental sensor suite for the mars science laboratory rover, *Space science reviews*, 170(1-4), 583–640. (Cité pages 13 et 15.)
- Gudkova, T., and V. Zharkov (2004), Mars : interior structure and excitation of free oscillations, *Physics of the Earth and Planetary Interiors*, 142(1-2), 1–22. (Cité page 8.)
- Gutenberg, B., and C. Richter (1956), Earthquake magnitude, intensity, energy, and acceleration : (second paper), *Bulletin of the seismological society of America*, 46(2), 105–145. (Cité page 92.)
- Haberle, R. M., M. M. Joshi, J. R. Murphy, J. R. Barnes, J. T. Schofield, G. Wilson, M. Lopez-Valverde, J. L. Hollingsworth, A. F. Bridger, and J. Schaeffer (1999), General circulation model simulations of the mars pathfinder atmospheric structure investigation/meteorology data. (Cité page 73.)
- Harder, H. (1998), Phase transitions and the three-dimensional planform of thermal convection in the martian mantle, *Journal of Geophysical Research : Planets*, 103(E7), 16,775–16,797. (Cité pages 12 et 4.)
- Hecht, M., S. Kounaves, R. Quinn, S. West, S. Young, D. Ming, D. Catling, B. Clark, W. Boynton, J. Hoffman, et al. (2009), Detection of

- perchlorate and the soluble chemistry of martian soil at the phoenix lander site, *Science*, 325(5936), 64–67. (Cité page 1.)
- Hess, S., R. Henry, C. B. Leovy, J. Ryan, and J. E. Tillman (1977), Meteorological results from the surface of mars : Viking 1 and 2, *Journal of Geophysical Research*, 82(28), 4559–4574. (Cité page 14.)
- Jackson, I., and U. H. Faul (2010), Grainsize-sensitive viscoelastic relaxation in olivine : Towards a robust laboratory-based model for seismological application, *Physics of the Earth and Planetary Interiors*, 183(1-2), 151–163. (Cité page 101.)
- Jordan, R., G. Picardi, J. Plaut, K. Wheeler, D. Kirchner, A. Safaeinili, W. Johnson, R. Seu, D. Calabrese, E. Zampolini, et al. (2009), The mars express marsis sounder instrument, *Planetary and Space Science*, 57(14-15), 1975–1986. (Cité page 1.)
- Kawamura, T., N. Kobayashi, S. Tanaka, and P. Lognonné (2015), Lunar surface gravimeter as a lunar seismometer : Investigation of a new source of seismic information on the moon, *Journal of Geophysical Research : Planets*, 120(2), 343–358. (Cité page 5.)
- Kawamura, T., P. Lognonné, Y. Nishikawa, and S. Tanaka (2017), Evaluation of deep moonquake source parameters : Implication for fault characteristics and thermal state, *Journal of Geophysical Research : Planets*. (Cité pages 21, 105 et 107.)
- Kaydash, V., M. Kreslavsky, Y. G. Shkuratov, G. Videen, J. Bell III, and M. Wolff (2006), Measurements of winds on mars with hubble space telescope images in 2003 opposition, *Icarus*, 185(1), 97–101. (Cité page 9.)
- Kenda, B., P. Lognonné, A. Spiga, T. Kawamura, S. Kedar, W. B. Banerdt, R. Lorenz, D. Banfield, and M. Golombek (2017), Modeling of ground deformation and shallow surface waves generated by martian dust devils and perspectives for near-surface structure inversion, *Space Science Reviews*, 211(1-4), 501–524. (Cité pages 16, 74 et 77.)
- Khan, A., and J. Connolly (2007), Constraining the composition and

- thermal state of mars from inversion of geophysical data, *LPI Contributions*, 1353, 3013. (Cité page 80.)
- Knapmeyer, M., J. Oberst, E. Hauber, M. Wählisch, C. Deuchler, and R. Wagner (2006), Working models for spatial distribution and level of mars' seismicity, *Journal of Geophysical Research : Planets*, 111(E11). (Cité page 8.)
- Kobayashi, N., and K. Nishida (1998a), Continuous excitation of planetary free oscillations by atmospheric disturbances, *Nature*, 395(6700), 357–360. (Cité pages 10, 11, 12, 90, 94 et 111.)
- Kobayashi, N., and K. Nishida (1998b), Atmospheric excitation of planetary free oscillations, *Journal of Physics : Condensed Matter*, 10(49), 11,557. (Cité page 10.)
- Kovach, R. L., and D. L. Anderson (1965), The interiors of the terrestrial planets, *Journal of Geophysical Research*, 70(12), 2873–2882. (Cité page 8.)
- Laske, G., and R. Widmer-Schmidrig (2015), *Treatise on geophysics, Theory and Observations : Normal Mode and Surface Wave Observations*, vol. 1.04, 117–167 pp., Elsevier. (Cité page 7.)
- Lognonné, P. (1991), Normal modes and seismograms in an anelastic rotating earth, *Journal of Geophysical Research : Solid Earth*, 96(B12), 20,309–20,319. (Cité pages 8 et 80.)
- Lognonné, P. (2005), Planetary seismology, *Annu. Rev. Earth Planet. Sci.*, 33, 571–604. (Cité pages 5, 8, 9, 11 et 55.)
- Lognonné, P., and E. Clévéde (2002), 10 Normal modes of the earth and planets, *International Geophysics*, 81(PART A), 0–12, doi : 10.1016/S0074-6142(02)80213-3. (Cité pages 5, 80 et 82.)
- Lognonné, P., and D. Giardini (2000), The NetLander very broad band seismometer, *Planetary and Space Science*, 48, 1289–1302. (Cité page 8.)
- Lognonné, P., and C. Johnson (2007), *Planetary Seismology*, vol. 10.03, 69–122 pp., Elsevier. (Cité pages 8, 11, 12, 55, 56, 74, 84, 94 et 111.)

- Lognonné, P., and C. Johnson (2015), *Planetary Seismology*, vol. 10.03, 65–120 pp., Elsevier. (Cité pages 5, 8, 74, 84 et 92.)
- Lognonné, P., and B. Mosser (1993), Planetary seismology, *Surveys in Geophysics*, 14(3), 239–302. (Cité pages 8, 58 et 66.)
- Lognonné, P., B. Mosser, and F. Dahlen (1994), Excitation of jovian seismic waves by the shoemaker-levy 9 cometary impact, *Icarus*, 110(2), 180–195. (Cité pages 12 et 82.)
- Lognonné, P., J. G. Beyneix, W. B. Banerdt, S. Cacho, J. F. Karczewski, and M. Morand (1996), Ultra broad band seismology on intermars-net, *Planetary and space science*, 44(11), 1237–1249. (Cité pages 5 et 8.)
- Lognonné, P., J. Beyneix, and W. Banerdt (1996), Ultra broad band seismology on InterMarsNet, *Planetary and Space Science*, 44(11), 1237—1249. (Cité page 27.)
- Lognonné, P., V. Zharkov, J. Karczewski, B. Romanowicz, M. Menvielle, G. Poupinet, B. Brient, C. Cavoit, A. Desautez, B. Dole, et al. (1998a), The seismic optimism experiment, *Planetary and space science*, 46(6-7), 739–747. (Cité pages 10 et 11.)
- Lognonné, P., E. Clévéde, and H. Kanamori (1998b), Computation of seismograms and atmospheric oscillations by normal-mode summation for a spherical earth model with realistic atmosphere, *Geophysical Journal International*, 135(2), 388–406. (Cité pages 68, 80 et 119.)
- Lognonné, P., T. Spohn, and D. Giardini (2003), Mars in depth, *Astronomy & Geophysics*, 44(4), 4–15. (Cité page 5.)
- Lognonné, P., G. Occhipinti, and R. Garcia (2005), Seismic interior/atmospheric coupling on venus. (Cité page 10.)
- Lognonné, P., W. Pike, V. Tong, and R. Garcia (2015), Planetary seismometry, *Extraterrestrial Seismology*, pp. 36–48. (Cité page 74.)
- Lognonné, P., F. Karakostas, L. Rolland, and Y. Nishikawa (2016), Modeling of atmospheric-coupled rayleigh waves on planets with

- atmosphere : From earth observation to mars and venus perspectives, *The Journal of the Acoustical Society of America*, 140(2), 1447–1468. (Cité pages 10, 11, 57 et 80.)
- Lognonné, P., W. B. Banerdt, D. Giardini, W. Pike, U. Christensen, P. Laudet, S. De Raucourt, P. Zweifel, S. Calcutt, M. Bierwirth, et al. (2019), Seis : Insight's seismic experiment for internal structure of mars, *Space Science Reviews*, 215(1). (Cité pages 3, 8 et 86.)
- Lognonné, P., W. Banerdt, W. Pike, D. Giardini, U. Christensen, R. F. Garcia, T. Kawamura, S. Kedar, B. Knapmeyer-Endrun, L. Margerin, et al. (2020), Constraints on the shallow elastic and anelastic structure of mars from insight seismic data, *Nature Geoscience*, 13(3), 213–220. (Cité pages 9, 67 et 112.)
- Lognonné, P. (2008), Seismology on mars with the seis/humboldt experiment on the exomars mission, pp. 1822–. (Cité page 57.)
- Lorenz, R. D. (1996), Martian surface wind speeds described by the weibull distribution, *Journal of spacecraft and rockets*, 33(5), 754–756. (Cité pages 49 et 50.)
- Lorenz, R. D. (2012), Planetary seismology-expectations for lander and wind noise with application to venus, *Planetary and Space Science*, 62(1), 86–96. (Cité page 27.)
- Love, A. E. H. (1908), The gravitational stability of the earth, *Philosophical Transactions of the Royal Society of London. Series A, Containing Papers of a Mathematical or Physical Character*, 207, 171–241. (Cité pages 21 et 22.)
- Madeleine, J.-B., F. Forget, E. Millour, L. Montabone, and M. Wolff (2011), Revisiting the radiative impact of dust on mars using the lmd global climate model, *Journal of Geophysical Research : Planets*, 116(E11). (Cité page 15.)
- Malin, M., M. Carr, G. Danielson, M. Davies, W. Hartmann, A. Ingersoll, P. James, H. Masursky, A. McEwen, L. Soderblom, et al. (1998), Early views of the martian surface from the mars orbiter camera of mars global surveyor, *Science*, 279(5357), 1681–1685. (Cité page 1.)

- McEwen, A. S., E. M. Eliason, J. W. Bergstrom, N. T. Bridges, C. J. Hansen, W. A. Delamere, J. A. Grant, V. C. Gulick, K. E. Herkenhoff, L. Keszthelyi, et al. (2007), Mars reconnaissance orbiter's high resolution imaging science experiment (hirise), *Journal of Geophysical Research : Planets*, 112(E5). (Cité page 1.)
- Millot-Langet, R., E. Clévéde, and P. Lognonné (2002), Realistic long period synthetic seismograms using normal modes of a 3d anelastic elliptic rotating earth, in *EGS General Assembly Conference Abstracts*, vol. 27. (Cité page 8.)
- Mimoun, D., N. Murdoch, P. Lognonné, T. Pike, K. Hurst, S. Team, et al. (2016), The seismic noise model of the insight mission to mars, *Space Sci. Rev.* (Cité page 87.)
- Mimoun, D., N. Murdoch, P. Lognonné, K. Hurst, W. T. Pike, J. Hurley, T. Nébut, W. B. Banerdt, S. Team, et al. (2017), The noise model of the seis seismometer of the insight mission to mars, *Space Science Reviews*, 211(1-4), 383–428. (Cité page 9.)
- Montabone, L., F. Forget, E. Millour, R. Wilson, S. Lewis, B. Cantor, D. Kass, A. Kleinböhl, M. Lemmon, M. Smith, et al. (2015), Eight-year climatology of dust optical depth on mars, *Icarus*, 251, 65–95. (Cité pages 19 et 78.)
- Montagner, J. P. (2015), *Treatise on geophysics, Deep Earth Structure : Upper Mantle Structure : Global Isotropic and Anisotropic Elastic Tomography*, vol. 1.19, 613–639 pp., Elsevier. (Cité page 7.)
- Murdoch, N., B. Kenda, T. Kawamura, A. Spiga, P. Lognonné, D. Mimoun, and W. B. Banerdt (2017), Estimations of the seismic pressure noise on mars determined from large eddy simulations and demonstration of pressure decorrelation techniques for the insight mission, *Space Science Reviews*, 211(1-4), 457–483. (Cité pages 16, 74, 77 et 87.)
- Murphy, J. R., C. B. Leovy, and J. E. Tillman (1990a), Observations of martian surface winds at the viking lander 1 site, *Journal of Geophysical Research : Solid Earth* (1978–2012), 95(B9), 14,555–14,576. (Cité page 9.)

- Murphy, J. R., L. CB, and T. JE (1990b), Observations of martian surface winds at the viking lander 1 site, *Journal of Geophysical Research*, 95(B9), 14,555–14,576. (Cité page 13.)
- Nakamura, Y. (1982), Apollo lunar seismic experiment—Final summary, *Journal of Geophysical Research*, 87(2), A117–A123. (Cité page 103.)
- Navarro, T., J.-B. Madeleine, F. Forget, A. Spiga, E. Millour, F. Montmessin, and A. Määttänen (2014), Global climate modeling of the martian water cycle with improved microphysics and radiatively active water ice clouds, *Journal of Geophysical Research : Planets*, 119(7), 1479–1495. (Cité page 15.)
- Nimmo, F., U. Faul, and E. Garnero (2012), Dissipation at tidal and seismic frequencies in a melt-free moon, *Journal of Geophysical Research : Planets*, 117(E9). (Cité pages 101, 103 et 104.)
- Nishida, K. (2013a), Global propagation of body waves revealed by cross-correlation analysis of seismic hum, *Geophysical Research Letters*, 40(9), 1691–1696. (Cité page 10.)
- Nishida, K. (2013b), Earth's background free oscillations, *Annual Review of Earth and Planetary Sciences*, 41, 719–740. (Cité page 10.)
- Nishida, K. (2014), Source spectra of seismic hum, *Geophysical Journal International*, 199(1), 416–429. (Cité page 10.)
- Nishida, K., N. Kobayashi, and Y. Fukao (2000), Resonant oscillations between the solid earth and the atmosphere, *Science*, 287(5461), 2244–2246. (Cité page 10.)
- Nishida, K., J.-P. Montagner, and H. Kawakatsu (2009), Global surface wave tomography using seismic hum, *Science*, 326(5949), 112–112. (Cité page 11.)
- Nishikawa, Y., A. Araya, K. Kurita, N. Kobayashi, and T. Kawamura (2014), Designing a torque-less wind shield for broadband observation of marsquakes, *Planetary and Space Science*, 104, 288–294. (Cité page 25.)

- Nishikawa, Y., P. Lognonné, T. Kawamura, A. Spiga, E. Stutzmann, M. Schimmel, T. Bertrand, F. Forget, and K. Kurita (2019), Mars' background free oscillations, *Space Science Reviews*, 215(1), 13, doi : 10.1007/s11214-019-0579-9. (Cité pages 73 et 82.)
- Okal, E. A., and D. L. Anderson (1978), Theoretical models for mars and their seismic properties, *Icarus*, 33(3), 514–528. (Cité page 8.)
- Panning, M. P., and S. Kedar (2019), Seismic response of the mars curiosity rover : Implications for future planetary seismology, *Icarus*, 317, 373–378. (Cité page 4.)
- Panning, M. P., P. Lognonné, W. B. Banerdt, R. Garcia, M. Golombek, S. Kedar, B. Knapmeyer-Endrun, A. Mocquet, N. A. Teanby, J. Tromp, et al. (2017), Planned products of the mars structure service for the insight mission to mars, *Space Science Reviews*, 211(1-4), 611–650. (Cité pages 8 et 88.)
- Park, J., T.-R. A. Song, J. Tromp, E. Okal, S. Stein, G. Roult, E. Clevede, G. Laske, H. Kanamori, P. Davis, et al. (2005), Earth's free oscillations excited by the 26 december 2004 sumatra-andaman earthquake, *Science*, 308(5725), 1139–1144. (Cité pages 13 et 7.)
- Petrosyan, A., B. Galperin, S. E. Larsen, S. Lewis, A. Määttänen, P. Read, N. Renno, L. Rogberg, H. Savijärvi, T. Siili, et al. (2011), The martian atmospheric boundary layer, *Reviews of Geophysics*, 49(3). (Cité page 13.)
- Phillips, R. J., and R. E. Grimm (1991), Martian seismicity, in *Lunar and Planetary Science Conference*, vol. 22. (Cité page 8.)
- Phinney, R. A., and R. Burridge (1973), Representation of the elastic-gravitational excitation of a spherical earth model by generalized spherical harmonics, *Geophysical Journal International*, 34(4), 451–487. (Cité pages 119 et 129.)
- Pottier, A., F. Forget, F. Montmessin, T. Navarro, A. Spiga, E. Millour, A. Szantai, and J.-B. Madeleine (2017), Unraveling the martian water cycle with high-resolution global climate simulations, *Icarus*, doi :10.1016/j.icarus.2017.02.016. (Cité page 18.)

- Read, P. L., and S. R. Lewis (2004), *The Martian climate revisited : atmosphere and environment of a desert planet*, Springer Science & Business Media. (Cité pages 9, 18 et 78.)
- Redmond, J. C., and F. F. Fish (1964), The luni-tidal interval in mars and the secular acceleration of phobos, *Icarus*, 3(2), 87–91. (Cité page 98.)
- Rhie, J., and B. Romanowicz (2004), Excitation of earth's continuous free oscillations by atmosphere–ocean–seafloor coupling, *Nature*, 431(7008), 552. (Cité pages 10 et 92.)
- Rhie, J., and B. Romanowicz (2006), A study of the relation between ocean storms and the earth's hum, *Geochemistry, Geophysics, Geosystems*, 7(10). (Cité page 10.)
- Rivoldini, A., T. Van Hoolst, O. Verhoeven, A. Mocquet, and V. Dehant (2011), Geodesy constraints on the interior structure and composition of mars, *Icarus*, 213(2), 451–472. (Cité page 80.)
- Romanowicz, B., and B. Mitchell (2015), *Treatise on geophysics, Deep Earth Structure : Q of the Earth from Crust to Core*, vol. 1.19, 789–827 pp., Elsevier. (Cité page 7.)
- Schofield, J., J. R. Barnes, D. Crisp, R. M. Haberle, S. Larsen, J. Magalhaes, J. R. Murphy, A. Seiff, and G. Wilson (1997), The mars pathfinder atmospheric structure investigation/meteorology (asi/met) experiment, *Science*, 278(5344), 1752–1758. (Cité pages 9, 13 et 14.)
- Smith, P., J. Bell, N. Bridges, D. Britt, L. Gaddis, R. Greeley, H. Keller, K. Herkenhoff, R. Jaumann, J. Johnson, et al. (1997), Results from the mars pathfinder camera, *Science*, 278(5344), 1758–1765. (Cité page 1.)
- Smrekar, S. E., P. Lognonné, T. Spohn, W. B. Banerdt, D. Breuer, U. Christensen, V. Dehant, M. Drilleau, W. Folkner, N. Fuji, et al. (2019), Pre-mission insights on the interior of mars, *Space Science Reviews*, 215(1), 3. (Cité pages 12, 1, 2, 3 et 80.)
- Soffen, G. A., and C. W. Snyder (1976), The first viking mission to mars, *Science*, 193, 759–766. (Cité page 1.)

- Sohl, F., and T. Spohn (1997), The interior structure of Mars : Implications from SNC meteorites, *Journal of Geophysical Research : Planets*, 102, 1613–1635. (Cité pages 80, 108 et 122.)
- Solomon, S. C., D. L. Anderson, W. B. Banerdt, R. G. Butler, P. M. Davis, F. K. Duennebier, Y. Nakamura, E. A. Okal, and R. J. Phillips (1991), Scientific rationale and requirements for a global seismic network on mars. (Cité page 8.)
- Spiga, A. (2011), Elements of comparison between martian and terrestrial mesoscale meteorological phenomena : Katabatic winds and boundary layer convection, *Planetary and Space Science*, 59(10), 915–922. (Cité page 13.)
- Spiga, A., and F. Forget (2009), A new model to simulate the martian mesoscale and microscale atmospheric circulation : Validation and first results, *Journal of Geophysical Research : Planets*, 114(E2). (Cité page 9.)
- Spiga, A., and S. R. Lewis (2010), Martian mesoscale and microscale wind variability of relevance for dust lifting, *Mars*, 5, 146–158. (Cité pages 13, 15 et 16.)
- Spiga, A., F. Forget, S. Lewis, and D. Hinson (2010), Structure and dynamics of the convective boundary layer on mars as inferred from large-eddy simulations and remote-sensing measurements, *Quarterly Journal of the Royal Meteorological Society*, 136(647), 414–428. (Cité pages 73 et 77.)
- Spiga, A., N. Teanby, F. Forget, A. Lucas, B. Kenda, D. Banfield, R. Widmer-Schmidrig, N. Murdoch, M. Lemmon, R. Garcia, L. Martire, O. Karatekin, S. Le Maistre, B. Van Hove, V. Dehant, L. Lognonné, R. Lorenz, D. Mimoun, S. Rodriguez, E. Beucler, I. Daubar, M. Golombek, T. Bertrand, Y. Nishikawa, E. Millour, L. Rolland, Q. Brissaud, J. Rodriguez Manfredi, T. Kawamura, A. Mocquet, N. Mueller, R. Martin, J. Clinton, E. Stutzmann, T. Spohn, S. Smrekar, and W. Banerdt (2018), Atmospheric Science with InSight, *Space Science Reviews* (submitted). (Cité pages 9 et 89.)

- Spohn, T., M. Acuña, and D. Breuer (2001), GEOPHYSICAL CONSTRAINTS ON THE EVOLUTION OF MARS, *Space Science reviews*, 96, 231–262. (Cité page 80.)
- Spohn, T., M. Grott, S. E. Smrekar, J. Knollenberg, T. L. Hudson, C. Krause, N. Müller, J. Jänchen, A. Börner, T. Wippermann, O. Krömer, R. Lichtenheldt, L. Wisniewski, J. Grygorczuk, M. Fittock, S. Rheershemius, T. Spröwitz, E. Kopp, I. Walter, A. C. Plesa, D. Breuer, P. Morgan, and W. B. Banerdt (2018), The heat flow and physical properties package (hp3) for the insight mission, *Space Science Reviews*, 214(5), 96, doi :10.1007/s11214-018-0531-4. (Cité page 3.)
- Suda, N., K. Nawa, and Y. Fukao (1998), Earth's background free oscillations, *Science*, 279(5359), 2089–2091. (Cité page 10.)
- Tanimoto, T. (2001), Continuous free oscillations : atmosphere-solid earth coupling, *Annual Review of Earth and Planetary Sciences*, 29(1), 563–584. (Cité page 11.)
- Tanimoto, T. (2005), The oceanic excitation hypothesis for the continuous oscillations of the earth, *Geophysical Journal International*, 160(1), 276–288. (Cité page 10.)
- Tanimoto, T., and J. Um (1999), Cause of continuous oscillations of the earth, *Journal of Geophysical Research : Solid Earth*, 104(B12), 28,723–28,739. (Cité page 10.)
- Taylor, P. A., D. C. Catling, M. Daly, C. S. Dickinson, H. P. Gunnlaugsson, A.-M. Harri, and C. F. Lange (2008), Temperature, pressure, and wind instrumentation in the phoenix meteorological package, *Journal of Geophysical Research : Planets*, 113(E3). (Cité pages 13 et 14.)
- Toyota, T., K. Kurita, and A. Spiga (2011), Distribution and time-variation of spire streaks at pavonis mons on mars, *Planetary and Space Science*, 59(8), 672–682. (Cité page 47.)
- Trebi-Ollennu, A., E. T. Baumgartner, P. C. Leger, and R. G. Bonitz (2005), Robotic arm in-situ operations for the mars exploration rovers surface mission, in *Systems, Man and Cybernetics, 2005 IEEE International Conference on*, vol. 2, pp. 1799–1806, IEEE. (Cité page 29.)

- Unno, W., Y. Osaki, H. Ando, and H. Shibahashi (1979), Nonradial oscillations of stars, *Tokyo, University of Tokyo Press; Forest Grove, Ore., ISBS, Inc., 1979. 330 p.* (Cité page 119.)
- Van Hoolst, T., V. Dehant, F. Roosbeek, and P. Lognonné (2003), Tidally induced surface displacements, external potential variations, and gravity variations on mars, *Icarus*, 161(2), 281–296. (Cité page 21.)
- Versteeg, H. K., and W. Malalasekera (2007), *An introduction to computational fluid dynamics : the finite volume method*, Pearson Education. (Cité page 34.)
- Vondrak, R., J. Keller, G. Chin, and J. Garvin (2010), Lunar reconnaissance orbiter (lro) : observations for lunar exploration and science, *Space science reviews*, 150(1-4), 7–22. (Cité page 103.)
- Watada, S. (1995), Part i. near-source acoustic coupling between the atmosphere and the solid earth during volcanic eruptions. part ii. nearfield normal mode amplitude anomalies of the landers earthquake, Ph.D. thesis, California Institute of Technology. (Cité page 119.)
- Watada, S., and H. Kanamori (2010), Acoustic resonant oscillations between the atmosphere and the solid earth during the 1991 mt. pinatubo eruption, *Journal of Geophysical Research : Solid Earth*, 115(B12). (Cité pages 11 et 68.)
- Watada, S., and G. Masters (2001), Oceanic excitation of the continuous oscillations of the Earth, *AGU Fall Meeting Abstracts*, S32A-0620. (Cité page 10.)
- Webb, S. C. (2007), The earth's hum is driven by ocean waves over the continental shelves, *Nature*, 445(7129), 754. (Cité page 10.)
- Williams, J. G., A. S. Konopliv, D. H. Boggs, R. S. Park, D.-N. Yuan, F. G. Lemoine, S. Goossens, E. Mazarico, F. Nimmo, R. C. Weber, et al. (2014), Lunar interior properties from the grail mission, *Journal of Geophysical Research : Planets*, 119(7), 1546–1578. (Cité pages 21, 103 et 107.)

- Woodhouse, J., and A. Deuss (2015), *Theory and Observations - Earth's Free Oscillations*, vol. 1.03, 79–115 pp., Elsevier. (Cité page 7.)
- Zeitlin, C., D. Hassler, F. Cucinotta, B. Ehresmann, R. Wimmer-Schweingruber, D. Brinza, S. Kang, G. Weigle, S. Böttcher, E. Böhm, et al. (2013), Measurements of energetic particle radiation in transit to mars on the mars science laboratory, *science*, 340(6136), 1080–1084. (Cité page 1.)
- Zharkov, V., and T. Gudkova (1997), On the dissipative factor of the martian interiors, *Planetary and space science*, 45(4), 401–407. (Cité page 8.)

